Dissertation zur Erlangung des Doktorgrades der Naturwissenschaften

vorgelegt im Fachbereich Biochemie, Chemie und Pharmazie
der Goethe Universität Frankfurt am Main

"Establishment of rhodopsin-based genetically encoded voltage indicators to study neuronal networks in the nematode *Caenorhabditis elegans*"

von
Negin Azimi Hashemi
aus Mashad/ Iran

Frankfurt am Main 2020
(D30)

Supervisor: Prof. Dr. Alexander Gottschalk

Vom Fachbereich Biochemie, Chemie und Pharmazie der Goethe-Universität als Dissertation angenommen.

Dekan: Prof. Dr. Clemens Glaubitz

Gutachter: Prof. Dr. Alexander Gottschalk
Jun. Prof. Inga Hänelt

Datum der Disputation:

ERKLÄRUNG

Ich erkläre hiermit, dass ich mich bisher keiner Doktorprüfung im Mathematisch-Naturwissenschaftlichen Bereich unterzogen habe.

Frankfurt am Main, den ....

Negin Azimi Hashemi………………………………

Versicherung

Ich erkläre hiermit, dass ich die vorgelegte Dissertation über ***"Establishment of rhodopsin-based genetically encoded voltage indicators to study neuronal networks in the nematode Caenorhabditis elegans"*** selbständig angefertigt und mich anderer Hilfsmittel als der in ihr angegebenen nicht bedient habe, insbesondere, dass alle Entlehnungen aus anderen Schriften mit Angabe der betreffenden Schrift gekennzeichnet sind.

Ich versichere, die Grundsätze der guten wissenschaftlichen Praxis beachtet, und nicht die Hilfe einer kommerziellen Promotionsvermittlung in Anspruch genommen zu haben.

Frankfurt am Main, den ....

Negin Azimi Hashemi ………………………………

Willst du dich am Ganzen erquicken,
so musst du das Ganze im Kleinen erblicken.

Gedichte: Gott, Gemüt und Welt
Johann Wolfgang von Goethe

Meiner D.N.A gewidmet!

Table of contents

3.3: Tracking Imaging action potentials in the pharynx of wild type *C. elegans*

I List of the abbreviations:

Abbreviation	**Definition**
ACh	Acetylcholine
AP	Action potential
Arch	Archaerhodopsin3
ATR	All- trans- Retinal
a.u	Arbitrary units
Bp	Base Pairs
BR	Bacteriorhodopsin
BFP	Blue Fluorescent Protein
BSA	Bovines Serum Albumin
BWM	Body wall muscles
Ca^{2+}	Calcium ion
Cl^{-}	Chloridoid
C. elegans	*Caenorhabditis elegans*
CGC	Caenorhabditis Genetics Center
ChR2	Channelrhodopsin-2
CFP	Cyan fluorescent protein
D	Aspartate
DMAR	(Dimethyl-amino)phenyl- retinal
DMSO	Dimethylsulfoxid
DNA	Deoxyribonucleic acid
E	Glutamate
egl	Egg laying defect
ER	Endoplasmic reticulum
e. Coli	*Escherichia Coli*
eFRET	Electrochromic Förster resonance energy transfer
fps	Frame per second

GEVI	Genetically encoded voltage indicator
GCaMP	GFP-Calmodulin-M13-Protein
GFP	Green fluorescent protein
H	Histidine
LB	Lysogeny broth
Min	Minutes
ms	Milli seconds
mW	Milli Watt
N	Aspargine
Nema-A	Nemadipine-A
NGM	Nematode growth medium
nM, µM, mM	Nano-,micro-, milli-Molar
nm, µm, mm^2	Nanometer, Micrometer, square Millimeter
n.s.	not significant
s	second
SEWLB	single egg/worm lysis buffer
TAE	Tris- Acetate- EDTA- Puffer
TE	Tris- EDTA Puffer
VSP	Voltage sensitive protein
wt	Wild type
YFP	Yellow fluorescent protein
zxEx	Systematic number of an extrachromosomal transgene
zxIs	Systematic number of an integrated transgene

II

A Zusammenfassung

Die Untersuchung von Mechanismen der Kommunikation in neuronalen Schaltkreisen und der Wechselwirkungen zwischen den Neuronen ist der Schlüssel zum Verständnis der Reaktion einzelner Zellen oder Zellensembles, die schlussendlich zu Verhalten, Bewusstsein, Emotion und Kognition führen. Die Kommunikation zwischen Neuronen geht mit einer Veränderung des Membranpotentials einher. Die Beobachtung solcher elektrischen Ereignisse ist die Voraussetzung für das Verständnis der Mechanismen in neuronalen Schaltkreisen.

Die Elektrophysiologie war jahrzehntelang das Standardverfahren zur Untersuchung elektrischer Signale in Zellen. Diese invasive Methode, die bei sezierten Tieren durchgeführt wird, weist jedoch gewisse Einschränkungen auf.

Zum einen kann sie nur in beschränktem Masse und mit großem experimentellem Aufwand die Aktivitäten vieler Zellen gleichzeitig aufzeichnen. Zum anderen können die natürlichen physiologischen Eigenschaften der Zellen durch die Anwendung elektrophysiologischer Instrumente, wie Elektroden oder diverse Lösungen, verändert werden.

Als alternative Methode zur Untersuchung elektrischer Ereignisse wurde die Aufzeichnung durch bildgebende optische Verfahren eingeführt. Hier werden spannungssensitive Farbstoffe, aber auch genetisch kodierte fluoreszierende Proteine eingesetzt. Letzterer Ansatz ist Teil einer relativ neuen Gruppe von Technologien, der sogenannten „Optogenetik“, bei der die lichtgesteuerte Proteine verwendet werden, um die neuronale Aktivität nicht-invasiv und genetisch gezielt zu steuern, oder eben aufzuzeichnen.

„Voltage Imaging“ hat seine Wurzeln in vor etwa 50 Jahren, als synthetisch hergestellte spannungsempfindliche Farbstoffe zur Visualisierung des Membranpotentials verwendet wurden. Diese Farbstoffe wiesen jedoch Mängel auf. Vor allem liessen sie keine zellspezifische Markierung zu, und die *in-vivo*-Bildgebung in Säugetierzellen - gewebe, sowie die räumlich-zeitliche Auflösung waren die Hauptfaktoren, die optimiert werden mussten. Somit stellt die Erzeugung genetisch kodierter optischer Sensoren eine Revolution für das Monitoring von zellulären Aktionspotentialen dar.

Optische Sensoren zur Visualisierung der neuronalen Aktivität umfassen auch noch Proteine, die intrazelluläre Signale, vor allem Ca^{2+} Ionen als indirektes Signal für

Aktionspotentiale. Es gibt also zwei Gruppen von Fluoreszenzproteinsensoren neuronaler Aktivität: Genetisch kodierte Calcium-Indikatoren (*genetically encoded calcium indicators*, GECIs) und genetisch kodierte Spannungsindikatoren (*genetically encoded voltage indicators*, GEVIs). Während die GECIs indirekt Membranpotentiale nachweisen, können GEVIs elektrische Ereignisse direkt überwachen.

GECIs bestehen aus einem fluoreszierenden Protein, dem Calcium-bindenden Protein Calmodulin und dem Calmodulin-bindenden Peptid M13. GECIs reagieren auf Calciumfreisetzung mit einer Konformationsänderung, gefolgt von einer Fluoreszenzänderung. Die Affinität des Calcium- bindenden Proteins zu Calciumionen bewirkt eine Verzögerung des Signalanstiegs, und vor allem, des Signalendes. Dies ist der Grund für die langsame Kinetik von GECIs und damit ein Defizit dieser Sensoren.

GEVIs wurden erstmals im Jahr 1997 von Siegel und Isacoff eingeführt. Sie haben den Vorteil, dass sie im Millisekunden-Bereich direkt Informationen über elektrische Ereignisse auch unterhalb der Reizschwelle für Aktionspotentiale liefern können. Jedoch waren die ersten Sensoren ineffizient und daher stellten stabile Expression und Lokalisation in der Säugetierzellmembran, schnelle Kinetik, hohe Empfindlichkeit, Stabilität des Signals (langsames Photobleichen), ein hohes Signal-Rausch-Verhältnis (Signal-to-Noise-Ratio, SNR) und geringe notwendige Lichtintensität für die Bildgebung Ziele für Optimierungsverfahren dar.

GEVIs können in drei Kategorien klassifiziert werden: Zu der ersten Kategorie gehören die Sensoren, die auf einer spannungssensitiven Domäne eines Proteins basieren (Voltage-sensitive-domain, *VSD- based*). Diese Sensoren bestehen aus einem spannungsempfindlichen fluoreszierenden Protein und der spannungssensitiven Domäne eines Ionenkanals (z.B. Kalium-shaker-kanal oder Natriumkanal). Die Veränderung der Membranspannung und die daraus resultierende Strukturveränderung des Kanals, die sich durch physische Kopplung auf die Zugänglichkeit des GFP Chromophors für Wasser als Fluoreszenz-Quencher auswirkt, ruft somit etwa 5,1% Fluoreszenzveränderung per 100 mV im GFP hervor, was in der gleichen Größenordnung liegt, wie die bis dahin verwendeten spannungssensitiven organischen Farbstoffe.

Im Jahre 2001 haben *Sakai et al* Förster Resonanz Energie Transfer (FRET) Paare aus Varianten des GFP (YFP und CFP) vorgestellt und aufgezeigt, dass Spannungsänderungen der Plasmamembran zu Konformationsänderungen im

Kaliumkanal führen, die sich auf den Förster Energietransfer zwischen den beiden Komponenten des FRET-Paares (YFP und CFP) messbar auswirken. SPARC (*sodium channel protein based activity reporting construct*) ist ein weiterer Spannungssensor, der durch die Fusion aus Voltage- sensitiver Domäne des Natrium-Kanals und GFP entsteht. Alle diese Sensoren haben aber keine signifikante Lokalisation in Säugerzellen gezeigt.

Die neue Generation von Spannungssensoren dieser Kategorie, bestehend aus der spannungssensitiven Domäne von Ci-VSP (*Ciona intestinalis-voltage sensitive protein; Ciona:* Ein auf dem Meeresboden lebendes Manteltier), produziert robuste Signale in Säugerzellen. Basierend auf der Aktivität von Ci-VSP, wurde ArcLight durch eine Fusion von *Ciona intestinalis* Voltage-sensitiver Domäne und pHluorin hergestellt. Der Begriff pHluorin bezieht sich auf mehrere pH-sensitive Mutanten von eGFP, die von Miesenbock und Mitarbeitern eingeführt wurden.

Im Laufe der Jahre sind viele weitere Mitglieder dieser Familie vorgestellt worden, wie z.B. VSFP2, Mermaid, Butterfly, VSFP-CR, ASAP1, Bongwoori und FlicR1. Ein Vorteil der VSD-basierten Sensoren besteht darin, dass sie zum *in-vivo* Monitoring spontaner Aktionspotentiale in einer Zellpopulation verwendet werden können. Dennoch ist die Verwendung dieser Sensoren bei einer Einzelzellauflösung, wie sie für das Imaging in Säugergewebe (beispielsweise für das Monitoring eines Säugetiergehirns mit enger Zellpopulation) notwendig wäre, nicht möglich. Durch die Erweiterung dieser Familie um zwei weitere Sensoren aus ASAP und ArcLight zu ASAP3 und ArcLight- MT ist ein Report der elektrischen Aktivität in vivo und über Zwei-Photonen- Anregung mit Einzelzellauflösung seit Kurzem möglich. Diese melden die elektrische Aktivität *in-vivo* (in intakten oder anästhesierten Mäusen) und über Zwei-Photonen-Anregung mit Einzelzellauflösung. Trotz dieser Entwicklungen und Bemühungen hinsichtlich der Optimierung von VSD-basierten Sensoren besteht immer noch die Notwendigkeit, weitere Verbesserungen durchzuführen, um ihre Anwendung, insbesondere für *in-vivo*-Bildgebungszwecke, praktikabler zu machen.

Die zweite Kategorie der GEVIs wird von mikrobiellen Rhodopsinen abgeleitet, deren Chromophor das all-trans-retinal (ATR) ist. Das prominenteste Mitglied der Rhodopsin-Familie, das als Spannungssensor funktioniert, ist Archaerhodopsin-3 (Arch-3).

Arch-3 ist eine lichtgetriebene Protonenpumpe. Angeregt mit grünem Licht pumpt dieses Protein Protonen aus der Zelle. Das Rhodopsin wurde in HEK-Zellen und Säugerneuronen exprimiert und kann Aktionspotentiale über der Membran innerhalb von Millisekunden in Form einer Fluoreszenzänderung des Chromophors visualisieren. Da die Fluoreszenzausbeute des Rhodopsins und dessen Chromophor ATR gering ist, wurden verschiedene Strategien durchgeführt, um die Leuchtkraft *(Quantum yield)* des auf Rhodopsin basierenden Spannungsindikators zu steigern.

Diese Bemühungen führten zur Entwicklung von *electrochromicFRETs* (eFRETs)-Sensoren, bei denen Rhodopsin in FRET mit einem Fluoreszenzprotein vorliegt. Ebenfalls wurden diversen Mutationen in Rhodopsinen (Besonders in Arch-3) durchgeführt, um ihre Eigenschaften als Spannungsindikatoren zu optimieren. Ein Nachteil der Sensoren dieser Gruppe ist die enorme Lichtintensität, die zur Bildgebung der Spannungsaktivitäten benötigt wird. Zudem musste die langsame Kinetik auch verbessert werden.

Zur dritten Kategorie der Spannungssensoren zählen die chemogenetischen Indikatoren, die die Vorteile ihrer Vorgänger nutzen, nämlich die seit Jahrzehnten verwendeten organischen, synthetischen Farbstoffe und die GEVIs. Diese Familie ist jedoch noch relativ wenig erforscht.

Wie schon beschrieben, wurden eine Reihe diverser Spannungssensoren in den letzten Jahrzehnten generiert und in verschiedenen Organismen verwendet. Jeder Sensor weist individuelle Eigenschaften gegenüber seinen Vorgängern und Nachkommen auf. Der optimale Sensor muss anhand des Organismus und basierend auf die Fragestellung gewählt werden.

Ziel dieser Arbeit ist die Etablierung genetisch kodierter Spannungssensoren zur Visualisierung von Aktionspotentialen in Zellen.

Als Modellorganismus eignet sich der Fadenwurm *C. elegans,* der sich durch folgende Eigenschaften auszeichnet: Einerseits ist seine Kultivierung *in vitro* aufgrund seiner geringen Körpergröße und besonderen Fortpflanzungsart unkompliziert. Zudem ist seine durchsichtige Körperhülle mikroskopisch gut anschaulich; besonders in der Optogenetik kann dadurch das Licht ohne zusätzliche lichtleitende Werkzeuge direkt die Zellen des Wurms durchdringen.

Was die Anwendung dieses Nematoden für dieses Projekt unersetzbar macht, ist sein primitives Nervensystem. Die geringe Anzahl der Neuronen sowie die bis jetzt gewonnenen Kenntnisse über deren Verbindungen und Verknüpfungen ermöglichen die Analyse der Prozesse, die von ihnen gesteuert werden, wie zum Beispiel die Kontrolle über die Muskulatur während der sinusförmigen Bewegung des Tieres, was im Zeitraum dieser Arbeit ebenfalls untersucht wurde.

Das Ziel dieser Arbeit, die Visualisierung der Spannungen in der Körperwandmuskulatur sowie im Pharynx des Fadenwurms, konnte erfolgreich aufgezeigt werden. Zu diesem Zweck wurden verschiedene GEVIs in den zwei erwähnten Geweben von *C. elegans* exprimiert und lokalisiert: Es wurden zwei Klassen von Rhodopsin-basierten Spannungsindikatoren getestet: Archaerhodopsin (Arch)- bzw. mutierte Varianten für die direkte Betrachtung der Fluoreszenzänderungen des Rhodopsins, sowie QuasAr-mOrange und MacQ-mCitrine als eFRET-Sensoren. Außerdem wurden ATR-Analoga verwendet, um die schwache Fluoreszenz von ATR zu verstärken. Alle getesteten Sensoren wiesen eine stabile Expression und Lokalisation in *C. elegans*- Pharynx und Körperwandmuskeln auf. Sie können über spannungsempfindliche Fluoreszenzänderungen berichten: z. B. bis zu 128% Anstieg in ΔF/F- pro 100 mV durch Arch (D95N), wenn exprimiert in Pharynx, und 45 bis 78% Abfall in ΔF/F- pro 100 mV gemessen mit eFRET-Sensoren).

Um die Fluoreszenzsignale des eFRET-Sensors MacQ-mCitrine in der Pharynx Muskulatur in ihrer Amplitude in Relation zu den absoluten Membranpotentialen zu setzen, wurden s*harp-electrode* Messungen gleichzeitig mit der optischen Aufzeichnung im sezierten Pharynx von Wildtyp-Tieren durchgeführt. Dieser Sensor zeigte eine Abnahme von 20% ΔF/F pro 100 mV.

Alle Sensoren konnten Unterschiede der Spannungssignale in Mutanten eines spannungsgesteuerten Ca^{2+}-Kanals im Vergleich zu den Wildtyp-Tieren aufzeigen. Hierzu wurden zwei Mutanten der *egl-19* verwendet, nämlich *egl-19(n2368)* und *egl-19(n582ad952)* mit Mutationen in zwei verschiedenen Allelen. EGL-19 ist ein Ortholog von menschlichem CACNA1D (Calcium-Voltage-Gated-Channel-Subunit Alpha1D) und CACNA1S (*Calcium-Voltage-Gated-Channel-Subunit Alpha1S*). EGL-19 trägt Ströme, die die Plateau-Phase des Pharynx-APs formen. Mutanten mit Funktionsverlust sind nicht überlebensfähig; jedoch wurden mehrere Allele isoliert und aufgrund ihres Einflusses auf den Muskeltonus in BWM als ‚gain-of-function' von *egl-19* charakterisiert.

Die eingesetzten Indikatoren waren in der Lage, über die schon beschriebenen, verlängerten Pumpaktivitäten in *egl-19* Mutanten zu anzuzeigen und sie zeigten signifikante Unterschiede in den spannungsabhängigen Fluoreszenzsignalen auf.

Darüber hinaus wurde der Effekt von Nemadipine-A (Nema-A), welches für die Herabsetzung der verlängerten Pumpdauer in *egl-19* Mutanten bekannt ist, untersucht. Nema-A ist ein Analogon zu 1,4-Dihydropyridin, einer Gruppe von Arzneimitteln zur

Behandlung von Bluthochdruck und ein *egl-19*-Antagonist. Eine Wiederherstellung der spannungsabhängigen Fluoreszenzsignale in Mutanten auf zum Wildtyps vergleichbare Werte konnte von allen getesteten Sensoren visualisier werden.

Als eine eindrucksvolle Demonstration der Möglichkeiten, die die optische Bildgebung des Membranpotentials eröffnen, konnte ich zeigen, wie sich das Membranpotential räumliche über den gesamten Pharynx entwickelt, mit einer deutlichen Kompartmentalisierung von anterior nach posterior, was die Repolarisierung betrifft. Zudem konnte durch Mittelung der zeitlichen Veränderung des Signals über den gesamten Pharynx ein optogenetisches Pendant des klassischen Elektropharyngeograms entwickelt werden. Mit der neuen Methode namens „Opto-EPG" lassen sich Befunde aus dem EPG mit der räumlichen und zeitlichen Entwicklung der Membranpotentialänderung des Pharynx korrelieren.

Des Weiteren wurde ein personalisierter Arbeitsablauf in Programm „Knime" zur Automatisierung der Analyse verwendet. Dieser Arbeitsablauf mit einem angepassten R-Skript (zur mathematischen Analyse) ermöglicht die automatische Erkennung der ausgelesenen Signale von Pharynx. Es ist in der Lage die Signale zu synchronisieren und die Eigenschaften der Signale wie Signaldauer, Tau-Werte und Pumpsignalverzögerung zu extrahieren. Es erleichtert die Charakterisierung der Sensoren, was Hinweise auf die Empfindlichkeit und das Potenzial jedes der untersuchten Sensoren bei der Überwachung der elektrischen Aktivität gab.

Diese Arbeit etabliert eine nicht-invasive, volloptische Methode zur *in-vivo* Beobachtung des Membranpotentials in erregbaren Zellen des Fadenwurms *C. elegans,* die als Ersatz oder komplementär zu invasiven, elektrophysiologischen Methoden verwendet werden kann.

B Abstract

Understanding the mechanisms that process information in neural circuits, and the interactions between them, is the key to understand the response of the cells or cell ensembles in generating behavior, consciousness, emotion, and cognition. This communication between excitable cells occurs through, or is based upon, electrical events. Monitoring these electrical events enables understanding the underlying mechanisms.

For decades, electrophysiology was the standard procedure for investigating electrical signals. This method has limitations as it cannot record the activities of more than a handful of individual cells simultaneously. The application of electrodes and solutions in electrophysiology alters the natural physiological properties of the cells. Although the application of the electrodes can occur in some model organisms via implantation (e.g., in mice), it is however an invasive method and can be performed only via dissection in many other model organisms like *C. elegans*.

To overcome these limitations, optical methods for recording of electrical events in excitable cells were explored and refined over the past years, to provide an alternative method to study electrical events.

Optical recording techniques are nowadays considered to be a part of the relatively new techniques subsumed under the term ‘optogenetics’, which use light-driven proteins to modulate, perturb, or monitor neural activity in a non-invasive, genetically targeted fashion. The protein tools used in optogenetics are actuators of membrane currents, enzymatic reactions, protein-protein interactions, protein conformational changes, and lastly, they can optically monitor intracellular concentration of metabolites or signaling molecules, as well as electrical activities of the cell membrane.

The origins of voltage imaging date back to around 50 years ago, when first synthetic voltage-sensitive dyes were introduced. These worked, however, they had limitations, for example, cell toxicity, specific labeling of cells, *in-vivo* imaging in mammalian cells and tissues were the main primary factors that had to be optimized.

The generation of genetically encoded optical sensors was a revolution in monitoring electrical activity of the membrane. Such sensors can be divided into two groups: Genetically encoded calcium indicators (GECIs) and genetically encoded voltage indicators (GEVIs).

While the GECIs report indirectly about membrane potential, GEVIs can monitor electrical events directly. GECIs consist of a fluorescent protein, the calcium-binding

protein Calmodulin, and Calmodulin-binding-peptide M13. GECIs undergo a conformational change upon a rise of the cytosolic calcium concentration, which is followed by a fluorescence change. The affinity of the calcium-binding protein to calcium ions causes a delay in the signal rise. This is the reason for the slow kinetics of GECIs, and thus a shortcoming of this group of sensors.

GEVIs have the advantage that they can report information directly about the electrical events at sub-millisecond timescales. GEVIs, first introduced in 1997 by Siegel and Isacoff, have undergone a remarkable evolution since then. Stable expression and localization in the mammalian cell membrane, fast kinetics, high sensitivity, the stability of the signal (not very fast bleaching signal), high signal-to-noise ratio (SNR), and low light intensity for imaging were decisive in their optimization procedure. The new generation of such GEVIs is derived from microbial rhodopsins, which use all-*trans*-retinal (ATR) as their chromophore. Since the fluorescence yield of retinal is low, diverse strategies were performed to boost the luminosity of rhodopsin-based voltage indicators. These efforts resulted in the development of electrochromic FRET (eFRET) sensors, in which the rhodopsin acts as a voltage-dependent quencher for a fluorescence protein.

The goal of this thesis was to establish genetically encoded voltage sensors for imaging in the nematode *C. elegans* as a model organism.

This goal could be achieved successfully. Various GEVIs could be expressed and localized in two tissues of *C. elegans*: 1) The pharynx, which is the feeding organ of *C. elegans,* which exhibits rhythmic pumping-like contractions, and 2) body wall muscles (BWMs). Two classes of rhodopsin-based voltage indicators have been tested: Mutated variants of archaerhodopsin(Arch) for direct imaging as well as QuasAr-mOrange and MacQ-mCitrine as eFRET sensors. Besides, ATR analogs were used to boost the dim fluorescence of ATR. All the tested sensors have shown the feasibility of stable expression and localization in *C. elegans* pharyngeal and body wall muscles. They could deliver voltage-sensitive fluorescence changes (e.g., up to 128% ΔF/F increase per 100 mV by Arch(D95N) expressed in the pharynx and 45 to 78% ΔF/F decrease per 100 mV by eFRET sensors in BWMs) during membrane depolarization in both tissues in wild type animals. Sharp electrode measurements in pharyngeal muscles were performed simultaneously to optical recordings in the dissected pharynx of the wild type animals expressing the eFRET sensor MacQ-mCitrine. This sensor revealed 20% ΔF/F decrease per 100 mV. All the sensors could report differences of the voltage signals in mutants of a voltage-gated Ca^{2+}-channel in comparison to the wild type animals. Besides, it was possible to analyze the spatial development of the voltage signal across the pharynx antero-posteriorly with a new method called opto-EPG. Optical induction of depolarization in BWMs via the activation of channelrhodopsin expressed in cholinergic neurons, increased (during rhodopsin direct-imaging) or reduced (during imaging with eFRET sensor) the fluorescence signal.

This work establishes non-invasive, all-optical methods for in-vivo voltage imaging in the nematode *C. elegans*.

1 Introduction

1.1: Optogenetics and light-sensitive proteins

Optogenetics defines the techniques that are used to manipulate, control, or monitor the activity of excitable cells using light-sensitive proteins, which can be expressed exogenously in cells of interest.

Optogenetics was awarded the title “method of the year 2010” (*Method of the Year 2010 Optogenetics : controlling cell function with light*, 2011). Although the term ”optogenetics” was first launched in 2006 (Deisseroth *et al.*, 2006), its roots go back to decades before (Deisseroth, 2015).

The spectrum of the optogenetic applications is comprehensive; it began in neurobiology with activation and deactivation of excitatory and inhibitory neurons, and nowadays, it is used for modulation of signal cascades and is an indispensable method in cell biology (Deisseroth, 2011).

As mentioned above, light-sensitive proteins are the tools of optogenetics. In the first generation of such sensitive proteins, one can choose between the so-called caged ligands, which bind to their specific receptor upon light illumination or tethered ligands, which bind already on their receptor and trigger its activity upon light stimulation. For this purpose, the ligand-controlled ion channels, the ionotropic purine receptor P2X2 or capsaicin relationships TRPV1 are expressed in neurons exogenously. The agonists that control conductivity of these receptors are given to the organism. These agonists are chemically modified and blocked in the form of “caged ligands”. Light radiation can break this blockade and thus the agonist can bind its receptor and evoke a reaction, e.g., some specific behavior (Dugué, Akemann and Knöpfel, 2012), (Deisseroth, 2011). Caged ligands were used for the first time in *Drosophila* to trigger specific behaviors in this insect (Zemelman *et al.*, 2003). More widely utilized, microbial rhodopsins play a leading role in optogenetics.

Soon after Oesterhelt and Stoeckenius (Oesterhelt and Stoeckenius, 1971) discovered in the early 70s, that microbial rhodopsins can transduce light into electrical currents, these proteins inspired many biologists for further investigations due to their molecular features (Deisseroth, 2015).

Three members of the microbial rhodopsin family form the first generation of opsins used in optogenetics (Knöpfel *et al.*, 2010). These are bacteriorhodopsin, which pumps protons out of the cell, halorhodopsin, which pumps chloride into the cell and channelrhodopsin, which is a channel that passes cations through the cell membrane (Bergs *et al.*, 2018),(Nagel *et al.*, 2003) (Fig I-1).

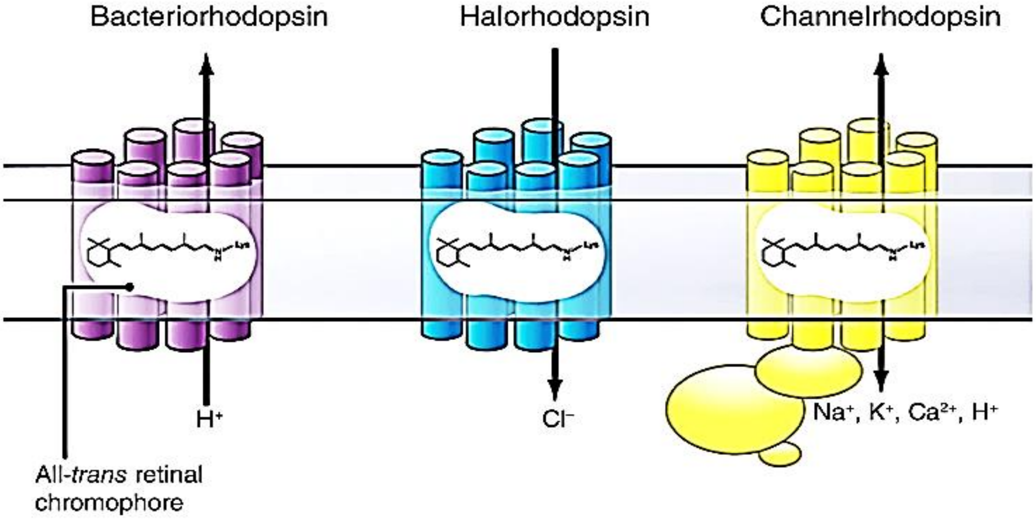

Fig. I-1: schematic structure of the first generation of opsins used in optogenetics. From left to right: Bacteriorhodopsin, which is an in outward-directed proton-pump, halorhodopsin, an inward-directed pump for chloride-ions and ChR2, which is a channel for positively charged ions. All the opsins use all-*trans*-retinal as their chromophore. Modified from (Deisseroth, 2015).

This toolbox expanded soon by the discovery and application of additional rhodopsins such as Archaerhodopsin-3 (Arch-3) and Mac (isolated from the fungus *Leptosphaeria maculans*) (Chow *et al.*, 2010),(Brown, 2004) (Fig. I-2) as neuronal silencers, or by the introduction of new actuators derived either from ChR1 or isolated from other organisms (All *et al.*, 2019) (Fig. I-3). The solving of the crystal structure of channelrhodopsin was a break-through, also aiding in the development of optogenetic tools (Kato *et al.*, 2012).

This exploration allowed the protein engineering of the channel pore to achieve new properties such as chloride-conductivity of the channel (Wietek *et al.*, 2014),(Berndt *et al.*, 2014). This development progressed ahead by the discovery of natural chloride-conducting channels (Govorunova *et al.*, 2015) or other members of this family, accompanied by further molecular engineering (Bergs *et al.*, 2018),(Brown *et al.*, 2018). These inhibitory tools could be applied in various model organisms from *Caenorhabditis elegans* (*C. elegans*) (Schultheis *et al.*, 2011; Erbguth *et al.*, 2012; Kocabas *et al.*, 2012) up to non-human primates (Boyden *et al.*, 2005),(Stauffer *et al.*, 2016).

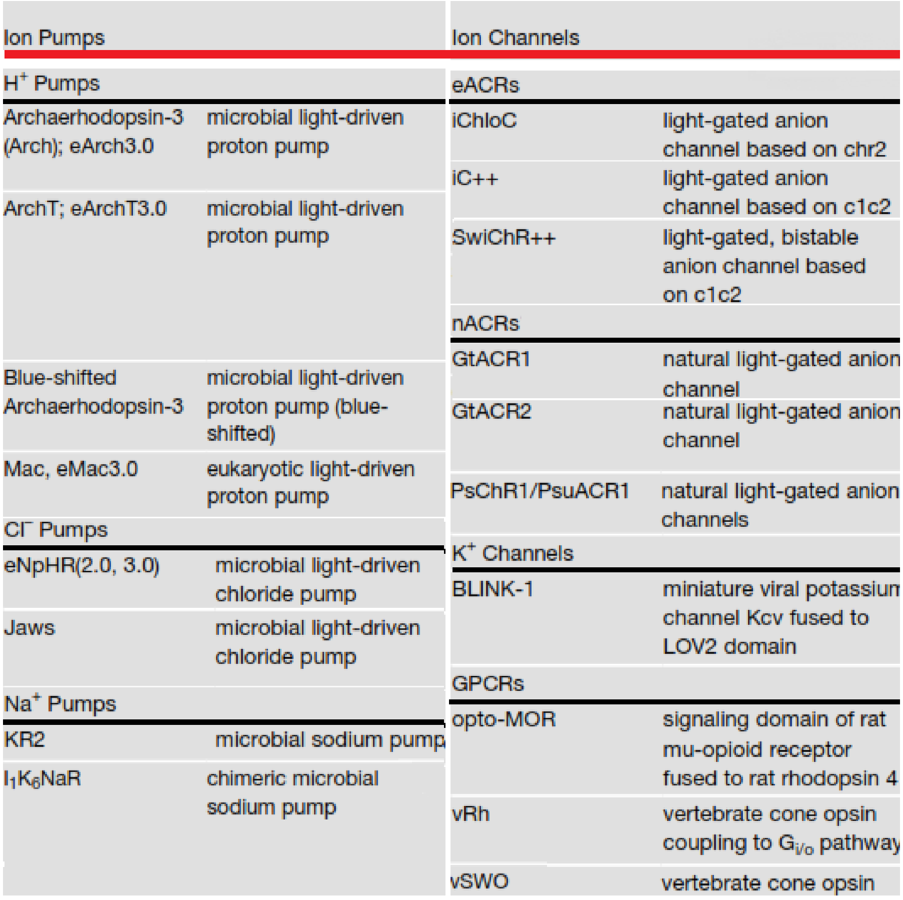

Ion Pumps	
H^+ Pumps	
Archaerhodopsin-3 (Arch); eArch3.0	microbial light-driven proton pump
ArchT; eArchT3.0	microbial light-driven proton pump
Blue-shifted Archaerhodopsin-3	microbial light-driven proton pump (blue-shifted)
Mac, eMac3.0	eukaryotic light-driven proton pump
Cl^- Pumps	
eNpHR(2.0, 3.0)	microbial light-driven chloride pump
Jaws	microbial light-driven chloride pump
Na^+ Pumps	
KR2	microbial sodium pump
I_1K_6NaR	chimeric microbial sodium pump

Ion Channels	
eACRs	
iChloC	light-gated anion channel based on chr2
iC++	light-gated anion channel based on c1c2
SwiChR++	light-gated, bistable anion channel based on c1c2
nACRs	
GtACR1	natural light-gated anion channel
GtACR2	natural light-gated anion channel
PsChR1/PsuACR1	natural light-gated anion channels
K^+ Channels	
BLINK-1	miniature viral potassiu channel Kcv fused to LOV2 domain
GPCRs	
opto-MOR	signaling domain of rat mu-opioid receptor fused to rat rhodopsin 4
vRh	vertebrate cone opsin coupling to $G_{i/o}$ pathwa
vSWO	vertebrate cone opsin

Fig. I-2: An overview of optogenetic tools for neuronal silencing. This table shows optogenetic tools, consisting of a variety of ion pumps and channels that are used for hyperpolarisation of the membrane and thus for neuronal silencing, emphasizing the expansion of such tools. Modified from (Wiegert *et al.*, 2017)

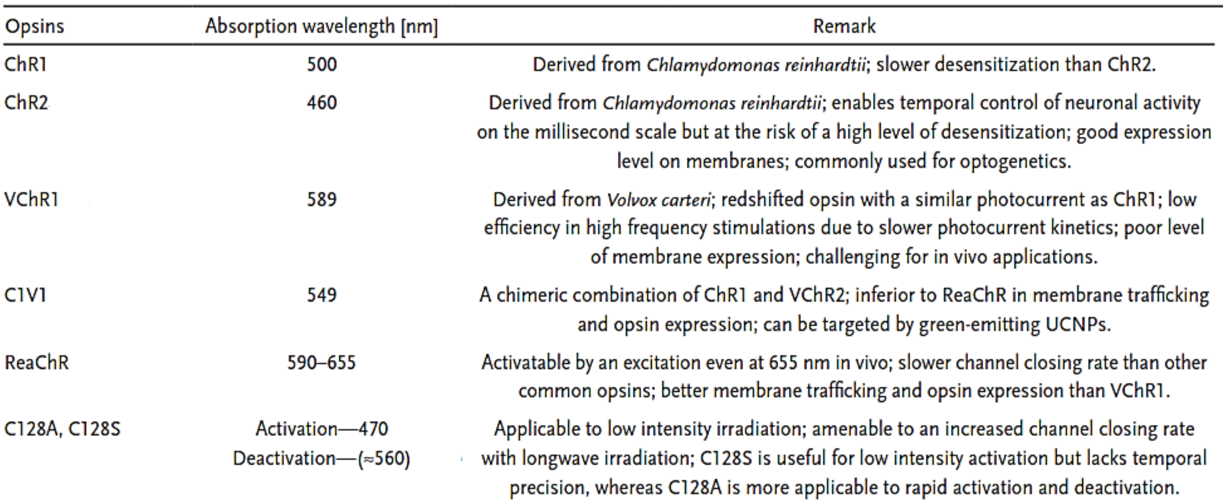

Opsins	Absorption wavelength [nm]	Remark
ChR1	500	Derived from *Chlamydomonas reinhardtii*; slower desensitization than ChR2.
ChR2	460	Derived from *Chlamydomonas reinhardtii*; enables temporal control of neuronal activity on the millisecond scale but at the risk of a high level of desensitization; good expression level on membranes; commonly used for optogenetics.
VChR1	589	Derived from *Volvox carteri*; redshifted opsin with a similar photocurrent as ChR1; low efficiency in high frequency stimulations due to slower photocurrent kinetics; poor level of membrane expression; challenging for in vivo applications.
C1V1	549	A chimeric combination of ChR1 and VChR2; inferior to ReaChR in membrane trafficking and opsin expression; can be targeted by green-emitting UCNPs.
ReaChR	590–655	Activatable by an excitation even at 655 nm in vivo; slower channel closing rate than other common opsins; better membrane trafficking and opsin expression than VChR1.
C128A, C128S	Activation—470 Deactivation—(≈560)	Applicable to low intensity irradiation; amenable to an increased channel closing rate with longwave irradiation; C128S is useful for low intensity activation but lacks temporal precision, whereas C128A is more applicable to rapid activation and deactivation.

Fig. I-3: An overview of commonly used optogenetic tools for neuronal activation. This table shows standard optogenetic tools that are used for the depolarization of the membrane and thus for the neuronal activation. Modified from (All *et al.*, 2019).

Besides biotechnological methods to generate chimeric proteins or genetic engineering of the wild type proteins, additional properties could be conveyed to rhodopsin based tools by the substitution of all-*trans*-retinal with different chemically modified analogs, which led to altered kinetics, conductance and shifted absorption-spectrum (Azimihashemi *et al.*, 2014; Manathunga, Yang and Olivucci, 2018; Shen *et al.*, 2018). All-*trans*-retinal and its analogs will be discussed later in this chapter.

A novel usage of microbial rhodopsin proton pumps, described first in 2011, is their ability to monitor action potentials (Kralj *et al.*, 2011, 2012). This discovery opened a new chapter in the history of voltage indicators, which will be introduced in detail in the next section.

1.2: Genetically encoded voltage indicators (GEVIs)

Over the last decades, voltage imaging was performed via voltage-sensitive dyes with the required temporal resolution (Grinvald *et al.*, 1988; Grinvald and Hildesheim, 2004; Baker *et al.*, 2005; Knöpfel, Díez-García and Akemann, 2006), which allowed addressing action potentials in a variety of neurons, including mammalian brain tissue (Hoppmann and Wang, 2019). Nonetheless, voltage-sensitive dyes have major limitations, particularly with respect to labeling of specific cell populations. If the dyes are not able to reach the cells of interest, the optical signal is overlaid by the background fluorescence of inactive cells and vanishes. Furthermore, unspecific labeling hampers the characterization of fluorescence signals in the desired cell group (Perron *et al.*, 2009). The necessity of specifically monitoring the activities of multiple neurons or cells resulted in the generation of genetically encoded proteins that can act as optical voltage sensors (genetically encoded voltage indicators: GEVIs). These proteins are sensitive to changes in electrical potential of the cell membrane and can visualize electrical events in form of optical signals and can be divided into three main families: VSD-based (voltage-sensitive domain), rhodopsin-based and chemogenetic voltage indicators (see Fig. I-4). Besides the feasibility of stable expression and localization in the membrane of the cell of interest, an optimal voltage indicator should fulfill different attributes. These attributes, such as fast kinetic, high sensitivity, the stability of the signal (slow photo-bleaching), high signal-to-noise ratio (SNR), and low light intensity required for imaging were decisive in the optimization procedure of different GEVIs (see Fig. I-5).

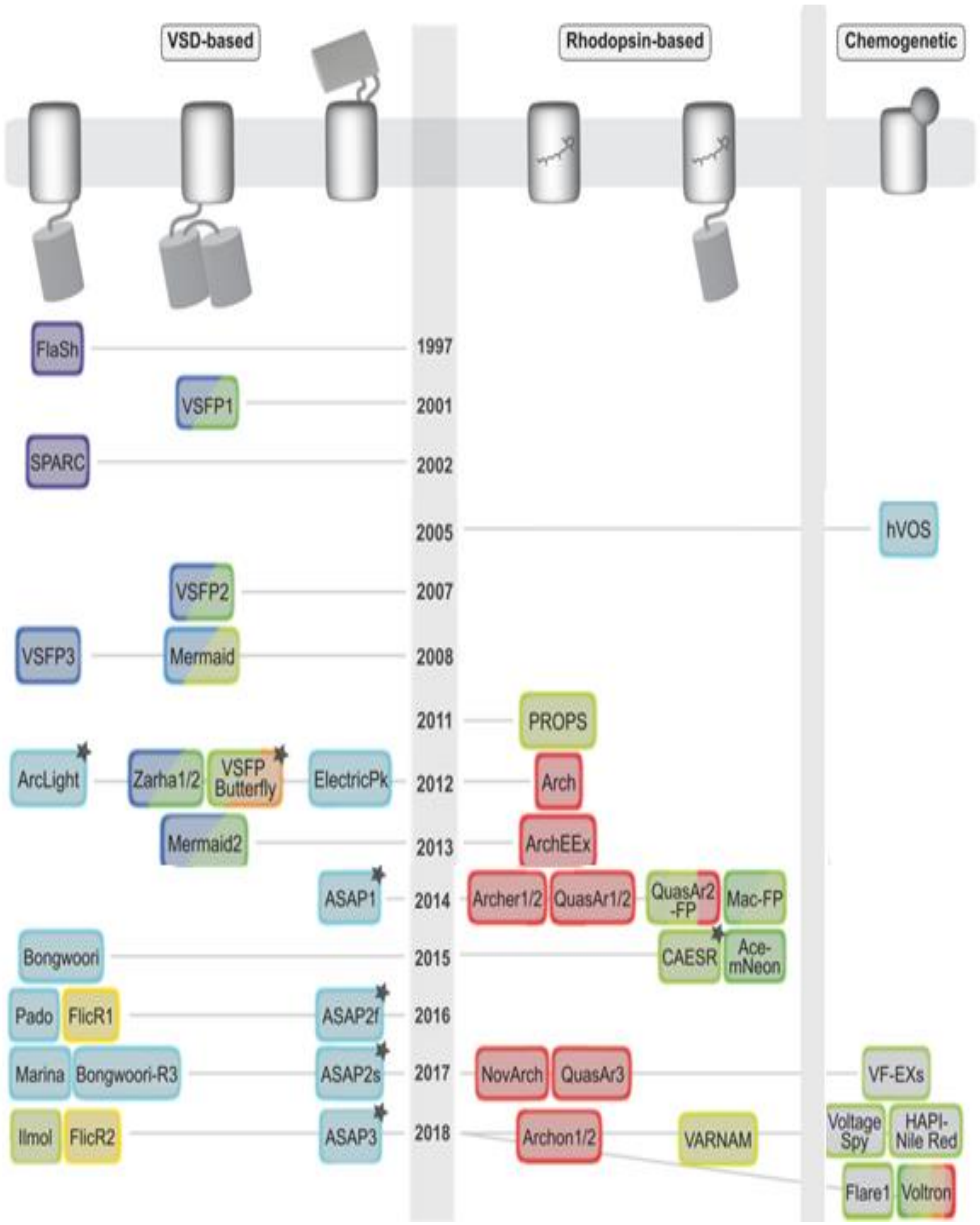

Fig. I-4: An overview of the different families of genetically encoded voltage indicators and their history. From left to right: GEVIs based on a voltage-sensitive-domains (left) or derived from microbial rhodopsins (middle) and chemogenetic sensors (right). All the sensors are listed chronologically by year of their discovery. The color of the box indicates the excitation wavelength, and asterisks indicate the feasibility of two-photon imaging (Modified from (Bando, Grimm, *et al.*, 2019).

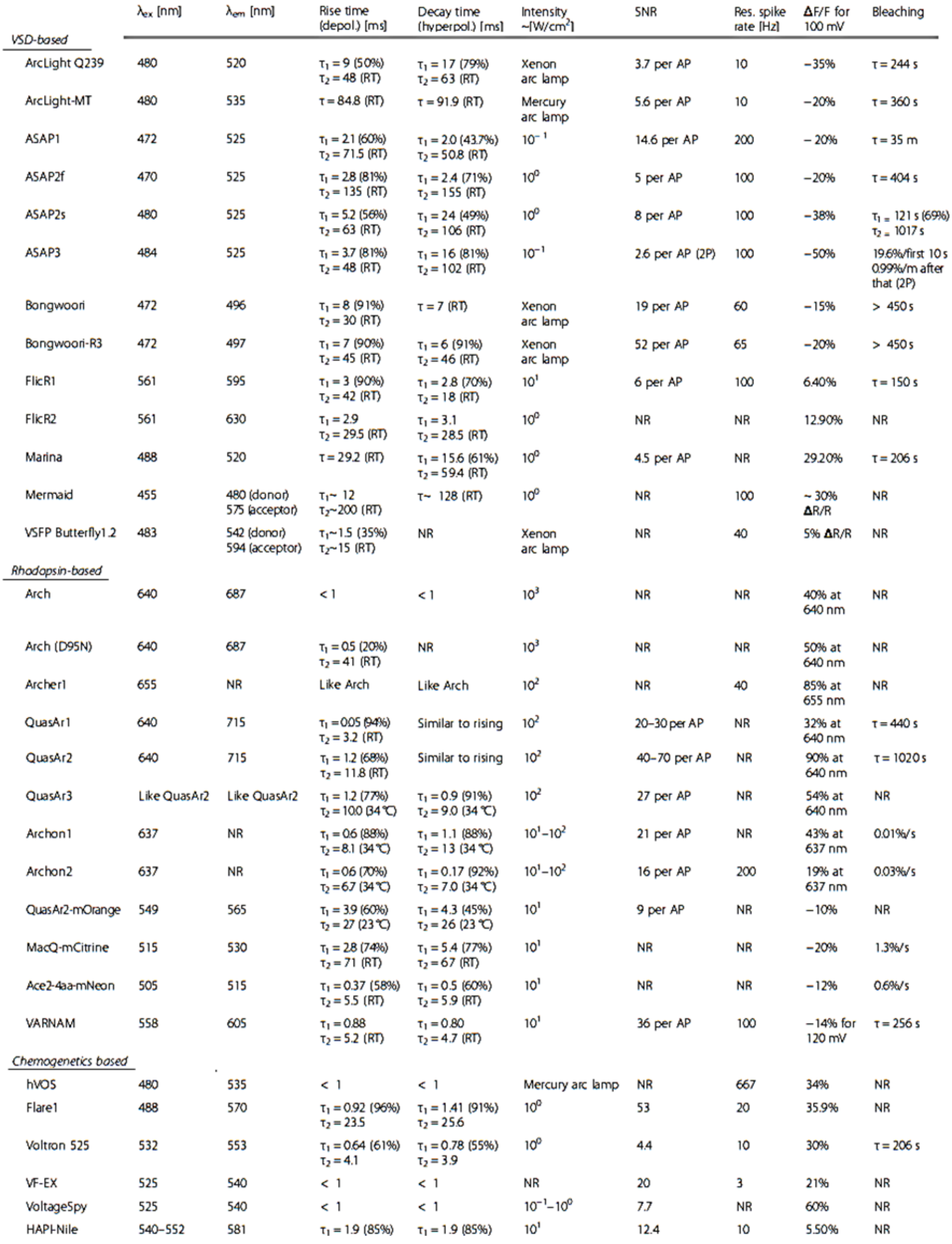

	λ_{ex} [nm]	λ_{em} [nm]	Rise time (depol.) [ms]	Decay time (hyperpol.) [ms]	Intensity ~[W/cm^2]	SNR	Res. spike rate [Hz]	ΔF/F for 100 mV	Bleaching
VSD-based									
ArcLight Q239	480	520	$\tau_1 = 9$ (50%) $\tau_2 = 48$ (RT)	$\tau_1 = 17$ (79%) $\tau_2 = 63$ (RT)	Xenon arc lamp	3.7 per AP	10	−35%	$\tau = 244$ s
ArcLight-MT	480	535	$\tau = 84.8$ (RT)	$\tau = 91.9$ (RT)	Mercury arc lamp	5.6 per AP	10	−20%	$\tau = 360$ s
ASAP1	472	525	$\tau_1 = 2.1$ (60%) $\tau_2 = 71.5$ (RT)	$\tau_1 = 2.0$ (43.7%) $\tau_2 = 50.8$ (RT)	10^{-1}	14.6 per AP	200	− 20%	$\tau = 35$ m
ASAP2f	470	525	$\tau_1 = 2.8$ (81%) $\tau_2 = 135$ (RT)	$\tau_1 = 2.4$ (71%) $\tau_2 = 155$ (RT)	10^0	5 per AP	100	−20%	$\tau = 404$ s
ASAP2s	480	525	$\tau_1 = 5.2$ (56%) $\tau_2 = 63$ (RT)	$\tau_1 = 24$ (49%) $\tau_2 = 106$ (RT)	10^0	8 per AP	100	−38%	$\tau_1 = 121$ s (69%) $\tau_2 = 1017$ s
ASAP3	484	525	$\tau_1 = 3.7$ (81%) $\tau_2 = 48$ (RT)	$\tau_1 = 16$ (81%) $\tau_2 = 102$ (RT)	10^{-1}	2.6 per AP (2P)	100	−50%	19.6%/first 10 s 0.99%/m after that (2P)
Bongwoori	472	496	$\tau_1 = 8$ (91%) $\tau_2 = 30$ (RT)	$\tau = 7$ (RT)	Xenon arc lamp	19 per AP	60	−15%	> 450 s
Bongwoori-R3	472	497	$\tau_1 = 7$ (90%) $\tau_2 = 45$ (RT)	$\tau_1 = 6$ (91%) $\tau_2 = 46$ (RT)	Xenon arc lamp	52 per AP	65	−20%	> 450 s
FlicR1	561	595	$\tau_1 = 3$ (90%) $\tau_2 = 42$ (RT)	$\tau_1 = 2.8$ (70%) $\tau_2 = 18$ (RT)	10^1	6 per AP	100	6.40%	$\tau = 150$ s
FlicR2	561	630	$\tau_1 = 2.9$ $\tau_2 = 29.5$ (RT)	$\tau_1 = 3.1$ $\tau_2 = 28.5$ (RT)	10^0	NR	NR	12.90%	NR
Marina	488	520	$\tau = 29.2$ (RT)	$\tau_1 = 15.6$ (61%) $\tau_2 = 59.4$ (RT)	10^0	4.5 per AP	NR	29.20%	$\tau = 206$ s
Mermaid	455	480 (donor) 575 (acceptor)	$\tau_1 \sim 12$ $\tau_2 \sim 200$ (RT)	$\tau \sim 128$ (RT)	10^0	NR	100	~ 30% ΔR/R	NR
VSFP Butterfly1.2	483	542 (donor) 594 (acceptor)	$\tau_1 \sim 1.5$ (35%) $\tau_2 \sim 15$ (RT)	NR	Xenon arc lamp	NR	40	5% ΔR/R	NR
Rhodopsin-based									
Arch	640	687	< 1	< 1	10^3	NR	NR	40% at 640 nm	NR
Arch (D95N)	640	687	$\tau_1 = 0.5$ (20%) $\tau_2 = 41$ (RT)	NR	10^3	NR	NR	50% at 640 nm	NR
Archer1	655	NR	Like Arch	Like Arch	10^2	NR	40	85% at 655 nm	NR
QuasAr1	640	715	$\tau_1 = 0.05$ (94%) $\tau_2 = 3.2$ (RT)	Similar to rising	10^2	20–30 per AP	NR	32% at 640 nm	$\tau = 440$ s
QuasAr2	640	715	$\tau_1 = 1.2$ (68%) $\tau_2 = 11.8$ (RT)	Similar to rising	10^2	40–70 per AP	NR	90% at 640 nm	$\tau = 1020$ s
QuasAr3	Like QuasAr2	Like QuasAr2	$\tau_1 = 1.2$ (77%) $\tau_2 = 10.0$ (34 °C)	$\tau_1 = 0.9$ (91%) $\tau_2 = 9.0$ (34 °C)	10^2	27 per AP	NR	54% at 640 nm	NR
Archon1	637	NR	$\tau_1 = 0.6$ (88%) $\tau_2 = 8.1$ (34 °C)	$\tau_1 = 1.1$ (88%) $\tau_2 = 13$ (34 °C)	10^1–10^2	21 per AP	NR	43% at 637 nm	0.01%/s
Archon2	637	NR	$\tau_1 = 0.6$ (70%) $\tau_2 = 6.7$ (34 °C)	$\tau_1 = 0.17$ (92%) $\tau_2 = 7.0$ (34 °C)	10^1–10^2	16 per AP	200	19% at 637 nm	0.03%/s
QuasAr2-mOrange	549	565	$\tau_1 = 3.9$ (60%) $\tau_2 = 27$ (23 °C)	$\tau_1 = 4.3$ (45%) $\tau_2 = 26$ (23 °C)	10^1	9 per AP	NR	−10%	NR
MacQ-mCitrine	515	530	$\tau_1 = 2.8$ (74%) $\tau_2 = 71$ (RT)	$\tau_1 = 5.4$ (77%) $\tau_2 = 67$ (RT)	10^1	NR	NR	−20%	1.3%/s
Ace2-4aa-mNeon	505	515	$\tau_1 = 0.37$ (58%) $\tau_2 = 5.5$ (RT)	$\tau_1 = 0.5$ (60%) $\tau_2 = 5.9$ (RT)	10^1	NR	NR	−12%	0.6%/s
VARNAM	558	605	$\tau_1 = 0.88$ $\tau_2 = 5.2$ (RT)	$\tau_1 = 0.80$ $\tau_2 = 4.7$ (RT)	10^1	36 per AP	100	−14% for 120 mV	$\tau = 256$ s
Chemogenetics based									
hVOS	480	535	< 1	< 1	Mercury arc lamp	NR	667	34%	NR
Flare1	488	570	$\tau_1 = 0.92$ (96%) $\tau_2 = 23.5$	$\tau_1 = 1.41$ (91%) $\tau_2 = 25.6$	10^0	53	20	35.9%	NR
Voltron 525	532	553	$\tau_1 = 0.64$ (61%) $\tau_2 = 4.1$	$\tau_1 = 0.78$ (55%) $\tau_2 = 3.9$	10^0	4.4	10	30%	$\tau = 206$ s
VF-EX	525	540	< 1	< 1	NR	20	3	21%	NR
VoltageSpy	525	540	< 1	< 1	10^{-1}–10^0	7.7	NR	60%	NR
HAPI-Nile	540–552	581	$\tau_1 = 1.9$ (85%)	$\tau_1 = 1.9$ (85%)	10^1	12.4	10	5.50%	NR

Fig. I-5: Comparative presentation of the properties of different GEVIs. Compared are parameters that were decisive in the optimization of different GEVIs: wavelength of excitation and emission, rise and decay time, required light intensity, Signal-to-Noise Ratio (SNR), spike rate, ΔF/F per 100 mV, and bleaching time. Modified from (Bando, Grimm, *et al.*, 2019). RT: room temperature, NR: not reported

The first generation of the family of protein-based voltage indicators was introduced in 1997 by Siegel and Isacoff (Siegel and Isacoff, 1997). This sensor, called FlaSh, is a fusion protein containing green fluorescent protein (GFP) and the voltage-sensitive domain (VSD) of a Shaker-type K^+-channel (see Fig. I-6). The sensor was tested in *Xenopus* oocytes. Potential changes across the membrane caused a structural reorientation in the channel, which rendered the GFP chromophore accessible for water molecules. This caused quenching of the GFP fluorescence and thus enabled monitoring the membrane voltage. The changes in the fluorescence signal of GFP were ca. 5.1% per 100 mV, which was in the same range as the signals monitored by voltage-sensitive dyes (Siegel and Isacoff, 1997). However, FlaSh kinetics were slow ($\tau_{off} > 85$ ms), and its expression in neurons may affect the cell's physiology, as the protein may co-assemble with native channel subunits (Perron *et al.*, 2009).

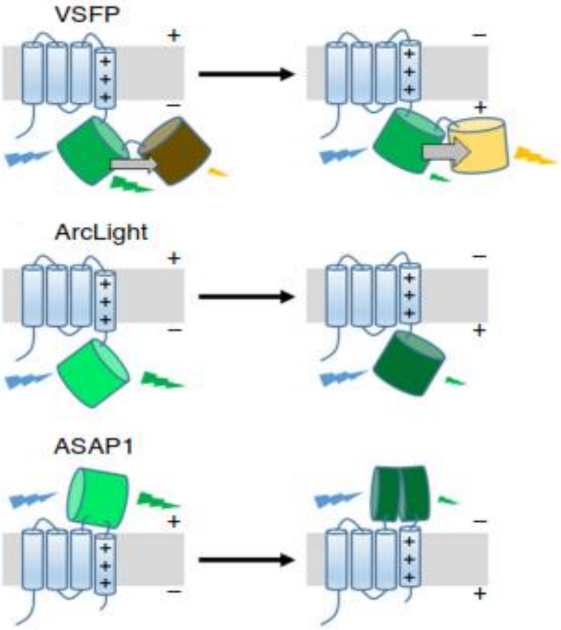

Fig. I-6: Voltage sensing mechanism of different members of VSD-based voltage indicators. Voltage-sensing domain (VSD) of voltage-sensing phosphatase fused with an intracellular FRET-Pair (up), with single fluorescence protein (middle) or the insertion of a circularly permuted GFP into the extracellular loop of the voltage sensing domain of the Ci-VSP, connecting the third and fourth transmembrane Helices (down). Adapted from (Xu, Zou and Cohen, 2017)

In 2001, a GEVI based on a pair of fluorescent proteins enabling Förster Resonance Energy Transfer (FRET), fused to the voltage sensor of a K^+-channel, was introduced under the name VSFP1 (voltage-sensitive fluorescent protein) by Sakai et al. This sensor revealed voltage-dependent signals in mammalian cells with a faster kinetic compared to its predecessors. These authors could show that action potentials induced conformational changes, which affected the FRET efficiency between CFP and YFP in a measurable manner (Sakai *et al.*, 2001).

In 2002, SPARC (sodium channel protein-based activity reporting construct) was introduced, which was generated by the fusion of the voltage-sensitive domain of a sodium channel and GFP (Ataka and Pieribone, 2002) (see Fig. I-6). One advantage of sodium channels in comparison to potassium channels is their ability to undergo rapid gating and conformational changes. This property is based on the functional form of a sodium channel that originates from a single polypeptide chain (α subunit), whereas potassium channels are formed from homo- or heterotetramers of a single domain. Besides, a recombinant sodium channel does not assemble with native sodium channels in the membrane. Although these sensors could track electrical changes and allowed monitoring them, their localization in the plasma membrane of mammalian cells was poor (Barnett *et al.*, 2012)·(Akemann *et al.*, 2010). Efforts to overcome this limitation led to the development of the second generation of VSD-based GEVIs, which consists of the voltage-sensing domain isolated from the voltage-sensing phosphatase of the sea squirt *Ciona intestinalis* (Ci-VSP). Ci-VSP became the prototype for many other voltage indicators. Its functionality could be enhanced, e.g., by the fusion of its VSD to the super ecliptic pHlourin resulting in another voltage sensor called ArcLight (Jin *et al.*, 2012). The term pHluorin refers to several pH-sensitive mutants of eGFP introduced by Miesenbock and coworkers (Miesenböck, De Angelis and Rothman, 1998). Ecliptic pHlourin is a mutated variant of the wild type aqGFP consisting of six point-mutation, which reveals a voltage-sensitive fluorescence change (-1.3% ± 0.3% $\Delta F/F$) to a 100 mV voltage step. The super ecliptic pHluorin consists of an additional mutation that boosts the fluorescence changes about 14-fold (Miesenböck, De Angelis and Rothman, 1998). However, ArcLight suffers from slow kinetics resulting in low signal amplitude and limited temporal resolution. Many additional members in this family were introduced, such as VSFP2 (Mutoh *et al.*, 2009)·(Dimitrov *et al.*, 2007), Mermaid (Tsutsui *et al.*, 2008)·(Tsutsui *et al.*, 2013), Butterfly (Akemann *et al.*, 2012), VSFP-CR (Lam *et al.*, 2012), ASAP1 (St-Pierre *et al.*, 2014)·(Yang *et al.*, 2016), Bongwoori (Piao *et al.*, 2015), and FlicR1(Abdelfattah *et al.*, 2016), which have shown faster kinetics compared to their forerunner ArcLight, but their voltage sensitivity was lower and they bleached very fast (See Fig. I-5 and I-6).

One advantage of the VSD-based sensors is that they could be used *in-vivo* to monitor sensory-induced or spontaneous action potentials in a population of cells, even though this is not feasible at single-cell resolution, which is necessary, e.g., for tissues of the mammalian brain with a densely packed cell population (Carandini *et al.*, 2015; Storace *et al.*, 2015; Bando, Sakamoto, *et al.*, 2019).

Recently, two other sensors were added to this family developed from ASAP and ArcLight, namely ASAP3 and ArcLight-MT, with the feasibility of reporting electrical activities in-vivo (in intact or anesthetized mice) via two-photon excitation and single-cell resolution (Bando, Sakamoto, *et al.*, 2019). Despite these developments and efforts regarding the optimization of VSD-based indicators, there is still a necessity for more improvements to make their application more feasible, particularly for *in-vivo* imaging purposes.

More biological engineering is still needed to achieve a higher SNR accompanied by reduced photobleaching. The FlicR-family and the sensor Marina have a lower fluorescence signal during resting potential, which increases during depolarization. This property has helped to overcome the problem with the fast photobleaching of other members of the VSD-family (Platisa *et al.*, 2017)'(Abdelfattah *et al.*, 2016).

The second family of genetically encoded voltage sensors is derived from microbial rhodopsins. The first member of this family, PROPS (proteorhodopsin optical proton sensor), was introduced in 2011 by *Kralj et al.* (Kralj *et al.*, 2011). It could be shown that the pH value of the culture affected the color of the bacteria expressing PROPS, which was attributed to the protonated state of the retinal Schiff base. This observation sparked the idea that electrical changes of the membrane may have an influence on the electrochemical potential surrounding the retinal Schiff base and thus could modify the fluorescence (Kralj *et al.*, 2011). Since PROPS could be expressed only in *E. coli*, the group focused on proteins that had shown a stable expression in the plasma membrane of eukaryotes. It was well-known that Archaerhodopsin-3 (Arch-3) expressing bacterial cultures exhibit a color transformation upon a change in the pH-value due to a same mechanism like in PROPs. Therefore, a new functionality, as a protein-based voltage sensor, was postulated for Arch-3.

The absorbed light excites the fluorescence of the chromophore retinal. The sensor can detect depolarization of the membrane due to the change of the electrochemical potential around the Schiff base, which alters the fluorescence intensity (see Fig. I-7). Over the next few years, targeted and random mutagenesis, in addition to functional screening, step by step led to the achievement of brighter signals .

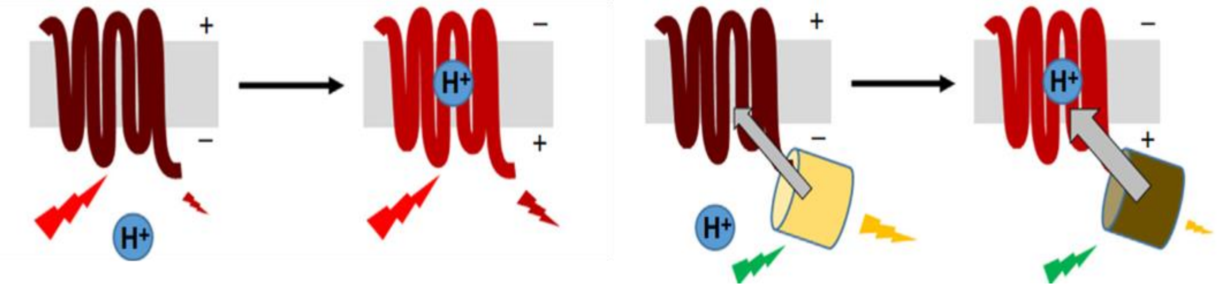

Fig. I-7: Voltage sensing mechanism in rhodopsin-based GEVIs. Left) changes in the electrochemical potential around the Schiff base increases the fluorescence intensity of the retinal. Right) Mechanism of voltage sensing in eFRET GEVIs. Changes in the absorption of the rhodopsin due to electrical activities of the membrane result in a radiation less quenching of the fluorescent protein, which is voltage-dependent in its amplitude. Adopted from (Xu, Zou and Cohen, 2017).

This advance began with a mutation abolishing the natural proton pumping functionality of Arch-3, while consecutive rounds of in vitro evolution improved the kinetics, brightness, and voltage sensitivity of the Arch-based GEVIs, leading to proteins termed Archer (Flytzanis *et al.*, 2014)' (McIsaac *et al.*, 2014), or Arch-EEN and Arch-EEQ (Gong, Li and Schnitzer, 2013). The terms, EEN and EEQ, refer to the mutations at D95N, D106E for EEN and D95Q, D106E for EEQ. The further optimization strategies in cell evolution of bacteria and mammalian cells led to the discovery of QuasAr1 and QuasAr2. These proteins exhibited voltage dependent fluorescence changes in the near-infrared region of up to 32% $\Delta F/F$ per 100 mV for QausAr1 and 90% for QuasAr2 (see Fig. I-4) (Hochbaum *et al.*, 2014).

Interestingly some of the point mutations are not close to the chromophore-protein-core, meaning that the changes in the structural conformation of the rhodopsin may also influence its voltage sensitivity. NovArch (Chien *et al.*, 2017) and QuasAr3 (Adam *et al.*, 2019) were the next members of this family, followed by Archon1 and Archon2 (Piatkevich *et al.*, 2018) (see Fig. I-3). 1-photon near infrared fluorescence of NovArch is reversibly enhanced by weak 2-photon excitation and has shown a rapid increase upon blue illumination. Furthermore, NovArch has revealed bright signals for deep tissue imaging and its infrared excitation wavelength makes it a suitable candidate for combinations with other optical tools (Chien *et al.*, 2017). QuasAr3 does not deliver significant advantages to its parental tools QuasAr1 and 2, whereas Archon1 and Archon2 seem to be faster than their predecessors and have a more stable signal (see Fig. I-3)

Despite these developments in the signal sensitivity of rhodopsin- based voltage indicators, these sensors still suffer from some shortcomings. The main problem lies in the fact that these proteins are proton pumps, and their fluorescence is only a 'side product' and this is the main reason for the inferior quantum yield, compared to prominent fluorescent proteins like GFP (30-80x dimmer) (Kralj *et al.*, 2012), demanding intense red laser illumination of 200-1000 mW/ mm².

The attempts to overcome this deficiency resulted in the generation of electrochromic FRET sensors (eFRET). This group of sensors consists of microbial rhodopsin, covalently linked to a fluorescent protein, enabling energy transfer from the fluorescent protein to the rhodopsin by FRET (Zou *et al.*, 2014),(Gong *et al.*, 2014).

The first two members of this group were derived either from QuasAr2 (Zou *et al.*, 2014) or the proton pump isolated from *Leptosphaeria maculans* (Mac) , which have built a FRET-pair with different fluorescent proteins, e.g., mCitrine or mOrange (Gong *et al.*, 2014). Changes in the absorption of the rhodopsin due to electrical activities of the membrane result in a radiation less quenching of the fluorescent protein, which is voltage-dependent in its amplitude (See Fig. I-7). eFRET sensors exhibit slower kinetics in comparison to their parental rhodopsins, since they monitor the voltage signal indirectly, as they receive the signals in form of the energy transfer in the FRET-pair from the rhodopsin and despite their bright fluorescence during resting potential, they seem to be less voltage-sensitive than their origin (13% per 100 mV for QuasAr2-mCitrine eFRET vs. 90% per 100 mV for QuasAr2). Recently, Ace-mNeon was introduced, which consists of *Acetabularia* rhodopsin (Ace), which built a FRET-pair with mNeon-Green.

The response-time of this sensor could be tuned up by the usage of the faster rhodopsin *Acetabularia* as the quencher for mNeon without a reduction in the sensitivity of the fluorescent protein (Gong *et al.*, 2015). Ace-mNeon could be applied *in-vivo* (in mice and fly brain). The latest and most red-shifted member of this group is VARNAM, based on the structure of Ace-mNeon, in which mNeon- Green is substituted with mRuby3. This protein has many advantages compared to its predecessors; it is more photostable and necessitates low light intensities at 1.5 mW/mm² (Kannan *et al.*, 2018), which is even 10 folds lower than earlier described eFRET sensors like MacQ-mCitrine or MacQ-mOrange at 15 mW/mm² (Gong *et al.*, 2014). The very red-shifted spectrum of VARNAM makes it compatible with blue-light activated optical tools for combined imaging. Albeit all these advantages, VARNAM could not overcome the low performance under two-photon imaging likewise other rhodopsin-based GEVIs.

Chemogenetic indicators are the third family of voltage indicators, which profit the advantages of their both forerunners namely the organic synthetic dyes (Salzberg *et al.*, 1977; Grinvald *et al.*, 1982; Cohen and Lesher, 1986) and the GEVIs. The main disadvantage of such lipophilic organic molecules, namely the unspecific staining of tissues, can be eliminated via a hybrid strategy, combining the optical properties of dyes with specifically targeted genetically encoded sensors (Kuhn, Fromherz and Denk, 2004; Hinner, Hübener and Fromherz, 2006; Ng and Fromherz, 2011). This family can be divided into three classes; FRET-based, enzymatic based, and Tag-anchored sensors.

The first member of this family, which was introduced in 2005, called hVOS, combined a small voltage-sensitive lipophilic dye dipicrylamine (DPA) and a genetically encoded farnesylated enhanced GFP (eGFP-F). In response to changes in membrane potential, DPA undergoes a translocation from one side of the membrane to the other side and also absorbs energy from GFP, which leads to a quenching effect in the GFP-signal (see Fig. I-8).The response time is ca. 500 µs and the sensitivity is 34% ∆F/F per 100 mV (Chanda *et al.*, 2005).

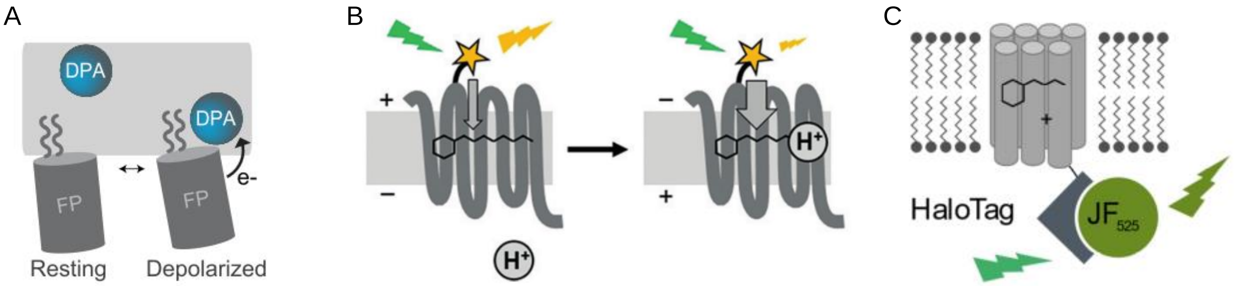

Fig. I-8: Voltage sensing mechanism in FRET-based chemogenetic indicators. A) voltage sensing in the indicator called hVOS, combined of a genetically encoded farnesylated eGFP and the lipophilic dye DPA, which undergoes a translocation upon depolarization and absorbs energy from eGFP leading to a quenching effect in eGFP-signal. B) Combination of a rhodopsin as a voltage sensitive part of the sensor and site -specifically ligated dye C) A rhodopsin with a self- labeling protein domain that binds to the synthetic JF dye. Modified from (Bando, Grimm, *et al.*, 2019),(Xu *et al.*, 2018), (Beck, Zhang and Gong, 2019)

The second type of FRET-based chemogenetic sensor uses rhodopsins as the GEVI component and site-specifically ligated organic dyes. The fluorophore ligation-assisted rhodopsin electrochromic FRET (FlareFRET) is the first example of a sensor with these properties (see Fig. I-8) (Xu *et al.*, 2018), followed by the development of Voltron using novel rhodamine dyes such as the Janelia Fluor (JF) series. Voltron consists of a microbial rhodopsin with a self- labeling protein domain that binds to the synthetic JF dye (Encell, 2012),(Grimm *et al.*, 2015). Voltron was successfully applied in larval zebrafish, fruit flies, and mouse brain (Abdelfattah *et al.*, 2016).

As mentioned above, one class of chemogenetic sensors is enzyme-based. In this class of indicators, a genetically encoded enzyme in the cell membrane, activates the precursor of an organic voltage sensor. For example, the enzymatic part of the indicator can be an alkaline phosphatase, which hydrolyses a water-soluble precursor dye. An example of a voltage sensitive dye precursor with a phosphate group attached to its head group is the chromophore aminostyrylpyridinium (ASP) (Hinner, Hübener and Fromherz, 2006). The advantage of this group of sensors is the fast staining time of internal organelles within seconds. Further generation of this class could show up to 50% ΔF/F per 100 mV (Ng and Fromherz, 2011).

The most prominent member of this class is VF-EX (Voltage Fluor-Esterase expression*)*. This sensor combines the activity of a genetically encoded esterase, which uncages a voltage-sensitive fluorescent dye. The advantage of this approach was the measurement of action potentials in cultured neurons. Besides, VF-EX shows improved SNR and fluorescence change, in labeling dendrites and dendritic spines (Liu *et al.*, 2017).

The tag-anchored sensors are the last class of chemogenetic sensors, which capture the chemical dye in the membrane with a protein structure. The so-called VoltageSpy system is a chemogenetic sensor that consists of a SpyCatcher protein, which is expressed on the cellular surface. The SpyCatcher interacts with the dye via a small peptide of 13 residues and through a polyethyleneglycol (PEG) linker (Grenier *et al.*, 2019) (see Fig. I-9)

Another member of this group is HAPI-Nile that uses the advantages of the voltage indicator Nile Red, exhibiting signals in the physiological range of electrical membrane potentials, making it possible to track supra and subthreshold activities in neurons (Sundukova *et al.*, 2019) (see Fig. I-9).

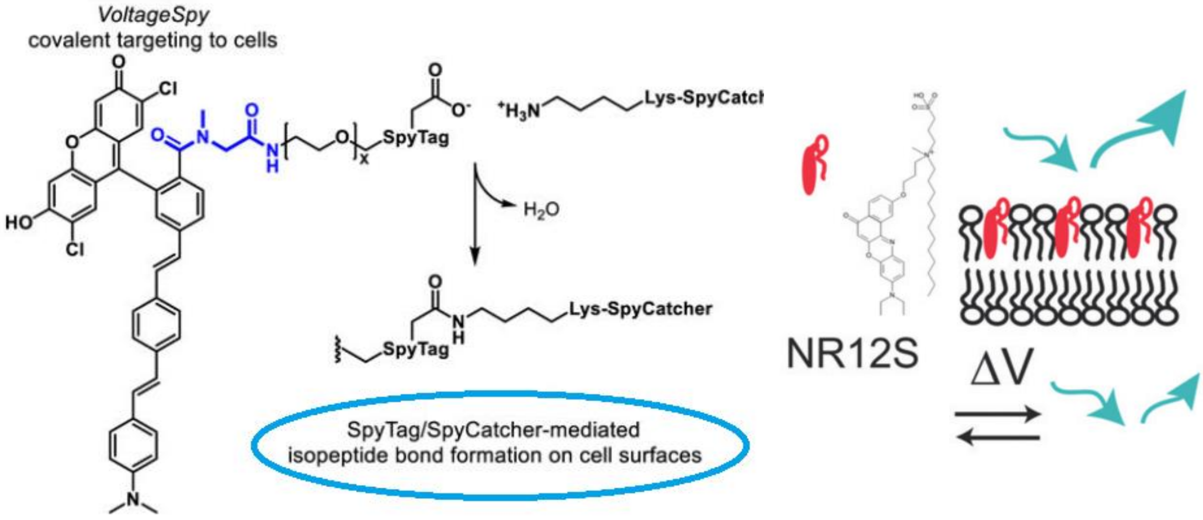

Fig. I-9: Genetic targeting of VoltageFluor (VF) dyes in a SpyTag/SpyCatcher system. Left) SpyCatcherprotein is expressed on the cellular surface and interacts via a small peptide through a PEG-linker. Right) Decrease of the fluorescence intensity of nile-red-based NR12S probe upon membrane depolarization. Modified from (Grenier *et al.*, 2019), (Sundukova *et al.*, 2019)

Besides the introduced GEVIs, Calcium Indicators should be mentioned as optical tools for monitoring the neuronal activity, (Miyawaki *et al.*, 1997; Hendricks, 2012). Genetically encoded calcium indicators (GECIs) such as GCaMP und RCaMP are fusion proteins, which consist of a fluorescent protein, the calcium-binding protein Calmodulin, and Calmodulin-binding-peptide M13 (Miyawaki *et al.*, 1997). The binding of calcium ions, whose cytosolic concentration increases in response to electrical activity by way of voltage gated Ca^{2+} channels, leads to changes in the structural conformation in the GECI, followed by fluorescence changes (Lin and Schnitzer, 2016). There was a great effort in the last decade to enhance the properties of GECIs, which made it feasible to combine these indicators with other optical tools (Looger and Griesbeck, 2012; Akerboom *et al.*, 2013; Chen *et al.*, 2013). However, GECIs suffer from a central problem; the monitored signals are not directly measured, meaning that they report about the cytosolic concentration of Ca^{2+}- ions in response to membrane depolarization. The strength of the signal is dependent on the Ca^{2+}-affinity of the GECI. More affinity to calcium means a stronger signal, but also a delay in the signal decay. It should be kept in mind that electrical activities are not consistently Ca^{2+-}-dependent (Williams *et al.*, 2018). Another fact is that under normal physiological circumstances, calcium concentration does not drop under resting concentration, even if a cell is hyperpolarized, which means that tracking of hyperpolarization in a cell is not achievable via the application of GECIs (Gong *et al.*, 2014; Hochbaum *et al.*, 2014; Zou *et al.*, 2014; Piatkevich *et al.*, 2018).

1.3: Optogenetic tools utilized in this project

Several optogenetic tools were used during this project. Most of the introduced voltage indicators were tested for their potential of voltage imaging in *C. elegans.* However, some of them like MacQ:mOrange, Arch-EEN/-EEQ or Archer from rhodopsin-based family and some members from VSD-based family indicators such as ASAP and ArcLight have shown disadvantages as GEVI when expressed in *C. elegans;* e.g., non-stable expression pattern, reduced expression levels in adult or aged animals or dim fluorescence signal. In this section, the tools that were used for the final experiments of voltage imaging will be introduced in detail.

1.3.1: Channelrhodopsin-2: Optical actuator

Channelrhodopsins are light-controlled cation channels isolated from the green algae *Chlamydomonas reinhardtii,* which are responsible for the phototaxis of the algae and function as a photoreceptor. Excitation of the channel leads to its opening and thus the depolarization of the membrane (Lin, 2010)' (Mattis *et al.*, 2012). The first channelrhodopsin (ChR1), isolated from *Chlamydomonas,* was characterized as a proton channel, whereas further investigations have shown that also ChR1 is capable of conducting cations like Na^+, K^+ and Ca^{2+} (G. Nagel *et al.*, 2005)'(Nagel *et al.*, 2003). The channel activity of ChR2 was confirmed via electrophysiology in HEK-cells and *Xenopus laevis* Oocytes, the first organism with exogenous expression of ChR2 (G. Nagel *et al.*, 2005). The first application of ChR2 as a light-activated actuator for depolarization of excitable cells was performed in mouse, *C. elegans,* HEK293 cells, cultured hippocampal neurons, and isolated chicken spinal cord. (Boyden *et al.*, 2005)'(Georg Nagel *et al.*, 2005)'(Li *et al.*, 2005).

Channelrhodopsin consists of 737 amino acids, of which only the first 300 are involved in forming the 7 transmembrane helix rhodopsin fold (Kato *et al.*, 2012). ChR2 uses all-*trans*-retinal as its chromophore, which binds covalently via a Schiff base to Lysin 257. The embedding of the chromophore retinal occurs via hydrophobic complex (formed by R120, E123, D253) around its aromatic ring and is stabilized with hydrogen-binding between water molecules and Schiff base (Müller *et al.*, 2011). The N-terminus of the protein looms out to the intracellular space, whereas the C-terminus with unknown function is localized intracellularly (see Fig. I-10, Left).

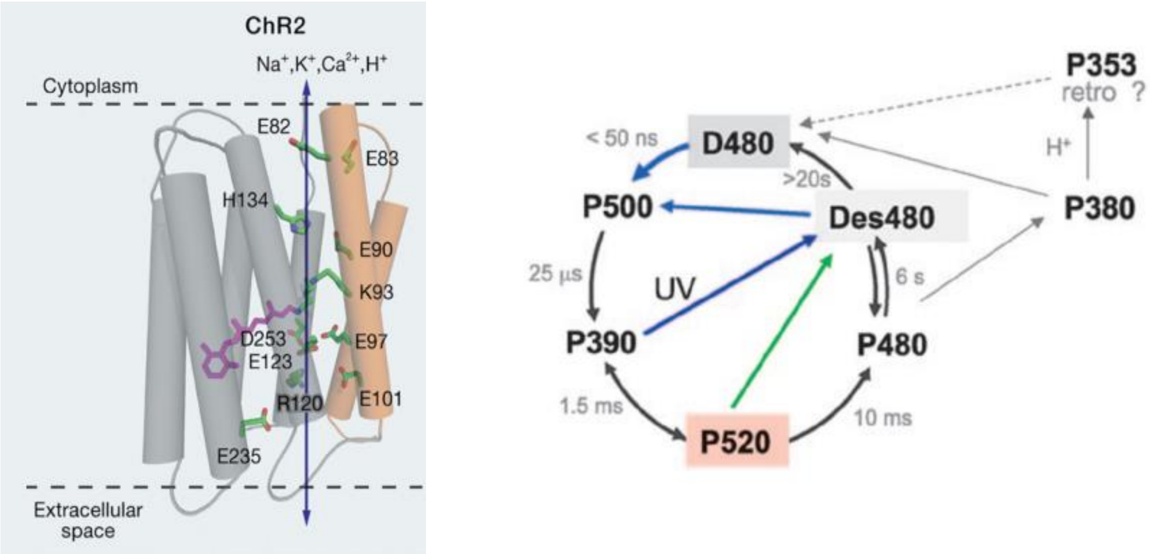

Fig. I-10: Schematic structure and photocycle of channelrhodopsin. A: 7TM Structure of ChR2 with the hydrophobic complex around all-*trans*-retinal (Zhang *et al.*, no date). B: Schematic illustration of the ChR2 Photocycle. Blue and green arrows indicate transitions from one state to another, induced by blue or green light, respectively. Different states of the photocycle are termed including their absorption wavelength. The lifetime of each state is indicated in gray (Stehfest and Hegemann, 2010).

Only a fragment encompassing TM 1-7, consisting of 314 amino acids, is used in optogenetic applications. Photon absorption results in a change of the configuration of the chromophore from all-*trans* to 13-*cis*, setting off the photocycle of the protein, which finally leads to cation transport via the channel due to conformational changes in the channel´s structure (Zhang *et al.*, no date; Bamann, Nagel and Bamberg, 2010; Stehfest and Hegemann, 2010; Spudich, Sineshchekov and Govorunova, 2014).

The ground state of the photocycle of ChR2 is the dark-adapted state (D470), which converts to conducting state (P520) upon illumination with blue light (470 nm), transitioning *via* two intermediates, the short-lived states P500 and P390. Absorption of a green photon in this phase leads to the elimination of the photocurrents by moving the channel back to a closed state, which can be D470 or D480 (Bamann *et al.*, 2008), (Berndt *et al.*, 2009) (see Fig. I-10, right panel). Retinal isomerizes during the transition from D470 to P520, which results in deprotonation of the Schiff base. At this moment, one proton transfers to the extracellular space. P520 results from P390 by the reprotonation of the Schiff base with the help of a proton from the cytosol. P520 converts back to D470 via the photostates P480 and Des480. In parallel, deprotonation of the Schiff base leads the conversion of P480 into the second blue-shifted intermediate P380. The fluorescent intermediate P353 is thought to be generated by the thermal conversion of P380 back to D470, which also relaxes back to D470. The return of P480 to the ground state is very slow. The photocycle is schematically demonstrated in figure I-10.

Many variants of channelrhodopsin have been discovered or engendered to achieve new properties like faster kinetics and larger channel conductivity. The variant used in this project was a gain-of-function containing the H134R mutation. It increased the photo-evoked currents, due to a slower kinetic, which, compared to the wild type protein, resulted in stronger responses to the same photo stimulation (G. Nagel *et al.*, 2005). ChR2 expression was addressed to cholinergic neurons under the control of the promotor of the *unc-17* gene. Blue light activation at 470 nm activates channelrhodopsin and results in acetylcholine release from cholinergic motor neurons and thus the depolarization of body wall muscles. In this manner, channelrhodopsin played a role as an optical actuator.

1.3.2: Genetically encoded voltage sensors for application in *C. elegans*

Arachaerhodopsin-3 (Arch-3) is a light-controlled outward proton pump, which functions as a photoreceptor in *Halorubrum sodomense* (Ihara *et al.*, 1999). Expressed exogenously in other organisms, e.g., in bacteria (Kralj *et al.*, 2012), mammalian cells (Chow *et al.*, 2010), mice (Madisen *et al.*, 2012) and *C. elegans* (Husson *et al.*, 2012; Okazaki, Sudo and Takagi, 2012; Okazaki *et al.*, 2014), it can lead to neuronal silencing via membrane hyperpolarization (Clair *et al.*, 2012; Takahashi and Takagi, 2017; Wiegert *et al.*, 2017) (see Fig. I-11). One possible reason for the successful heterologous expression of Arch-3 in comparison to its predecessor bacteriorhodopsin might be either due to the structure of its cytoplasmic and extracellular loops or just its origin from archaea that have more similarities to eukaryotes (Saint Clair *et al.*, 2012). Arch-1 and Arch-2 are the founding members of this family, isolated from *Halobacterium sp.aus-1* und *sp.aus-2*, two halobacterium species living along the Australian coast (Mukohata *et al.*, 1988), (Uegaki, Sugiyama and Mukohata, 1991). They have up to 88% sequence homology with each other and 55-58% homology with the prominent proton pump bacteriorhodopsin. Their crystal structure confirms the differences of their conformation with each other and with bacteriorhodopsin (Enami *et al.*, 2006). Arch-3 exhibits 90% homology to Arch-1 and Arch-2. It has 75% homology to bacteriorhodopsin as well, which is significant in the region of conserved amino acids concerned in proton transport. (Clair *et al.*, 2012). A folding model, based on the structure of Arch-1 and Arch-2, was suggested by *Saint Clair et al.*, which is shown in figure I-5 (Saint Clair *et al.*, 2012). Besides, the attempts for understanding the structure of the protein led to *in-silico* modeling (Nikolaev *et al.*, 2017) (see Fig. I-11), since the protein could not be crystallized yet.

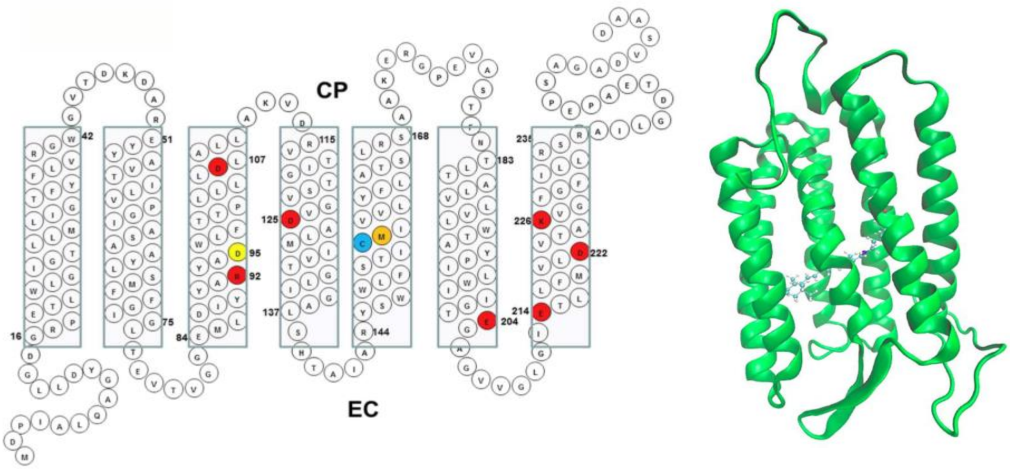

Fig. I-11: **Schematic demonstration of a folding model and structure of Arch-3.** Left) Suggested folding model based on the well-known structure of Arch-1 and Arch-2 and Arch3´s sequence. The amino acids, which are involved in proton transport, are red- highlighted (Saint Clair *et al.*, 2012). Right) Predicted 3-D structure of Arch-3 via *In-Silico* remodeling (Modified from (Nikolaev *et al.*, 2017)).

As referred previously, Kralj *et al.* have discovered a new functionality for Arch-3 as an optical voltage indicator besides its already well-known activity as a neuronal silencer. They mentioned that Arch-3 could detect action potentials along the membrane and visualize electrical changes in the form of fluorescence changes of its chromophore ATR. They had the hypothesis that the detection ability may get enhanced if the natural ability of proton pumping is deactivated. To prove this idea, they introduced the first mutation in Arch-3; Arch(D95N), which is homologous to the known mutation (with the same effect) in bacteriorhodopsin; this amino acid is known to be involved in proton transport chain (Fig. I-12) (Kralj *et al.*, 2012). Arch-3 exhibits ~ 35-40% ∆F/F per 100 mV within sub-milliseconds, which increased up to ~50% ∆F/F per 100 mV in Arch(95N).

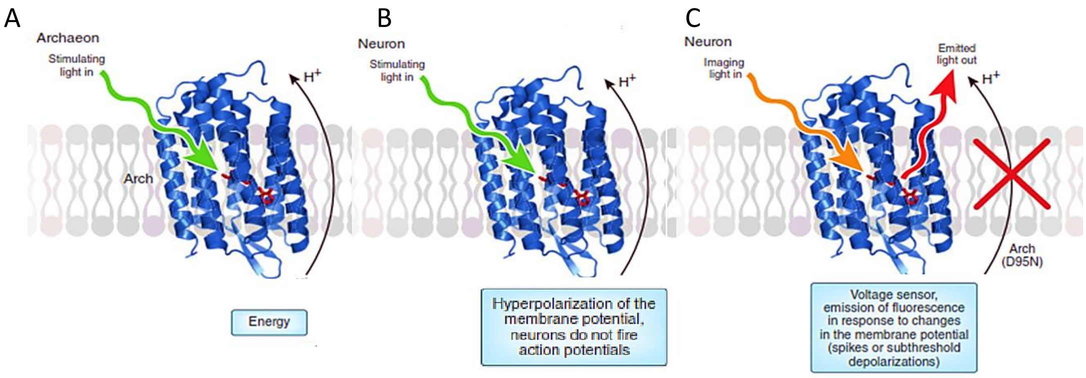

Fig. I-12: Schematic illustration of three different functionalities of Arch-3. A) Arch-3 is a proton pump found in the archaeon *Halorubrum sodomense* acting as a photoreceptor B) It functions as a neuronal silencer when expressed heterologous in other organisms C) Arch-3 can detect action potentials and emit out light as a response to the changes in the electrical activity of the membrane. This response is enhanced if its natural proton pumping functionality is turned-off via mutations in the proton transport chain (Looger, 2012).

In the framework of this project, Arch(D95N) was examined for the feasibility of tracking action potentials in both pharyngeal and body wall muscles of *C. elegans*. The attempts to understand the mechanisms of voltage sensitivity of the newly described functionality of Arch-3 via fluorescence spectroscopy in *E. coli* and HEK-cells resulted in the introduction of a proposed photocycle. This photocycle, based on bacteriorhodopsin´s photocycle, consists of a ground state that converts to the blue-absorbing state within 50 µs up on green light illumination with a decay time constant of 390 µs. The red absorbing O-state appears with two time-constants, 390 µs or 4,1 ms and decay of ca. 14 ms. The N-state is due to its overlapping with the ground state not directly visible. The short-living N-state can convert to the voltage-sensitive intermediate Q upon green light excitation. Q-intermediate emits near red light while detecting action potentials and illumination with a second photon illumination at 570 nm (Fig. I-13) (Maclaurin *et al.*, 2013).

Fig. I-13: Proposed photocycle for Arch-3. A proposed photocycle for Arch-3, based on the photocycle of bacteriorhodopsin. Green light starts the cycle at the ground state converting it to M state, which is followed by the nonvisible N-state. N-state has a decay constant of 4 ms leading to the arise of O-state with slow decay, finishing the cycle back to the ground state. The nonvisible N-state can produce the voltage-sensitive Q-intermediate that emits near red light upon illumination at 570 nm during action potentials. Modified from (Maclaurin *et al.*, 2013; Brinks *et al.*, 2016)

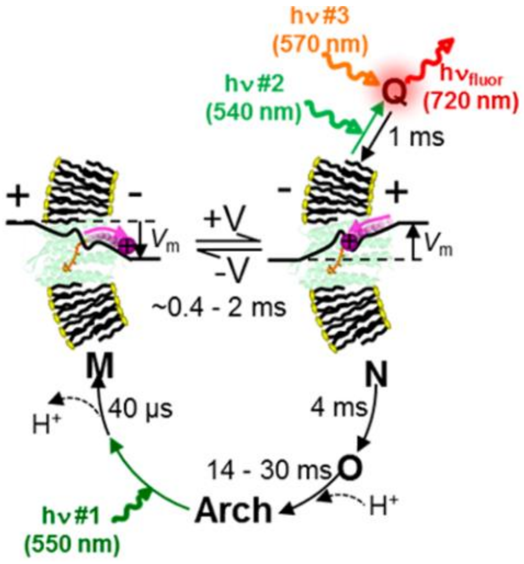

The fluorescence of the ground state is very dim, but through a proposed sequence of absorption of three photons at different stages of the photocycle, a state ‘Q’ is reached which has largely increased fluorescence. The more photons are provided for excitation, the more proteins can be shifted into this state. The start of the photocycle is accompanied by the conversion of all-*trans* retinal to the 13-cis configuration. Voltage sensitivity is an attribute of 13-cis configuration and is intensified by the protonation of the Schiff base from the intracellular side. It was suggested to generate proteins with a 13-cis ground state, to enhance the voltage sensitivity and the fluorescence signal of the sensor. It was known from bacteriorhodopsin that D96N/D115N mutations prolong the lifetime of this state since its reprotonation is the final step of the photocycle. This position is homologous to D106 and D125 in Arch-3 (Maclaurin *et al.*, 2013). Two constructs were introduced containing a mutation at amino acid D106; Arch-EEN, which contained the previously introduced D95N and D106E and Arch-EEQ with D95Q and D106E mutations. These two sensors have shown faster kinetics and higher voltage sensitivity (20% $\Delta F/F$ per 100 mV for EEN and 60% $\Delta F/F$ per 100 mV for EEQ). However, high illumination intensities (1400 mW/ mm^2) were required for enrichment of the fluorescent Q state (Gong, Li, and Schnitzer, 2013).

Archer-1 (or Arch-DETC; D95E, T99C) and Archer-2 (or Arch-DETCAM; D95E, T99C, A225M) were the next enhanced rhodopsin-based voltage indicator that exhibited five-fold brighter fluorescence signal comparing to Arch(wt) when expressed in *E.coli*. They could be expressed in cultured rat hippocampal neurons (Flytzanis *et al.*, 2014),; in addition, Archer-1 was expressed in *C. elegans* (Flytzanis *et al.*, 2014). Odor stimuli induced action potentials in olfactory AWC neurons of the nematode. This induced depolarization caused 40% changes in $\Delta F/F$. Although signal changes were significant, high intensities of excitation (~ 880 mW/ mm^2) and long exposure time (100 ms) were needed to achieve this result (Flytzanis *et al.*, 2014). A new enhanced Arch-variant will be introduced in this project, which combines the advantages of Archer-1 and the mutation at D106. This new mutant is Arch(DETCDE), containing D95E, T99C, D106E. This sensor was expressed in body wall muscles, and its ability to track action potentials was tested during spontaneous muscle activity as well as by optogenetically induced depolarization.

The last Arch-based sensor, which was expressed in *C. elegans* pharyngeal muscles during this work, was Arch(D95H). Illuminated with blue light, this mutant with optical bistability changes to a state which is fluorescent. Red light agitates this fluorescence on the one hand and resets it back to its non-fluorescent state step by step (Brinks *et al.*, 2016). A biexponential rise in fluorescence signal could be detected as the response to a voltage step. Outward photocurrents of 5 pA have been measured, which is 200 times lower than the 1 nA photocurrents measured by Arch(wt) and thus can be neglected (Hou, Venkatachalam, and Cohen, 2014).

Besides the enhanced Arch-variants for direct-imaging of rhodopsins, two eFRET sensors were tested in this project as well; QuasAr-mOrange and MacQ-mCitrine. The first introduced members of the eFRET GEVIs are a combination of the microbial opsin derived from the fungus *L. maculans* (Mac) as a FRET-pair with the fluorescent proteins mCitrine or mOrange. As mentioned in the first section, Mac is also a proton pump, which was used in neural silencing (Boyden, 2011; Husson *et al.*, 2012). A homologous mutation to ArchD95 was performed to deactivate its natural functionally. This mutation led to the formation of Mac139Q that was then used in the structure of the eFRET sensor. The absorption spectrum of Mac has shown the most extensive overlap with mCitrine and mOrange (see Fig. I-14, panel B). Both MacQ- derived eFRET sensors exhibited ~ 20% ΔF/ F per 100 mV. QuasAr variants were described as improved Arch-variants for direct imaging, containing the prominent mutations D95 and D106 with additional mutations discovered by generating a mutant library via error-prone PCR. The resulting QuasAr-2 exhibited a 10-fold brighter signal compared to Arch(D95N) and contains the mutations P60S, T80S, D95H, D106H, F161V (Hochbaum *et al.*, 2014). It was used in the generation of an eFRET sensor, in which QuasAr was combined with a fluorescent protein. Investigating the overlap of the emission spectra of different fluorescent proteins with the absorption spectrum of QuasAr, it can be supposed that QuasAr-mOrange and QuasAr-mRuby should be the most sensitive eFRET sensors in this group (see Fig. I-14, panel A). These sensors show up to -13% ΔF/F per 100 mV.

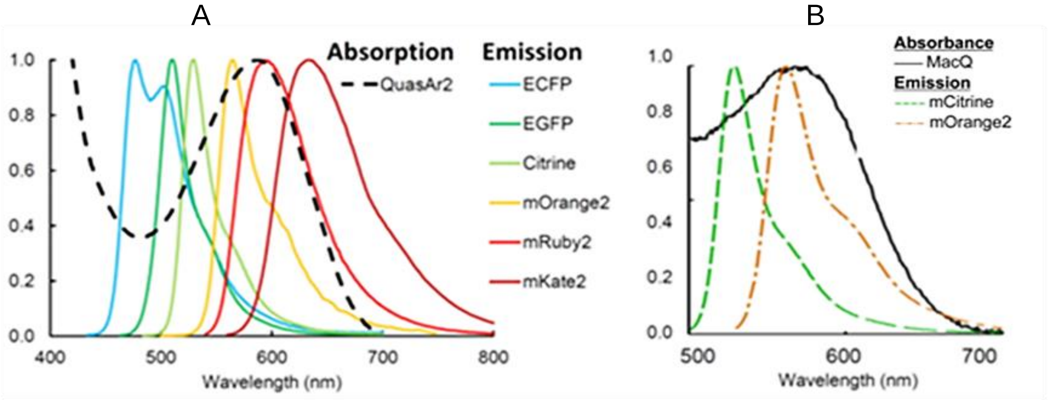

Fig. I-14: Illustration of the overlap between the absorption spectra of MacQ and QuaAr-2 with emission spectra of different fluorescent proteins. A) The absorption spectrum of QuasAr-overlapping with different fluorescent proteins that were tested for the formation of QuasAr-based eFRET sensor B) the same as A for MacQ-based sensors. Modified from (Gong *et al.*, 2015).

Table I-1 summarizes the GEVIs utilized in this work. Another strategy to overcome the dim fluorescent signal of ATR was substituting it with chemically modified retinal analogs, which enhanced the fluorescence signal of the sensors. These synthesized analogs will be introduced in the next section.

GEVI	Target tissue	Chromophore
Arch(D95N)	Pharynx, BWMs	ATR, DMAR
Arch(D95H)	Pharynx	ATR, DMAR
Arch(D95E,T99C,D106E)	BWMs	ATR, DMAR
QuasAr-mOrange (eFRET)	Pharynx, BWMs	ATR
MacQ-mCitrine (eFRET)	Pharynx	ATR

Table I-1: Overview of the applied GEVIs. The listed GEVIs were tested during this doctoral thesis for their ability to track electrical activities in *C. elegans* muscles. Target tissues and the respective chromophores are listed as well.

1.4: All-*trans*-retinal (ATR) and ATR-analogs

Retinal is a derivative of β-carotene. Addition of oxygen to the central double bond of β-carotene and subsequent hydrolysis results in vitamin A-aldehyde, also called all-trans retinal. The chromophore retinal exists in two configurations. 11-*cis*/all-*trans* isomerization occurs in animal rhodopsins, whereas microbial rhodopsins undergo an all-t*rans*/13-*cis* isomerization. Retinal binds via a Schiff base to a lysin residue. As briefly mentioned, the absorption of light provokes interaction between the opsin and retinal, which leads to proton transport through a cascade of de- and reprotonation steps of the amino acid residues that constitute the photocycle of the protein (see Fig. I-15) (Ernst *et al.*, 2014).

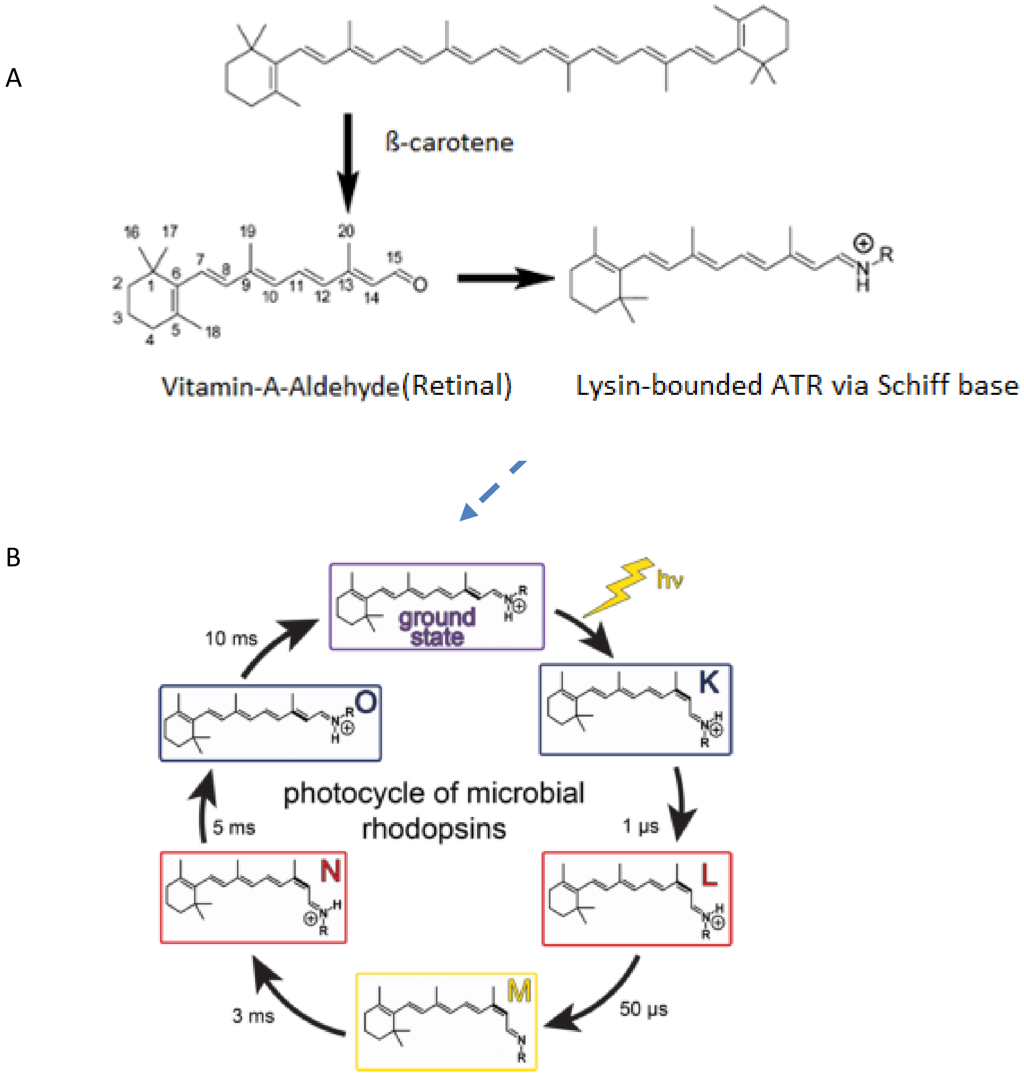

Fig. I-15: All-*tans*-Retinal; its formation from ß-carotene and isomerization to 13-*cis* during a typical microbial photo cycle A) ß-carotene oxidizes to vitamin-A (not shown), which hydrolyses to vitamin-A-aldehyde. B) Opsin photocycle, illustrating the isomerization of All-*trans* to 13-*cis* retinal (Modified from (Ernst *et al.*, 2014)).

Substitution of ATR with different synthetic analogs was a great aid to understand the mechanism of opsin´s photocycle. The importance of some structural properties of the molecule and their effect on opsin-chromophore interaction could thus be analyzed very well (Foster *et al.*, 1989).

To achieve this, different modifications have been introduced into the structure of the natural chromophore, e.g., removing the ß-ionone ring entirely or substituting it with an aromatic ring, shortening or extension of the polyene chain or locking the isomerization using saturated instead of unsaturated bonds (Albeck *et al.*, 1989; Foster *et al.*, 1989, 2011). In addition to being informative about the opsin-retinal interactions, some of the analogs granted the opsins new properties, such as a shifted absorption spectrum or acceleration or deceleration of the photocycle and thus the kinetics of the protein (Ganapathy *et al.*, 2017; Hontani *et al.*, 2019).

Another observation was made while exploring different ATR- analogs for their properties and their feasibility to be used in different opsins expressed in *C. elegans*, namely robust fluorescence signal by some of these synthetic retinals (Azimihashemi *et al.*, 2014). This observation spiked the idea to test these analogs for voltage imaging as a strategy to overcome the dim signal of ATR. The structure of these two analogs is illustrated in figure I-16.

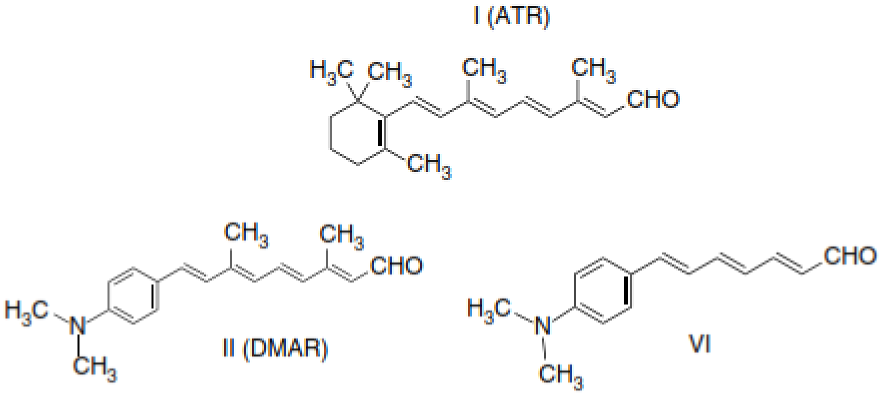

Fig. I-16: The chemical formula of ATR and two synthetic retinals. For comparison, the formula of ATR is illustrated above. Unbound analogs reveal a red-shifted absorption spectrum (analog VI: 430 / DMAR: 450 nm) compared to ATR (380 nm). These spectra vary in different opsins when the chromophore is bound, however, they were still red-shifted in comparison to ATR (Adopted from (Azimihashemi *et al.*, 2014)).

1.5: *Caenorhabditis elegans (C. elegans)* as a model organism

Introduced as a model system in biology in 1965 by Sydney Brenner*, C. elegans* began to have a significant role in biology. This free-living non-parasitic nematode has revealed many advantages as a model organism, e.g., the fast life cycle, which eases its cultivation in biological labs*. C. elegans* is very small; 80-100 µm in diameter and 1,5 mm long. It is known to be the multicellular organism with a fully sequenced ('Genome sequence of the nematode *C. elegans*: A platform for investigating biology', 1998), which makes effective genetic manipulations straightforward.

It appears in two genders: self-fertilizing hermaphrodites and males. Hermaphrodites consist exactly of 959 somatic cells, while the males have 1031 cells. The differences originate from additional neurons, which are involved in the mating behavior of the males (Donald L Riddle, 1997). Its transparency makes *C. elegans* a favorite model organism in optogenetics, which enables the deep penetration of light without the need for any additional manipulations.

1.5.1: The life cycle *of C. elegans*

C. elegans transits through four larval stages (L1- L4) to become a fertile adult. Hermaphrodites can produce sperm in a short phase of life before they begin with the formation of oocytes. The oocytes can be fertilized either with the own sperm (which is stored in a special structure, termed spermatheca) or with sperm transmitted from males. This either leads to the generation of animals isogenic to the mother, or a cross between genetic lines, respectively. The eggs exit the body through the vulval opening as soon as they consist of 20-30 cells. Embryogenesis is completed after 13 hours *ex utero*, which is visualized by the formation of the 3-fold larva that contains 558 cells. Hatching occurs immediately after the formation of the 3-fold structure followed by the L1 larval stage. If the animal has been fed well, it can grow and go through the next four stages of development until adulthood. However, if conditions are adverse, it undergoes an evolutionary strategy to survive the non-optimal circumstances and converts into the so-called dauer larva. Dauer larvae can survive stress conditions, e.g., absence of food or sub-optimal temperature up to 4 months. Upon recurrence of optimal requirements, the dauer larva can resume the normal life cycle. L1 animals need ca. thirty-eight hours to become a young adult. After another 8 hours, a young adult can produce the first eggs for the next generation (see Fig. I-17) (Corsi, 2006).

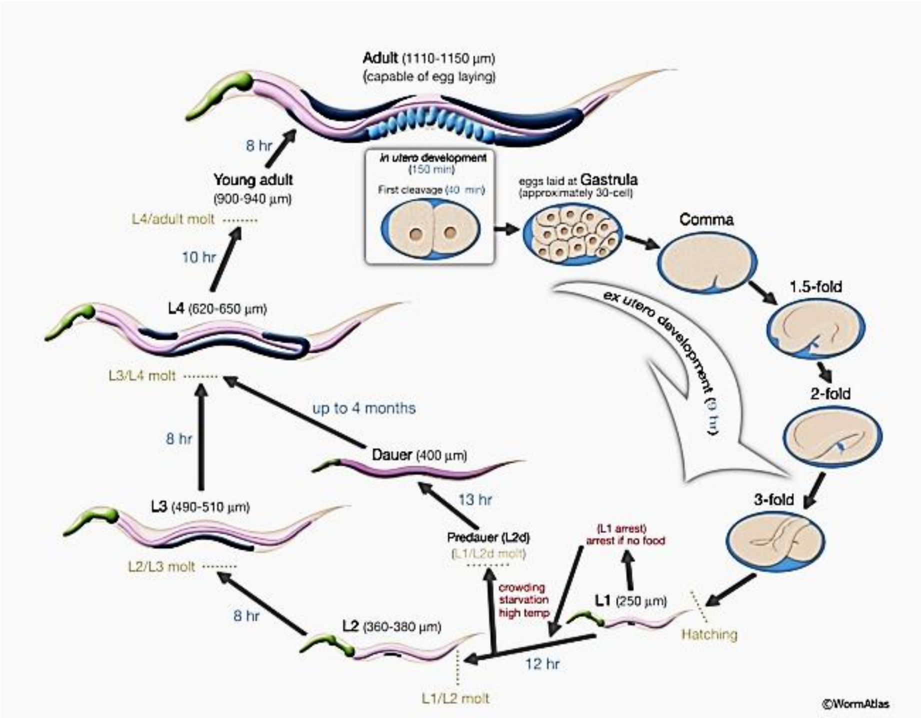

Fig. I-17: The life cycle of the nematode *C. elegans.* The life cycle consists of four larval stages beginning after hatching. Under non-optimal situations such as lack of food, L1 animals convert to dauer larvae, which are very stress- resistant. L4 animals need 10 hours to become young adult animals with the ability of fertilization. The produced eggs can be laid as soon as they consist of 20-30 cells and undergo their further development outside the maternal animal (*ex utero* biogenesis) for more 9-13 hours until hatching (Adopted from (Corsi, 2006)).

1.5.2: The pharynx

The pharynx, the feeding organ of *C. elegans,* is a neuromuscular tube, which transfers food via pump-like muscle contractions to the intestine. Catching the food occurs via an opening to the environment at the anterior side of the pharynx called the buccal cavity followed by procorpus, metacorpus, isthmus, terminal bulb and pharyngeal - intestinal valve, which connects the pharynx to the intestine. It is assembled of seven cell types: 9 epithelial cells, 20 muscle cells, 9 marginal cells, 4 gland cells, 20 neurons, six posterior valve cells, and the arcade cells with 95 nuclei in total (see Fig. -18) (Albertson and Thomson, 1976).

The pharynx can grow to 100 µm length in a young adult animal. The terminal bulb with a diameter of 20 µm is the widest part of this organ. The pharynx is isolated from the rest of the body via a basal lamina. This organ has its own muscular and nervous system and acts independently from the remaining organs. Its nervous system, containing 20 neurons, moderates the intrinsic myogenic activity and sets internal signals, e.g., signals about the presence or absence of food (Avery and Horvitzt, 1989; Franks *et al.*, 2006). Pumping rate decreases to ca. 1 Hz in the absence of food and increases to 200-300 per minute during feeding.

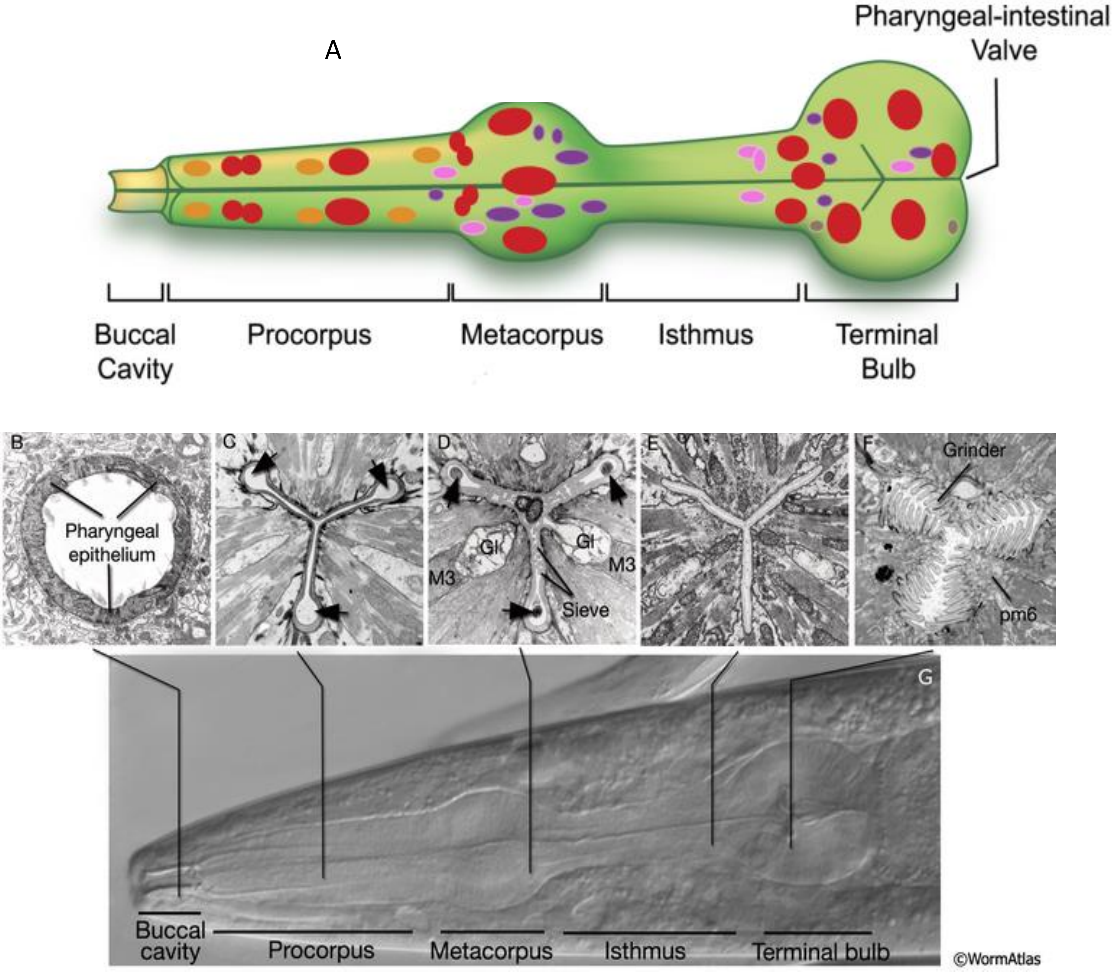

Fig. I-18: Pharynx anatomy. A) 6 different segments of pharynx beginning anteriorly with the buccal cavity and ending posteriorly at the pharyngeal-intestinal-valve as a connection between pharynx and intestine. The Color index of the shown nuclei: red muscles, purple neurons, orange epithelia, pink marginal cells and brown glands, arcade cells, and pharyngeal intestinal valves (not shown). B-F) electron microscopy sections through various parts of the pharyngeal lumen. The location of the sections is shown in G with an arrow indicated in G**.** F) Grinder in the terminal bulb. G) DIC micrograph of the pharynx (From worm atlas.org)

The 20 pharyngeal muscle cells encircle it in an arrangement of eight consecutive rings (pm1- pm8). Most of these muscles are formed from three syncytial cells with a trigonally symmetric organization, forming a cylinder that surrounds the lumen containing the food particles. There are also some exceptions; pm1 and pm 8 contain just a single syncytial cell. As a result of fusion during hatching, each of these cells possesses two nuclei. Only pm1 with 6 nuclei and pm6-8 with one nucleus differ. Three marginal cells separate the three cells in each segment, and the cells from the neighboring ring are connected via gap junctions. The nerve cord encircles the cell body and is situated on the basal side. It contains neurons, gland cells, and anterior epithelial cells. Many synapses, including neuromuscular junctions to the pharyngeal muscles, occur along these cords (see Fig. I-19).

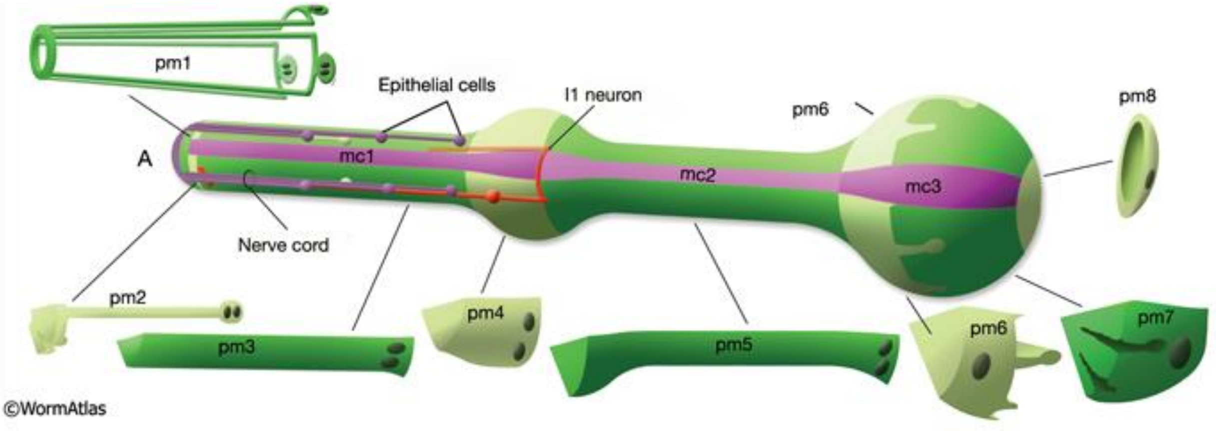

Fig. I-19: Muscle cells of the pharynx. Pharyngeal muscles are divided into 8 segments; pm1-pm8. Except for pm6-8, all the others form syncytia. The most interior pm1 is a single cell with 6 nuclei, whose terminal posterior part is in ring form. Each pm2 soma has two nuclei and projects into a nerve ring to extend anteriorly. Pm3 cells are positioned in the procorpus, pm4 cells in the anterior bulb, and pm5 cells in the isthmus. The terminal bulb contains pm6-pm8. The last muscle segment contains a single cell, pm8, that has a single nucleus located on the left side (Adopted from (Mango, 2007)).

Pharyngeal pumping occurs upon contraction-relaxation phases of pharyngeal muscles in which the corpus, anterior half of the isthmus, and terminal bulb are involved. Pumping begins with the almost parallel contraction of these muscles, which leads to the opening of the lumen. The lumen gets filled by the sucked-in food, while the posterior isthmus is still closed. As soon as the contraction is forwarded to the terminal bulb, it starts to move the grinder plates and accordingly breaking up the food particles. The final step during the contraction phase is the transport of food debris into the intestine. An almost simultaneous relaxation occurs after the contraction and sets the grinder back to its resting position and also, closes the lumen. The liquid part of the food flows back through the corpus and anterior isthmus, whereas the ground bacteria are transported back to the terminal bulb through a further movement called, posterior isthmus peristalsis (see Fig. I-20). On average, one out of four pumps is followed by a posterior isthmus peristalsis (Avery and Shtonda, 2003; Trojanowski, Raizen and Fang-Yen, 2016).

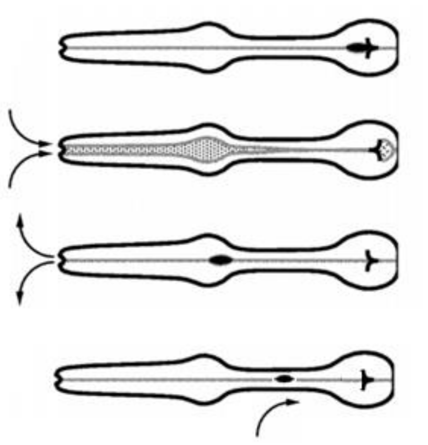

Fig. I-20: Schematic illustration of pharyngeal pumping. An almost simultaneous contraction of muscles opens the lumen and fills it up with liquid food, which has particles as well. Contraction of the terminal bulb activates grinder plates and breaks up the food particles. Debris is transported to the intestine. The following relaxation leads to the backflow of the food into the lumen. Liquid constituents stream back to the environment, and isthmus peristalsis delivers the ground bacteria back to the terminal bulb (Modified from (Avery and Shtonda, 2003)).

The cell bodies of the 20 pharyngeal neurons all reside in the anterior or posterior bulb. They comprise 14 different types; six bilaterally paired and eight single neurons (see Fig. I-21). The three longitudinal extensions form the nerve cord with a small network within the anterior bulb, where they cross to the other side and build the nerve ring. Besides, there is a half-ring in the anterior part of the terminal bulb formed by neuronal processes. All the pharyngeal neurons and muscles are connected via neuromuscular synapses.

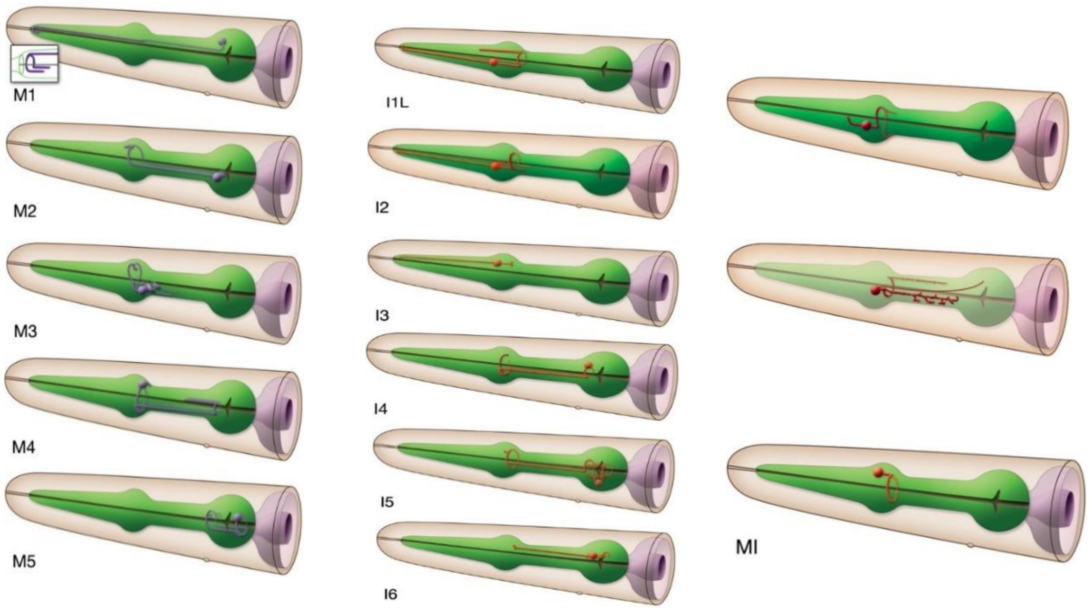

Fig. I-21: Neuron of the pharyngeal nervous system. Pharyngeal neurons are categorized in three groups (from left to right) 5 motor neurons (M2 and M3 are paired), 6 interneurons (I1 and I2 are paired-neurons) and the three other neurons containing the paired MC- motor interneurons, paired NSM-neurons (neurosecretory neurons) and MI (motor interneuron) (Modified from wormatals.org).

Pharyngeal pumping has been described as rather a myogenic and not a neurogenic procedure, since neither laser ablation of the pharyngeal nervous system (Trojanowski, Raizen and Fang-Yen, 2016) nor optogenetic hyperpolarization of pharyngeal motor neurons stopped pumping (Trojanowski *et al.*, 2014; Schüler *et al.*, 2015). Genetic manipulations, which eliminated cholinergic synaptic transmission, caused pumping abolishment (Alfonso *et al.*, 1993). These observations indicate that pumping does require the nervous system for its proper functionality. It seems that two cholinergic MC motor neurons aas well as M3 and M4 neurons are the most critical neurons for pumping regulation since the ablation of MC neurons decreases the pumping rate massively.

This hypothesis could be confirmed via optogenetic methods; The stimulation of MC neurons led to an increase of the pumping rate, whereas its inhibition resulted in the same observation as laser ablation. M3 and M4 neurons seem to be involved in the regulation of pumping. M3 neurons, which are inhibitory-type motor neurons, initiate the relaxation in response to corpus muscle contraction. M4 neurons are reported to affect posterior isthmus peristalsis. This statement is based on the observations from M4 ablations, which led to growth failure (Avery and Horvitzt, 1989).

Two neural pathways were introduced for pumping regulation via the nervous system as a response to food uptake. On the one hand, the acetylcholine transmission from MC neurons is activated via a $G\alpha_s$- signaling pathway by the SER-7 serotonin receptor, which activates pumping. On the other hand, the SER-7 receptor in M4 motor neurons activates neurotransmission from M4 neurons to pharyngeal muscles via a $G\ \alpha_{12}$ – signaling pathway (Song and Avery, 2012).

The electrical activity of the pharynx can be recorded via electropharyngeograms (EPGs), which was one of the leading applications used to achieve the described results about pharynx pumping regulation (to be introduced in detail in the methods section). This method measures currents from the extracellular environment running into pharyngeal muscles. A typical EPG consists of spikes representing the de- or hyperpolarization of the membrane due to the excitatory or inhibitory activity of neurons (see Fig. I-22) (Cook, Franks and Holden-Dye, 2006).

Fig. I-22: Typical EPG of a wild type *C. elegans*. An EPG starts with two positive spikes indicating the contraction of the terminal bulb.Followed by inhibitory potentials triggered by M3 neurons. The two last negative spikes are regarding the relaxation of the corpus and the terminal bulb (adopted from (Cook, Franks and Holden-Dye, 2006).

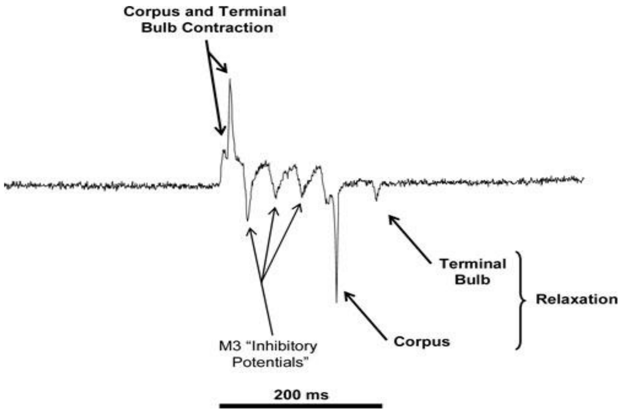

With the help of EPGs, it could be shown that three major voltage-gated currents take part in the regulation of action potentials in the pharynx. These currents are conducted by a T-type calcium channel CCA-1, an L-type calcium channel EGL-19, and a potassium channel EXP-2 (Shtonda and Avery, 2005). It is well known that action potential from MC neurons leads to an excitatory postsynaptic potential (EPSP) via the EAT-2/EAT-18 nicotinic acetylcholine receptor, which in turn activates the T-type calcium channel CCA-1. Calcium release through CCA-1 drives a rapid membrane depolarization via an inward current and thus the activation of the EGL-19 L-type calcium channel (Raymond *et al.*, 1997). Pharynx contraction is triggered due to its depolarization by calcium influx through EGL-19. Next, M3 firing during contraction causes inhibitory postsynaptic potential (IPSP), which in turn leads to the recovery of potassium channel EXP-2 from inactivation (Davis *et al.*, 1999). Speeding up the repolarization due to the generation of large outward current from EXP-2 is the final step of the action potential (Shtonda and Avery, 2005; Steger *et al.*, 2005) (see Fig. I-23).

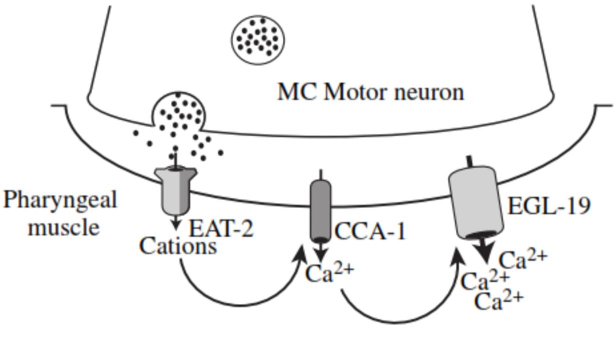

Fig. I-23: Proposed role of voltage-gated channels in the regulation of action potentials in the pharynx. Pharyngeal muscle APs are triggered by neurotransmitter (ACh) release from MC neurons, which activates the nAChR EAT-2 and depolarizes the membrane, which in turn leads to Ca^{2+} -influx via the T-type VGCC CCA-1. The further rise of the membrane potential activates the L-type VGCC EGL-19, which sustains the pharynx contraction (Modified from (Steger *et al.*, 2005)).

Mutations in *egl-19,* which encodes for the α1 subunit of the L-type VGCC were shown to cause malfunctions in muscle contraction. So far, 26 mutant alleles of the *egl-19* gene exist, which can be categorized into three classes based on their genetic or phenotypic properties. The myotonic groups are the ones with a semi-dominant excessive muscle contraction due to increased misregulation in gene activity. A light reduction in gene functionality leads to recessive weak muscle contraction forming the flaccid class. Severely reduced function of the gene is the reason for the lethal mutations that are recessive and block the embryonic muscle contraction (Williams and Waterston, 1994).

Monitoring the action potential of two myogenic *egl-19*-mutants with the help of GEVIs was performed in this work: *egl-19(n2368)* with a mutation in amino acid G365R, which is located close to the pore domain of the channel and *egl-19(n582ad952),* with double mutations in the pore and voltage sensor of the channel causing amino acid changes S372L and R899H). *egl-19(n2368)* is a gain of function mutant that shows a delayed relaxation of the terminal bulb. This delay seems to be a result of prolonged muscle excitation in this segment. They reveled prolonged contraction in several muscles as well and exhibited a dumpy phenotype (short, likely contracted body).

The *egl-19(n582ad95)* double-mutant did not show a typical and dominant phenotype, except some minor dumpy phenotype and a slight delay in repolarization. These observations propose that this mutant is a weak gain-of-function mutant (Raymond *et al.*, 1997) (see Fig. I-24).

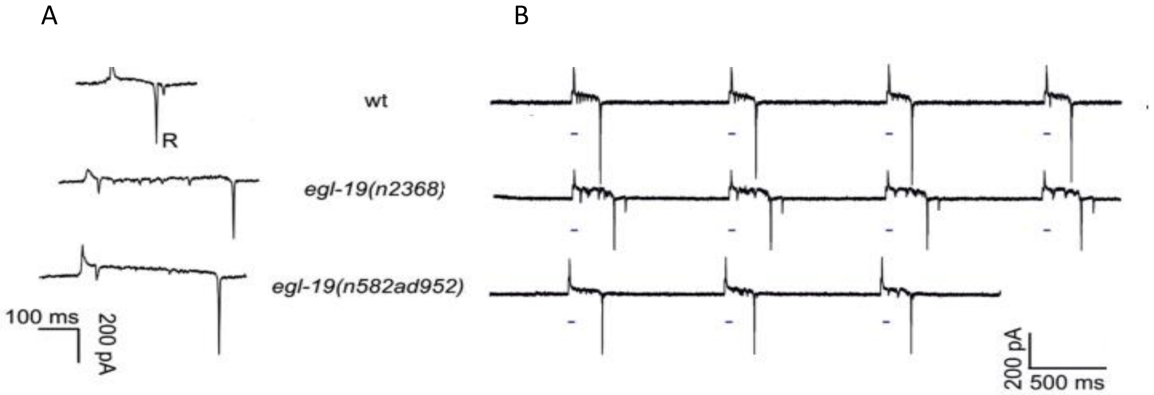

Fig. I-24: Electropharyngeograms from wild type as well as *egl-19(n2368)* and *egl-19(n582ad952)* mutants. A) original EPGs from wt in comparison to both mutants showing the prolonged pump duration and the delayed relaxation B) As in A, however, measured during optically triggered contraction via ChR2 activation with blue light. Light pulses are indicated by blue dashes (Adopted from(Schüler *et al.*, 2015)).

Last but not least, it should be mentioned that in addition to EPGs, which are measuring extracellular currents, action potentials can also be demonstrated via intracellular measurements from terminal bulb (Cook, Franks and Holden-Dye, 2006). A typical pharyngeal AP starts with a fast depolarization up to +20 to +35 mV, which is followed by a slow plateau phase around 150 to 250 ms. The final phase is a quick hyperpolarization to ca. −70 mV. A slow depolarization of ca. -40 mV to the resting potentials occurs at the end and terminates the action potential (see Fig. I-25) (Davis *et al.*, 1999).

Fig. I-25: Typical action potential of the pharynx in wildtype animals. The AP begins with a rapid depolarization up to +35 mV, followed by a plateau phase that lasts ca. 250 ms. The final step is a subthreshold hyperpolarization to ca. -70 mV and additional depolarization termination the AP and setting the membrane potential back to resting potential (Modified from (Davis *et al.*, 1999)).

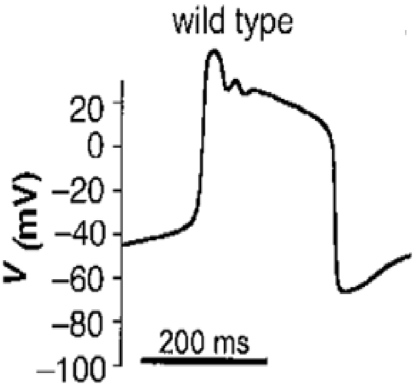

1.5.3: Body wall muscles (BWMs)

The muscle-system of *C. elegans* consists of 136 muscle cells, classified into two groups: multiple sarcomere/obliquely striated, also called somatic muscles, and nonstriated muscles, which are called the single sarcomere. Ninety-five body wall muscles belong to the multi sarcomere group and are located longitudinally. The rest are nonstriated muscles, including the 20 described pharyngeal muscles, eight vulval muscles, eight uterine muscles, one anal depressor muscle, one anal sphincter muscle, two stomato-intestinal muscles, and contractile gonadal sheath. Vulval and uterine muscles of the hermaphrodite are substituted by forty-one mating muscles and gonadal sheath in the male animal. These male-specific muscles are a mix of the single sarcomere and obliquely striated types. Except for some described pharyngeal muscles with multiple nuclei, all the other muscles have only one nucleus (Altun and Hall, 2009).

Body wall muscles are arranged in 4 quadrants at the dorsal and the ventral side of the body. However, with asymmetry since the three dorsal quadrants contain 24, and the ventral group contains 23 cells (Sulston *et al.*, 1983). This phenomenon is caused by a gap on the left ventral quadrant of the embryo, slightly posterior to the gonad primordium. A basal lamina separates muscles from hypodermis and cuticle, which stays in connection with motor neurons in some regions via synapses. Sarcomeres are the units of the contractile machinery of muscles. In vertebrates, these units form the Z discs, which are positioned at the end of the sarcomere. The analogous structure in *C. elegans* is the dense body (DB), which anchors actin filaments. The M-Line is the other main structure in a sarcomere that anchors myosin chains. M-lines and dense bodies together stabilize the sarcomere by anchoring all the filaments to the cell membrane and underlying hypodermis and cuticle (Altun and Hall, 2009) (see Fig. I-26).

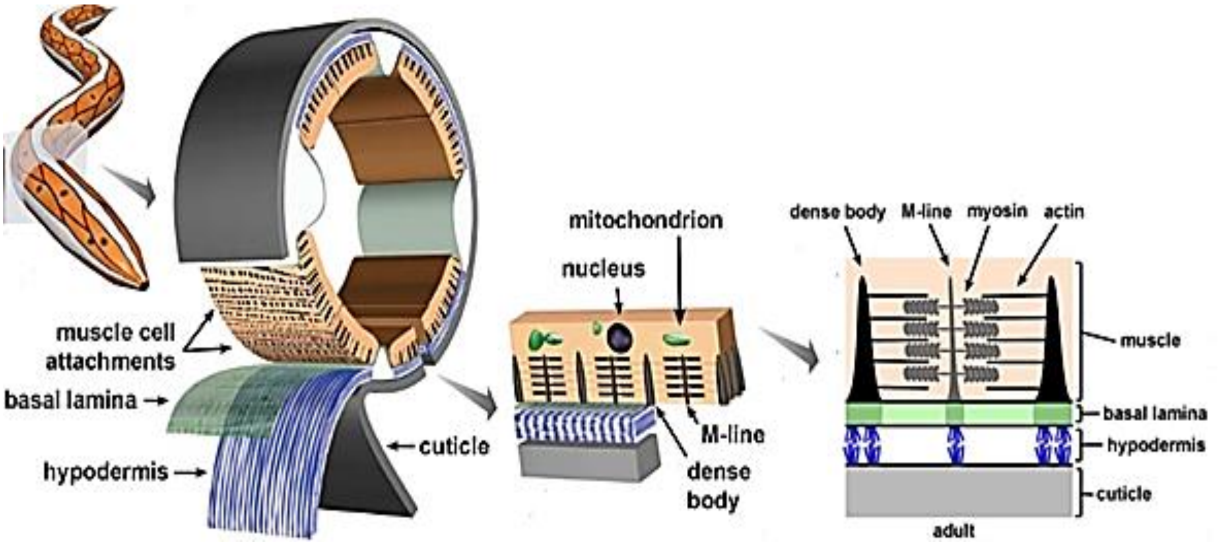

Fig. I-26: Schematic structure of *C. elegans* body wall muscles. From Left to right: Arrangement of body wall muscles shown in cross-section. Illustrated are the described dorsal and ventral quadrants. Sarcomeres are the basal units of muscle cells containing dense bodies and M-lines as the main structure for forming a network anchoring actins and myosins (Modified from (Mackinnon *et al.*, 2002)).

The sinusoidal forward movement is the result of muscle activations that is triggered by neuronal signals. These signals are both excitatory and inhibitory, fired from cholinergic and GABAergic motor neurons, respectively. Contraction and elongation of muscles occur dorsoventrally, meaning the elongation on the dorsal side accompanies the contraction on the ventral side. This phenomenon takes place in an anterior-posterior reciprocal fashion and leads to the forward movement of the animal (see Fig. I-26) (Gao and Zhen, 2011).

As soon as a muscle cell receives an electrical signal, Ca^{2+} streams into the cytosol via voltage-gated calcium channels (VGCCs, encoded by *egl-19*), which forward the electrical signal throughout the body wall muscles. Additionally, there is a Ca^{2+} release via the ryanodine-receptor from the smooth endoplasmatic reticulum (ER). Calcium imaging via calcium sensors such as GCaMP or RCaMP contributed a lot to understanding the signal transfer in BWMs (see Fig. I-27). The mechanisms of both VGCCs and of Ca^{2+}- sensors were described in the previous section (see 1.5.2).

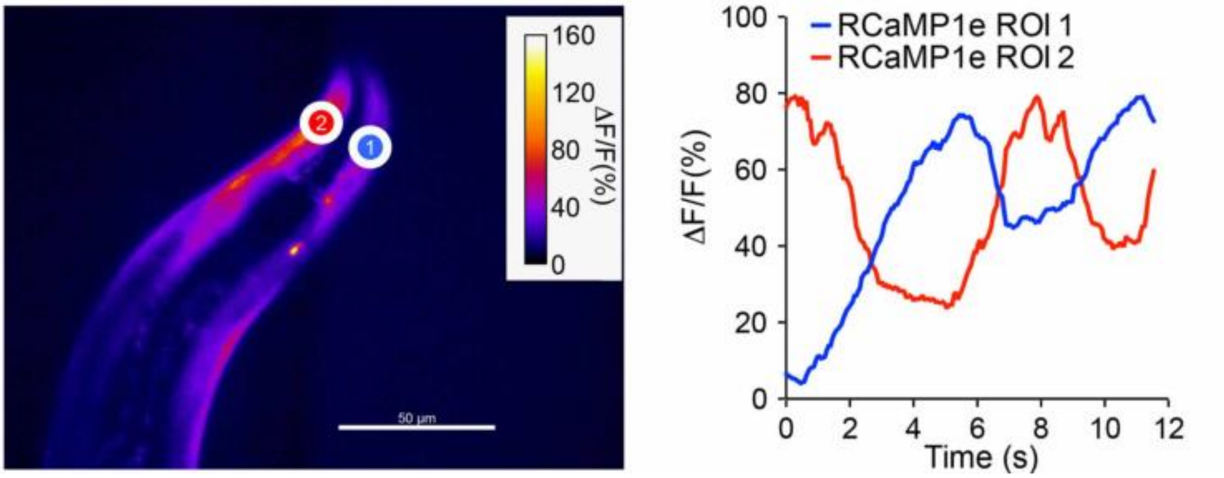

Fig. I-27: Calcium imaging in the body wall muscles of a *C. elegans* expressing RCaMP1e. The transduction of de- and hyperpolarization of the two encircled head muscles in blue and red in the right side based on Ca^{2+}- imaging. Depolarization occurs due to the activity of cholinergic motor neurons, whereas GABAergic signals induce hyperpolarization. The anterior-posterior signal transfer on the dorsal side is encircled, whereas the respective reciprocal muscles are hyperpolarized. Adopted from (Akerboom *et al.*, 2013)

1.5.4: The nervous system

The 302 neurons of a hermaphrodite *C. elegans* can be divided into two independent nervous systems; on the one hand, the already described pharyngeal nervous system and, on the other hand, the somatic neuronal network with 282 neurons, while the male animals possess 383 neurons. The additional neurons are involved in the mating behavior of the male. Somatic and pharyngeal nervous systems connect via only a single pair of RIP interneurons (White *et al.*, 1983) (see Fig. I-28). One of the differences between these two systems is their topology. Pharyngeal neurons and muscles are in direct connection. This structure is a contrast to that of the somatic nervous system, where neurons and their extensions are located between hypodermis and BWMs. Based on the topology and synaptic connection, neurons can be categorized into 118 classes (White *et al.*, 1986). *C. elegans* ganglia are located in the head and tail region, where the cell bodies of most of the neurons are clustered. *C. elegans* has 56 support cells that associate only with the somatic nervous system. The neuronal communication occurs via circa 900 gap junctions, 1500 neuromuscular junctions, and 6400 chemical synapses. The nomenclature of the neurons consists of two or three letters indicating class and a number indicating the number of a neuron. This can be accompanied by an additional letter L (left), R (right), D (dorsal), or V (ventral) in case of radially symmetrical neurons. The nervous system controls a broad spectrum of sensory modalities, behavior, forward motion, feeding, egg-laying, olfactory and gustatory sense, oxygen perception, mechanoreception, temperature sensing, male mating, avoidance of toxic substances and even some simple mechanism of learning and memory (Corsi, 2006).

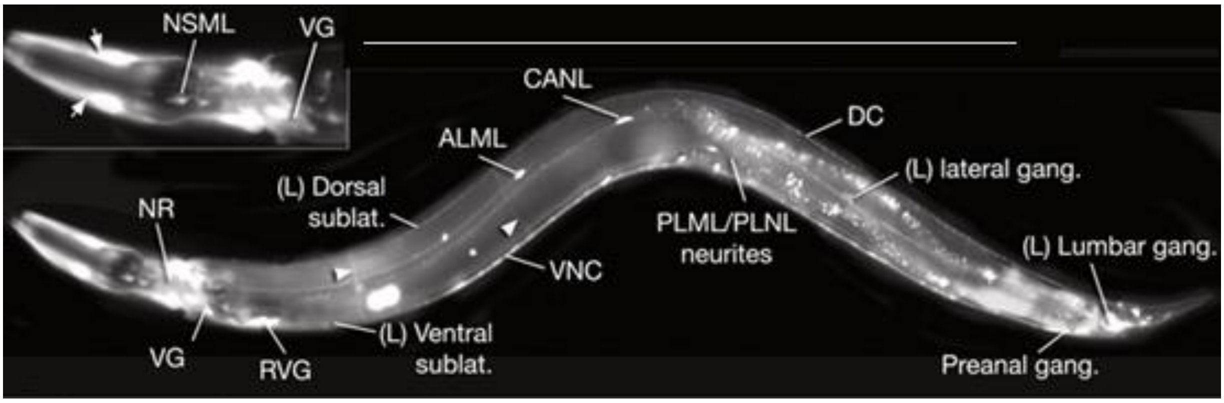

Fig. I-28: The *C. elegans* nervous system. Epifluorescent image of a transgenic animal expressing a pan-neuronal reporter (left lateral view). The most extensive collection of neurons is found around the nerve ring (NR) within several head ganglia, including the retrovesicular ganglion (RVG) and ventral ganglion (VG; also, *inset*). Tail ganglia are the second most extensive collection of cell bodies (the left lumbar ganglion and pre-anal ganglion are shown). Some single neurons, including ALM, CAN, or small groups of neurons (lateral ganglia), are also found along the lateral body wall. Longitudinal nerve tracts travel along the body at ventral, subventral, lateral, subdorsal, and dorsal positions and connect cell bodies to major neuropils. Anterior to the ring, several sensillar nerves reach the tip of the head. VNC (ventral nerve cord) motor neurons are scattered along the VNC and send processes to the DC via commissures (*arrowheads*). The pharyngeal nervous system is an autonomous network of 20 pharyngeal neurons (NSML, which is situated within the anterior bulb, *inset*). Note that this reporter is also expressed in head muscle cells (*arrows*, *inset*). Magnification, 400x. Strain marker: *unc119::GFP* (Adopted from (Altun and Hall, 2010)).

As described briefly in the last section, the locomotion of *C. elegans* is controlled via motor neurons. Locomotion starts with receiving the environmental stimulus by sensory neurons that forward this signal to command interneurons AVB and PVC. Both interneurons are involved in controlling the forward movement. They are, in turn, linked to motor neurons DB and VB, which starts up the forward locomotion.

AVA, AVD, AVE are interneurons that stimulate motor neurons VA und DA. These neurons form the network responsible for backward movement. The interneuron RIM delegates a kind of negative regulation of backward locomotion by activation or inhibition of the whole forward or backward locomotion systems (Pirri and Alkema, 2012). The neuronal network, which controls the locomotion and head movements, is illustrated in figure I-29.

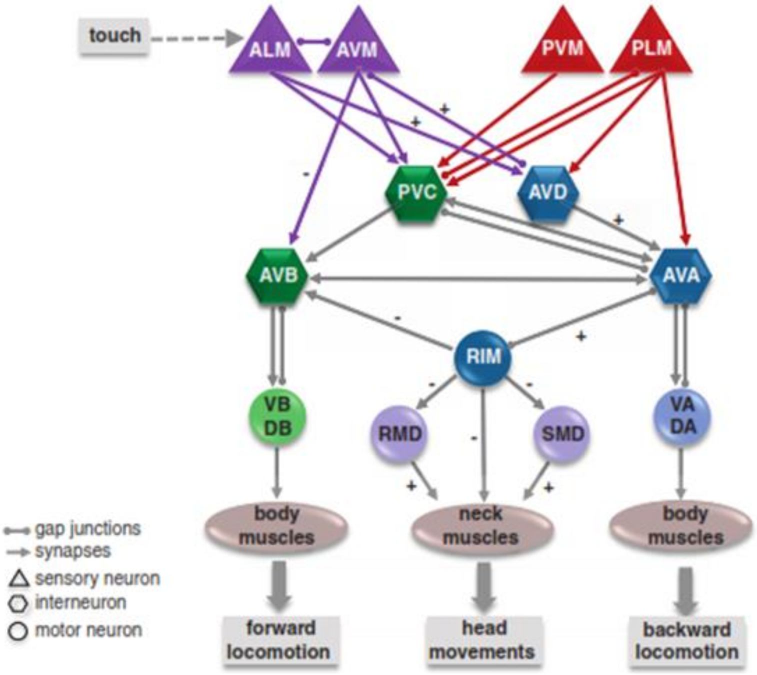

Fig. I-29: Schematic illustration of the neural network controlling the locomotion in *C. elegans*. Red and violet triangles indicate sensory neurons, which perceive environmental stimuli and pass this information to interneurons (green and blue hexagons). Interneurons, in turn, analyze the signal and send an output to motor neurons (circles). These are the end-point in the neuronal signaling hierarchy and startle muscle contraction or elongation via neurotransmitter release. Plus- or minus- signs indicate excitation or inhibition (Adopted from (Pirri and Alkema, 2012)).

1.6: Goals of this project

The goal of this project is the establishment of genetically encoded voltage indicators based on the microbial rhodopsins, for studying neuronal networks in the nematode *C. elegans.* The electrical activity of an excitable cell is characterized by changes in membrane voltage. Neurotransmitter and Ca^{2+}- release are affected downstream of electrical activity, meaning that the most direct way of monitoring neuronal activity is to track electrical events of the membrane. One method is to use electrophysiology, which is very challenging for multiple cells or cell ensembles. Moreover, this method is often not possible in live animals and is very complicated and invasive, showing the necessity of developing imaging methods and tools. In the past, monitoring the electrical events in *C. elegans* was mostly done by Ca^{2+}- sensors. The application of GEVIs was introduced just in some neurons and not in muscles (Akerboom *et al.*, 2012, 2013; Flytzanis *et al.*, 2014). For the establishment of such imaging tools in this thesis, transgenic animals expressing different GEVIs are supposed to be generated. This heterologous expression should be addressed via specific promoters for body wall and pharyngeal muscles.

Two classes of such sensors have to be tested for their feasibility of tracking the voltage changes in *C. elegans* muscle cells; on the one hand, rhodopsin based GEVIs, in which voltage signals can be read out in the form of changes in the fluorescence signal directly from the opsin protein and thus its chromophore. On the other hand, electrical activity should be monitored with eFRET voltage indicators that can demonstrate signals in the form of changes in the fluorescence signal of a fluorescent protein that builds a FRET-pair with rhodopsin (Arch or Mac). eFRET sensors can reveal bright fluorescent signals in comparison to direct rhodopsin signaling. As an alternative, it has to be analyzed, if the substitution of all-*trans*-retinal with some synthetic analogs can help to overcome the dim fluorescence of ATR under the maintenance of appropriate kinetic and sensitivity.

Besides, GEVIs will to be used to quantitatively compare mutants of the L-type voltage-gated Ca^{2+} channel EGL-19 with wild type animals to study the effect of mutations on voltage changes. Two different *EGL-19* gain-of-function mutants are to be tested with GEVIS; *egl-19(n2368) and egl-19(n582ad952)*. Moreover, the application of the drug Nemadipin-A (Nema-A, an analog of hydrodipiridin), which is a VGCC-blocker, has to be performed. The influence of the drug Nema-A on reorganizing the voltage signals will be analyzed by voltage monitoring after drug application. Electrophysiology will be performed to calibrate the monitored voltage signals with the electrically measured voltages (by Dr. Liewald). The electrical voltage signals induced by blue light activation of channelrhodopsin-2 in the cholinergic neurons of animals will be compared with optically monitored signals induced due to channelrhodopsin activation and thus the depolarization of the muscle cells. For the calibration of the optical signals monitored from pharyngeal muscles, electrophysiology in pharyngeal muscles will be used, by the application of sharp electrodes for intracellular recording (by Dr. Schuler). It should be attempted to achieve an all-optical EPG and to analyze whether it would be consistent with electrically recorded EPGs.

2 Material and methods

2.1: Materials

2.1.1: Reagents

Table M-1: Reagents

Substance	Supplier
Acetic acid	Carl Roth
Acetone	Carl Roth
Agar	Carl Roth
Agarose	Biozym Scientific GmbH
All-trans-Retinal	Sigma Aldrich
Ampicillin	Applichem
BSA	NEB
Calcium chloride	Carl Roth
Cholesterol	Carl Roth
DMSO	NEB
Disodium hydrogen phosphate	Carl Roth
Ethanol 99% pure	Carl Roth
Ethanol 96% methylated	Carl Roth
Ethidium bromide 5%	Carl Roth
Gelatin	Carl Roth
Gene Ruler 1 kb	Fermentas
Gene Ruler 1 kb plus	Fermentas

Glycerin	Carl Roth
Halocarbon oil	Carl Roth
Hydrochloric acid	Applichem
Isopropanol	Carl Roth
Magnesium chloride	Carl Roth
Magnesium sulfate	Carl Roth
Methanol	Carl Roth
Nemadipine-A	
Nitrogen	Linde
Nucleotides	Fermentas/Invitrogen
Nystatin	Applichem
Oligonucleotides	Eurofins MWG
Polystyrene beads: 0.1 µm diameter	POLYCIENCES
Potassium chloride	Carl Roth
Potassium citrate	Carl Roth
Potassium hydrogen phosphate	Carl Roth
Potassium phosphate	Carl Roth
Sodium azide	Carl Roth
Sodium chloride	Carl Roth
Sodium hypo chloride 12%	Carl Roth
Sodium hydroxide	Carl Roth
Retinal analogs	Endotherm

Streptomycin sulfate	Applichem
Tris	Carl Roth
Yeast extract	Carl Roth

2.1.2: Enzymes

Table M-2: Enzymes

Enzyme	Buffer	Manufacturer
AgeI	NEB Buffer 1	New England Biolabs
Acc65I	NEB Buffer 3	New England Biolabs
AleI	NEB Buffer 4	New England Biolabs
BamHI	NEB Buffer 3	Fermentas
EcoRI	NEB Buffer 1 - 4	New England Biolabs
EcoRV	NEB Buffer 3 + BSA	New England Biolabs
HindIII FD	FD-Buffer	New England Biolabs
KpnI	NEB Buffer 3	Fermentas
SapI	NEB Buffer 4	New England Biolabs
XbaI	NEB Buffer 4 + BSA	New England Biolabs
XmaI	NEB Buffer 4	New England Biolabs
XhoI	NEB Buffer 3	New England biolabs
Phusion® DNA Polymerase	HF Buffer	Finzymes
T4 DNA Ligase	Ligase-Buffer	Fermentas
Taq-DNA-Polymerase	PCR-Buffer	New England Biolabs

2.1.3: Kits

Table M-3: Kits

Kit	Manufacturer
In-Fusion HD Cloning	Clon Tech
NucleoBond PC100	Macherey Nagel
NucleoSpin Plasmid Kit	Macherey Nagel/Carl Roth
Gel extraction	Avegene life sciences

2.1.4: Devices

Table M-4: Devices

Device	Description/ Type	supplier
Autoclave	Serie FVS 5075 ELVC	edgari Tuttnauser
Bunsen burner	Labogaz 470	Campingaz
Cameras	ORCA-Flash 4.0 V2C11440-22CU, EMCCD Evolve Delta	Hamamatsu Photometrics
Centrifuges	Centrifuge Pico 17 Centrifuge 5415 R Microcentrifuge Rotanta	Heraeus Eppendorf Carl Roth Hettich
Compressor	BT-AC 200/24 OF	Einhell
ddH$_2$O-Equipment	Milli-Q Plus	Millipore

Electrophoresis chamber	Varia 1	Carl Roth
Filter-sets	F 36 – 525 (GFP) F 11 – 007 (mCherry) F 20- 308 (Cy5) F 20- 302 (Rhodamin) 740nm 780 nm	AHF- Analysetechnik AHF- Analysetechnik AHF Analysetechnik AHF Analysetechnik AHF Analysetechnik AHF Analysetechnik
Gel documentation system	EOS 500 Dark Hood DH-40	Canon Biostep
Heat block	AccuBlock Digital Dry bath	Labnet
Incubators	FOC 225 E refrigerated Kelvitron T Unitron Vinothek 37°C 37°C Incubator	VELT Scientific Heraeus Heraeus Liebherr Infors AG Memmert
Injection micro pipette puller	Modell P 97	Sutter
Lamps	HBO 50 HBO100	Osram
LED Power supply	KSL 70	Rapp
Magnetic stirrer Stuart	Magnetic stirrer Stuart	Magnetic stirrer Stuart

Micromanipulator		Märzhäuser
Microscopes	Axiovert 100 Axio Observer Leica MZ 16 F Axiovert 40	Zeiss Zeiss Leica Zeiss
Microwave oven	CC6459	CyberCom
Optical power meter	PM 100 S120UV	Thorlabs Thorlab
PCR machines	My Cycter	Biorad
pH Meter	Cyberscan pH 510	Eutech
Photometer		Thermo Scientific
Pipettes	LabMate	Abimed
Pipette controller	Pipetus	Hirschmann
Shutter	Smart Shutter	Sutter
Shutter controller	Lambda SC utility	Sutter
Vortex	Vortex Genie 2	Scientific Industries
Weighing machines	Analysewaage 770 Adventurer Pro Emb 600 – 2	Kern Ohaus Kern

2.1.5: Diverse laboratory facilities (Glass- and plasticware)

Table M-5: Diverse laboratory facilities

Facility	Description/ Type	supplier
Conical centrifuge tubes	15 and 50 mL	Greiner Bio-One
Cover slip	Coverslip 22x22 mm	Carl Roth
Glass capillary	B100F-4	World precision Instruments
Galls pipettes	5,10,25 mL	Brand
Microcentrifuge tube	200 µL 8x or 12x 200 µL Tubes 1,5 or 2 mL Tubes	Sarstedt NeoLab CarlRoth
Microscope slide	76x26 mm	Carl Roth
Parafilm	Parafilm M	Alcan
Petri dish	Different sizes	Greiner Bio-One
Pipet tips	Different volumes	Carl Roth
Protective gloves	Roti protect	Carl Roth

2.1.6: Software

Table M-6: Software

Software/ Program	Description/ Type	supplier
Argus	X1 V.3	Biostep
Clone manager	Version 9.0	Sci Ed Central
Image J	Version 1.48	NIH

Knime analytics Platform	3.5.3	Knime AG
Micro Manager	Version 1.4	Vale lan
Microsoft office 365	Word, Excel	Microsoft
Mendeley	Mendeley desktop	Mendeley Ltd.
R	Version 3.5.1	R core team

2.1.7: Media and buffer

Buffers and media have been produced with sterile ddH_2O as a solvent. The pH was adjusted afterwards. LB and Nematode-Growth-medium were additionally autoclaved.

Table M-7: Buffer and media

Buffer/ Medium	Content/ Supplier
Bleaching solution	25% Natriumhypochlorid 50% 1 M Natriumhydroxid
DNA Loading buffer (6x)	Fermentas
dNTPs-Mix	10 mM dATP 10 mM dCTP 10 mM dGTP 10 mM dTTP
Injection buffer (10x) pH 7,5	20% (w/v) Polyethylenglykol, 200 mM Potassium Phosphate 30 mM Potassium Citrate in H_2O

Potassium phosphate buffer (1M) pH 7,5	1 M Potassium hydrogen phosphate 1 M di-Potassium hydrogen phosphate 1: 5,5
LB Agar	1% Sodium chloride 1,5% Agar 1% Trypton/ Pepton 0,5% Yeast extract Added antibiotics: 100 µg/ml Ampicillin 200 µg/ml Streptomycin
LB Medium	1% Trypton/ Pepton, 0,5% Yeast extract 1% Sodium Chloride Added Antibiotics: 100 µg/ml Ampicillin 200 µg/ml Streptomycin
M9 Puffer (1x)	20 mM Potassium-dihydrogen-phosphate 40 mM di-Sodium hydrogen phosphate 85 mM Sodium chloride 1 mM Magnesium sulfate
NEB Puffer 1 – 4 (10x)	New England Biolabs

Nematode Growth Medium (NGM)	1,7% Agar-Agar 0,25% Trypton/Pepton 0,3%Sodium chloride 1mM Calcium chloride 1 mM Magnesium sulfate 25 mM Potassium phosphate 0,0005% Cholesterol in EtOH 0,001% Nystatin
Phusion HF	Puffer (5x)
PCR Puffer (10x)	100 mM Tris-HCl pH 8.3 500 mM KCl 5 mM, $MgCl_2$ 0,001% Gelatin
Single egg worm lysis buffer (SEWLB) x10	mM Tris/HCl pH 8.3 50 mM KCl 2.5 mM MgCl 0.45% Tween-20 0.05% Gelatin
T4 DNA Ligase Puffer (10x)	Fermentas
TAE Puffer (50x) pH 8,5	40 mM TRIS/ Acetic acid 2 mM EDTA

2.1.8: Oligonucleotides

Table M-8: Oligonucleotides

Oligo.-No.	Sequence (5´- 3´)	Description
oNH7	TAT GCC AGG TAC GCC AAC TGG CTG TTT ACC ACC	Forward primer for SDM in Arch(D95N)
oNH8	GGT GGT AAA CAG CCA GTT GGC GTA CCT GGC ATA	Reverse primer for SDM in Arch(D95N)
oNH9	ATCTAGAGGATCCGCCACCATGGACC	Forward primer for Arch-3 digestion site: BamHI
oNH10	CTCTACCGGTCGGTCGGCGGCACTGACATC	Reverse primer for Arch-3 digestion site: AgeI
oNH27	TAT GCC AGG TAC GCC CAG TGG CTG TTT ACC ACC	Forward primer for SDM in Arch(D95Q)
oNH28	GGT GGT AAA CAG CCA CTG GGC GTA CCT GGC ATA	Reverse primer for SDM in Arch(D95Q)
oNH29	CCA CTT CTG CTG CTG GAG CTG GCC CTT CTG GCT	Forward primer for SDM in Arch(D106E)
oNH30	AGC GAG AAG GGC CAG CTC CAG CAG CAG AAG TGG	Reverse primer for SDM in Arch(D106E)
oNH37	GCC AGG TAC GCC GAG TGG CTG TTT TGC ACC CCA CTT CTG CTG	Forward primer for SDM in Arch(D95E;T99C)
oNH38	CAG CAG AAG TGG GGT GCA AAA CAG CCA CTC GGC GTA CCT GGC	Reverse primer for SDM in Arch(D95E,T99C)
oNH61	TTTGGGATCCGCCACCATGGAC	Forward primer for Arch amplification from pmyo-2 vector

oNH62	ACCGGCGCTCAGTTGGAATTCAC	Forward primer for Arch amplification from pmyo-2 vector
oNH63	TAT GCC AGG TAC GCC CAC TGG CTG TTT ACC ACC	Forward primer for SDM in Arch(D95H)
oNH64	GGT GGT AAA CAG CCA GTG GGC GTA CCT GGC ATA	Reverse primer for SDM in Arch(D95H)
oEF100	TCGAGCCATGATTCCTTTGC	Forward primer for genotyping of *egl-19*
oEF101	TCTAGCTGCCCATTTACTCG	Reverse primer for genotyping of *egl-19*
oCS394	CACAACTAGTGGTAATGGTAGCGACCG	Sequencing reverse primer in *pmyo-3*
oCS228	CCTGTTACCAGTGGCTG	Sequencing reverse primer in *pmyo-3 and -2*

2.1.9: Plasmids

Table M-9: Plasmids

Name	Description	Source
pNH2	*pmyo-3::Arch::2xMyc-Tag*	Previous work
pNH10	*pmyo-2::Arch(wt)::2xMycTag*	This work
pNH11	*pmyo-2::Arch(D95N)::2xMycTag*	This work
pNH12	*pmyo-2::MacQ::mCitrine*	This work
pNH13	*pmyo-2::QuasAr::mOrange*	This work
pNH14	*pmyo3::Arch(D95N,D106E)::2xMycTag (EEN)*	This work

pNH15	*pmyo3::Arch(D95Q,D106E)::2xMycTag (EEQ)*	This work
pNH17	*pmyo-3::Arch(D95E,T99C,D106E)::2xMyc-Tag (DETCDE)*	This work
pNH19	*pmyo-2::Arch(D95H)::2xMycTag*	This work
pNH20	*pmyo-3::QuasAr::mOrange (eFRET)*	This work
	pmyo-2::mCherry	Addgene
	pmyo-3::CFP	Addgene
	Pmyo-3:mCherry	Addgene #19328

2.1.10: Organisms

Table M-10: Organisms

Organisms	**Strain**	**Source**
Caenorhabditis elegans	N2	CGC (*Caenorhabditis* Genetics Center)
Caenorhabditis elegans	**MT6129** *egl-19(n2368)*	CGC (*Caenorhabditis* Genetics Center)
Caenorhabditis elegans	**DA952** *egl-19(n582ad952)*	CGC (*Caenorhabditis* Genetics Center)
Escherichia coli	DH5α	Invitrogen
Escherichia coli	OP 50	CGC (*Caenorhabditis* Genetics Center)

2.1.11: Transgenic *C.elegans* strains

Transgenic strains, used or generated during this project, are described using their genetic background (genotype) and the injected transgene. The transgene is injected as a plasmid and is present in the worm as an extrachromosomal array or is integrated into the genomic DNA. The strains are additionally characterized by the co-injection marker, which is listed after the transgene. This allows the selection of transgenic over non-transgenic worms. The integration of the extrachromosal array into the genomic DNA in two strains (ZX1920 and ZX1954) was performed by Alexander Hirschhäuser and Amelie Bergs.

Table M-11: Strains generated during this thesis (*) or by other supplier or members in the Gottschalk group

Strain	Genotype	
ZX460	*zxIs6[punc-17::chop-2(H134R)::yfp;lin-15+]*	MB
ZX499	*zxIs5[punc-17::chop-2(H134R)::yfp;lin-15+]*	MB
ZX1338	*egl-19(n582ad952)*	*CGC*
ZX1383	*egl-19(n2368)*	*CGC*
ZX1901	*N2;zxEX916[Pmyo-3::ArchD95N::2xMyc-Tag; pmyo-3::CFP]*	*
ZX1904	*N2;zxEX920[Pmyo-3::Arch(D95E,T99C,D106E)::2xMyc-Tag; pmyo-3::CFP]*	*
ZX1906	*N2;zxEX925[pmyo-3::QuasAr::mOrange(eFRET); pmyo-3::CFP]*	*
ZX1907	*N2;zxEX922[Pmyo-2::Arch(wt)::2xMycTag; pMyo-3::CFP]*	*
ZX1917	*N2;zxEX942[pmyo-2::QuasAr::morange;pmyo-3::CFP]*	*
ZX1918	*N2;zxEX943[pmyo-2::MacD139Q::mCitrine;pmyo-3::mCherry]*	*
ZX1920	*zxIS121[pmyo-3::QuasAr::mOrange(eFRET); pmyo-3::CFP]*	AH

ZX1951	*egl-19(n2368); zxEX942[pmyo-2::QuasAr::morange;pmyo-3::CFP]*	RS
ZX1952	*egl-19(n2368); zxEX943[pmyo-2::MacD139Q::mCitrine;pmyo-3::mCherry]*	RS
ZX1953	*N2;zxIS120[pmyo-3::ArchD95N::2xmyctag; pmyo-3::CFP]*	AB
ZX1954	*zxIS6;zxIS120[pmyo-3::ArchD95N::2xmyctag; pmyo-3::CFP]*	*
ZX1955	*egl-19(n582ad952); zxEX942[pmyo-2::QuasAr::morange;pmyo-3::CFP]*	*
ZX1956	*egl-19(n582ad952); zxEX943[pmyo-2::MacD139Q::mCitrine;pmyo-3::mCherry]*	*
ZX1958	*N2; zxEX944[pmyo-2::ArchD95N::2xmyctag;pmyo-3::CFP]*	*
ZX1959	*egl-19(n2368); zxEX944[pmyo-2::ArchD95N::2xmyctag;pmyo-3::CFP]*	*
ZX1960	*zxIS5;zxIS121[pmyo-3::QuasAr::mOrange(eFRET); pmyo-3::CFP]*	*
ZX1961	*N2;zxEX[pmyo-2::ArchD95H::2xmyctag;pmyo-3::CFP]*	*
ZX1962	*zxIS5;zxEX920[Pmyo-3::Arch(D95E,T99C,D106E)::2xMyc-Tag; pMyo-3::CFP]*	*

“MB= Martin Braunr, AB= Amelie Bergs, RS= Rebecca Scheiwe, AH= Alexander Hirschhäuser“

„CGC: Caenorhabditis Genetics Center”

2.2: Methods

2.2.1: Molecular biological methods

2.2.1.1: Restriction digestion

Restriction enzymes can cut the double-stranded DNA. This property is used in the molecular biological method "Restriction digestion" to open a plasmid in order to cut a gene out of the plasmid and replace it with another gene, to identify the plasmid or to cut the genomic DNA in shorter sequences. The restriction enzymes recognize specific DNA sequences, which usually occur as palindrome sequences. They split off the phosphodiester bond between two bases. The most commonly used restriction enzymes are endonucleases, i.e., these enzymes recognize a sequence within a strand. Endonucleases can cut a sequence both symmetrically and asymmetrically, which leads to two different linear DNA sequences, which either have a flat interface and are known as "blunt ends" or have a 5 'or a 3' overhang and are referred as "sticky ends". In order to show their maximum activity, the restriction enzymes need magnesium, ATP, and organic solvents, which are added to the restriction mixture by a buffer.

In this work, restriction enzymes were used to open the backbone vectors with the aim of the ligation of transgenes for voltage indicators into their structure. One restriction enzyme was also used in genotyping since the mutation in the transgenic animals led to a new restriction site.

2.2.1.2: Polymerase chain reaction (PCR)

The polymerase chain reaction is carried out to amplify a specific sequence of DNA. The method can also be used for analytical purposes, such as genotyping a genome. Information on the nucleotide sequences of the DNA that has to be amplified is a prerequisite for the use of PCR methods. This sequence can be used to design two oligonucleotides, the so-called primers, which recognize the two ends of the DNA sequence. A forward primer, usually consisting of 20 to 30 nucleotides, can recognize the 5'-3'-start of the template DNA. The reverse primer also consists of approx. 20 to 30 nucleotides and recognizes the antiparallel sequence of the approx. 20-30 last nucleotides of the DNA template. At the beginning of the PCR, the double-strand is denatured by heating at 95 ° C for approx. 5-10 minutes, whereby the hydrogen bonds between the bases break down, and DNA single strands are formed so that the two forward and reverse primers can attach to single strands. The attachment of the two primers to the template DNA is known as "annealing". The suitable temperature for annealing depends on the nucleotide composition of the two primers. It can vary between 45-70 °C. After the primers have attached to the template DNA, the temperature is set to approximately 72 °C., which corresponds to the optimum temperature for Phusion polymerase. The synthesis of the complementary DNA strand by the DNA polymerase can thus take place. Phusion has a domain with 3 'to 5' exonuclease function and therefore has a lower error rate in the amplification. For the continuing of DNA t polymerizing, enough dNTPs as building blocks of the newly synthesized strand, ATP, and magnesium as co-factors for the optimal activity of the polymerase in the PCR approach must be available. The duration of this step called elongation depends on the length of the DNA segment that has to be synthesized. After the first elongation step is ended, the temperature is raised so that the newly synthesized double strands are denatured. Thus, single-stranded DNA sequences are created again, and the polymerization can be restarted. This cycle of denaturation, hybridization, and DNA synthesis can be repeated 20-50 times.

A PCR machine is used to carry out a polymerase chain reaction. It acts like a heating block that automatically adjusts the temperature changes during the chain reaction.

The PCR product can be separated from other possible by-products, the primers, and templates, which are still present in the reaction-mix by an agarose gel. The extracted PCR product can be used for ligation.

By the application of additional nucleotides on the 5’ or at the 3 'end of a primer, new cutting sites can be inserted into the newly synthesized DNA. The following pipetting schemes were used for the amplification of the DNA.

5X Phusion	4 µl
10 mM dNTPs	0,4 µl
10 µM forward primer	1 µl
10 µM reverse primer	1 µl
Template DNA	variable <250 ng
DMSO (optional)	0,6 µl
Phusion DNA polymerase	0,2 µl

ddH_2O fill up to 20µl

In general, the following protocol for the cycler was used for the amplification of DNA.

Cycle	Temperaure [°C	Duration	Repeats
Initial denaturation	98	10 min	1
Denaturation	98	15 sec	x35
Annealing	Primer specific	15 sec	
Elongation	72	length specific	
Final elongation	72	10 min	1
Cooling	4	∞	1

2.2.1.3: Site-directed mutagenesis (SDM)

Site-specific mutagenesis is carried out in order to generate a targeted change in a DNA sequence. The method is based on carrying out several polymerase chain reactions. The primers used in this method are designed in such a way that they contain a mutation in their sequence. In the first step, forward and reverse primers are modeled, which are about 30 nucleotides long and are mutated precisely in the middle of their sequence by a nucleotide of the desired codon. Two primers are also required for the amplification of the whole desired gene (see Fig. M-1). In the beginning, two different PCR approaches are prepared. In one approach, the forward primer for the wild type and the mutant reverse primer are given, and in the second approach, the reverse primer for the wild type and the mutant forward primer. The PCR products from these two approaches are two oligonucleotides, each with the mutated 5 'end and wild type 3' end or the mutated 3 'end and wild type 5' end. These two newly synthesized oligonucleotides are used as templates in another PCR, this time using only the primers for the entire gene. In the end, the complete DNA with the desired mutated codon is created.

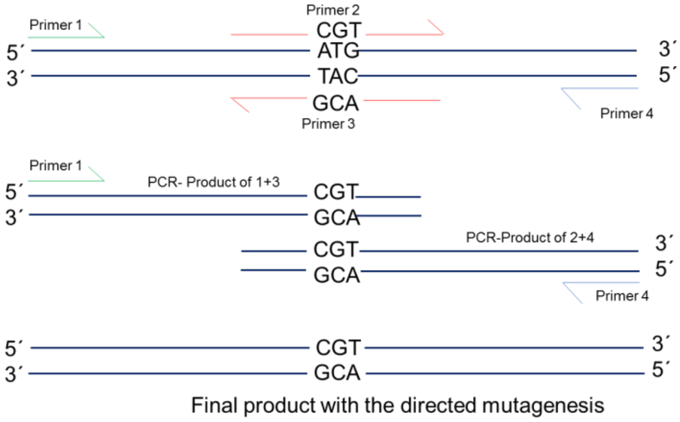

Fig. M-1: Schematic presentation of the primers used in site-directed-mutagenesis. Forward and reverse primers containing ca. 30 nucleotides and are carry the mutated sequence in the middle by a nucleotide of the desired codon (P2 and P3). Two primers are also required for the amplification of the whole desired gene (P1 and P4)

2.2.1.4: Agarose gel electrophorese

Different DNA fragments can be separated from each other using agarose gel electrophoresis. This method can be used for analytical and preparative purposes.
To prepare an agarose gel, agarose (in powder form) was given to 1x TAE buffer. This mix was heated in the microwave until all of the agaroses has dissolved. The solution is then poured into a gel chamber. The size of the pockets was adjusted due to the volume of each sample with a convenient comb. DNA samples were mixed with loading buffer before loading into the pockets (One-fifth volume). A reference DNA containing different fragments with the known size is placed in at least one pocket.
By applying a voltage across the gel, the DNA fragments migrate towards the positively charged anode. The strength of the applied voltage should be at 6.5 ± 1.5 V / cm. The concentration of the agarose gel depends on the length of the DNA fragments that have to be separated. 1% agarose gel is generally suitable. The concentration of the gel is reduced if two fragments larger than 2000 bp are to be separated. Higher concentrations are used for smaller fragments below 1000 bp. The duration of the process depends on the size of the fragments as well. In this work, gel electrophoresis was carried out at a voltage of 110-165 mV for 30-60 minutes.
To monitor the separated fragments, the gel is placed in a 1% ethidium bromide solution for about 15-30 minutes. Ethidium bromide is an organic dye that intercalates in the furrows of the double-stranded DNA and fluoresces when exposed to UV radiation.

2.2.1.5: Gel extraction

After the desired DNA band has been cut out of the agarose gel using a scalpel, it is transferred to a reaction vessel and only melted by adding a buffer. Once the whole gel has melted, the DNA fragment can be extracted from the agarose gel using an extraction kit. The extraction in the context of this diploma thesis was carried out using the Avegene gel / PCR extraction kit based on their instructions.

2.2.1.6: DNA purification

The purification of plasmid and genomic DNA from bacterial residues and proteins was performed with phenol-chloroform-isoamyl alcohol (PCA) extraction. For this aim, the DNA was filled with ddH2O up to 200 µL, mixed with 100 µL PCA, and vortexed for 30 seconds. 5 minutes of centrifugation at maximum Speed leads to the formation of two phases. Bacterial residues and proteins are present in the organic phase and the DNA in the aqueous phase in the supernatant. DNA was removed and mixed with 2.5 times the amount of an ethanolic NaOAc solution (ratio 25: 1, 3 M NaOAc). This mixture was again strongly vortexed and then incubated at -80 ° C for 30 min. This step is used to precipitate the DNA. This step was followed by 10 minutes centrifugation at maximum speed. The supernatant was discarded, and the pellet was washed with 500 µL 70% EtOH. After removing the EtOH, the remaining DNA was dried and solved in the desired amount ddH_2O.

2.2.1.7: DNA concentration

The concentration must be known to use it with the correct and appropriate concentration in different molecular biological methods such as ligation. For this purpose, the absorption of the DNA sample is measured at a wavelength of 260 nm. According to Lambert-Beer’s law, the absorption of the sample is relative to the concentration of the DNA in the sample. The higher the absorption, the more concentrated the DNA solution. The other organic solutions and proteins that may still be present in the sample have absorption at 280 nm. The ratio between the absorbance of 260 nm and 280 nm serves as an indicator of the purity of the sample and usually has to be about 1,8. The solvent of DNA must be taken ss a reference for the absorption measurement.

2.2.1.8: Ligation

The ligation is carried out to link two separate DNA fragments. For this purpose, the ATP-dependent enzyme "T4 ligase" is used, which can connect either the DNA fragments with blunt ends or mutually matching sticky ends. In most of the cases, the ligation is performed to insert a DNA fragment into a plasmid, which is already opened by restriction digestion. In general, a 1: 3 ratio of plasmid: insert is used for ligation. The incubation period is either 1-3 hours at room temperature or overnight at 16 ° C. The success of the ligation is determined by means of transformation in bacterial cells.

2.2.1.9: Dephosphorylation

The DNA Dephosphorylation was achieved using the enzyme Antarctic Phosphatase (AP). Since dephosphorylated backbone cannot be religated through T4 DNA Ligase, the procedure prevents vector re-ligations and false-positive clones. AP dephosphorylates, specifically the 5'-end of linear DNA fragments. The reaction mixture was incubated for 20 minutes at 37 °C, followed by inactivation of the AP at 70 °C for 5 minutes. The DNA solution could be used without further purification for the ligation of the insert to the backbone, as mentioned in the accompanying manual.

2.2.1.10: Competent bacteria

Competent bacteria are able to take up DNA, which is present in their environment. The naturally competent bacteria have genes that grant the bacteria this property.

In the molecular biological laboratory, competent bacterial cells serve to amplify the plasmids. This ability is artificially conferred on the incompetent bacteria by treating them with salt solutions.

The competent cells used in this work originate from the E. coli strain DH5-α. In order to make the bacterial cells competent, a 10 ml LB medium preculture was inoculated with E. coli DH5-α and was shaken at 37 ° C. overnight. The next day, 2-3 ml of the preculture were given into 200 ml of LB medium and have been shaken at 37 ° C. until they reached an OD600 value of 0.4-0.5. After an hour of incubation on ice, the cells were pelleted at 2000g and 4 ° C for 10 minutes. The pellet was placed in 35 ml of TFB-I buffer and incubated again on ice for one hour. The cells were harvested at 3000 g and 4 ° C and were resuspended in 6 ml TFB-II. 150 µl aliquots were frozen in liquid nitrogen and have been stored at -80 °C.

2.2.1.11: Transformation in competent bacteria

The transfer of plasmids into competent bacterial cells is called transformation. The artificially produced plasmids have a DNA sequence, which is called the "Origin of Replication" and sets the starting point for replication. The plasmids can thus be replicated in host bacteria.

In order to transform the plasmids into bacteria, 10 µl of the ligation mixture (in the case of retransformation only 1 µl of the dissolved plasmid) were added to 200 µl of competent bacteria and incubated on ice for 10-15 minutes. After the incubation, a heat shock was carried out at 42 ° C. for 45 s. The transformation mixture was again placed on ice for 2-3 minutes. After adding 500 µl of LB medium, the mixture was shaken at 37 ° C for 1 hour. The bacterial cells were centrifuged for 2 minutes at 4000 rpm. The supernatant was discarded to 20-30 µl, and the harvested cells were spread on LB plates containing an antibiotic and have been incubated at 37 °C overnight. The plasmids, which contain an antibiotic resistance gene, can survive in an antibiotic containing medium. This phenomenon is used as a selection marker of the potentially positive clones.

2.2.1.12: DNA isolation from bacteria

In order to isolate the plasmid DNA from bacterial cells, the potentially positive clones are picked from a plate using a sterile pipette tip and are placed in a 3-4 ml LB medium with antibiotics for duplication and have been shaken at 37 ° C. overnight. This procedure is known as a mini-preparation, which means that 50 to 100 µg of plasmid DNA can be harvested at the end. If a larger amount of DNA is required, a midi preparation can be carried out. For this, about 100 ml of LB medium must be inoculated with bacteria.

The harvested bacterial cells are first treated with various buffers so that the cells are accessible, and proteins and lipids are lysed. The lysate is applied over a DNA-binding membrane; the other components of the cell are removed using an organic washing buffer. In the end, the DNA molecules are eluted by adding water or an elution buffer.

The isolation of the plasmid DNA during this thesis was carried out using a kit from Carl Roth for mini-preparation and a kit manufactured by Machery Nagel.

2.2.1.13: Colony PCR

Sometimes it is necessary to examine more than 24 clones to find the clone with the desired plasmid. A colony PCR was suitable for this aim. For this purpose, specific primers were used that characterize a successful ligation. Using sterile pipettes, 50-60 clones were transferred to an LB agar plate, which is marked with a numbered grid. The rest of the clones was then used as a template in a PCR approach. The PCR products were examined by gel electrophoresis. The positive clones could be verified by mini preparation and test digestion.

2.2.1.14: Sequencing

All plasmids produced during this work were sequenced by the company "Euro fins MWG Operon". Approximately 100 ng / µl of a plasmid and 2 nmol / µl of the sequencing primer in a mixture of 15 µL total volume were sent for sequencing. The sequencing was performed according to the Sanger model.

2.2.2: Cloning strategies to generate the extrachromosomal arrays for application in *C. elegans*

The plasmid pNH10 (*pmyo-2::Arch(wt)::2xMyc-Tag)* was generated from plasmid pNH2 (*pmyo-3::Arch(wt)::2xMyc-Tag) via restriction digestion with the enzyme PciI and BamHI by exchanging the exchanging of pmy-2 and pmyo-3.*

pNH11 (*pmyo-2::Arch(D95N)::2xMycTag*), was generated from pNH10 using primers oNH7and oNH8 for the site directed mutagenesis at D95N and primers oNH61 and oNH62 for the amplification of the whole Arch(D95N) gene in *pmyo-2* vector.

pNH13 (p*myo-2*::QuasAr::mOrange) and pNH12 (*pmyo-2::MacQ::mCitrine)* were generated by subcloning of plasmids #59173 and #48762 (Addgene) into pPD132.102 (*pmyo-2*, #1662, Addgene) via restriction with *Bam*HI and *Eco*RI.

pNH17 (*pmyo-3::Arch(D95E,T99C,D106E)::2xMyc-Tag (DETCDE))* was generated via SDM using the vector pNH16 *(pmyo3::Arch(D95Q,D106E)::2xMycTag (EEQ))* as backbone vector and oNH37 and oNH38 for the mutagenesis at D95E,T99C.

pNH19 (*pmyo-2::Arch(D95H)::2xMycTag)* was generated via SDM with pNH10 as backbone vector and 0NH63 and 0NH64 for the mutagenesis at D95H.

pNH20(*pmyo-3::QuasAr::mOrange (eFRET))* was generated via an exchange of *QuasAr::mOrange* from addgene plasmid #59173 in the plasmid pNH2(*pmyo-3::Arch(wt)::2xMyc-Tag)* via restriction digestion with BamHI and EcoRI. The maps of all the plasmids are shown in the appendix.

2.2.3: Methods for cultivation and manipulation of *C. elegans*

2.2.3.1: cultivation of *C. elegans*

Small Petri dishes with a diameter of 3.5 cm filled with 3.5 ml of NGM, were used to cultivate the nematode C. elegans. The E. coli strain OP50 served as food. At room temperature, the worms can be kept on a plate inoculated with OP50 for about 4-6 days. The worms are then transferred to a freshly inoculated plate; otherwise, the plate will overgrow after this time, and the animals will starve. A platinum wire, which is bent at the tip and fastened in a Pasteur pipette, serves as a tool for moving the animals. For this purpose, the tip of the wire is overlooked with bacteria so that the animals can attach to it and can thus be transferred to the new plate. If the animals are kept at 16 ° C, their growth rate slows down, so that one implementation per week ensures optimal living conditions.

2.2.3.2: Preparing ATR plates

The chromophore ATR is required to investigate the functionality of different rhodopsins. Since *C. elegans* is unable to produce ATR, the external retinal must be given through food. For this purpose, a 100 mM stock solution of ATR in 100% ethanol was prepared, which was diluted 1: 1000 in OP50. This corresponds to a final concentration of 0.1 mM ATR solution. Each plate (diameter: 3.5 cm) was inoculated with 250 µl of this solution (OP50 + ATR). For rhodopsin direct-imaging, the concentration was increased x10.

2.2.3.3: Preparing ATR- analog plates

Various retinal analogs were examined during this work for their fluorescence in combination with different rhodopsins. For this purpose, 1 mM stock solution (dissolved in 100% ethanol) of the different analogs were prepared. The stock solution was mixed 1:10 with OP50, which corresponds to a final concentration of 0.1 mM analog. Each plate (diameter: 3.5 cm) was inoculated with 250 µl of this solution (OP50 + analog). The plates inoculated with retinal analogs could be kept for a maximum of two days.

2.2.3.4: Decontamination

In everyday laboratory work, it happens that the cultivation plates are contaminated by unwanted bacteria, mold, or fungi. These contaminants must be removed because they can harm the animal.

In order to treat bacterial contamination or fungal attack, approx. 5-10 µl bleaching solution was placed on a bacteria-free area of a freshly inoculated plate. Approximately Ten adult animals containing a relatively high number of eggs were added to the bleaching solution. The bleaching solution lyses contamination and worm so that ultimately only the eggs of the animals that have a protective chitin shell survive. The bleach solution evaporates, and larvae can hatch from the eggs.

2.2.3.5: Generation of transgenic animals via microinjection of plasmids

To create transgenic animals, the extrachromosomal DNA is injected into the gonads of an adult animal. The *C. elegans* gonad consists of two U-shaped arms. The maturation of the eggs begins at the end of these arms and is ended shortly before they are deposited by the vulva. The foreign DNA is injected into the upper arm of the gonad using a needle, the opening of which is only a few µm.

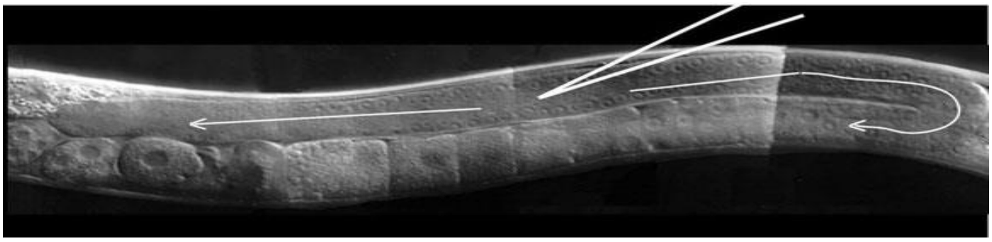

Fig. M-2: Microinjection of the extrachromosomal DNA into the gonads of *C. elegans*. Source:http://www.wormbook.org/chapters/www_transformationmicroinjection/transformation microinjection.

The plasmid is opened at any point after ingestion by the animal and is present in the form of a tandem array in hundreds of copies, which results from homologous recombination. The extrachromosomal array is then passed on to the next generation. The transgenic animals of the F1 generation are isolated. If there are transgenic animals in the F2 generation, the injection is said to be successful, and the transmission can be between 5-95%. The foreign DNA is injected in a mixture consisting of the plasmid, a co-injection marker, and injection buffer, the total concentration of DNA should not be below 100ng / µl; otherwise it can lead to the loss of the plasmid. A hose connects the needle to an air pump, which pumps a small amount of the injection mix into the gonad by pressing a pedal. Transgenic progeny can be selected using the conjugation marker.

2.2.3.6: Genomic integration of extrachromosomal DNA in *C. elegans*

The transmission of an extrachromosomal multicopy tandem transgene does not take place to all the progeny of a transgenic strain, and there exists mosaicism in the expression. Therefore, a method was used to integrate the transgene into the genomic DNA. For this purpose, 100 transgenic animals at L4 larval stage were transferred to 55 mm NGM plates without OP50 bacterial lawn and irradiated with 66.6 mJ UV light. The irradiated animals were transferred in lots of 10 to OP50 seeded 55 mm NGM plates and incubated until the bacteria lawn was completely eroded, and the F2 generation was transferred to fresh plates. Around 1000 transgenic animals were singled on fresh plates and were checked in the next generation for 100% presence of the transgene. The successfully integrated animals were subsequently out-crossed 4 times with wild-type animals to eliminate background mutations in other regions of the genome.

2.2.3.7: Crossbreeding

The crossbreeding procedure, according to Mendel´s laws, was applied to transmit transgenes and mutations from strain to strain. For this, a small amount of OP50 bacteria (just a drop of 5 µL) was placed in the middle of an NGM plate, and 25 males of one strain and 5 L4 hermaphrodites of the other strain were transferred in these bacteria. The following day, the young adult hermaphrodites were isolated and put on fresh plates. The F1 generation of these animals is heterozygous for the genetic background. A total number of 5-10 animals of this generation were isolated. According to Mendel, the F2 generation consists of 50% heterozygous and 25% homozygous animals for each genetic background. After another separation of 20-30 animals, the F3 generation was checked for corresponding properties, which can be a dominant phenotype or a fluorescence marker. Potential homozygous animals can be genotyped.

2.2.3.8: Genotyping

Genotyping was performed to verify the homozygous transmission of the desired allele after the crossing procedure. An individual or a group of animals can be used for this aim. In the first step, worm lysis was carried out with Proteinase-K in SEWLB buffer, whereby the desired number of animals were given to a mixture of 2.5 µL SEWLB + Prot-K. During an incubation for 30 minutes at -80 ° C the worms have been broken, which supports the subsequent one-hour lysis at 60 ° C. After that, the Proteinase-K was inactivated at 95 ° C for 15 min. The now available genomic DNA can be used either directly or after purification via phenol-chloroform extraction as a template for genotyping PCR using Taq polymerase. In the mutants with a deletion, 3 primers were usually used. A pair of primers, which binds outside the deletion and a primer (either forward or reverse) which binds within the deletion. Gel electrophoresis allowed conclusions to be drawn about the genotype on the basis of the corresponding fragment sizes. New restriction sites, which are caused by a point mutation, can be used to detect the homozygous. The detection was also carried out via gel electrophoresis.

2.2.3.9: Induction of *C. elegans* males

Male animals are needed for crossbreeding. Since the natural occurrence of male animals is shallow, their generation should be induced. This aim was achieved via heat shock. For this purpose, 10 L4 animals were placed on an NGM plate and have been incubated at 30 ° C for different periods (4,5h, 5h, and 5,5h). The resulting males from the F1 generation were isolated and have been put together with hermaphrodites of the same genotype for further pairing to increase the yield of male animals.

2.2.4: Analytical methods

2.2.4.1: Voltage imaging during spontaneous depolarization

In order to observe the basic fluorescence of the voltage indicator or to follow the changes in the fluorescence during spontaneous activity in the muscle cells of an animal (either BWMs or pharynx), the animals had to remain intact. However, to minimize the movement artifact, they had to be immobilized. 24 hours before imaging, animals were transferred to either ATR or ATR-analog holding NGM-plates. For this aim, 10% agarose pads were produced (solved in M9 buffer). A drop (about 1 µl) of polystyrene beads (0.1 µm in diameter) was placed on the agarose pad, and the worms were placed on it. The polystyrene beads adhere to the edge of the animal's body and allow the animal to be immobilized, so that motion artifacts are reduced during optical recording. Covered with a cover glass, the preparations are ready for video recording. For the observation of fluorescence changes in the animals expressing the GEVI in the pharynx, pumping was induced via exogenous 20% serotonin prior to the immobilization in the beads. The reason for this step is that the immobilization of the worms in beads and the application of cover glass has reduced the pumping rate massively so that it had to induced exogenously. A drop of 20% serotonin was placed on the agarose pad. The testing animals swam for 2 minutes in serotonin. The solution was then sucked dry with the tip of tissue, and the worms could be immobilized with beads as described above.

Imaging was performed on an inverted microscope (Zeiss Axio Observer Z1), equipped with a 40× oil immersion objective (Zeiss EC Plan-NEOFLUAR 40×/N.A. 1.3, Oil DIC ∞/0.17). A 637-nm laser (OBIS FP 637LX, Coherent) for excitation of voltage sensors, a Galilean beam expander (BE02-05-A, Thorlabs) was used for rhodopsin direct-imaging and an HBO-lamp 100 for eFRET imaging at 545/30- or 472/30-nm respectively. Voltage sensor fluorescence was imaged at 700 or 747 nm for ATR, and at 780 nm for DMAR. eFRET sensors were imaged with and 610/75- or 520/35-nm emission, respectively. The imaging setup was equipped with an EMCCD Camera (Evolve 512 Delta, Photometrics). Acquisition with the camera was controlled via the program „µManager". Exposure time and the gain value could be optimized for every sensor via µManager.

2.2.4.2: Voltage imaging during optically induced depolarization

The preparation of the animals for the optically induced depolarization was identical to the description in 2.2.4.1. The only difference was in the application of LED light sources (KSL 70, Rapp OptoElectronic) for the blue light pulse for the photostimulation of channelrhodopsin expressed in cholinergic neurons. The light pulse was controlled via a shutter. The lighting protocol was running by a shutter controller regulated via the program Lambda SC utility.

2.2.4.3: Drug application

As described already, Nema-A was shown to reduce the allele-specific malfunctions in *egl-19* mutants. Nema-A, a blocker of voltage-gated calcium channel, is a dihydropyridine derivative and analog to a group of anti-hypertensions (see the structure, Fig. M-3)

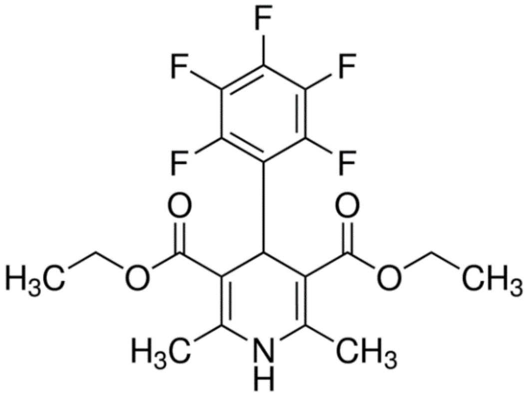

Fig. M-3: The structure of Nemadipine-A (adopted from sigma-Aldrich)

In this project and to evaluate the GEVIs expressed in the pharynx, Nema-A was applied in *egl-19* mutants. The fluorescence changes of the mutants were observed after drug application. Nema-A was solved in 2% DMSO. Prior to immobilization, animals were incubated in 500 µL Nemadipin (30 µM) or 2% DMSO for 15 minutes. They were then transferred to an NGM-plate (without food) and were allowed to move for 2 minutes to get rid of the rest of the drug. The following procedure of immobilization for optical imaging was then identical to the description in 2.2.4.1.

2.2.4.4: Electropharyngeogram (EPG) and sharp electrode measurements (Performed by Dr. Schüler)

For electropharyngeogram (EPG) recordings, L4 animals were placed for ca. 24 h on NGM plates seeded with OP50 and supplemented either with or without ATR; for PM intracellular recordings, this time was extended to 2-3 days. Animals were transferred into a recording chamber containing a Sylgard-coated coverslip and filled with 1.5 mL of EmD50 buffer (NaCl, 140 mM; KCl, 3 mM; $CaCl_2$, 3 mM; $MgCl_2$, 1 mM; Hepes, 10 mM; D-Mannitol, 50 mM; pH 7.3 adjusted with NaOH) containing 2-20 µM 5 Hydroxytryptamin to stimulate pumping. Cut-head preparation and EPG recording of strain ZX1918 were performed as described previously (Schüler *et al.*, 2015). Intracellular recordings were performed following a previously described protocol (Cook, Franks and Holden-Dye, 2006), also for the manufacturing of intracellular electrodes and the positioning of the holding and the intracellular electrodes. For combined voltage imaging, an EMCCD Camera (Evolve 512 Delta) was used. Data were analyzed by OriginPro (Description of the method adopted from (Azimi Hashemi *et al.*, 2019).

2.2.4.5. Current clamp measurements (Performed by Dr. Liewald)

Recordings were conducted from dissected BWM cells on the ventral side of the body anterior to the vulva, as described earlier (Liewald *et al.*, 2008). Animals were immobilized with Histoacryl glue (B. Braun Surgical, Spain), and a lateral incision was made to access neuromuscular junctions along the ventral nerve cord. The basement membrane overlying muscles was removed by incubation in 0.5 mg/ml collagenase for 10 s (C5138, Sigma-Aldrich, Germany). BWMs were patch-clamped in whole-cell mode at 22°C using an EPC10 amplifier with head stage connected to a standard HEKA pipette holder for fire-polished borosilicate pipettes (1B100F-4, WPI, USA) of 4-7 MΩ resistance. The extracellular (bath) solution contained: NaCl 150 mM; KCl 5 mM; CaCl2 5 mM; MgCl2 1 mM; glucose 10 mM; sucrose 5 mM; HEPES 15 mM, pH7.3 with NaOH, ˜330 mOsm. The pipette solution contained: K-gluconate 115 mM; KCl 25 mM; CaCl2 0.1 mM; MgCl2 5 mM; BAPTA 1 mM; Hepes 10 mM; Na2 ATP 5 mM; Na2 GTP 0.5 mM; cAMP 0.5 mM; cGMP 0.5 mM, pH7.2 with KOH, ˜320mOsm. Current clamp recordings were conducted using Patchmaster software (HEKA, Germany). Light activation was performed using an LED (KSL-70, Rapp OptoElectronic, Hamburg, Germany; 470 nm, 1 mW/mm²) and controlled by the EPC10 amplifier. Data were analyzed by Patchmaster software (Description of the method adopted from (Hashemi *et al.*, 2019)).

2.2.4.6: Analysis of the voltage imaging

2.2.4.6.1: Analysis of the fluorescence changes in the pharynx

The acquisition of the recordings was performed via the Photometrics PVCAM Device Adapter for µManager, which is a program based on the image processing software ImageJ. For the analysis of the fluorescence changes in pharyngeal muscles, the recorded images were recalled in the program ImageJ. A region of interest (ROI) was defined around the whole pharynx (see Fig. M-4, red-marked region) referring to the voltage changes. Another smaller circular ROI was positioned over the grinder to track the contractions of pharyngeal muscles upon pumping (green ring in Fig. M-4). The fluorescence decreases in the ROI upon the opening of lumen since fluorescing tissue retracts radially (Yellow ring in Fig. M-4). The voltage-dependent changes in the signal of the whole pharynx increases in the animals with GEVIs for rhodopsin direct-imaging and decreases in animals with eFRET GEVIs. For background correction, another ROI was defined in an arbitrary dark region outside the worm, or, for contrast measurements, 'inside' the worm (the marked region in blue in Fig. M-4), but avoiding the gut or tissue expressing the respective voltage sensor.

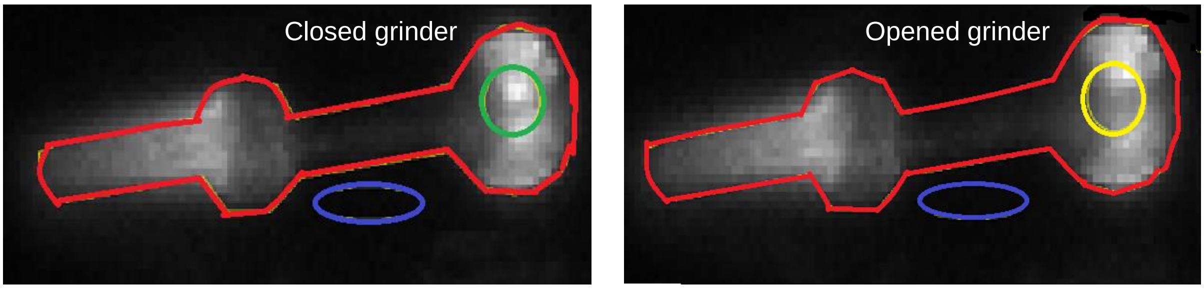

Fig. M-4: Schematic representation of opened and closed grinder. The left figure shows the pharynx (marked in red) and its closed grinder (marked in green) during resting potential. The right picture shows the opened grinder (marked in yellow) during pharyngeal depolarization and thus contraction. Background region is marked in blue.

To indicate the luminosity of each sensor, the contrast between mean fluorescence of a ROI across the pharyngeal or BWM tissue expressing the voltage sensor and the mean fluorescence of a ROI from the background was calculated. Signal to noise ratio (SNR) was calculated as the ratio of the mean fluorescence of all peaks (=APs) observed during a pump train, and the standard deviation of the fluorescence in the ROI during resting phases (Fig.M-5)

Fig. M-5: Schematic representation of Signal to noise ratio (SNR). (SNR) was calculated as the ratio of the mean fluorescence of all peaks (APs) observed during a pump train, and the standard deviation of the fluorescence in the ROI during resting phases.

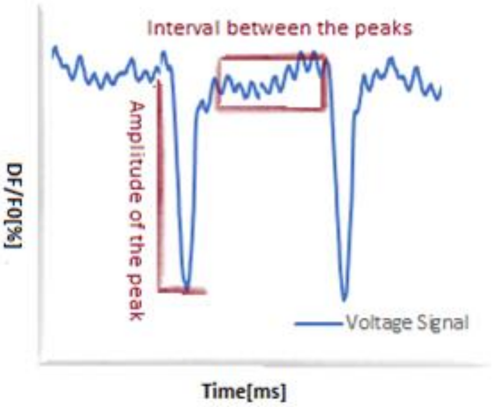

2.2.4.6.2: KNIME workflow for analysis automation

The readout data in arbitrary units have been recalled in microsoft excel to calculate $\Delta F/F_0$. F_0 is the mean fluorescence (F_{mean}) of the ROI, calculated for the entire imaging period. The excel data containing the calculated $\Delta F/F$ for both pumping and voltage signals were then loaded in the customized workflow in KNIME to synchronize pump and voltage events across animals by calling an R (R 3.5.1, to process each of the Excel tables (see Fig. M-6).

The R script (included in the KNIME workflow) proceeds to fit a spline curve to the input data with as many anchor points as data points present (Fig. M-7). The fit curve is sampled at constant 200 data points per second to account for the variable camera timing. Pumps are found as local minima with a centered time window of 625 ms (see Fig. M-8 left). Manual input of indices can be used to correct this peak registration. The signals that passed manual control are synchronized first to the pump minimum. The voltage signal is then analyzed for the peak onset by searching for the minimum of the scaled difference with a lag of 50 ms of a centered moving average with a window size of 105 ms (Fig.M-8, right).The events are subsequently synchronized to the onset of the voltage peak and grouped per animal, or analyzed individually, where appropriate (See Fig. M-9). Description of the method is adopted from (Azimi Hashemi *et al.*, 2019)

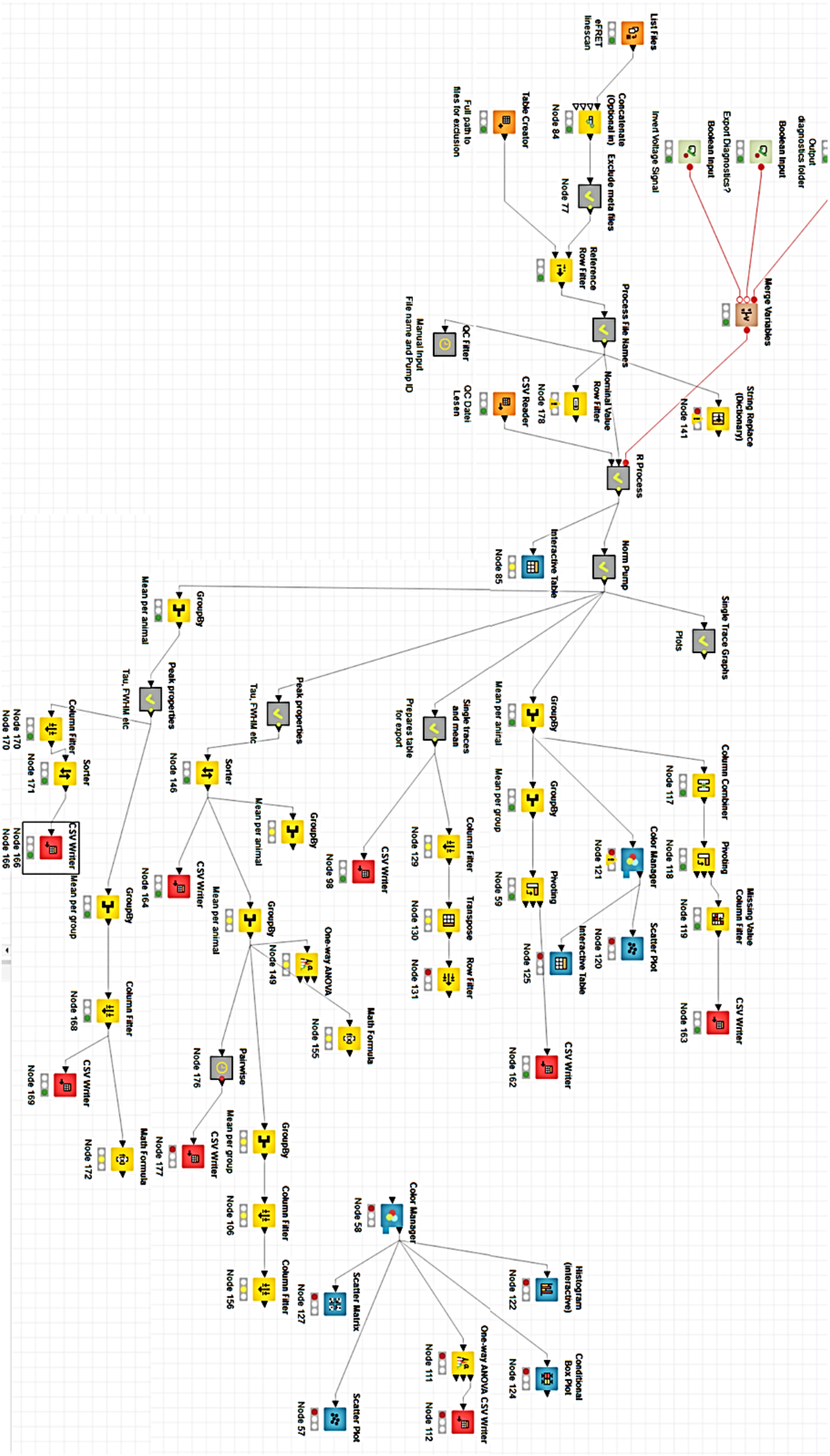

Fig. M-6: The workflow in KNIME for the automation of the analysis

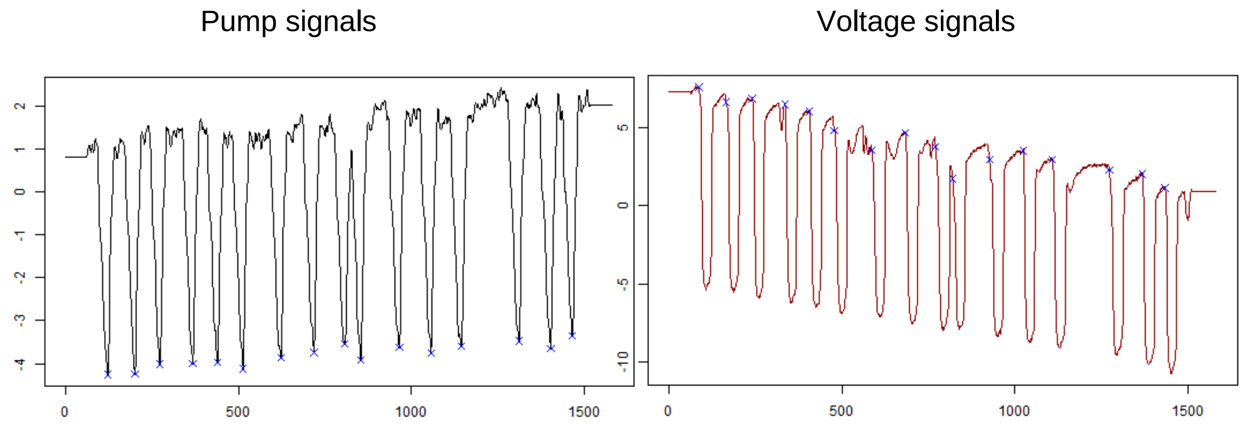

Fig. M-7: Detection of pump and respective voltage signals by KNIME from an exemplary animal

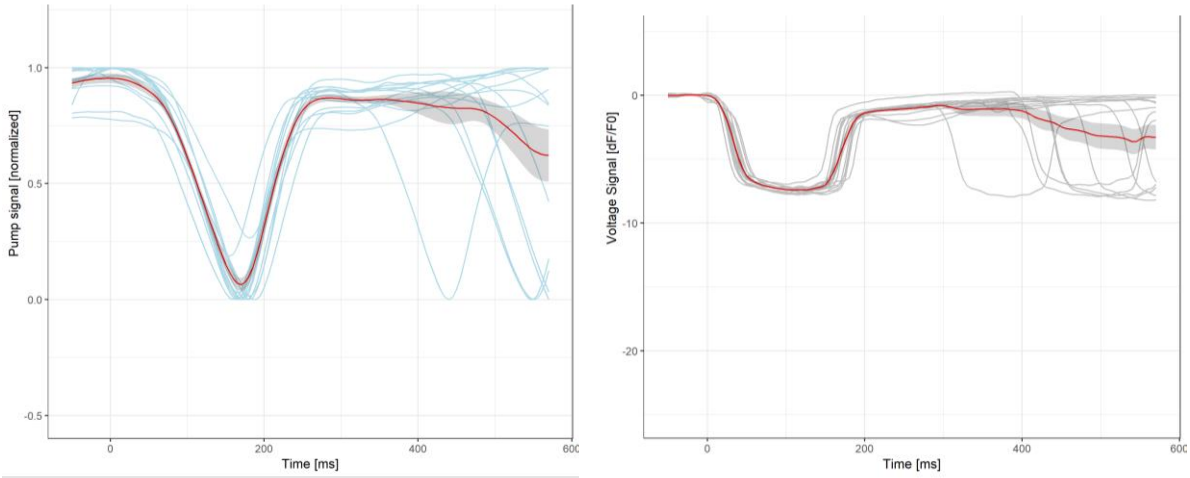

Fig. M-8: Synchronized pump (left) and voltage (right) signals in a time window of 600 ms by KNIME from and exemplary animal. Synchronized pump and voltage signals are shown in blue and gray and the mean of them is marked in red.

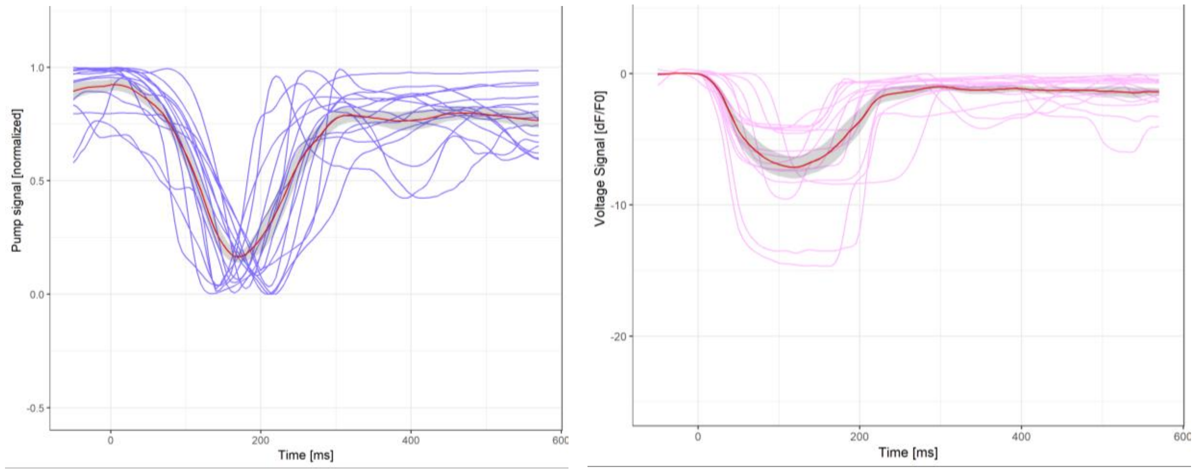

Fig. M-9: Synchronized mean pump (left) and voltage (right) signals from the animals in a group in a time window of 600 ms by KNIME from exemplary animal. Synchronized pump and voltage signals are shown in blue and gray and the mean of them is marked in red.

The signals are further analyzed to extract the start and end of the peak by searching for the first and last data point to cross a line at 10% of the distance from the baseline to the peak minimum, respectively (Fig. M-10).

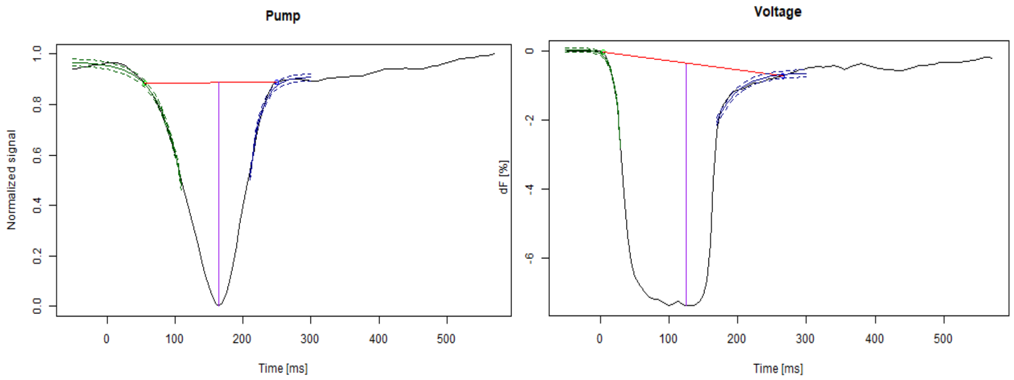

Fig. M-10: Detection of the start and the end of a signal by KNIME. KNIME crosses a line at 10% of the distance from the baseline to the peak minimum. This line is used to extract further information about the signal properties

Analogously, the full width at half maximum (FWHM) is calculated by searching for the two data points that cross the 50% line between baseline and peak minimum. Duration is defined as the time difference between the start and end of a peak (Fig. M-11).

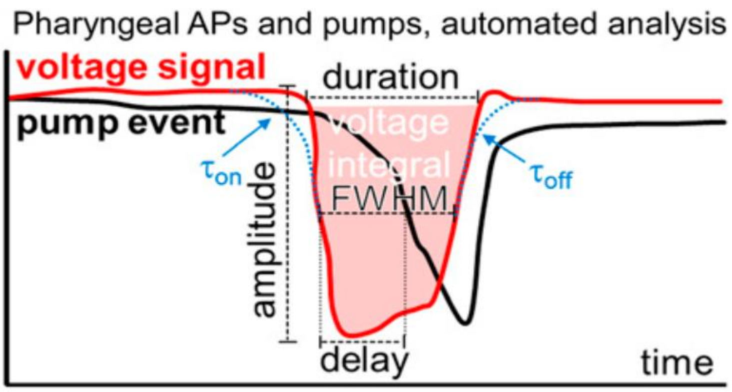

Fig. M-11: Schematic presentation of the detection and definition of pharyngeal APs and contractions by KNIME. Fluorescence traces derived from the calculated ΔF/F are derived from the changed of ROI defined over grinder. Traces shown as voltage signal are from the red marked region in Fig.M-4 (Adopted from (Azimi Hashemi *et al.*, 2019)).

The kinetic parameters TON and TOFF are modeled, each with a mono-exponential curve fit accounting only for the time frames from (-50 ms, FWHM start) and (FWHM, 305 ms), respectively. The area (voltage integral) is calculated as the integral from start to end of the peak from the baseline. The amplitude is calculated as the peak minimum to the maximum value at a negative time after synchronization in the depicted time frame. The delay is reported as the time difference between the FWHM start of the voltage and FWHM start of the pump peaks. However, it should be mentioned that not all of the signals could be fitted to a mono-exponential curve. Therefore, the number of the analyzed peaks for the kinetics was reduced, respectively (The automation procedure was described by Dr. Steuer Costa, (adopted from (Azimi Hashemi *et al.*, 2019)).

2.2.4.6.3: Analysis of “difference recordings” to generate opto-EPG and following the spatiotemporal voltage changes in pharynx

To generate the so called opto-EPGs and to calculate the step changes in the voltage and to follow the spatiotemporal development of voltage in pharyngeal muscles, difference videos have been analyzed. For this aim two duplicates of a video have been generated in a manner that the first frame in the first duplicate and the last frame in the second duplicate have been deleted. Every pixel in the second duplicated was subtracted from the same pixel in the first duplicate. Electrical events have been extracted and aligned and the fluorescence changes have been analyzed. To generate opto-EPGs a ROI was set around the whole pharynx. Analysis of a line scan along the longitudinal axis helped to follow the spatiotemporal development of voltage among different sections of pharyngeal muscles.

2.2.4.6.4: Analysis of fluorescence changes in body wall muscles

The analysis of the fluorescence changes in body wall muscles was performed in the same manner as pharyngeal muscles. Recorded videos were recalled in ImageJ, and a ROI was defined over muscles of interest with bright fluorescence. Another area out of the worm was then defined as background. The readout values were extracted in arbitrary units, which were loaded in excel. $\Delta F/F$ was calculated in excel. This procedure was performed for the analysis of both spontaneous and optically induced depolarization in body wall muscles.

3 Results

3.1: Expression and localization of GEVIs in *C. elegans*

During this project, different genetically encoded voltage indicators (Akerboom *et al.*, 2012) (GEVIs) were tested for their ability of monitoring membrane voltage and action potentials in *C. elegans*. Two muscle groups were chosen as GEVI test-systems, to address this aim; the body wall muscle (BWM) and the animal feeding´s organ, the pharynx.

3.1.1: Expression and localization in the pharynx

The expression of GEVIs in pharynx was achieved by putting their cDNAs under the control of the *myo-2*-promotor. Stable expression in wild type *C. elegans* was achieved with a concentration of 3 ng/µl *pmyo-2::GEVI* (5 ng/ µl for Arch(wt)) and 30 ng/µl *pmyo-3::XFP* as a co-injection marker. All the sensors have shown a stronger expression and thus fluorescence signal in the anterior and posterior bulb in comparison to the rest of the pharynx. This observation is consistent with the already described expression pattern of the *myo-2* promotor (Okkema *et al.*, 1993; Okkema and Fire, 1994).

3.1.1.1: MacQ-mCitrine

The *C. elegans* line expressing MacQ-mCitrine from an extrachromosomal transgene, showed a high transmission rate, meaning that up to 85% of the animals in every upcoming generation was transgenic. Transgenic animals revealed no abnormality in their morphology or development in comparison to wild type. Mosaicism in the expression pattern could be observed among different animals since the transgene was not integrated into the genome. Expression could be observed in membranous structures, both localized along the outer lining of the pharyngeal muscle cells (apical side), but also at the basolateral membranes delineating the muscle cells from marginal cells and each other, as well as in internal membranes. Besides, the localization of clusters (the white arrows in Fig. R-1) could be observed in both anterior and posterior bulbs (see Fig. R-1).

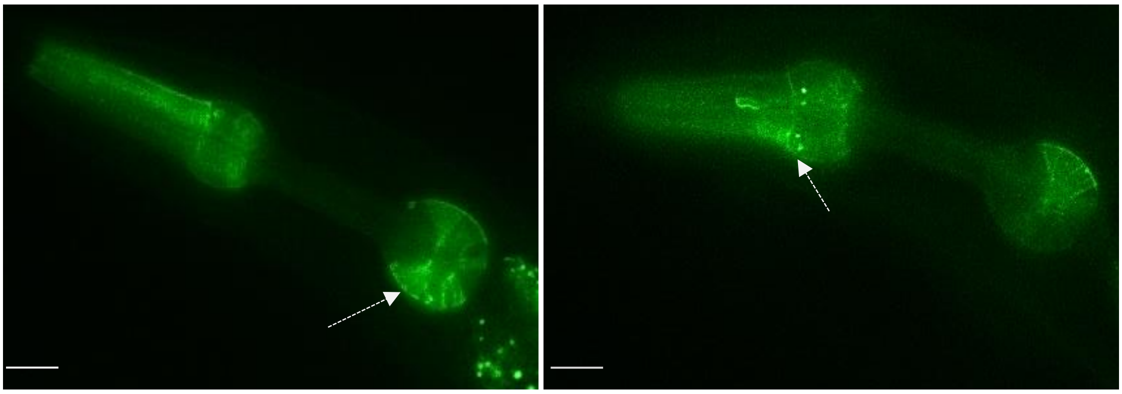

Fig. R-1: Expression and localization of MacQ-mCitrine in pharyngeal muscles under the control of *myo-2* promotor. The membrane expression is visible in all pharyngeal muscles (stronger in both bulbs vs. isthmus), whereas some clusters are also visible (white arrow). [Scalebar 20 µm, 40x objective, 20 ms Exposure time, Ex.: 470nm, Em.: 520nm, Light source: HBO-lamp 100, 10 mW/ mm²]

3.1.1.2: QuasAr-mOrange

The expression of QuasAr-mOrange was readily observable and did not affect the viability of the animals. The transmission rate of the extrachromosomal transgene was above 70%. As for MacQ-mCitrine, QuasAr-mOrange was found in all parts of the plasma membrane, but also in internal membranes. There were many punctate clusters along the procorpus and in both pharyngeal bulbs. Besides these clusters, there were also protein accumulations, occurring randomly in all pharyngeal muscles (see the circles in Fig. R-2). The latter may be due to protein accumulation in the endoplasmic reticulum (ER).

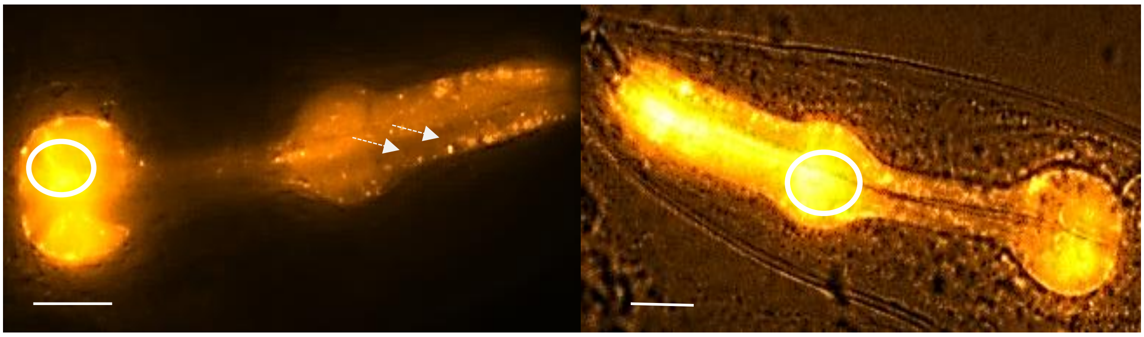

Fig. R-2: **Expression of QuasAr-mOrange in the pharyngeal muscle under the control of the *myo-2* promotor.** Two exemplary animals expressing QuasAr-mOrange are shown. The membrane expression is visible in all pharyngeal muscles (right: merged fluorescent and transmitted light micrographs), whereas some clusters (white arrows) and accumulations are also visible, respectively (circles). [Scalebar 20µm, 40x objective, 20 ms Exposure time, Ex.: 560/15 nm, Em.: 610nm, Light source: HBO-lamp 100, 35 mW/ mm²]

3.1.1.3: Arch(wt)

Although the transgenic animals expressing Arch(wt) (with 5 ng/µl of plasmid) did not develop any abnormal phenotype in comparison to wild type animals, the transmission rate of the transgene was just 20-30%, and expression successively became worse in every new generation. Injections using less than 5 ng/µl of plasmid did not result in any transgenic animals and injections above this concentration appeared to be toxic, since the transgene was expressed only in the first generation after injection. However, these transgenic animals did not survive to produce offspring. Arch(wt) was not fused to a fluorescent protein but was tagged with two copies of the myc-tag, meaning that the expression and localization of the protein had to be verified after its equipment with a chromophore. Arch(wt)did not show any fluorescence signal in the presence of ATR. However, retinal analog VI could be used to track the expression of Arch(wt).

The expression pattern of Arch(wt) was very diffuse. There were animals showing fluorescence signals in only a few pharyngeal muscles, in both bulbs, demonstrating a high degree of mosaicism. However, this observation might also be the result of inhomogenous incorporation of the analog VI in pharyngeal muscles.

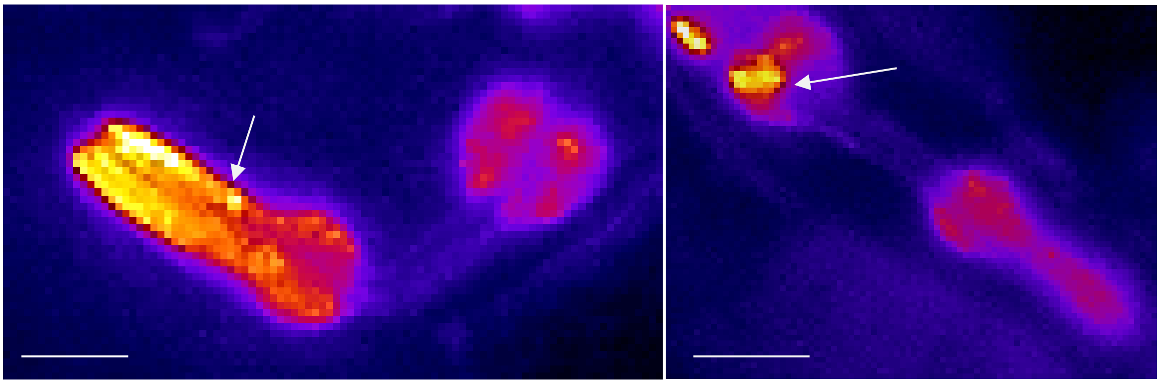

Fig. R-3: Expression and localization of Arch(wt)-2xMyc-tag in pharyngeal muscles under the control of *myo-2* promotor, and supplemented with retinal analog VI. Two exemplary animals, expressing Arch(wt), are shown. The membrane expression is visible in most pharyngeal muscle cells, but clustered appearance (white arrows) was more present in comparison to the other GEVIs expressed in the pharynx. This observation may also have resulted from the non-homogenous incorporation of retinal analog VI in the protein. [Ex.: 560/15 nm, Em.: 610 nm, Scalebar 20 µm, 40x objective, 1 ms Exposure time, Light source: HBO-lamp 100, 35 mW/mm²]

3.1.1.4: Arch(D95N)

The construct for the expression of Arch(D95N) lacked a fluorescence reporter. The expression of the co-injection marker was the first hint for the presence of transgenic animals. The transmission rate was above 95%, and non-transgenic animals were observed very rarely. The expression of Arch(D95N) could be verified first after the incorporation of a fluorescence chromophore in the protein, either ATR or its analog DMAR (see Fig. R-4). The fluorescence of ATR is very dim in comparison to DMAR under the same imaging conditions (concentration, gain value of EMCCD camera, and the light intensity). One idea to increase the fluorescence signal was the application of 1mM ATR (10x more vs. 0.1 mM for DMAR) and changing the gain value in the setting of the camera imaging program from 1 to 50 to get similar images to some degree.

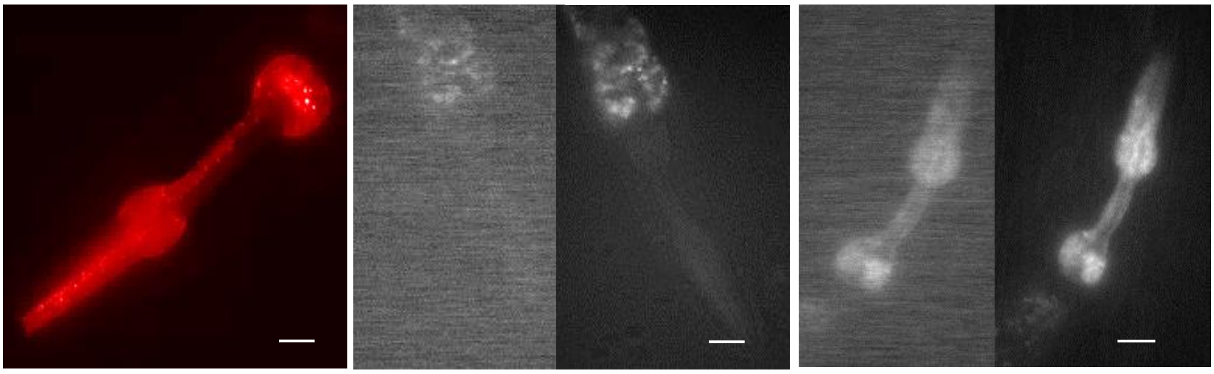

Fig. R-4: Expression and localization of Arch(D95N)-2xMyc-tag in pharyngeal muscles under the control of *myo-2* promotor. Shown are three animals expressing Arch(D95N), after equipping the protein with DMAR (left) and ATR (0.1 mM (gain 1 and 50) middle and 1 mM (gain 1 and 50) right). The membrane expression is visible, whereas the fluorescence signal is weaker with ATR vs. DMAR. [Scale bar 20 µm, 40x objective, 20 ms exposure time. Ex.: 637nm, Em.: 780nm (DMAR), 740nm (ATR), Light source: 637 nm Laser, 180 mW/mm²]

3.1.1.5: Arch(D95H)

Arch(D95H) was tagged with 2xMyc-tag and not with a fluorescent as well, meaning the verification of the sensor´s expression could be performed after the protein was supplemented with chromophores ATR or DMAR (figure R-5). Transgenic animals were selected in the first step only with the help of the co-injection marker. The presence of punctual clusters was minimized in these animals in comparison to the other mutants, but it seemed that the DMAR did not incorporate in the protein homogenously. The fluorescence of ATR was still very dim, even with a higher concentration and gain-value.

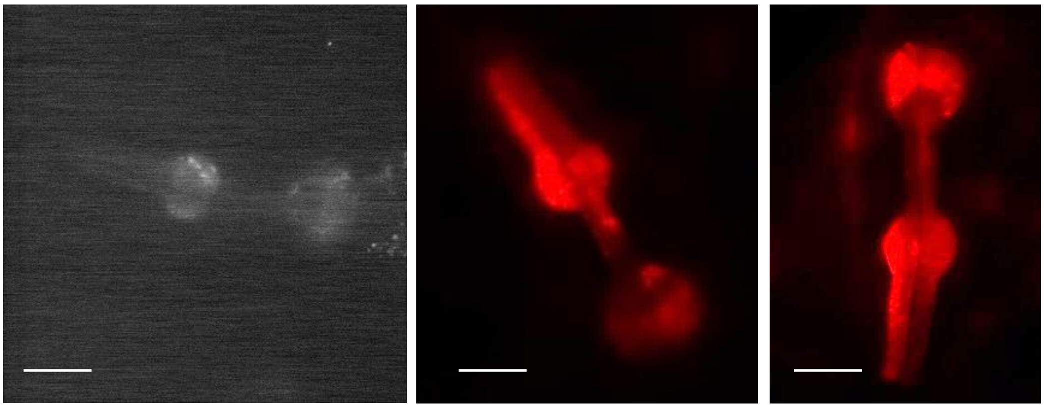

Fig. R-5: Expression and localization of Arch(D95H)-2xMyc-tag in pharyngeal muscles under the control of *myo-2* promotor. Shown are three animals expressing Arch(D95H) after equipping the protein with DMAR (middle and right, gain 1) and ATR (left, gain 50). The membrane expression is visible, whereas the ATR-fluorescence signal is weaker than the DMAR signal. [Scale bar 20 µm, 40x objective, 20 ms exposure time, Ex.: 637nm, Em.: 780nm (DMAR), 740nm (ATR), light source: 637nm laser, 180 mW/ mm²]

3.1.2: Expression and localization of GEVIs in body wall muscles (BWMs)

The expression of GEVIs in BWMs occurred under the control of *myo-3* promotor. The stable expression in wild type *C. elegans* was achieved with a concentration of 10 ng/µl *pmyo3::GEVI* and 30 ng/µl *pmyo3::CFP* as a co-injection marker. The expression of all the GEVIs in BWMs was stronger in the head and vulval muscles. This observation is consistent with the already described expression pattern of the promotor *myo-3*, which shows that the expression of MYO-3 is stronger in head and vulval muscles (Fire and Waterston, 1989). The extrachromosomal arrays for two transgenic lines Arch(D95N) and QuasAr-mOrange (eFRET) were then integrated into the genomic DNA of the animals via UV-treatment (see methods). Male animals of the integrated strains were used for crossbreeding with hermaphrodites of a strain carrying the integrated transgene *zxIs5*, expressing channelrhodopsin-2 in cholinergic neurons. Genotyping confirmed the homozygosity of the obtained animals.

3.1.2.1: QuasAr-mOrange (eFRET)

The expression of QuasAr-mOrange could be observed in the body wall, head, and vulval muscles clearly, visualizing the cell shapes with a high resolution. Even muscle arms could be detected, especially in the head region. The expression was stronger in vulval muscles, revealing a strong fluorescence signal. Punctate clusters and protein accumulations were detected as well (see Fig. R-6). The expression of QuasAr was not homogenous for all the body wall muscles. The strongest expression occurred at the head and vulva region.

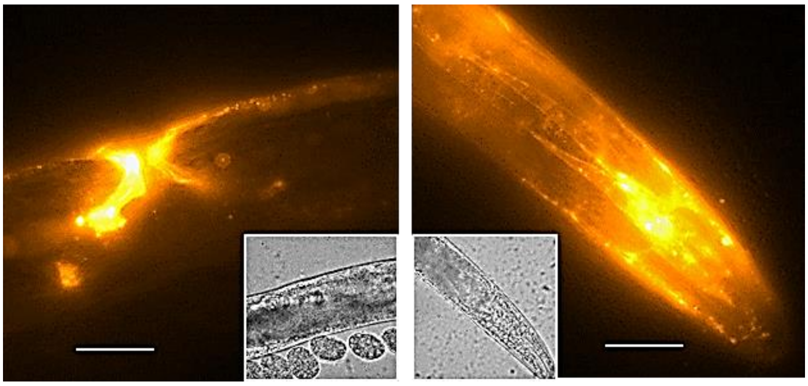

Fig. R-6: Expression and localization of QuasAr-mOrange in BWMs under the control of the *myo-3* promotor. Two exemplary animals, expressing QuasAr-mOrange in the vulva (left), and head (right) muscles are shown. [Scale bar 20 µm, 40x objective, 20 ms exposure time, Ex.: 540nm, Em.: 610nm, Light source: HBO-lamp 100, 35 mW/ mm²]

3.1.2.2: Arch(D95N)

Arch(D95N) was expressed in BWMs, and the transgene was integrated into the genomic DNA. Like for QuasAr-mOrange, the expression of Arch(D95N), was stronger in head and vulva muscles in comparison to the other body wall muscles. Localization and expression of Arch(D95N) could be observed only after the animals were equipped with ATR or DMAR as this sensor was only tagged with two copies of the myc-tag. There were many punctate clusters visible. Since the fluorescence of ATR is very dim in comparison to DMAR, the concentration of ATR was increased to 1mM (10x more vs. 0.1 mM for DMAR) for the imaging in BWMs, and the gain value of the camera imaging program was set from 1 to 50 to get similar images to some degree.

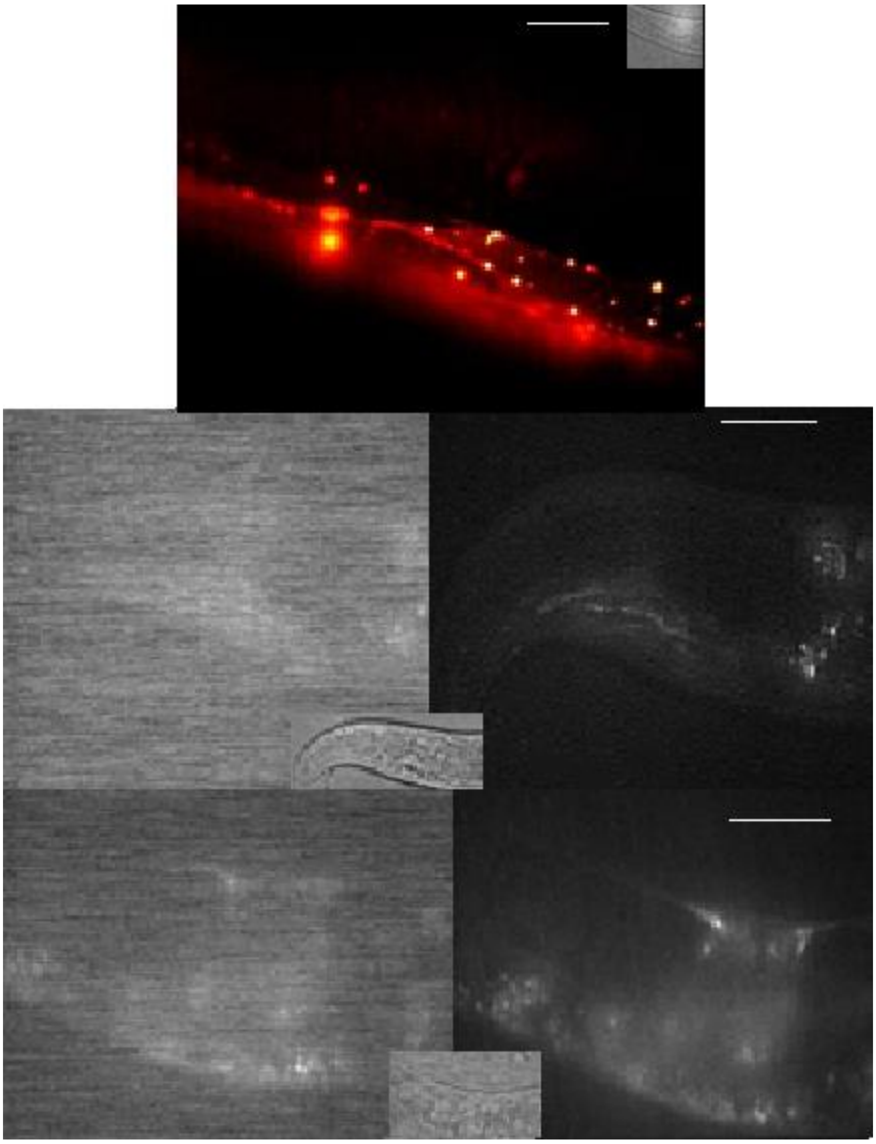

Fig. R-7: Expression and localization of Arch(D95N)-2xMyc-tag in BWMs under the control of *myo-3* promotor. Shown are animals expressing Arch(D95N) after equipping the protein with DMAR (up) and 0,1 mM ATR middle (left to right gain 1 and gain 50) and 1 mM ATR down with (left to right: gain 1 and gain 50). The fluorescence signal is weaker with ATR vs. DMAR. [Scalebar 20 µm, 40x objective, 20 ms exposure time, Ex.: 637nm, Em.: 780nm (DMAR), 740nm (ATR), Light source: Laser, 180 mW/mm²]

3.1.2.3: Arch(DETCDE)

The transmission rate of transgenic animals expressing the triple mutant Arch(DETCDE) was ca. 50%. Arch(DETCDE) was tagged with 2x myc-tag, meaning that the expression of the protein could be varified after the incorporation of a chromophore, either ATR or DMAR. The fluorescence signal of ATR was dimmer in comparison to DMAR with this sensor as well. So the same strategy of increasing the concentration of ATR to 1mM (10x more vs. 0.1 mM for DMAR) and changing the gain value in the setting of the camera imaging program from 1 to 50 was performed. Despite the weak signal, the expression could be detected along the body wall and vulval muscles (see Fig. 8).

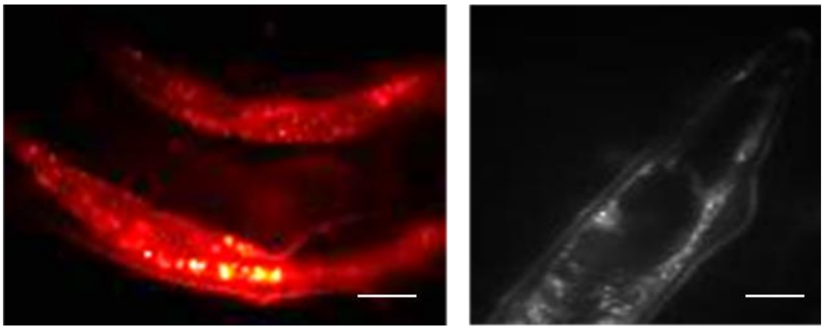

Fig. R-8: Expression and localization of Arch(DETCDE)-2xMyc-tag in BWMs under the control of the *myo-3* promotor. Two exemplary animals expressing Arch(DETCDE) are shown after the incorporation of either DMAR (left, 0.1 mM, gain 1) or ATR (right, 1mM, gain 50) in the protein. [Scale bar 20 µm, 40x objective, 15 ms exposure time, Ex.: 637nm, Em.: 780nm (DMAR), 740nm (ATR), light source: 637nm laser, 180 mW/ mm²]

3.2: Quantification of basal fluorescence of different GEVIs

The first step to verify the capability of GEVIs in monitoring voltage activities is to quantify their absolute fluorescence signal. eFRET sensors can be excited with low light intensities of about 10-30 mW/ mm² with a standard HBO lamp and deliver robust signals. Direct imaging requires a powerful light source such as a laser with intensities of 800 mW/mm² or more (Kralj *et al.*, 2011). This high intensity could be reduced to 160 mW/mm² by the usage of retinal analogs.

Furthermore, the application of an EMCCD camera with a high sensitivity could also detect similar fluorescence signals from ATR, however, with the optimization of the camera setting.

The fluorescence signal of both eFRET sensors QuasAr-mOrange and MacQ-mCitrine originates from their fluorescent proteins, namely mOrange and mCitrine, therefore it is much stronger than the observed signal from rhodopsin direct-imaging.

The basal fluorescence signal was quantified in two ways: on the one hand, as the mean of the absolute gray value and, on the other hand, as the raio of the fluorescence signal in muscles (either pharynx or BWMs) to the background. The latter indicates the luminosity of every sensor.

This analysis does not deliver any information about the voltage sensitivity of the sensors, e.g. during action potentials. It is just an indication of the basal fluorescence of every GEVI. The electrical sensitivity of each sensor will be discussed individually and in detail in the next section for each sensor, and there will be another overall comparison about signal-to-noise ratio for all the sensors to analyze their voltage sensitivity.

3.2.1: Quantification of basal fluorescence of GEVIs expressed in the pharynx

The average gray value of the basal fluorescence signal of eFRET sensors QuasAr-mOrange and MacQ-mCitrine is around 20000 and 5000 a.u, which is ca. 3000 times and 750 times higher than that of Arch(D95N), supplemented with ATR, which had a mean gray value of ca. 6 a.u (see Fig. R-9). The substitution of ATR with DMAR in Arch(D95N) increased the mean gray value of the fluorescence signal up to 1600 a.u. Increasing the concentration of ATR in Arch(D95N) from 0,1 to 1 mM and the adjustment of the camera gain value from 1 to 50 could increase the fluorescence signal up to 2000 a.u, which is in a comparable range with the average gray value of DMAR signal.

The averaged gray value of the fluorescence signal of Arch(D95H), even with the application of 1 mM ATR and the adjustment of the camera gain value to 50, was still only around 10 a.u. The substitution of ATR with DMAR in Arch(D95H) increased the fluorescence yield up to ca. 3500 a.u. However, this mean value is still 6 and 1.5 fold weaker than both eFRET sensors, QuasAr-mOrange and MacQ-mCitrine, respectively.

As described above (section 3.2), the quality of the basal fluorescence signal of the sensors was also analyzed as the contrast of the mean gray value of pharynx to the background signal (noise). QuasAr-mOrange was the brightest sensor, followed by Arch(D95H)+DMAR. Interestingly this opsin and chromophore combination was even brighter than MacQ-mCitrine. This analysis revealed that although the aroused concentration of ATR and the optimized camera setting by Arch(D95N)+ATR has increased the mean gray value of basal fluorescence signal to a comparable level as that of Arch(D95N)+ DMAR, however, the clarity of ATR fluorescence signal is 50% less than the DMAR fluorescence signal.

The retinal analog VI, which also exhibited a high fluorescence signal, was used during this project. However, it was only used in Arch(wt). This chromophore was incorporated, but did not reconstitute the pumping functionality of Arch-3. Thus, analog VI in Arch(wt) did not induce hyperpolarisation of the membrane. This property of analog VI was already shown in BWMs (Azimihashemi *et al.*, 2014). However, the basal fluorescence with an averaged gray value of ca. 1000 a.u is a newly introduced feature of analog VI. This analog was not compatible with any of the mutant variants of Arch. It is not clear if this analog could not incorporate in the mutated opsins, or whether it loses its fluorescence after the insertion in the protein.

Besides the quantification of the basal fluorescence signal, it could also be shown that the supplementation of the eFRET sensors with ATR does not affect the absolute fluorescence signal during resting.

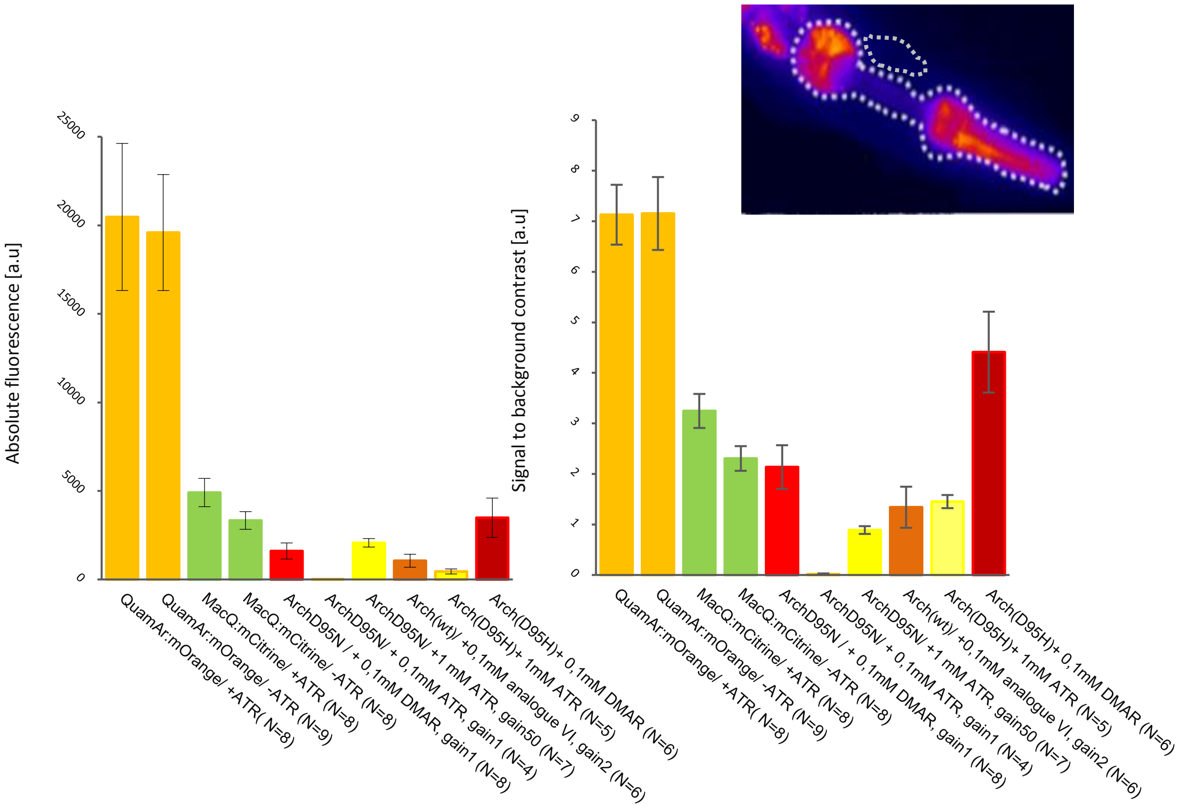

Fig. R-9: Quantification of the absolute fluorescence in different GEVIs expressed in the pharynx. Analysis of the fluorescence signal as the mean grey value of a region including the whole pharynx (left) or the ratio of the signal of this region to the background outside of the pharynx (right). Demonstrated are the means± SEM in arbitrary units [a.u]. The exposure time was 1 ms. The gain value, number of the animals, and the concentration of ATR / ATR analog are indicated under the bars in the graph.

3.2.2: Quantification of basal fluorescence of GEVIs expressed in BWMs

The basal fluorescence signal was quantified for GEVIs expressed in BWMs as well, QuasAr-mOrange, Arch(D95N) and Arch(DETCDE). In general, the basal fluorescence signal was weaker in BWMs in comparison to the pharynx (under the same conditions, e.g., gain value, exposure time, and chromophore concentration). This observation might be either due to the natural morphology and structure of body wall muscle cells or to the different expression levels of the GEVIs in pharynx and BWMs.

The averaged gray value for QuasAr-mOrange was ca. 1750 a.u. This eFRET sensor was twofold brighter than Arch(D95N) with both ATR and DMAR (see Fig. R-10, left). When equipped with 1 mM ATR, Arch(D95N) revealed a mean gray value of about 1500 a.u. (The fluorescence yield of 0.1 mM ATR in BWM was so dim, that it could not be quantified). The basal fluorescence of Arch(D95N) in BWMs was about 500 a.u. when the sensor was equipped with DMAR. However, the brightness of both ATR and DMAR signals in Arch(D95N) was in a similar range. The averaged grey value for Arch(DETCDE) with both ATR (1 mM) and DMAR (0,1 mM) was ca. 250 a.u. The signal contrast and brightness were identical for all the sensors for direct imaging (Fig R-10, right).

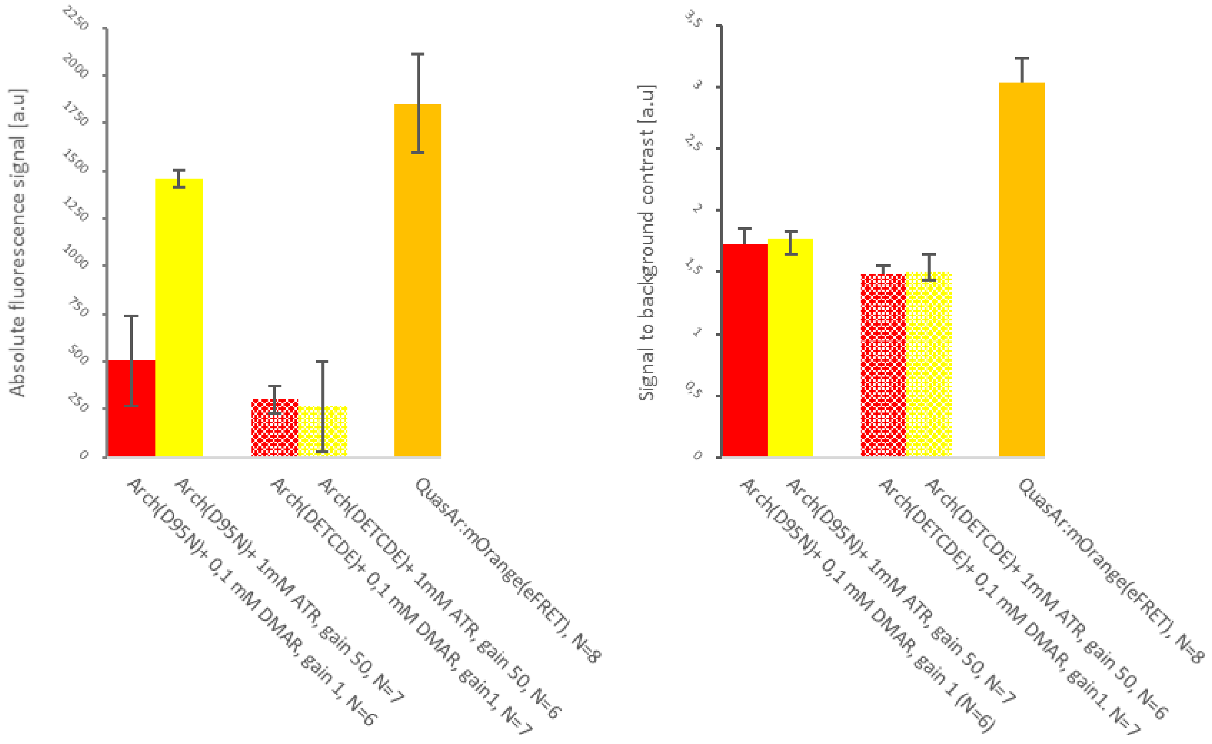

Fig. R-10: **Quantification of the absolute fluorescence in different GEVIs expressed in BWMs.** The mean gray value of the fluorescence in BWMs (left) or the ratio of the signal in BWMs to the background (right). Shown are the means± SEM in arbitrary units [a.u.]. The exposure time was 1 ms. The gain value, number of the animals, and the concentration of ATR /ATR analog are indicated below the bars.

3.3: Imaging action potentials in the pharynx of wild type *C. elegans*

Contraction of pharyngeal muscle cells, which leads to peristaltic motion in this organ, is the result of changes in the membrane potential of these cells, typically considered as Ca^{2+}-driven action potentials. Thus, the pharyngeal muscle was a suitable model to examine the potential of GEVIs for reporting on electrical activities in excitable cells in *C. elegans*.

The first question to be answered was if the sensor fluorescence would exhibit a change in response to membrane depolarization of pharynx. Thus, membrane fluorescence was recorded during spontaneous pumping. As pharyngeal activity amongst others is driven by food sensing that is mediated by the neurotransmitter serotonin, pumping was induced by external serotonin in immobilized animals (for details see methods). For the analysis of the action potentials, the fluctuations of the fluorescence signal were tracked in a region of interest (ROI) including the whole pharynx (see methods). The lumen of the grinder opens as a result of pharynx contraction, which leads to the reduction of the fluorescence signal, which made it possible to monitor also the actual contraction via defining a small ROI set to grinder.

To examine that the motions of the pharynx would not induce fluorescence changes per se, it was first analyzed a voltage insensitive fluorescent protein. For this aim an eFRET sensor was analyzed in the absence of retinal as in these animals, fluorescence changes should not differ from a non-voltage sensitive protein. This experiment confirmed that no changes in the fluorescence signal could be observed with the inactive sensor lacking the chromophore It was only possible to monitor the reduction in the fluorescence signal in the grinder region of pharynx, which shows the actual contractions. (see Fig. R-11 and video no. I).

The data, representing the events over time from each animal, were processed with a script using the KNIME software package. This script (written by Dr. W. Steuer Costa) is able to detect the electrical events on the basis of the maximal changes in the fluorescence signal as a drop from the baseline, align, and synchronize them for every animal.

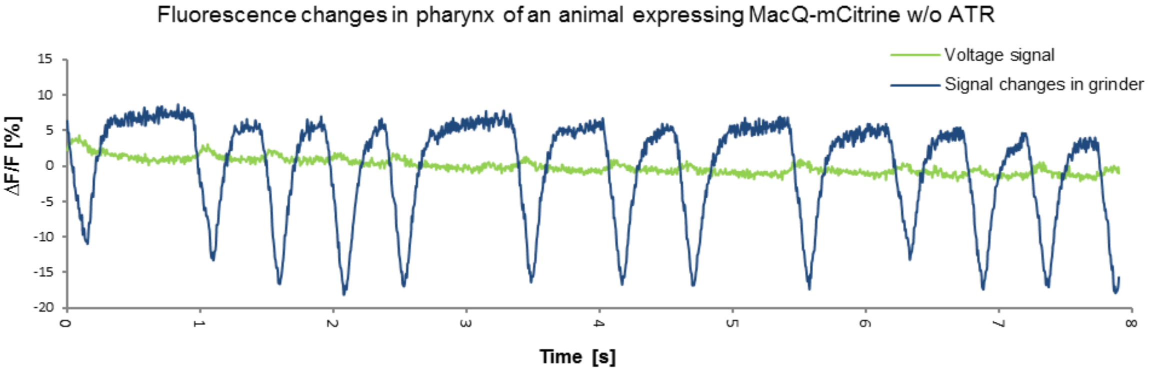

Fig. R-11: Fluorescence changes recorded with an inactive GEVI lacking ATR. Signals from an exemplary animal expressing MacQ-mCitrine to control if there are any recordable changes in the fluorescence signal and, thus, to exclude movement artifacts. Signal changes could just be observed in the small region over the grinder, due to its unclosing upon pumping. The overall fluorescence of the whole pharynx did not show any drop, which confirms that the changes recorded with an active GEVI containing ATR are voltage sensitive. Fluctuations observed from the grinder are shown in dark blue and from the whole pharynx in green.

After proving that the fluorescence changes are not caused by movement artefacts via recording the changes with an insensitive sensor, fluorescence changes were then recorded with the active eFRET GEVI supplemented with ATR. In this case, clear drops in fluorescence could be observed that correlated with each pumping event (see the upcoming results for MacQ-mCitrine and QuasAr-mOrange). In case of the direct rhodopsin imaging supplemented either with ATR or with ATR-analogue, it could be seen that there is an increase in the fluorescence signal correlated with each pumping event (see the upcoming results for Arch(D95N) or Arch(D95H)). It could be observed that there is a delay between the actual contraction signal and the voltage signal from the whole pharynx.

3.3.1: MacQ-mCitrine

Despite mosaic expression, the monitored signals in every single animal were remarkably uniform, as shown in Fig. R-12, A (data extracted from one animal; see video no. II). In the single trace, one can see that each individual event appears quite uniform, however, fluctuations of the baseline, likely due to movement of the animal or a shift of the focal plane, need to be accommodated when an average signal amplitude is deduced. Even though the aligned and synchronized events from this example confirm this homogeneity (Fig. R-12, Panel B), the mean signal could be quite different when multiple animals were compared. The mean of the drop of the fluorescence signal of mCitrine during the pharyngeal AP with a mean of ca. -23% ∆F/F varied between -20 to -27% across the group of measured animals (Fig. R-12, Panel C). The variation may be a result of different expression levels from animal to animal.

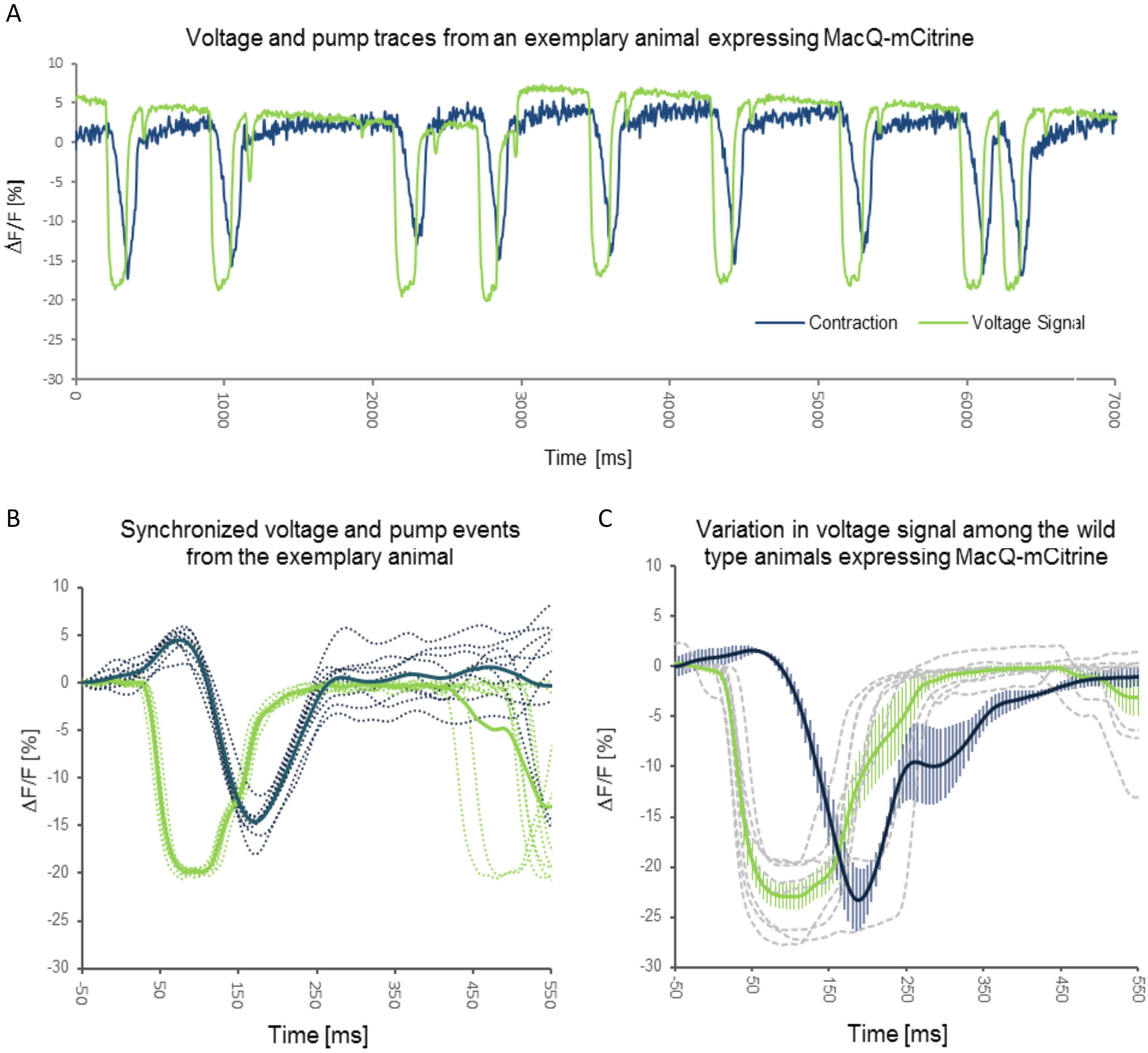

Fig. R-12: Monitoring action potentials in the pharyngeal muscles of animals expressing MacQ-mCitrine. A) Decrease of the fluorescence signal (∆F/F0%) during pumping events from an exemplary animal expressing MacQ-mCitrine. Voltage signals are shown in green and contraction signals in dark-blue (see video no. II). B) Aligned and synchronized AP and contraction signals from the animal shown in panel A. Single events are shown in dashed lines, and the solid line shows their mean. C) The variation of measured signal in a group of animals expressing MacQ-mCitrine. The gray dashed lines show the mean of APs in every single animal within the group. The green line shows the mean of the AP signals from all the animals in the group with SEM. The mean of all contraction signals from the animals in the group is shown in dark blue with SEM.

3.3.2: QuasAr-mOrange

Next, signals in animal expressing QuasAr-mOrange in the pharyngeal muscle have been monitored. Fluorescence fluctuation associated with APs have been very uniform in every single animal analyzed, as demonstrated from a representative example (Figure R-13 A, see video no. III). Thus, the mosaicism, the observed clusters and likely intracellular aggregates cannot sense a difference in the plasma membrane potential, so that all the events from each animal show a homogenous fluctuation (see panel B, Fig. R-13). However, different expression levels resulted in variation among the fluorescence changes of the sensor between animals. Although the basal fluorescence of QuasAr-mOrange was about two times stronger than MacQ-mCitrine, it seems that its voltage sensitivity was weaker: The strongest observed drop of fluorescence signal by QuasAr-mOrange was around -14.5% with a mean of -10% in a group of 10 animals (Fig. R-13, Panel C).

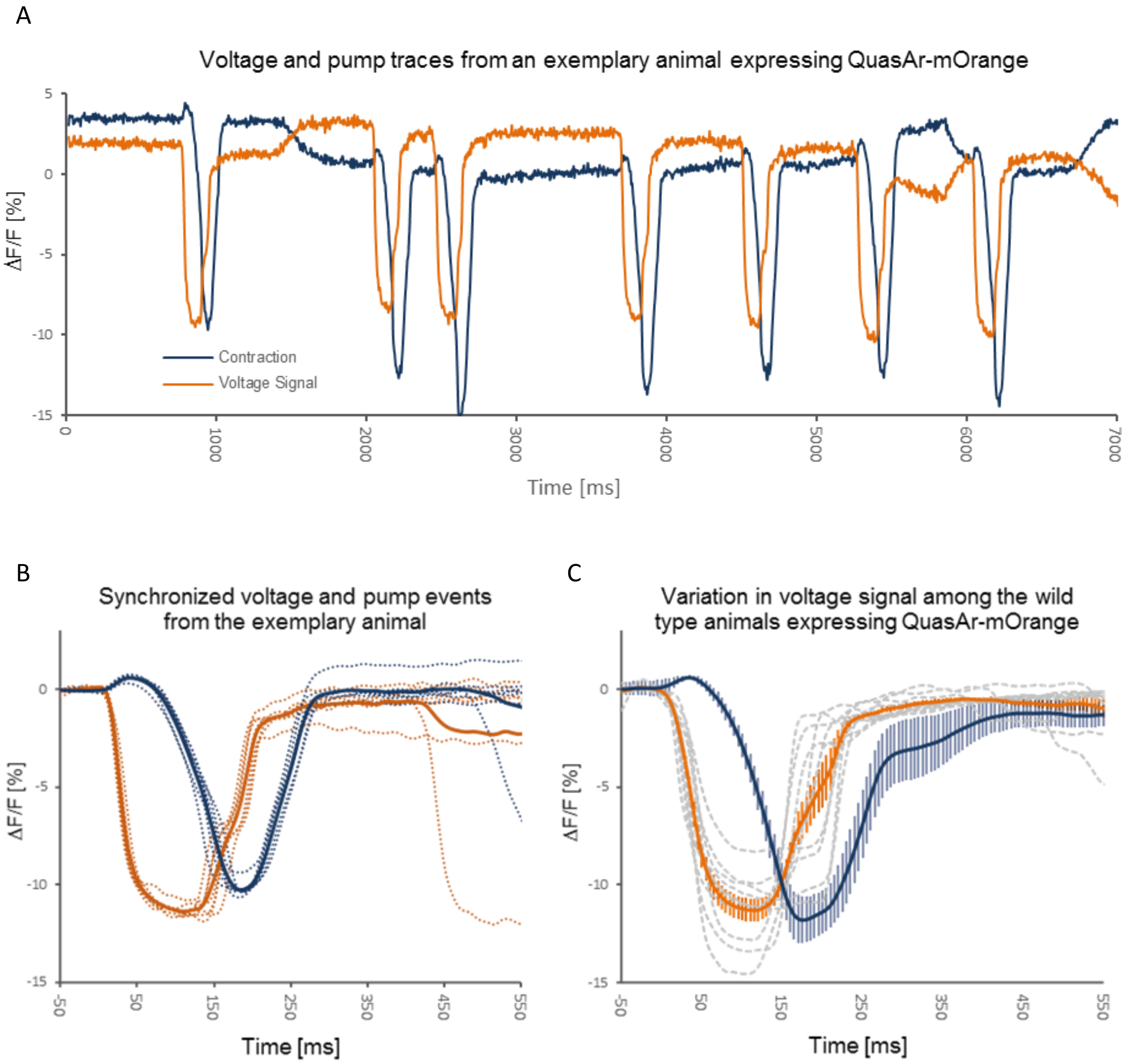

Fig. R-13: Monitoring action potentials in the pharyngeal muscles of animals expressing QuasAr-mOrange. A) Decreasing of the fluorescence signal (ΔF/F%) during pumping events from an exemplary animal expressing QuasAr-mOrange. Voltage signals are shown in dark orange and contraction signals in dark blue B) aligned and synchronized AP and contraction signals from the animal shown in panel A, dashed lines show the single events and the line shows their mean, whereas APs are still in dark orange and contractions in dark blue. C) The variation of measured signal in a group of animals expressing QuasAr-mOrange. The gray dashed lines show the mean of APs in every single animal within the group. The orange line shows the mean of the AP signals from all the animals in the group with SEM. The mean of all contraction signals from the animals in the group is shown in dark blue with SEM.

3.3.3: Arch(D95N)

Arch(D95N) was examined for its potential for monitoring voltage signals as a rhodopsin-direct-imaging GEVI, which means that unlike eFRET sensors, it was expected that the fluorescence signal increases during membrane depolarization. As described before, both ATR and the ATR-analog DMAR were used as chromophores of the GEVIs. Although the basal fluorescence of DMAR was robust and exhibited excellent contrast (see Fig. R-9), monitoring action potentials was possible only with excitation by the laser, however at lower intensities (ca. 160 mW/mm^2) than the very high reported intensities at ca. 800 mW/ mm^2 (Kralj *et al.*, 2011). Like the eFRET-GEVIs, Arch(D95N)+DMAR also showed uniform signals in single animals (Fig. R-14, panel A and see video no.IV), whereas the variation of the measured signals across 15 animals was between 10 to 40% F/F0 with a mean of ca. 23%, when equipped with DMAR (Fig. R-14, C). For easier comparison with eFRET-GEVIs, all the signals observed with Arch(D95N) and the other direct-imaging tools are shown inverted in form of drop in the fluorescence signal.

In addition to DMAR, ATR was tested for its ability to monitor action potentials in combination with Arch(D95N) as well. The basal fluorescence of ATR in Arch(D95N) was very weak, and its contrast was very low so that monitoring the pump events was not possible. Moreover, voltage signals from the whole pharynx dominated over pump signals measured from the small region of the grinder. The voltage signals measured with ATR were very homogenous in single animals (Fig. 15, panel A, see video no. V). The signal amplitude across different animals varied bewtween 95-170% rise in the fluorescence signal with a mean of ca. 130%, as shown in figure R-15, panel C (illustrated inverted as a drop).

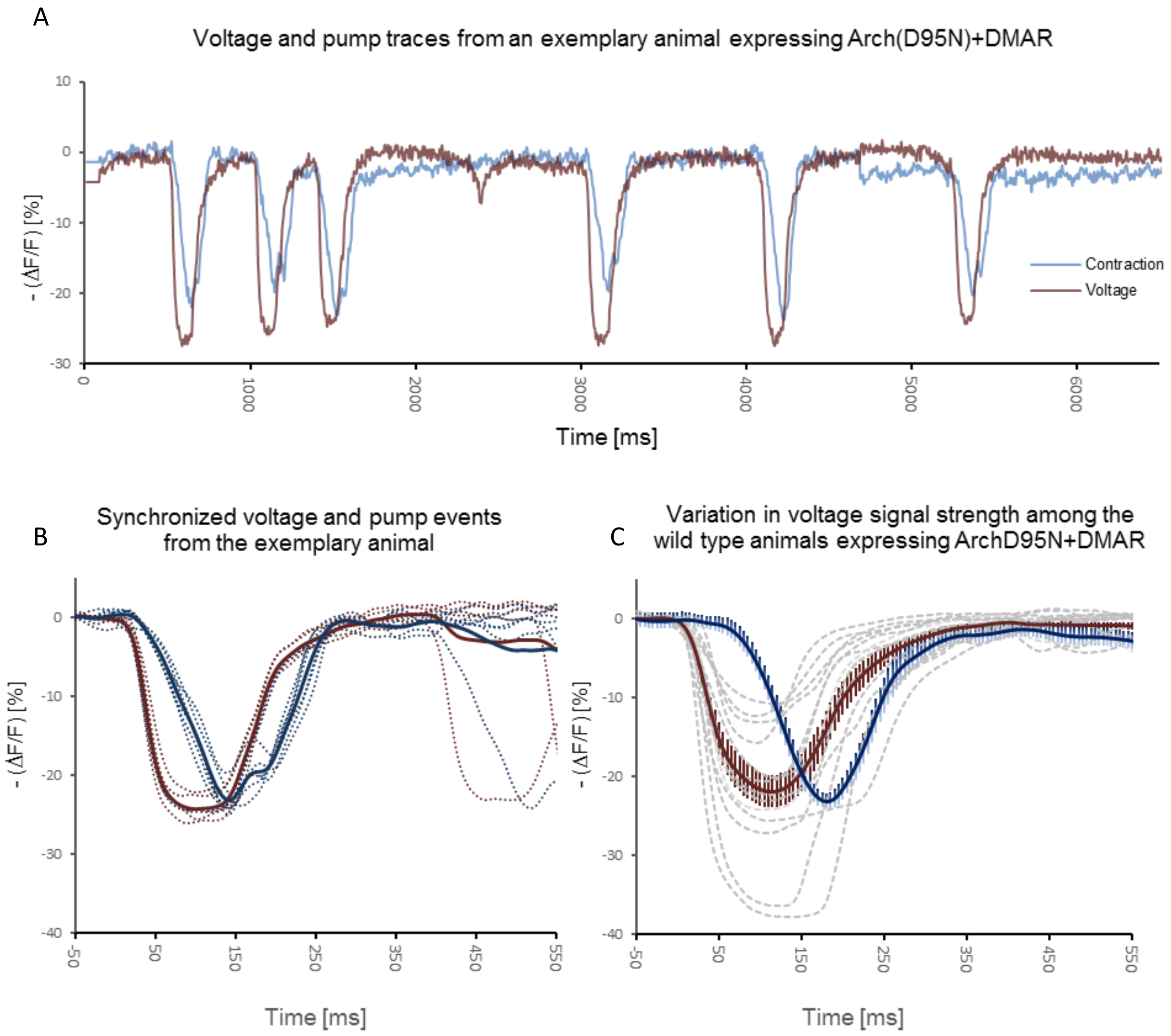

Fig. R-14: Monitoring action potentials in pharyngeal muscles of animals expressing Arch(D95N)+DMAR. A) Changes in the fluorescence signal during pumping events from an exemplary animal expressing Arch(D95N)+DMAR. Voltage signals are shown in the dark red, and contraction signals in dark blue (Voltage signals are shown in an inverted fasgion for an easier comparison with eFRETs). B) Aligned and synchronized AP and contraction signals from the animal shown in A. Dashed lines show the single events and the line shows the mean, whereas APs are still in dark red and contractions in dark blue C) The variation of measured signal in a group of 15 animals expressing Arch(D95N)+DMAR. The gray dashed lines show the mean of APs in every single animal within the group. The dark red line shows the mean of the AP signals from all the animals in the group with SEM. The mean of all contraction signals from the animals in the group is shown in dark blue with SEM.

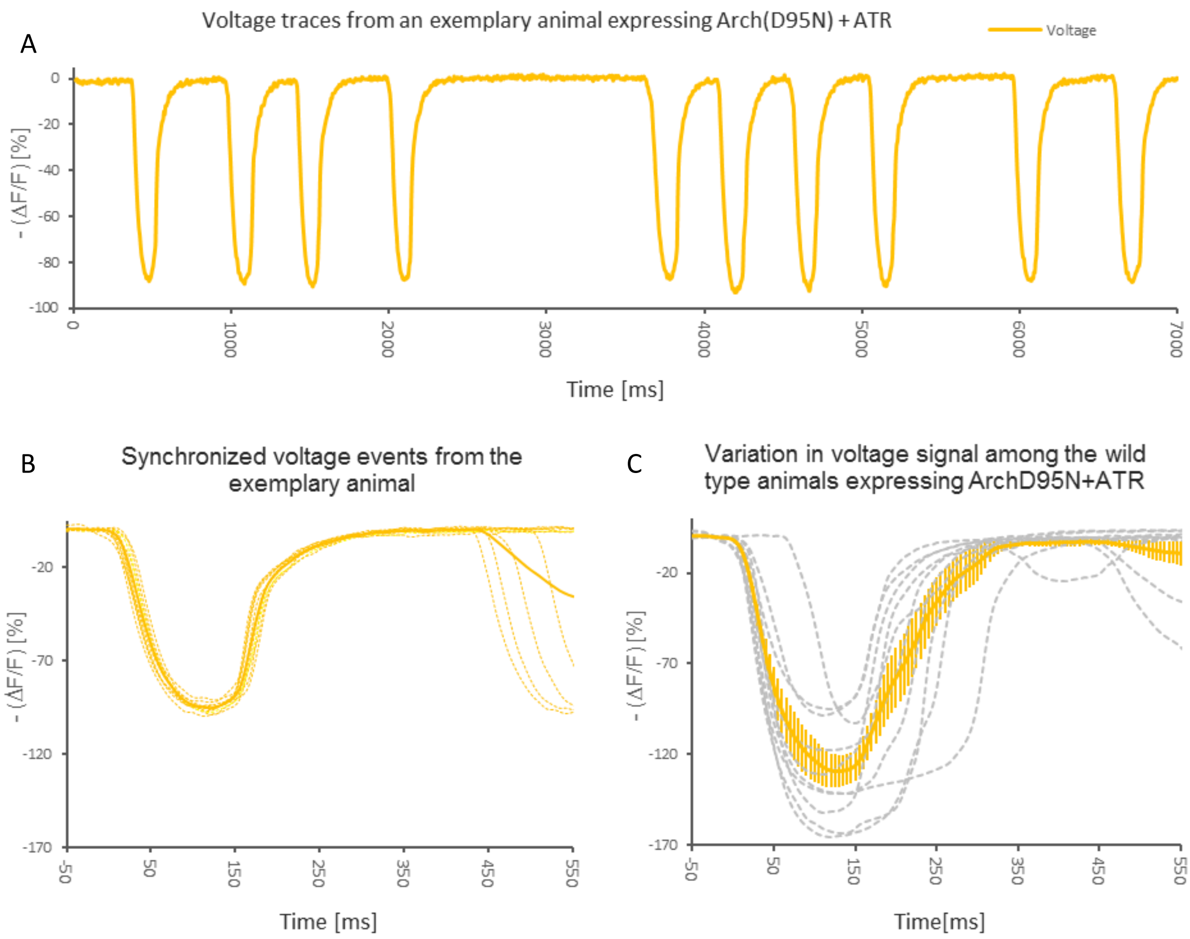

Fig. R-15: Tracking action potentials in pharyngeal muscles of animals expressing Arch(D95N) + ATR. A) Changes of the fluorescence signal (ΔF/F0%) during pumping events from an exemplary animal expressing Arch(D95N) supplemented with ATR. Voltage signals are shown in orange. They are shown in an inverted fashion for easier comparison with the data obtained from eFRET sensors. B) aligned and synchronized AP signals from the animal shown in panel A. Dashed lines show the single events, and the line shows their mean. C) The variation of the measured signal in a group of 11 animals expressing Arch(D95N) equipped with ATR. The gray dashed lines show the mean of APs in every single animal within the group. The orange line shows the mean of the AP signals from all the animals in the group with SEM.

3.3.4: Arch(D95H)

Arch(D95H), another Archaerhodopsin non-pumping variant, was tested for its ability to track action potentials. This sensor was supplemented with both ATR and DMAR. The basal signal of ATR was feeble also in this sensor, and in the same range as for Arch(D95N). The basal fluorescence of Arch(D95H)+DMAR was ca. 2-2,5 fold stronger than Arch(D95N)+DMAR (Fig. R-9). However, this sensor/chromophore combination showed a drop in fluorescence signal (ca. -8%) during membrane depolarization. There was an increase of ca. 71% (mean) in the fluorescence signal during pumping events if the sensor was equipped with ATR, which is also quite similar for all single animals. The homogeneity in signal changes could be observed in every single animal (Fig. 16, panel A and video no VI) and among all the tested animals in the group (Fig. R-16 , panel C).

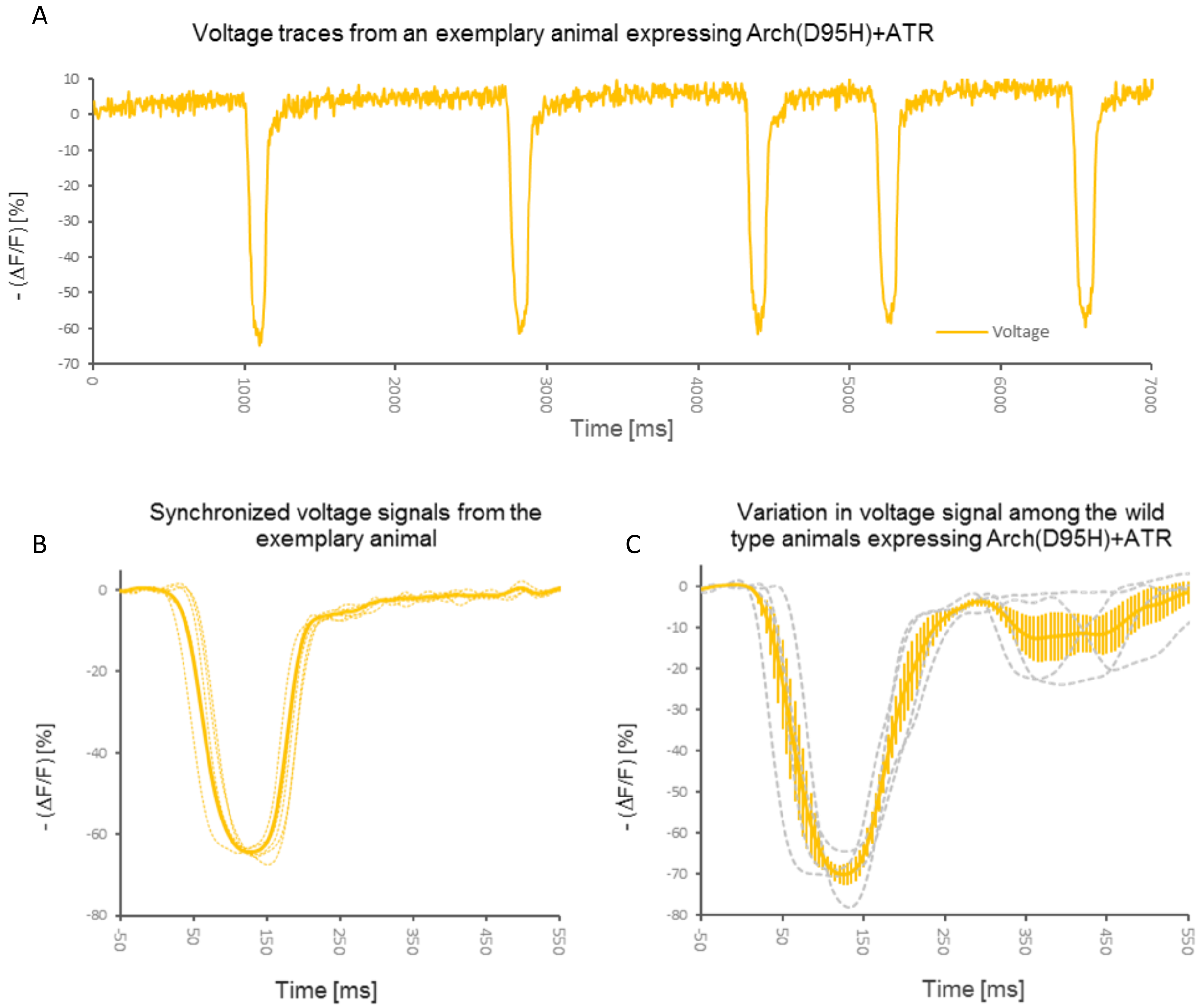

Fig. R-16: **Monitoring action potentials in pharyngeal muscles of animals expressing Arch(D95H) + ATR.** A) Changes of the fluorescence signal (ΔF/F%) during pumping events from an exemplary animal expressing Arch(D95H) supplemented with ATR. Voltage signals are shown in orange. Voltage signals are inverted and shown as drops for easier comparison with eFRETs. B) aligned and synchronized AP signals from the animal shown in panel A. Dashed lines show the single events, and the line shows their mean. C) The variation of the measured signal in a group of 4 animals expressing Arch(D95H) equipped with ATR. The gray dashed line show the mean of APs in every single animal within the group. The orange line shows the mean of the AP signals from all the animals in the group with SEM.

As mentioned briefly, Arch(D95H) showed a drop of ca. 8% in the fluorescence signal during pharyngeal action potentials, if it was supplemented with DMAR. The duration of voltage signals was around 500 ms, which seems to be prolonged in comparison to all other sensors, whereas pump duration (ca. 300 ms) was as measured by the other sensors (Fig. R-17). All these observations might be due to a decelerated photocycle of Arch(D95H) in combination with DMAR. During this project, this sensor could be introduced briefly for the application in *C. elegans*, and it has to be studied more in detail in the future.

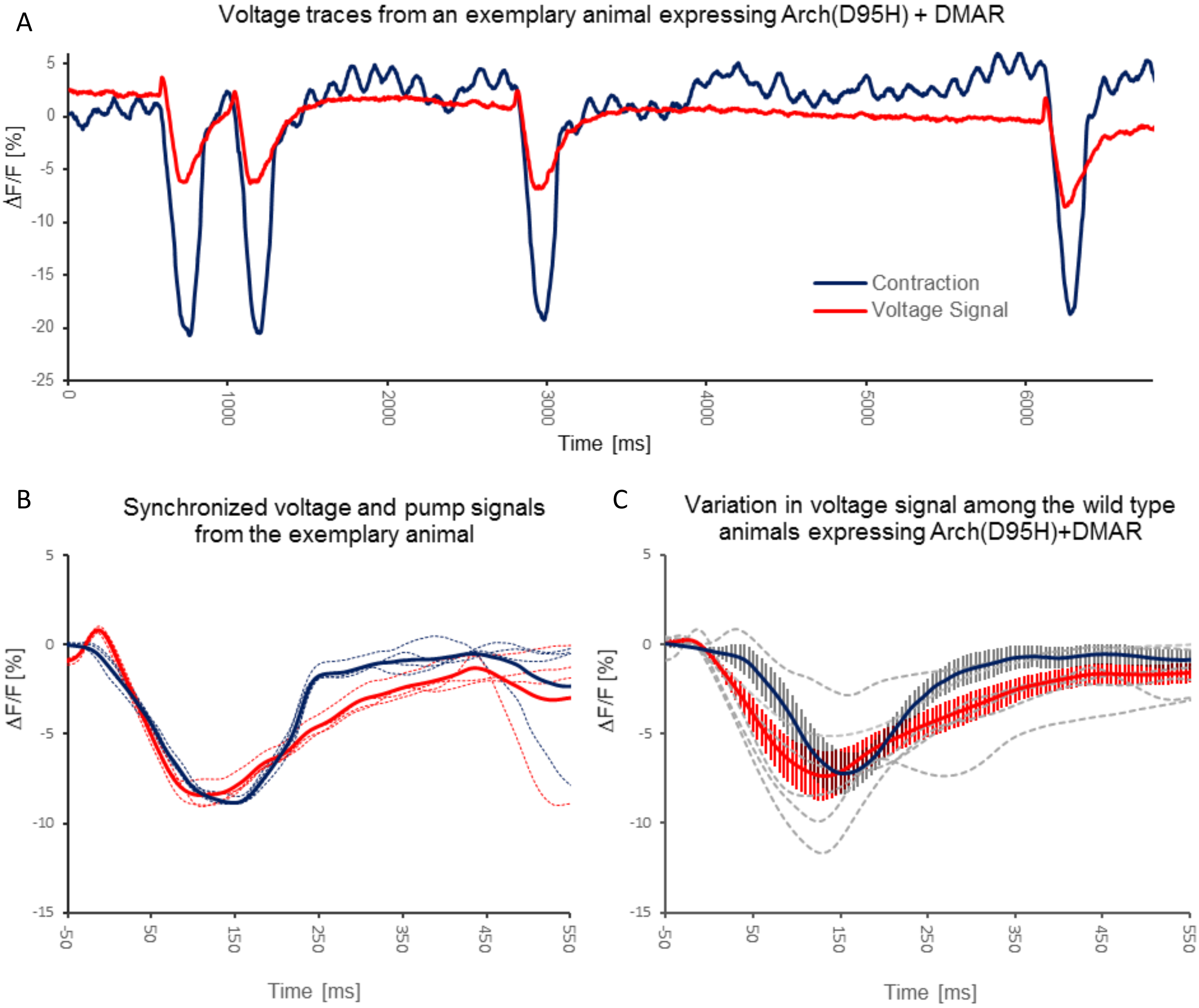

Fig. R-17: Monitoring action potentials in the pharyngeal muscles of animals expressing Arch(D95H)+DMAR. A) Changes of the fluorescence signal (ΔF/F%) during pumping events from an exemplary animal expressing Arch(D95H) supplemented with DMAR. Voltage signals are shown in red and pump signals in dark blue B) aligned and synchronized AP signals from the animal shown in panel A. Dashed lines show the single events, and the line shows their mean. C) The variation of the measured signal in a group of 6 animals expressing Arch(D95H) equipped with DMAR. The gray dashed lines show the mean of APs in every single animal within the group. The red line shows the mean of the AP signals from all the animals in the group with SEM, and the dark blue line shows the mean of all contraction signals in the group with SEM.

3.4: Overall comparison of the sensitivity of the GEVIs expressed in the pharynx

Besides the quantification of the basal fluorescence signal of GEVIs during resting potential, and automated deduction of signal properties, the signal-to-noise ratio of APs was also calculated manually. In this analysis, noise is defined as the deviation in signal fluctuations in the baseline of the curve, which demonstrates the pharyngeal activity of each tested animal, and the peak amplitude during action potentials corresponds to the signal (see Fig. R-18, A). SNR is then the ratio of this amplitude to the deviation of signal fluctuations in the baseline. The highest values for the amplitude were observed for Arch(D95N), and Arch(D95H) supplemented with ATR. However, they also had the worst noise values among all the other GEVIs, specifically 6-10-fold more than the noise if they were supplemented with DMAR or in eFRET sensors.

All in all, it seems that MacQ-mCitrine, with an SNR value of ca. 88 is the most sensitive voltage indicator among all tested GEVIs (see Fig. R-18).

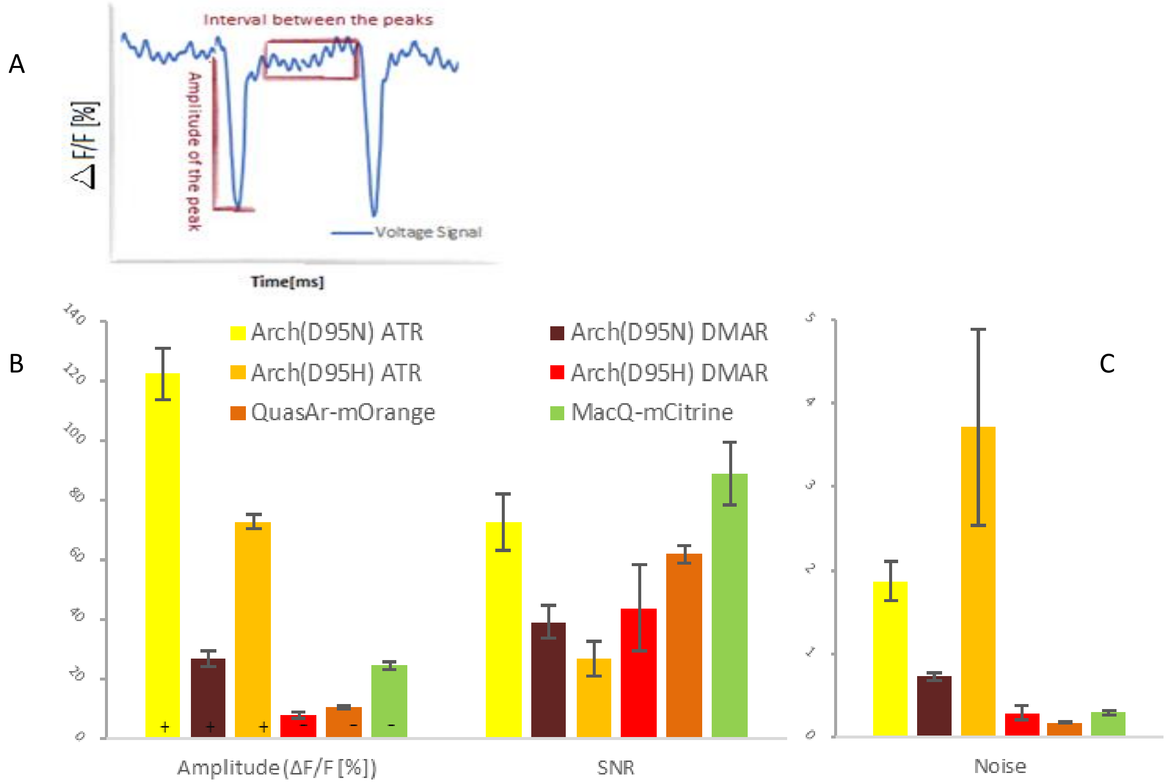

Fig. R-18: **Signal to noise ratio (SNR) of different GEVIs.** A) Schematic presentation how noise and signal are defined. The signal is defined as the amplitude of the AP-Peak, and noise is the fluorescence fluctuation around the base line (i.e., between AP peaks). B) From left to right: Amplitude and SNR of all the tested GEVIs. +/- indicate an increase or a decrease in the signal amplitude during APs. C) Graphical demonstration of the noise among all GEVIs.

3.5: Evaluation of GEVIs via imaging action potentials in the pharynx of *egl-19* mutants of *C. elegans*

To evaluate the GEVIs for their ability to monitor alterations in electrical events, they have been tested in two different *egl-19* mutants. As described (see 1.5.2) , EGL-19 is an L-type voltage-gated Ca^{2+}-channel, which is expressed in pharynx and body wall muscles. *egl-19(n2368)* is a gain of function mutant that shows a delayed relaxation of the terminal bulb. This delay seems to be a result of prolonged muscle excitation in this segment. They reveled prolonged contraction in several muscles and exhibited a dumpy phenotype (short, likely contracted body), (Schüler *et al.*, 2015).

Action potentials could be monitored in both mutants with eFRET GEVIs MacQ-mCitrine and QuasAr-mOrange. In *egl-19(n2368)* APs could be monitored additionally with Arch(D95N) supplemented either with ATR or ATR-analogue (DMAR). For the experimental procedure transgenic animals expressing the sensor in pharynx were crossbred with *egl-19(n2368) and egl-19(n583ad952)* mutants to compare the monitored action potentials in wt vs. mutants.

The alteration in duration and amplitude of the fluorescence signal could be observed for both mutants with MacQ-mCitrine, which dropped to ca. -12% ∆F/F for *egl-19(n2368)* and -20% ∆F/F for *egl-19(n582ad952).* Furthermore, the prolonged pumping could also be monitored with the application of MacQ-mCitirne as a GEVI (Fig. R-19).

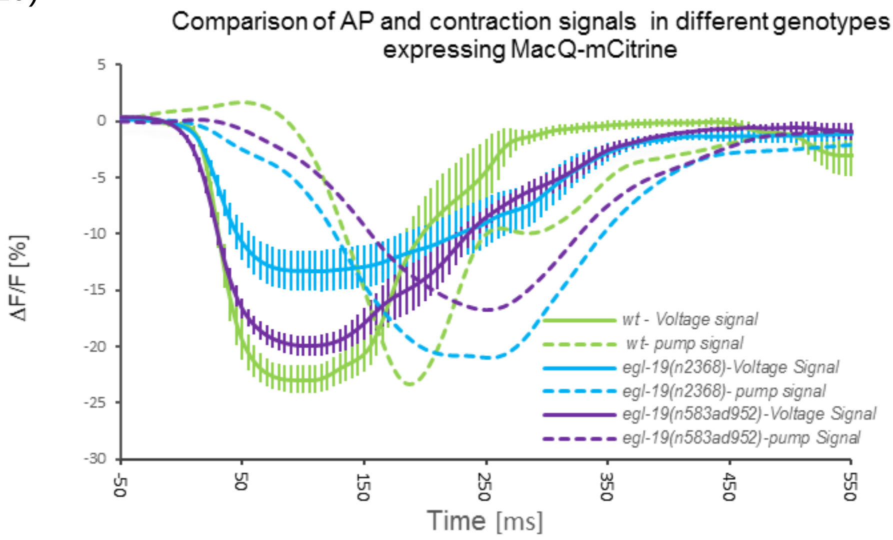

Fig. R-19: Monitoring action potentials in the pharyngeal muscles of animals expressing MacQ-mCitrine in different genotypes. Comparison of the mean of AP (lines) and contraction signals (dashed lines) monitored with MacQ-mCitrine in a group of animals in wild type demonstrated in green and *egl-19(n2368)* in blue and *egl-19(n583ad952)* inpurple with SEM.

QuasAr-mOrange was tested in both *egl-19* mutants as well and seems to be qualified for monitoring the alteration in duration and amplitude of the fluorescence signal, although with a smaller sensitivity than that of MacQ-mCitrine. Besides, the prolonged pumping event in mutants could be monitored by QuasAr-mOrange, just as for MacQ-mCitrine. There was ca. 5% reduction in the mean value of voltage amplitude of both mutants (-7% ΔF/F for both mutants vs. ca. -12% ΔF/F for wild type, Fig. R-20)

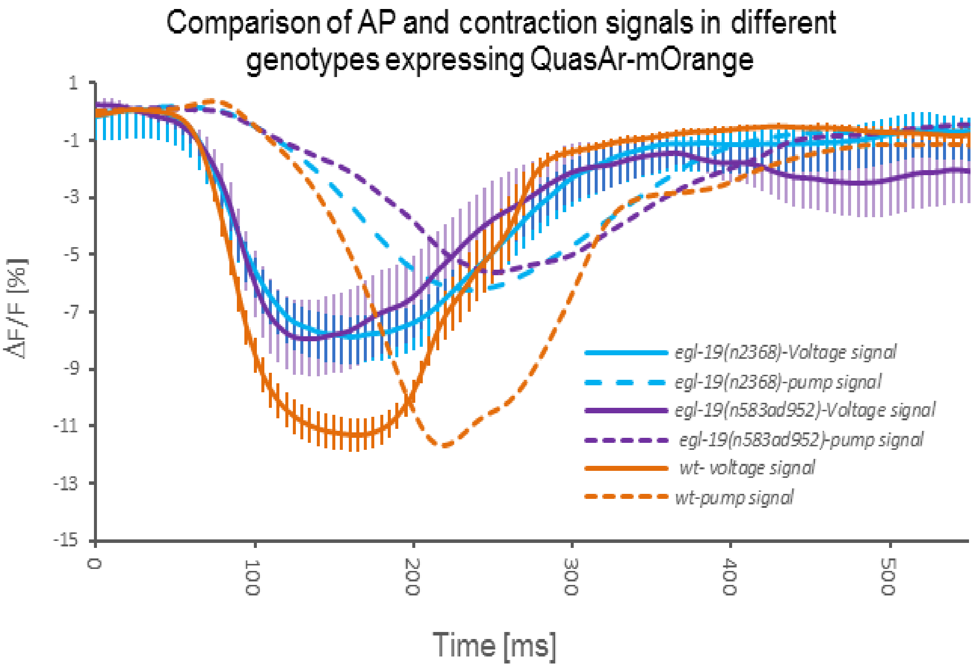

Fig. R-20: Monitoring action potentials in the pharyngeal muscles of animals expressing QuasAr-mOrange in different genotypes. Comparison of the mean of AP (lines) and contraction signals (dashed lines) tracked with QuasAr-mOrange in a group of animals in wild type, *egl-19(n2368)* and *egl-19(n583ad952)* (line and dashed lines).

During voltage imaging with Arch(D95N) supplemented with DMAR, the voltage amplitude was reduced significantly from 23% to ca. 13% ΔF/F in *egl-19(n2368)* mutants (Fig. R-21, A). Reduction in voltage amplitude (from 130% to 70% ΔF/F) and a prolonged voltage duration in egl-*19(n2368)* mutants could be monitored with Arch(D95N) supplemented with ATR as well (Fig. R-21, B).

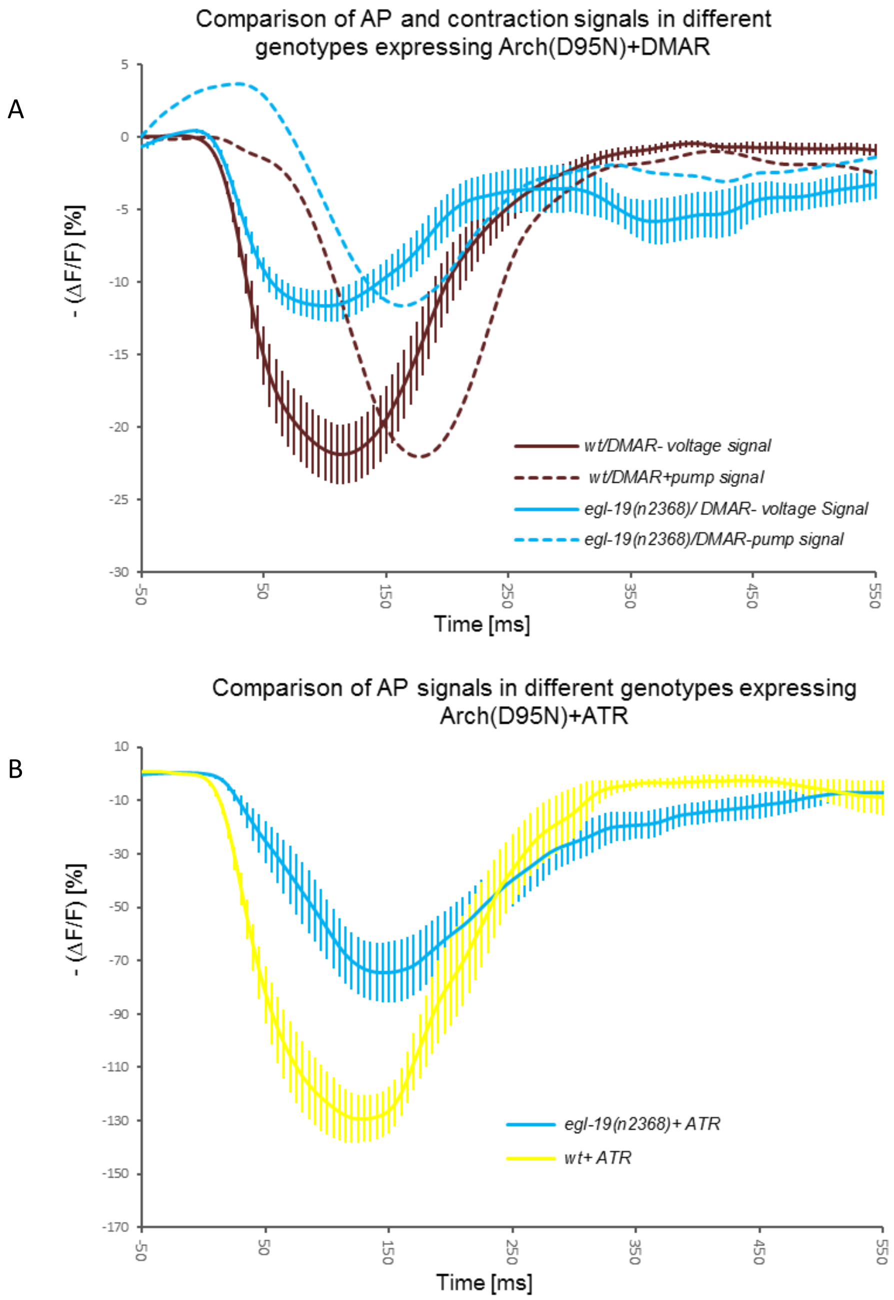

Fig. R-21: Monitoring action potentials in pharyngeal muscles of animals expressing Arch(D95N) in different genotypes. A) Comparison of the mean of AP (lines) and contraction signals (dashed lines) monitored with Arch(D95N) with DMAR in a group of animals in wild type demonstrated in dark red and *egl-19(n2368)* background demonstrated in blue with SEM. B) Comparison of the mean of AP signals tracked with Arch(D95N) with ATR in a group of animals in wild type (yellow lines) and *egl-19(n2368)* (blue lines) background with SEM.

3.6: Quantification of action potentials in pharyngeal muscles monitored with different GEVIs in wild type and *egl-19* mutants

As described in 3.3, a script was written in KNIME software to systematically analyze the fluorescence traces. In addition to the ability of detection the electrical events on the basis of the maximal changes in the fluorescence signal as a drop from the baseline, aligning, and synchronizing them for every single animal (shown in panel B of figures R-12 to R-17) and averaging the signals in a group of animals (shown in panel C of figures R-12 to R-17, and R-19 to R-21), it could also analyze the properties of every detected signal such as its duration (defined as fullwidth- or a fullwidth half maximum of signal rise or drop to the baseline), amplitude, area under the peak, rise and drop as τ_{on} and τ_{off}, have been extracted with the software. These properties were collected for both depolarization and contraction signals from wild type and *egl-19* mutants to characterize and evaluate every sensor.

3.6.1: Quantified properties of monitored signals with MacQ-mCitrine

It could be shown that the amplitude of voltage signals with -3.6% ∆F/F in *egl-19(n2368)* was significantly weaker than the wild type (- 23.5% ∆F/F), whereas *egl-19(n583ad952)* with just -20.9% ∆F/F has shown less defect in this regard (Fig. R-22, A). However, the area under the peak was more significantly bigger in this mutant (4.3) than the wild type (3.7) (Fig. R-22, B). The duration of both voltage and contraction signal was also significantly longer in both *egl-19* mutants in comparison to wild type animals (Voltage duration [ms]: wt/238, *egl-19(n2368)*/409, *egl-19*(n583ad957)/366, pump duration [ms]: wt/238, *egl-19(n2368)*/384, *egl-19*(n583ad957)/376) . There was a delay of around 100 to 130 ms between the first drop of fluorescence signal defined as voltage signal and the contraction signal from the grinder region, which was in a same range for wild type and mutants. Voltage and pump rise and decay were slower in *egl-19(n2368)* and *egl-19(n582ad952)* than wild type (Fig. 22,F).

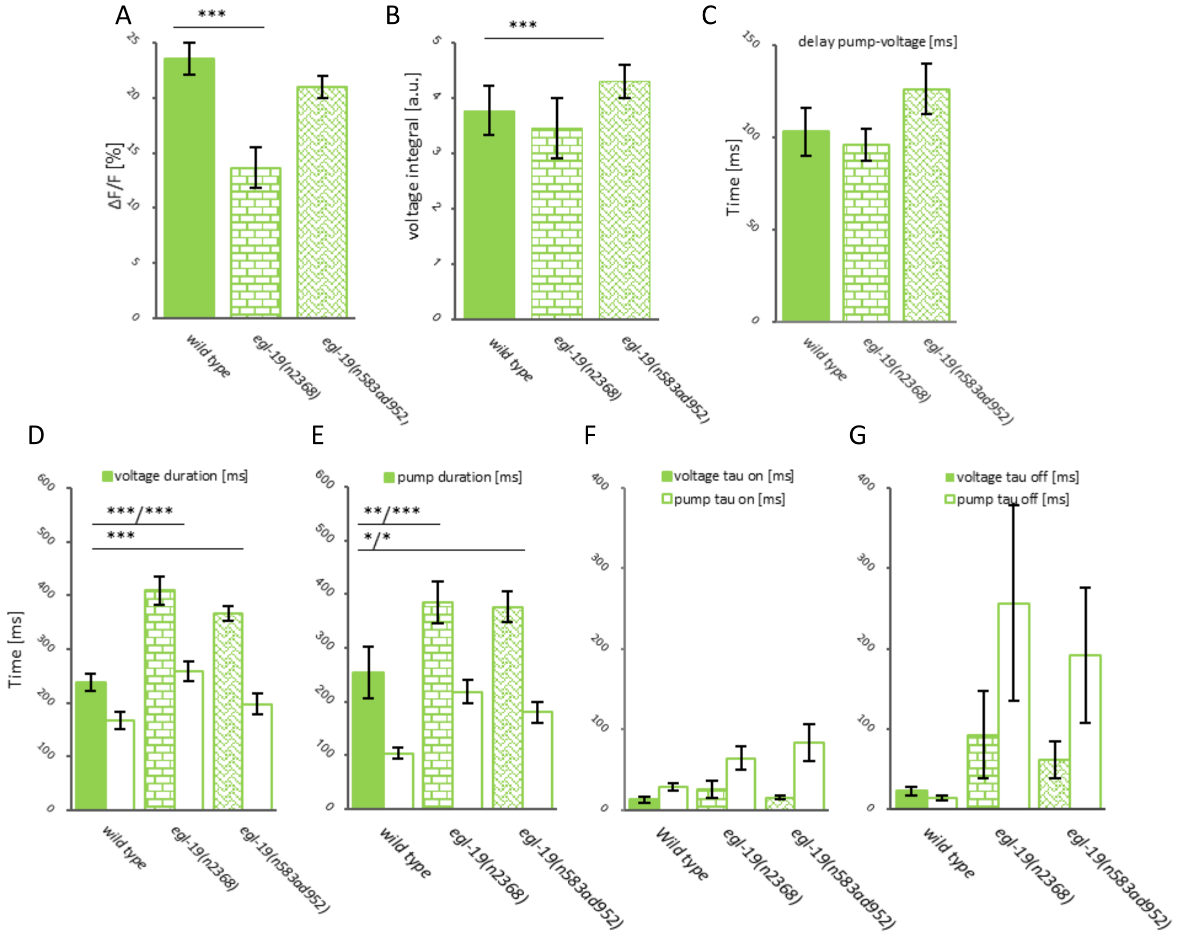

Fig. R-22: The properties of measured signals in animals expressing MacQ-mCitrine in different genotypes via the automated script. A) The amplitude of the drop in the fluorescent signal with SEM. B) The area under the peak as an indicator of the changes in the fluorescence signal with SEM. C) Delay time between the rise of APs and contraction signals without any significant difference. D, E) Duration of voltage and pump signal with SEM. F, G) The time of rising and decay of voltage and contraction signal with SEM. N= 8,11,9 for A-D, which was reduced to >5 for E-F, since the automatization could not deduce these data out of all the animals. Statistically significant differences were analyzed by ANOVA, Bonferroni correction. Reported are p-values: *≤0.05 **≤0.01 ***≤0.001.

3.6.2: Quantified properties of monitored signals with QuasAr-mOrange

The *egl-19(n2368)* mutant showed a significantly weaker amplitude of voltage signals than the wild type, whereas the *egl-19(n583ad952)* strain showed a smlaller defect in this parameter. The area under the peak does not show any differences in both mutants compared to the wild type. The duration of both voltage and contraction signal was also significantly longer in both *egl-19* mutants in comparison to wild type animals. There was a delay of around 100 ms between the first drop of fluorescence signal defined as voltage signal and the contraction signal from the grinder region, which was not significantly different for wild type and mutants. There is a tendency for prolonged voltage and pump rise and decay in *egl-19(n2368)* and *egl-19(n582ad952)* (Fig. R-23).

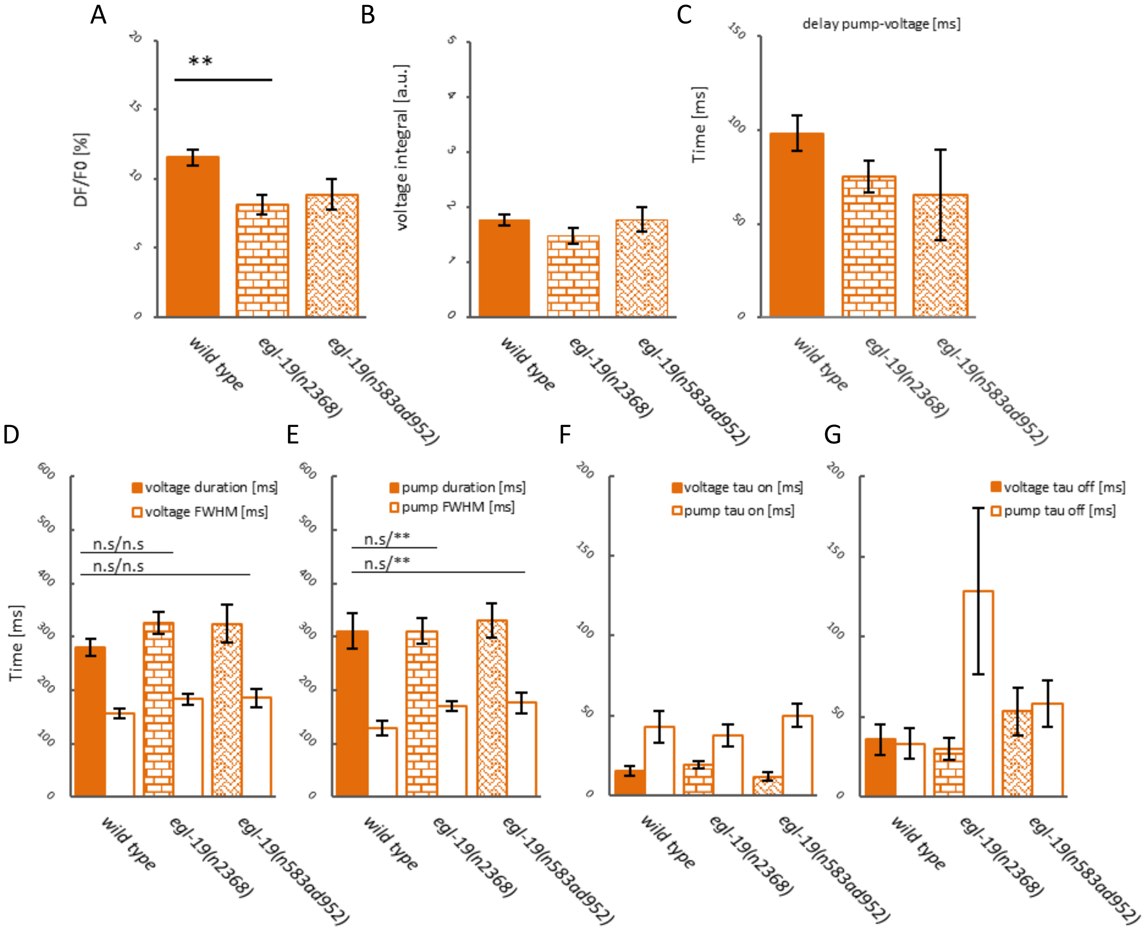

Fig. R-23: Properties of measured signals in animals expressing QuasAr-mOrange in different genotypes. A) Amplitude of the drop in the fluorescent signal with SEM. B) The area under the peak as an indicator of the changes in the fluorescence signal with SEM. C) Delay time between the rise of APs and contraction signals without any significant difference. D, E) Duration of voltage and pump signal with SEM. F, G) The time of rising and decay of voltage and contraction signals with SEM. N= 10,11,10 for A-D, which was reduced to 4-5 for E-F, since the automatization could not deduce these data from all of the animals

3.6.3: Quantified properties of monitored signals with Arch(D95N)

Like with both eFRET sensors, egl-*19(n2368)* mutant has shown a significantly weaker amplitude of voltage signal (80.7% ∆F/F) compared to the wild type with Arch(D95N)+ATR (130% ∆F/F). The area under the peak from this mutant does not show a significant difference in comparison to the wild type. There has been a tendency for prolonged voltage and contraction signals in *egl-19(n2368)* mutant in comparison to wild type animals.

There was a delay of around 80 ms between the voltage signal and the contraction signal from the grinder region, which was not significantly different from wild type to *egl-19* mutant (Fig. R-24).There is a tendency As described in 3.3.3, detected voltage signals with this sensor dominated over pump signals, so that it was not possible to detect pump signals with this sensor and read out their properties respectively.

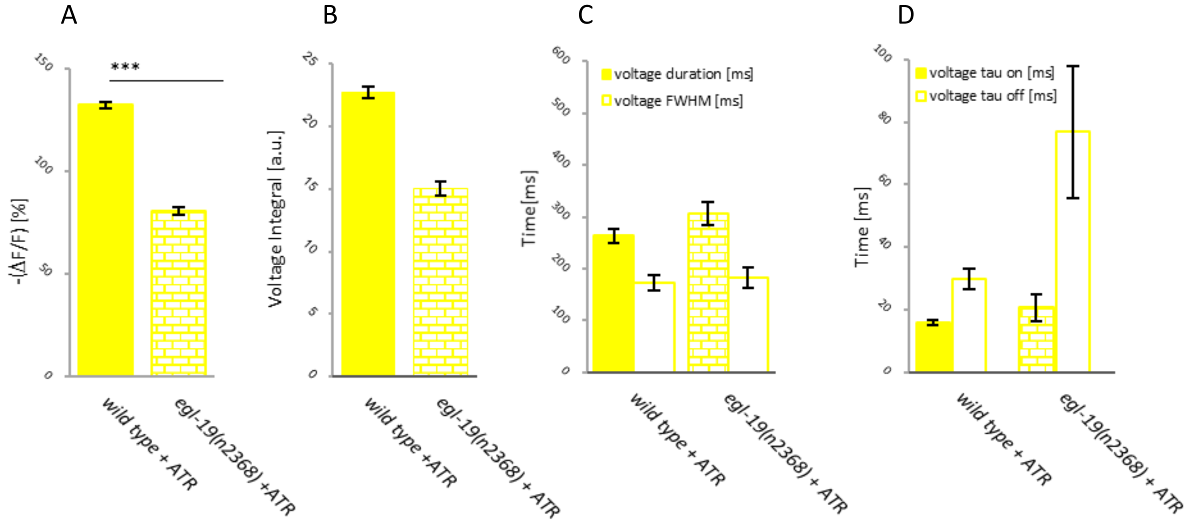

Fig. R-24: Characterisation of measured signals in animals expressing Arch(D95N) supplemented with ATR in different genotypes. A) Amplitude of the voltage signal B) area under the peak C) duration of voltage signal as fullwidth maximum and fullwidth half maximum D) voltage signal rise and decay time in wild type and *egl-19(n2368)* mutants. N= 10 for wild type and 12 for *egl-19(n2368).*

The properties of voltage and pump signals measured by Arch(D95N)+DMAR are shown in figure R-25. The *egl-19(n2368)* mutant showed a significantly weaker voltage amplitude (12.3% ΔF/F) than the wild type (22.6% ΔF/F) also with voltage indicator. The area under the peak from this mutant does not show a significant difference in comparison to the wild type. Voltage and contraction signals show a tendency for prolonged duration in the *egl-19(n2368)* mutant (Voltage signal: 283 [ms] in wt vs. 353 [ms] in mutant, Pump signal: 255 [ms] in wt vs. 282 [ms] in mutnat). There was a delay of around 80 ms between the voltage signal and the contraction, which was not significantly different between wild type and *egl-19* mutant. This value is in the same range meausred with both described eFRET sensors.

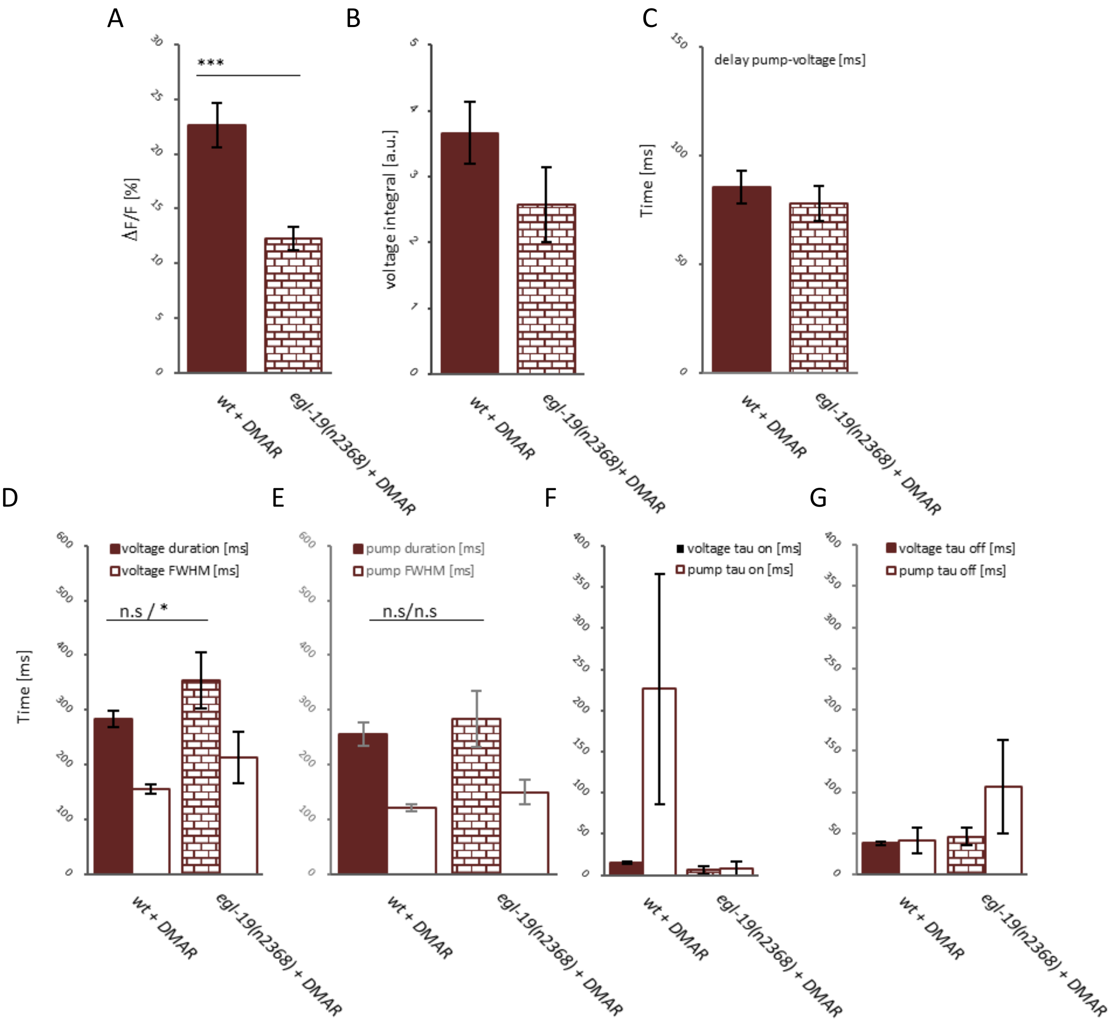

Fig. R-25: Characterisation of measured signals in animals expressing Arch(D95N) supplemented with DMAR in different genotypes. A) The amplitude of the drop in the fluorescent signal with SEM. B) The area under the peak as an indicator of the changes in the fluorescence signal with SEM. C) Delay time between the rise of APs and contraction signals without any significant difference. D, E) Duration of voltage and pump signal with SEM. F, G) The time of rising and decay of voltage and contraction signal with SEM. N= 15 for wild type and 8 for *egl-19(n2368).*

3.6.4: Quantified properties of monitored signals with Arch(D95H)

The properties of measured voltage and contraction signals with Arch(D95H) have been also quantified with the automated script.

Supplemented with ATR, the voltage amplitude was 71.2% ΔF/F. AP duration was around 225 ms, which is comparable with the time measured with other sensors (Fig. R-26). Since the basal signal of ATR in Arch(D95H) was shallow (like in Arch(D95N)+ATR), it was not possible to detect and read out the properties of pump signals.

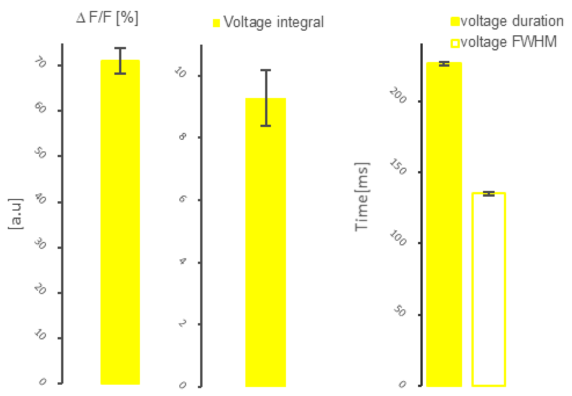

Fig. R-26: Quantified properties of measured AP signals with Arch(D95H) supplemented with ATR. From left to right: Amplitude, area under the peak and voltage duration with SEM (N=4).

Supplemented with DMAR, Arch(D95H) has shown a prolonged duration of voltage signal (500 [ms]) in comparison to all other sensors (250-300 [ms]), whereas pump duration (ca. 30 [ms]) was as measured by the other sensors. The delay between a voltage rise and the following pump signal is around 30 ms, which is shorter than the time measured with other GEVIs. All these observations might be due to a decelerated photocycle of Arch(D95H) in combination with DMAR. During this project, this sensor could be introduced briefly for the application in *C. elegans*, and it has to be studied more in detail in the future

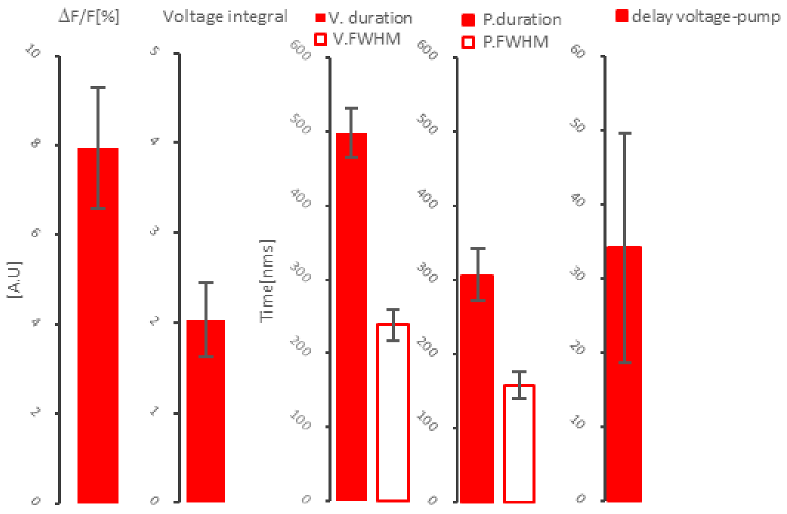

Fig. R-27: Quantified properties of measured AP and contraction signals with Arch(D95H) supplemented with DMAR. From left to right: Amplitude, area under the peak and voltage and pump duration and the delay between voltage and pump signal with SEM (N=6).

3.7: Drug application

The voltage and contraction signals observed in both *egl-19* mutants were altered, primarily in amplitude, in comparison to wild type animals.

It was shown in a previous project in the lab that Nemadipine-A (Nema-A) could relieve malfunction of pumping in some *egl-19* mutants in an allele-specific manner (Schüler *et al.*, 2015).

Nema-A is an analog to a group of anti-hypertension pharmaceuticals named 1,4-dihydropyridines. Therefore, the electrical activity of animals expressing GEVIs in both wild type and *egl-19* mutants was monitored under Nema-A and 0.2% DMSO (Nema-A solvent) application to control if Nema-A also affects the voltage signal.

As expected, all the sensors in wild type showed a reduction in their voltage signal after Nema-A application in comparison to the DMSO-control and to non-treated animals.

In general, DMSO affected the voltage signal, especially in both mutants, though at different levels. However, both *egl-19* mutants, which were treated with Nema-A, showed a rescue effect. This rescue was visible as an increase in the amplitude of the voltage signal, which was significantly reduced in the mutants. After drug application the voltage amplitude has shown a voltage amplitude approximately at the same level as DMSO-, and non-treated wild type animals.

The monitored signals by each sensor during drug application are shown in detail in this section.

3.7.1: MacQ-mCitrine

In wild type animals expressing MacQ-mCitrine, DMSO application caused a slight and non-significant prolonged pump-event. Nema-A decreased the voltage signal significantly compared to the DMSO control. DMSO affected voltage signals in both mutants, however, in a different manner: It increased the voltage signal in *egl-19(n2368)* and decreased it in *egl-19(n583ad952*). Yet, the properties of voltage signals of both mutants after Nema-A application were in a similar range of wild type-DMSO control. Furthermore, the rescue effect of Nema-A on pump duration could also be observed with MacQ-mCitrine (see Fig. R-28).

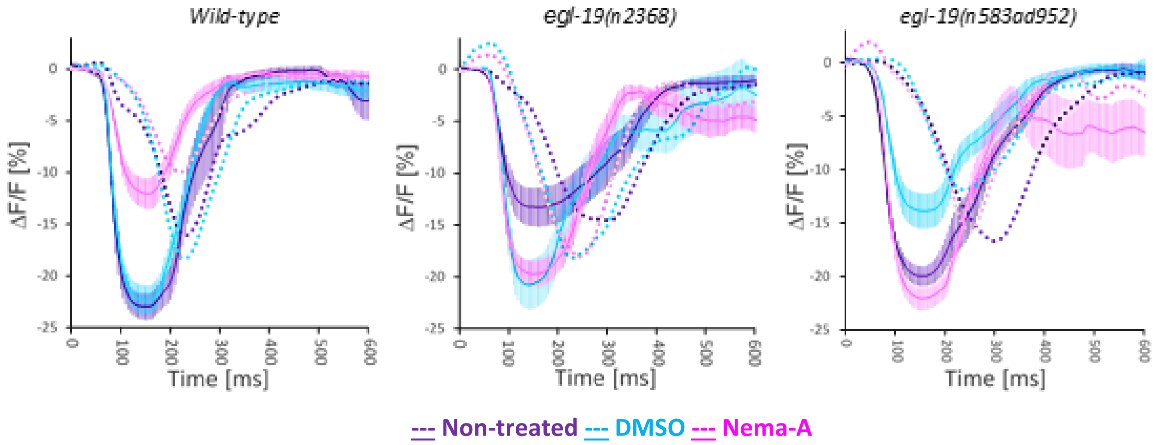

Fig. R-28: Nemadipine-A treatment affected voltage signals as monitored by MacQ-mCitrine in different genotypes. (Left-right: wild type, *egl-19(n2368), egl-19(n583ad952)*). Non-treated animals are shown in purple, DMSO in blue, and Nema-A in pink (with SEM). Dashed lines represent the respective pump signals.

The statistical analysis of the properties of all single experiments following drug application was performed with the automated KNIME script and is shown in figure R-24. The signal amplitude rises to 20- 22% upon Nema-A application in *egl-19(n2368)* and *egl-19(n583ad952).* This amplitude is comparable with the maximal changes in fluorescence signal in DMSO and non-treated wild type animals and confirms the rescue effect of Nema-A. The significantly prolonged voltage and pump duration in both mutants decrease after Nema-A usage and exhibits on a similar time scale as wild type animals. Nema-A application affected neither pump- nor voltage duration in wild type animals. There was not any significant difference in pump and voltage signal rise, and Nema-A and DMSO did not affect this factor significantly. There was a slight extension in pump and voltage signal decay of both mutants, which was reduced to a time-scale comparable to that of wild type animals (see Fig. R-29).

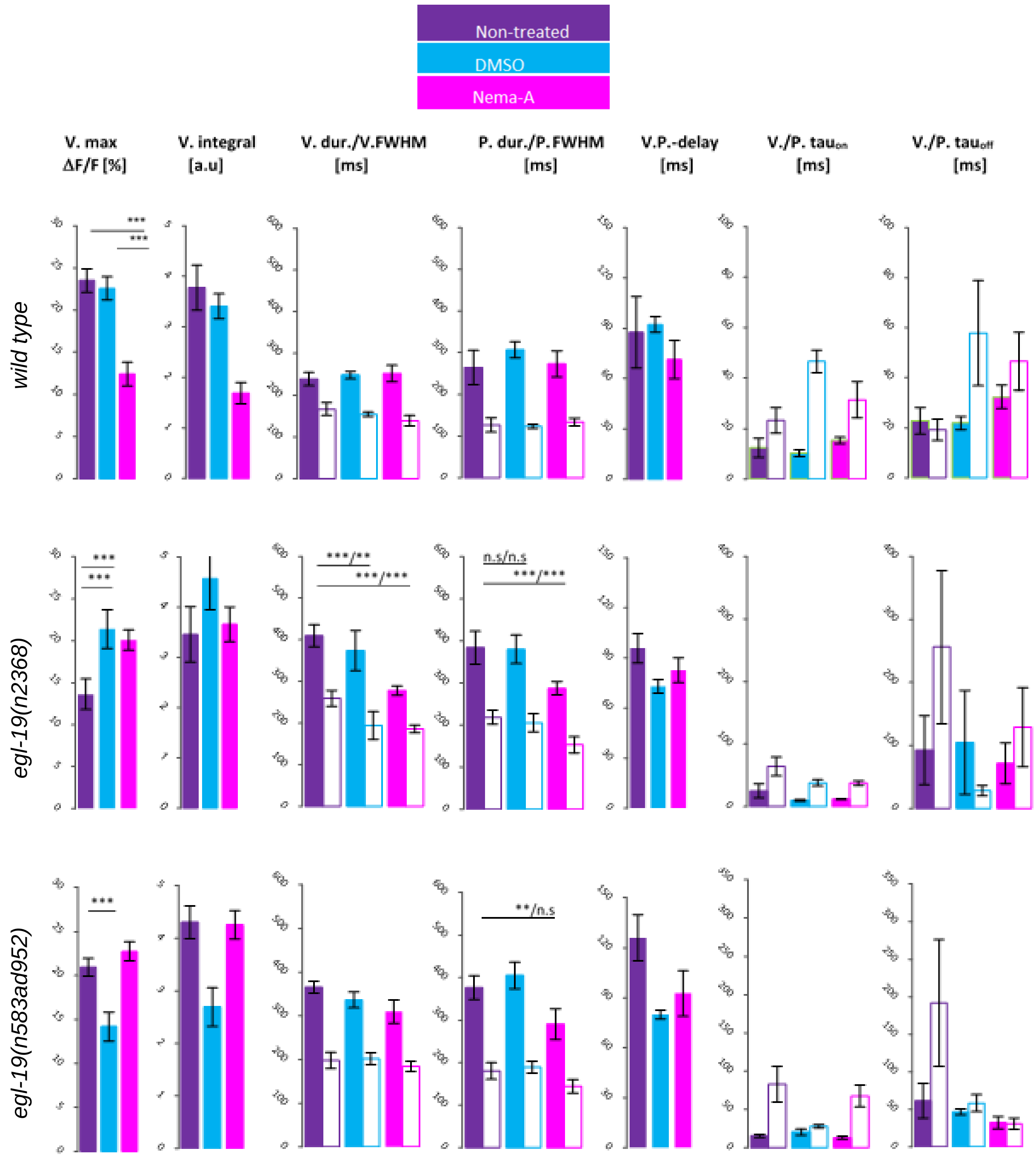

Fig. R-29: The properties of voltage signals monitored by MacQ-mCitrine after Nema-A treatment in three different genotypes. (from up to down: wild type, *egl-19(n2368) and egl-19(n583ad952)).* Color index: Purple: non-treated, blue: DMSO, pink: Nema-A, Number of analyzed events/animals: **wild type:** Non-treated: 48/8, DMSO: 78/13, Nema-A: 32/8. ***egl-19(2368)*****:** Non-treated: 79/11, DMSO:55/11, Nema-A: 94/15. ***egl-19(n583ad952):*** Non-treated: 39/9, DMSO: 29/9, Nema-A: 69/9. The N-Value was reduced for Tau$_{on}$ and Tau$_{off.}$

3.7.2: QuasAr-mOrange

Nema-A decreased the voltage signal in wild type animals expressing QuasAr-mOrange as expected. Both Nema-A and DMSO did not affect any other properties in wild type animals. Nema-A treated *egl-19(n2368)* animals showed an increase in ΔF/F compared to their DMSO-treated group. However, this rise was still much lower than the values measured for wild type animals. DMSO affected the signals in *egl-19* mutants, compared to non-treated animals. However, Nema-A treated mutants showed signals that were comparable with the DMSO control group in wild type animals.

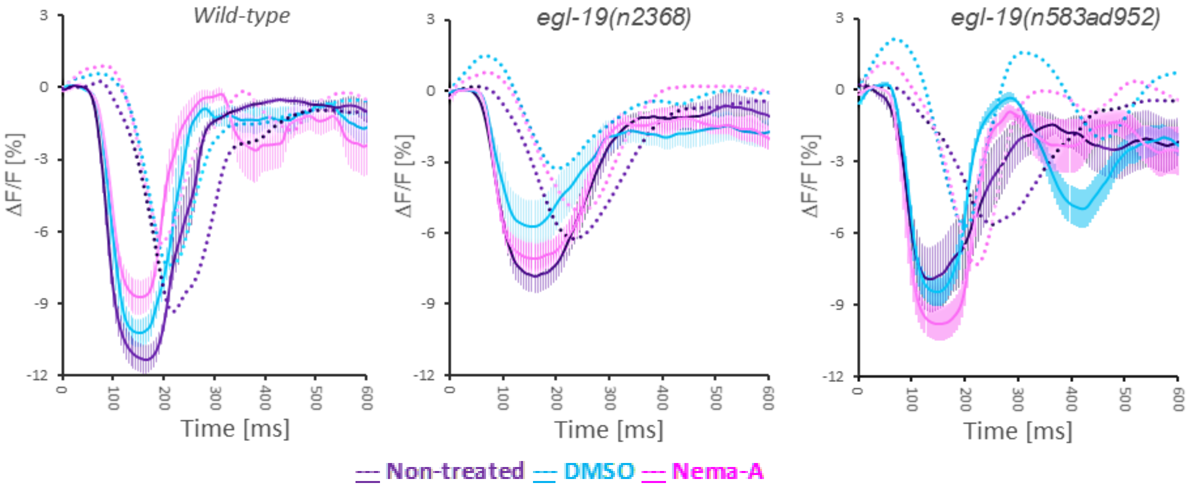

Fig. R-30: Nema-A affected voltage signals as monitored by QuasAr-mOrange in three different genotypes. (Left to right: wild-type, *egl-19(n2368)* and *egl-19(n583ad952))*. Non-treated animals are shown in purple, DMSO in blue, and Nema-A in pink (with SEM). Dashed lines show the respective pump signals.

The analysis of the properties of the tracked signal with the automated script shows that the signal amplitude rises non-significantly just ca. 2% upon Nema-A application in *egl-19(n2368)* in comparison to the DMSO control group and non-treated animals. *egl-19(n583ad952)* animals with Nema-A treatment show similar signal amplitude like wild type animals with DMSO-treatment. The significantly prolonged voltage and pump duration of *egl-19(n583ad952)* animals decreases after Nema-A treatment and exhibits similar dynamics as in wild type animals. Nema-A application affected neither pump- nor voltage duration in wild type animals. There was not any significant difference in pump and voltage signal rise, and Nema-A and DMSO did not affect this factor significantly (see Fig. R-31).

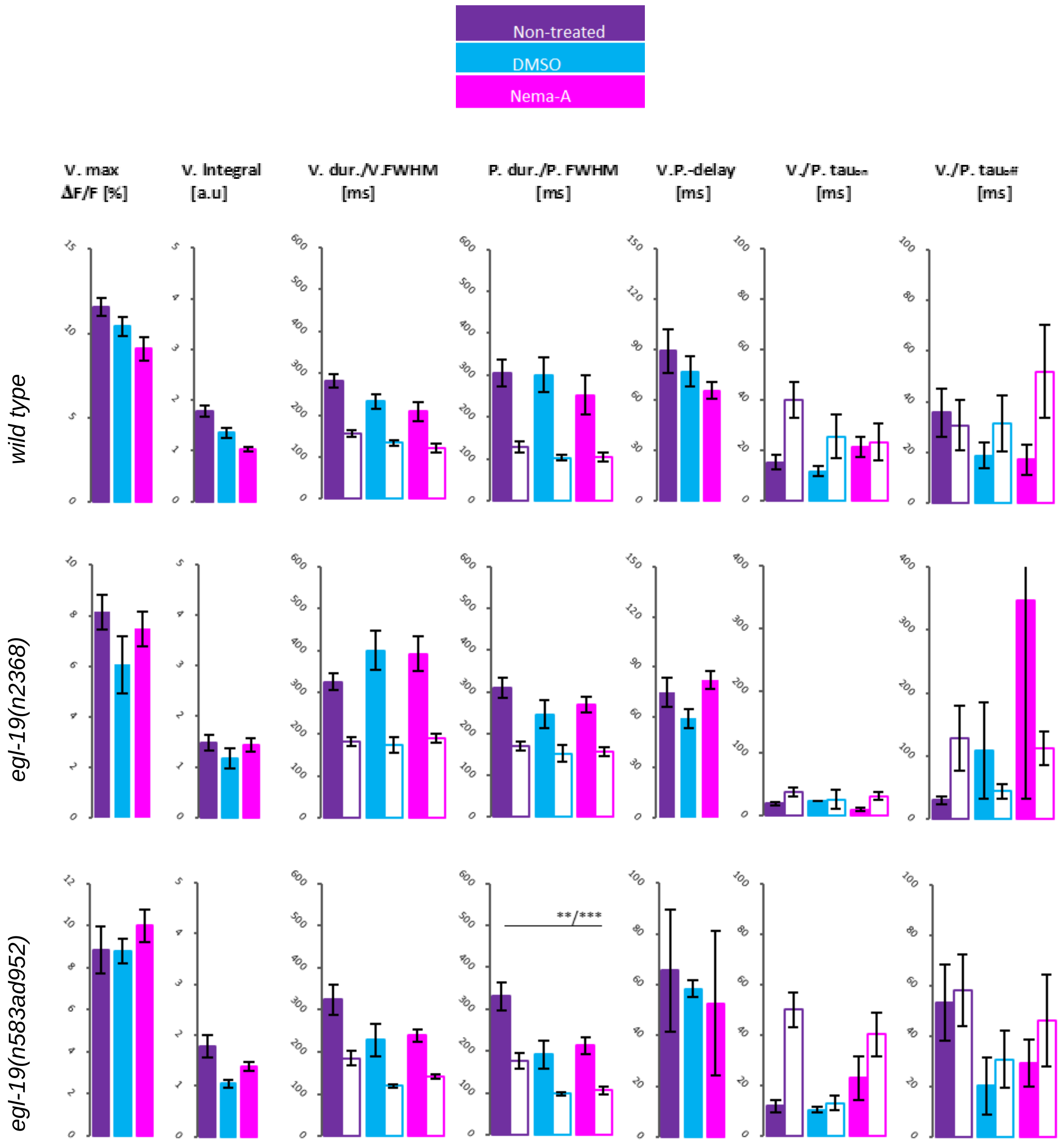

Fig. R-31: The properties of monitored signals by QuasAr-mOrange after Nema-A treatment in three different genotypes. (from up to down: wild type, *egl-19(n2368)* and *egl-19(n583ad952)* after drug treatment. Non-treated animals are shown in purple, DMSO in blue, and Nema-A in pink (with SEM). Number of analyzed events/animals: wild type: Non-treated: 40/10, DMSO:37/8, Nema-A: 71/8 *egl-19(n2368)*: Non-treated:88/11, DMSO:120/11, Nema-A: 60/10 *egl-19(n583ad952):* Non-treated:76/10, DMSO: 178/9, Nema-A: 89/8. The N-Value was reduced for Tau$_{on}$ and Tau$_{off}$.

3.7.3: Arch(D95N)

Wild type animals expressing Arch(D95N) supplemented with ATR showed a decrease in the amplitude of voltage signals after Nema-A and DMSO treatment. Thus, the 'vehicle' DMSO itself affected sensor function, or even the electrical activity in this group of animals. DMSO also affected the voltage signal in *egl-19(n2368)* animals. These animals had a strongly reduced depolarization amplitude compared to wild type. However, Nema-A application in mutants appeared to restore function of the mutant EGL-19 channel, as the amplitude of the voltage signal was increased from ca. 65% to ca. 100% ∆F/F, which is in the same range of non-treated wild type animals.

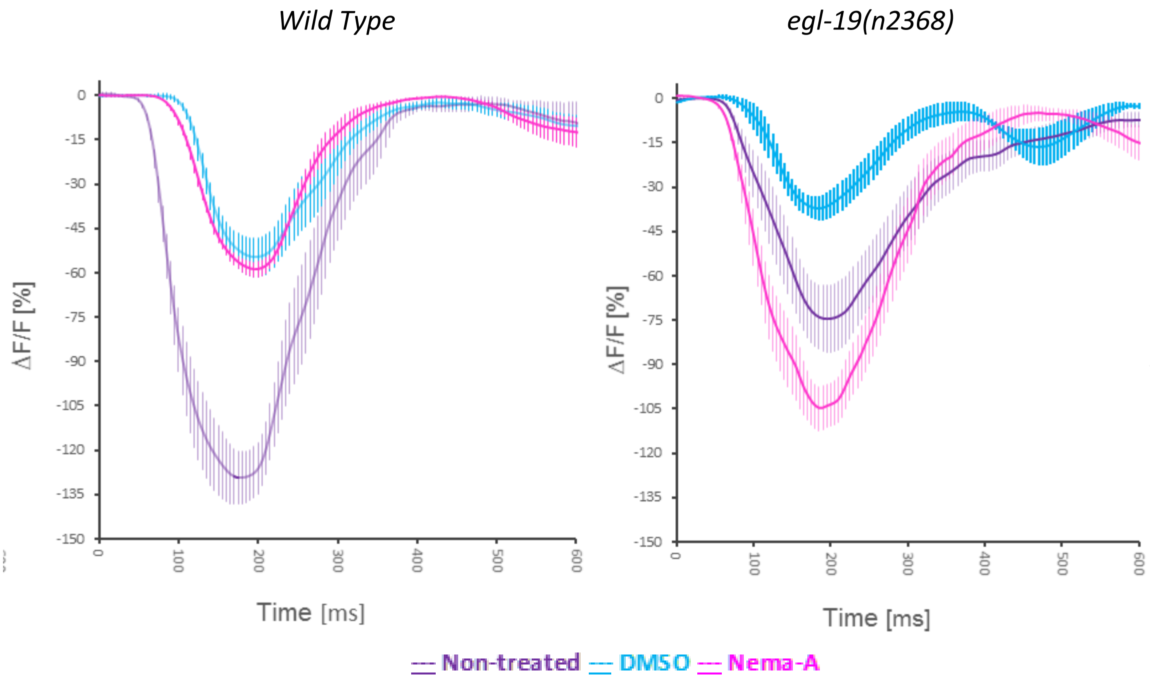

Fig. R-32: Nema-A affected voltage signals as monitored by Arch(A95N)+ATR in two different genotypes. Left to right: wild-type and *egl-19(n2368)*. Non-treated animals are shown in purple, DMSO in blue, and Nema-A in pink (with SEM). Dashed lines show the respective pump signals.

The statistical analyses of voltage signals measured by Arch(D95N), supplemented with ATR, across groups of animals are demonstrated in figure R-33. As shown above in figure R-32, the Nemadipine-A application reduced the signal amplitude in the wild type. This observation is in line with the findings made using the other sensors in wild type animals. However, in contrast to other sensors expressed in wild type, that have shown no effect of DMSO on voltage amplitude compared to non-treated animals, this vehicle (DMSO) affected the voltage amplitude in wild type animals expressing Arch(D95N) supplemented with ATR and was reduced to – 55% ∆F/F. It could be shown that Arch(D95N)+ATR is able to significantly monitor the Nema-A rescue-effect on egl-19(n2368) mutants.

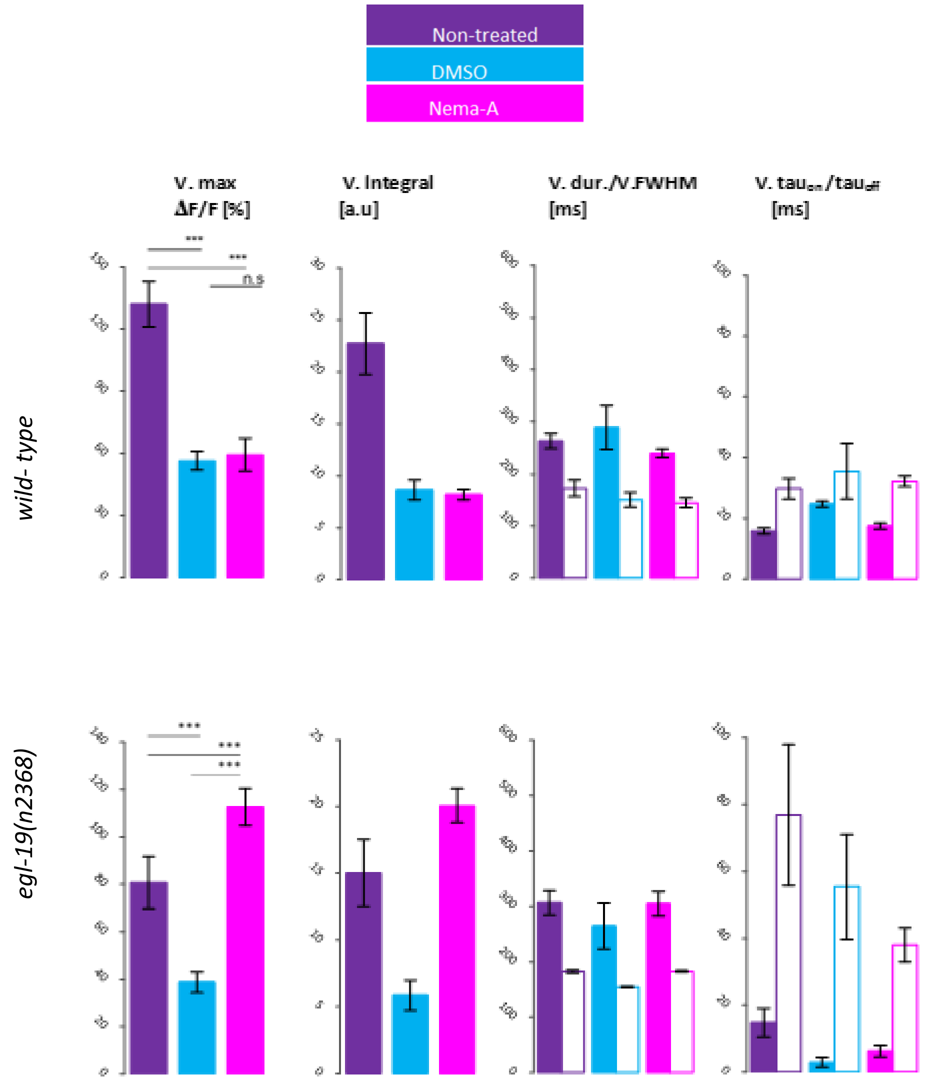

Fig. R-33: Reading out the properties of monitored signals by Arch(D95N)+ATR in two different genotypes. From up to down: wild type and *egl-19(n2368)* after drug treatment. Non-treated animals are shown in purple, DMSO in blue, and Nema-A in pink (with SEM). The number of analyzed events/animals: wild type: Non-treated: 56/11, DMSO:54/7, Nema-A: 77/10 *egl-19(n2368):* Non-treated:110/12, DMSO:74/6, Nema-A: 83/13. The N-Value was reduced for Tau$_{on}$ and Tau$_{off.}$

Voltage signals monitored with Arch(D95N) expressed in wild type animals were not affected by DMSO when this indicator was supplemented with DMAR. This finding is consistent with the observations with eFRET indicators in wild type animals treated with DMSO. Nema-A decreased the voltage signals in comparison to DMSO and non-treated animals in wild type group, which is also in line with other tested sensors.

DMSO also affected the voltage signal in *egl-19(n2368)* animals. Nema-A increased voltage signals in this mutant to a similar level as in DMSO-treated or in non-treated wild type animals (see Fig. R-34).

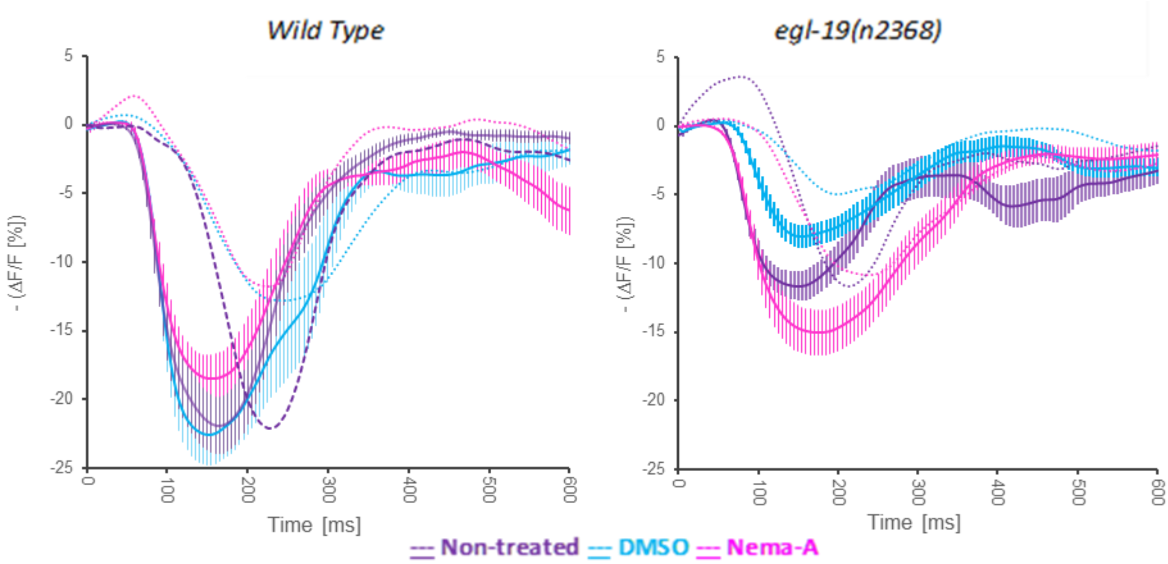

Fig. R-34: Nema-A affected voltage signals as monitored by Arch(A95N)+DMAR in two different genotypes. Left to right: wild-type and *egl-19(n2368)*. Non-treated animals are shown in purple, DMSO in blue, and Nema-A in pink (with SEM). Dashed lines show the respective pump signals.

Figure R-35 represents the properties of voltage and pump signals measured with Arch(D95N) supplemented with DMAR after drug application. As described before, there is a tendency in the reduction of fluorescence signal upon Nema-A application in wild type animals. Although this abatement is minimal, it matches with previous observation with all the other indicators upon Nemadipine application. There is a rescue effect upon Nema-A application in *egl-19(n2368)* animals, which shows a significant rise in the amplitude of voltage signal comparing to DMSO and non-treated animals. However, this increase is still not comparable with amplitudes measured in wild type animals.

No other significant effects could be observed during drug application by Arch(D95N) equipped with DMAR.

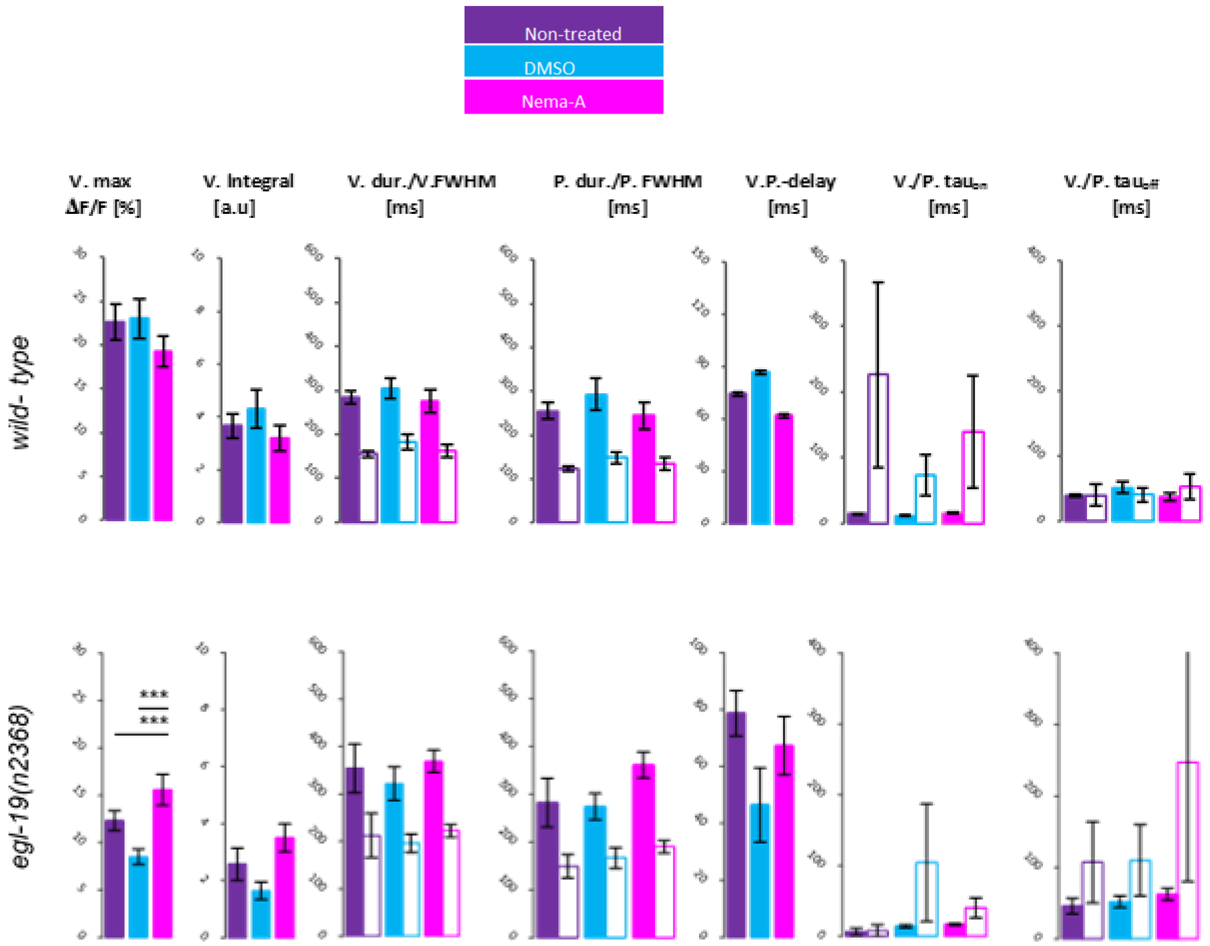

Fig. R-35: Reading out the properties of monitored signals by Arch(D95N)+DMAR in two different genotypes. From up to down: wild type and *egl-19(n2368)* after drug treatment. Non-treated animals are shown in purple, DMSO in blue, and Nema-A in pink (with SEM). The number of analyzed events/animals: The number of analyzed events/animals: wild type: Non-treated: 61/15, DMSO:86/9, Nema-A: 111/8 *egl-19(2368)*: Non-treated:68/8, DMSO:114/10, Nema-A: 111/15. The N-Value was reduced for Tau$_{on}$ and Tau$_{off.}$

3.8: Optical electropharyngeogram (opto-EPG) and compartmentalized electrical activity in pharyngeal muscles

Changes in the membrane potential of pharyngeal muscles are caused by currents, which can be recorded by electrophysiology. Such recorded currents are called electropharyngeograms (EPG). EPGs are comparable with electrocardiograms or electroencephalograms since they are recorded from the outside of an intact animal. EPGs consist of different positive and negative changes, which correlate with ionic currents through ion channels in the pharyngeal plasma membrane, and which cause compensatory currents from the outside through the mouth of the animal. They can be measured if the head of the animal is tightly inserted in a glass pipette, between the bath electrode and the pipette interior. Thus, depolarization of the membrane and the following repolarization are readily observed as positive and negative spikes in the recording. However, these signals can only be observed across the pharynx as a whole structure, providing temporal, but no spatial resolution. By optically recording membrane voltage changes, and by focusing on the frame-by-frame change of the voltage (i.e. the first derivative of the voltage signal) local alterations in voltage, reporting on local currents may be deduced from. If the current changes are analyzed across the whole structure, such an analysis would be an optical equivalent of the electropharyngeogram, which also records the summed-up currents (or voltage) across the entire pharynx / head of the animal. For such analysis, “difference records” were generated. For this aim, two duplicates of the recorded video have been generated, whereas in first duplicate the first frame and in the second duplicate the last frame were deleted. Every pixel in a “one frame forward- shifted” video was subtracted from the same pixel in a “one frame backward-shifted” duplicate. For better representation, and as single depolarization and repolarization events were quite noisy in the difference videos, similar events from recordings with very regular pharyngeal pumping were aligned and synchronized (each pump event spanned ca. 100 frames ~ ca. 500 ms, see video no. IIX) and the fluorescence changes were read out via a defined region around the pharynx in the same way as voltage imaging was performed before (see Fig. 36). This way of evaluating of voltage changes across the pharynx resembled the characteristics of the classical EPG and led to the generation of was titled as “opto-EPG). As it is demonstrated in figure 36, all the pharyngeal muscles depolarized simultaneously. However, the repolarization occurred in a spatially compartmentalized manner, i.e. it was observed first in the corpus and then appeared ca. 50 ms later in the isthmus and terminal bulb. This phenomenon could be observed for both sensors in the two representative videos within a different time scale. The first step of repolarization was observed after ca. 145 ms with MacQ-mCitrine, which was first detectable after 170 ms with Arch(D95N)+ATR. This analysis was done for MacQ-mCitrine as an example for eFRET sensors and Arch(D95N) as an example for rhodopsin direct-imaging.

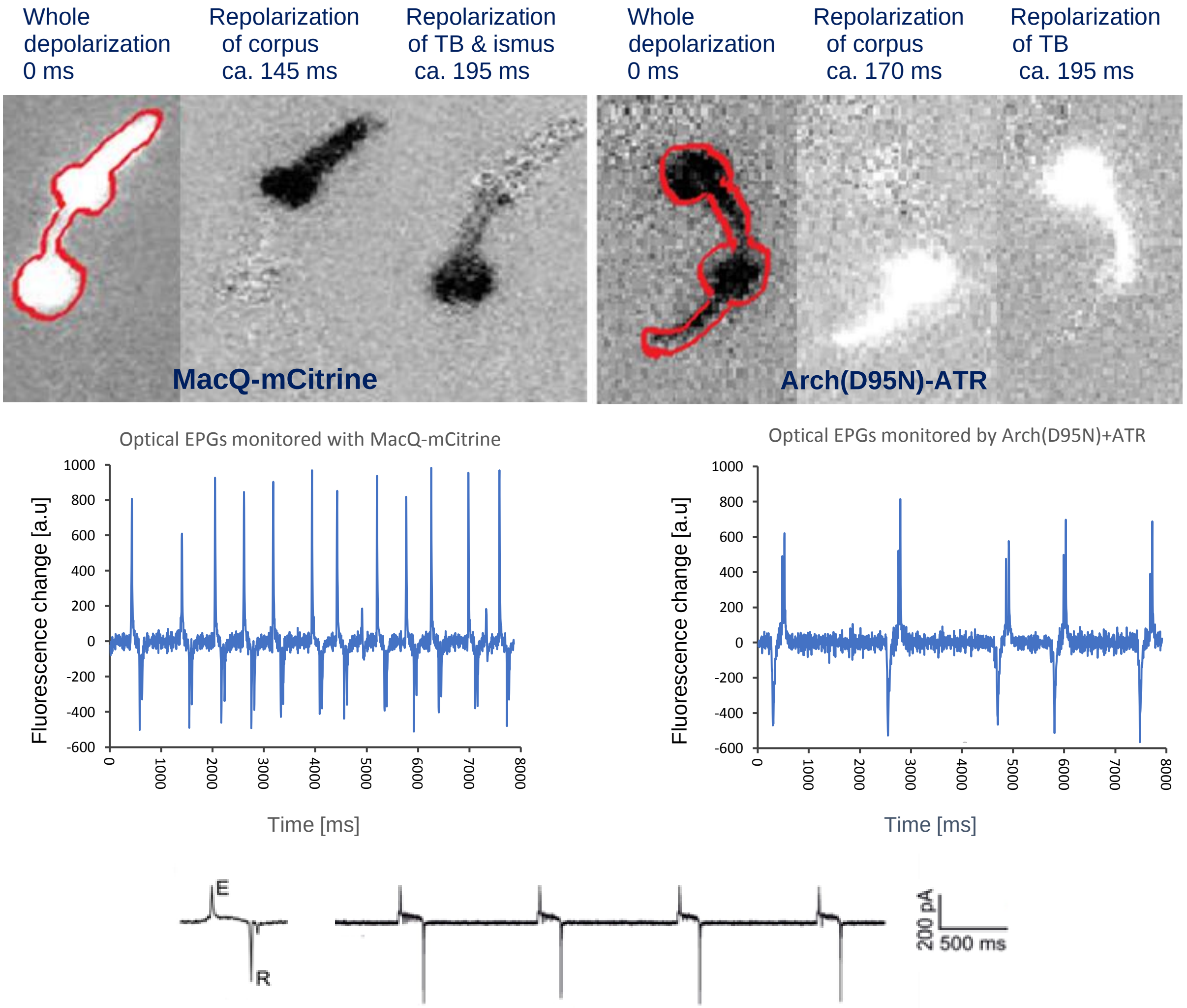

Fig. R-36: **Optical electropharyngeograms in the pharyngeal muscle.** Analysis deduced from a difference-video, monitoring the depolarization of pharynx, and the repolarization procedure from a representative animal expressing MacQ-mCitrine in the left side and an animal expressing Arch(D95N)+ATR at the right side. EPGs from electrophysiology (Modified from (Schüler *et al.*, 2015)) are attached underneath the opto-EPGs in order to have a comparison.

Besides this, a spatiotemporal change of the voltage signal could be deduced from the isolated and concatenated electrical events from the difference video via a longitudinal line scan over pharynx (Fig. 37).

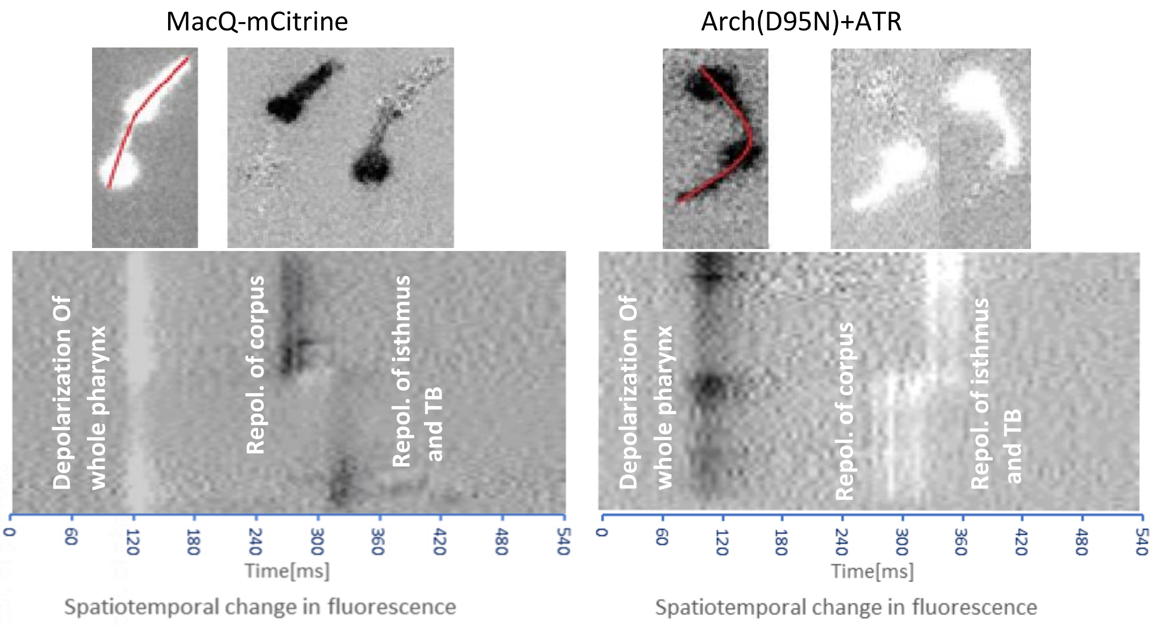

Fig. R-37: Spatiotemporal development of voltage in pharynx. For this analysis a line scan was performed along the longitudinal axis of the pharynx, which indicates the spatiotemporal differences in voltage-change of pharynx in a representative animal expressing MacQ-mCitrine in the left side and in an animal expressing Arch(D95N) supplemented with ATR presented in the right side.

3.9: Monitoring action potentials in body wall muscles

As described before, the expression of different voltage indicators in body wall muscles of *C. elegans* was achieved using the promotor of the *myo-3* gene. Changes in the fluorescence signal were measured during spontaneous activity to examine the ability of GEVIs in monitoring action potentials in BWMs. Furthermore, channelrhodopsin-2, expressed in cholinergic motor neurons, was used as an actuator in animals expressing GEVIs to evoke action potentials. ChR2 stimulation with blue light led to the release of acetylcholine from motor neurons and accordingly the depolarization of BWMs. Such optically evoked action potentials can be measured in electrophysiology by current clamp; their amplitude is in the range of ca. 30 mV (Azimi Hashemi *et al.*, 2019). Thus, optically induced action potentials can be compared between optically measured voltage signals and electrical activities analyzed by current clamp recordings. For this aim, changes in the fluorescence signals in animals expressing one of the voltage indicators were compared to the ones expressing both GEVI in BWMs and ChR2 in cholinergic neurons during blue light stimulation. The stimulation lasted 10 ms for both measurements in electrophysiology and voltage imaging. In the upcoming section, every sensor and its ability for monitoring APs in BWMs is introduced and discussed individually.

3.9.1: QuasAr-mOrange

QuasAr-mOrange was the only eFRET sensor tested in BWMs. Since the extrachromosomal array expressing QuasAr-mOrange in BWMs was integrated into the genomic DNA, it was expected that uniform voltage fluorescence signals should be monitored in all animals. The fluorescence signal should be reduced during depolarization of the muscle cells due to spontaneous muscle activity. For such analyses, a region of interest was defined across the head muscles, which have shown the brightest expression. However, since the animals were immobilized, spontaneous activity occurred rarely, and the fluctuations in the fluorescence signal were not very high, as shown in figure 38 (see video X).

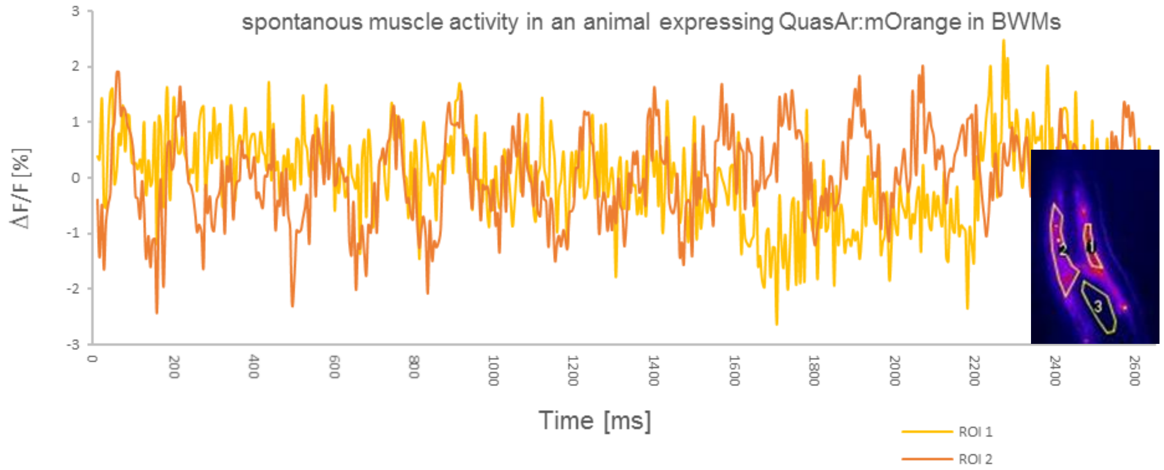

Fig. R-38: Monitoring action potentials during spontaneous muscle activity in BWMs with QuasAr-mOrange. The analyzed regions (1&2) are shown in the picture underneath the graph. ROI3 was defined for background correction. The dorsal and ventral changes are demonstrated in ΔF/F [%]. Recording speed: ca. 190 frames per second (fps).

For calibration of the optically monitored APs with the ones recorded electrically (current clamp), the changes of the fluorescence signals in animals expressing only the voltage indicator in BWMs were compared to those from animals expressing both the GEVI (in BWMs) and channelrhodopsin (in cholinergic neurons) during a 10 ms blue light stimulation. This was necessary due to the spectral overlap of imaging light (mOrange) and the light stimulation of ChR2. For this purpose, male animals expressing the GEVI were crossed with hermaphrodites expressing channelrhodopsin in cholinergic neurons. Blue light stimulation leads to a stronger excitation of QuasAr-mOrange, which increases the fluorescence signal during light pulse for both groups. This rise in the signal lasts ca. 12 ms longer than the programmed lighting protocol, since the shutter needs this time to close again. However, this increase is ca. 10% weaker in animals with optically stimulated acetylcholine release, which is shown as a difference graph Δ in figure 39.

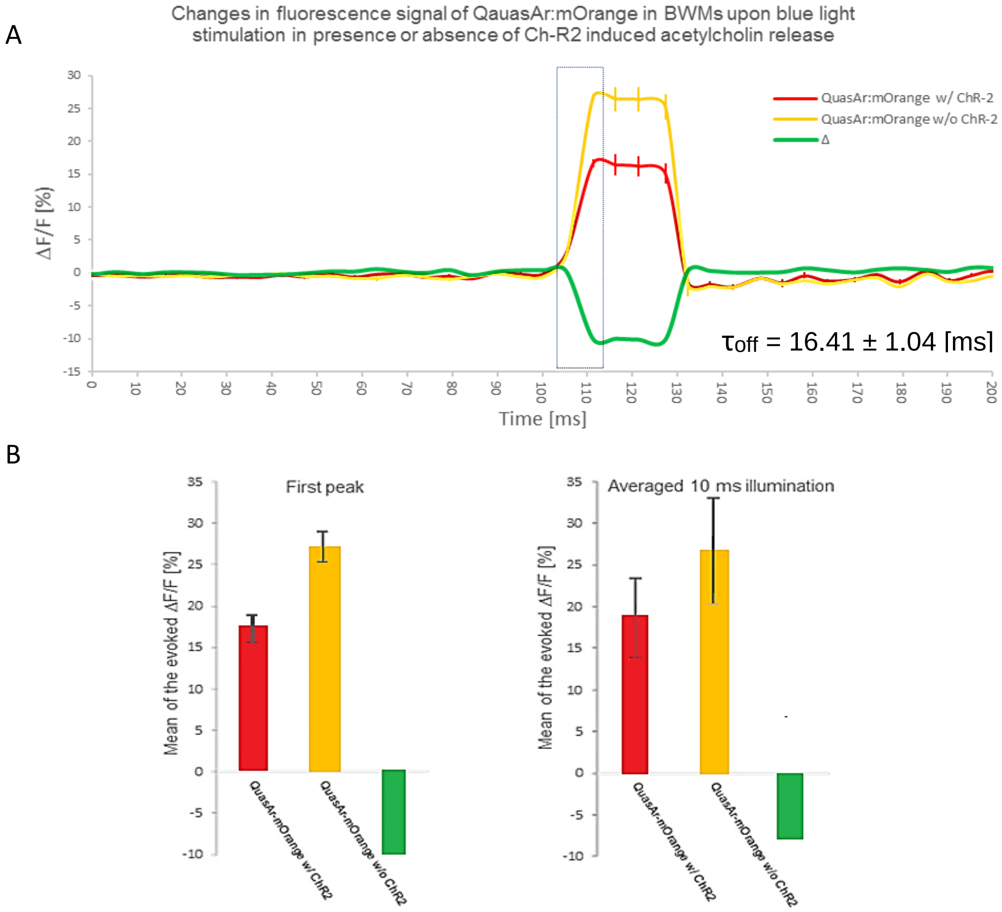

Fig. R-39: Changes in fluorescence signal of QuasAr-mOrange in BWMs upon blue light stimulation in the presence or absence of ChR2 induced acetylcholine release. A) Prior to blue light stimulation, fluorescence signals were recorded for 5 seconds (only 100 ms is shown in the graph), followed by a blue light stimulation lasting for 10 ms. The prolonged signal rise is due to the shutter´s closing-time. Both groups show an increase in the signal upon excitation. Fluorescence signal from animals expressing both GEVI in BWMs and ChR2 in cholinergic neurons are shown in red (+SEM), animals expressing just the GEVI are shown in orange (+SEM). The animals with optically evoked acetylcholine release show ca. 10% weaker signal, which is shown as a difference graph in green marked as Δ. N=12-13. Signal decay time (Tau_{off}) was analyzed for the Δ-curve (τ_{off} = 16.41 ± 1.04 [ms]). B) Quantification of the evoked ΔF/F [%] illustrated either as the peak maximum or the average of evoked fluorescence change within 10 ms illumination.

3.9.2: Arch(D95N)

Arch(D95N) was supplemented with either ATR or DMAR to examine the potential of this sensor to monitor action potentials in BWMs as an increase in the fluorescence signal. Like for experiments in which I recorded APs in the pharynx, the concentration of ATR was 10- fold higher than DMAR. Besides higher concentration, the gain value was also set at 50 for experiments performed with ATR to achieve a stronger signal. First, changes in the fluorescence signal were measured during spontaneous muscle activity. It was possible to track action potentials in BWMs with Arch(D95N) supplemented with ATR. For recording such signals, high laser intensities were needed. The changes in the fluorescence signal were between 10-15%, which is much weaker than the signals measured with this sensor in pharyngeal muscles. Representative, spontaneous signals are shown in figure 40. Since the basal fluorescence signal of ATR is very weak, it was not possible to track the signal in both dorsal and ventral muscles (see video no. XI).

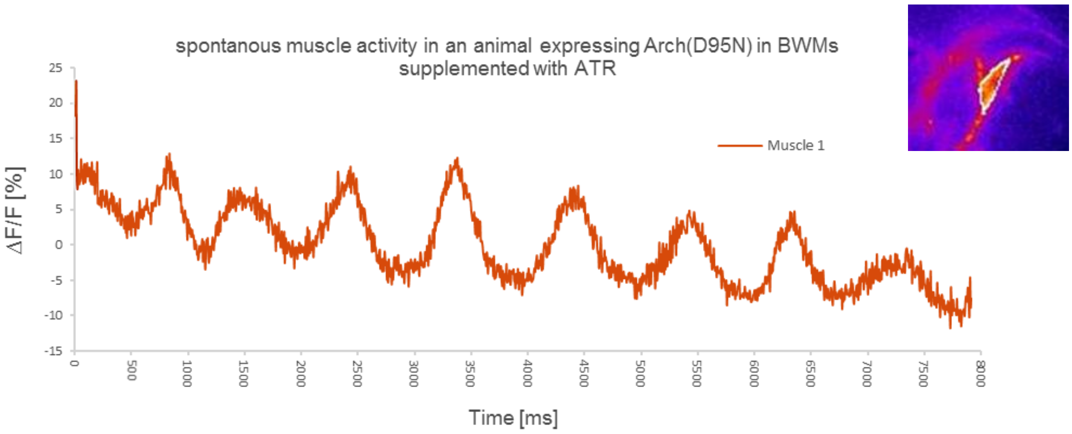

Fig. R-40: Monitoring action potentials during spontaneous muscle activity in BWMs with Arch(D95N) supplemented with ATR. The analyzed region in the ventral side of the body is shown in the picture in the graph. The basal signal on the dorsal side was so weak that no changes could be observed during electrical activity (see video XI). Recording speed: ca. 190 fps.

The experiments for calibration of the optically monitored APs with the ones recorded by current clamp were also performed for animals expressing Arch(D95N) supplemented with ATR. The two groups of animals with and without optically induced muscle depolarization were compared. Since the excitation of Arch(D95N) supplemented with ATR is in the far-red region of the spectrum, the blue light pulse did not lead to a rise in the signal of animals lacking channelrhodopsin. This means that the signal increase, which was observed in the group of animals with ChR2 and thus acetylcholine release, is the pure response to muscle depolarization. However, the decay of the signal back to the baseline lasts longer when compared to the QuasAr-mOrange eFRET sensor. The $\mathrm{Tau}_{\mathrm{off}}$ value indicating the decay time of the signal was 16.41 ± 1.04 [ms] for QuasAr-mOrange eFRET sensor, which increases to 413.75 ± 14 [ms] in Arch(D95N) supplemented with ATR. This finding supports the hypothesis that the kinetics of repolarization of muscles expressing Arch(D95N) is slower than that of cells expressing other sensors since this phenomenon was also observed in the repolarization phase of pharyngeal muscle expressing Arch(D95N), supplemented with ATR (see Fig. R-36, Opto-EPG).

Alternatively, the signal returns more slowly to the baseline, possibly as the photocycle or the decay of the fluorescent state of Arch(D95N) differs from that of QuasAr. The rise in fluorescence signal after the optically induced depolarization of body wall muscles was around 20% $\Delta F/F$ and thus is in the same range of the signal increase observed during spontaneous muscle activity, however still far away from the mean of the signals measured during the depolarization of pharyngeal muscles. Besides, the mean of provoked $\Delta F/F$ was calculated for the first peak and for the averaged 10 ms of blue light stimulation, which is illustrated in figure 41 (panel B).

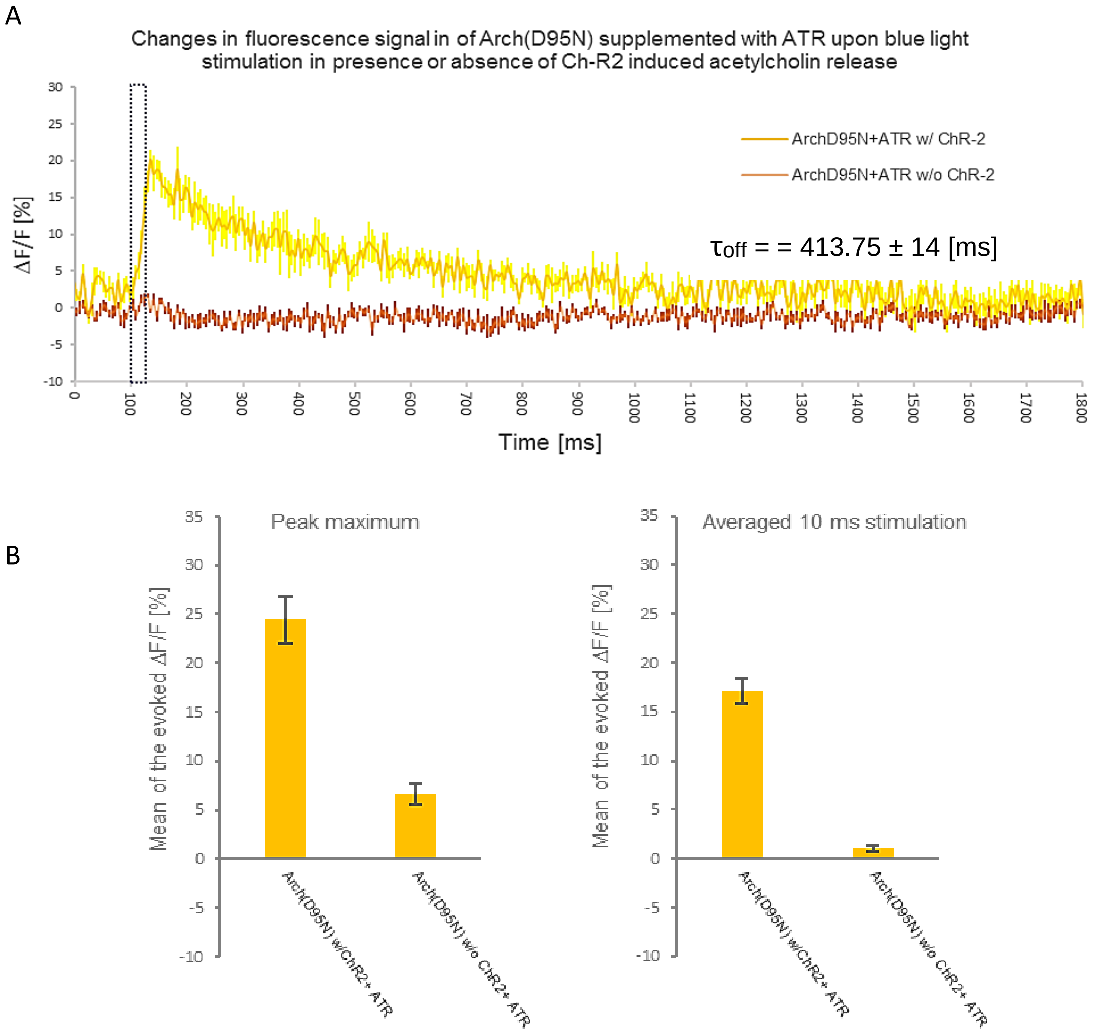

Fig. R-41: Changes in fluorescence signal of Arch(D95N) supplemented with ATR in BWMs upon blue light stimulation in the presence or absence of ChR2 induced acetylcholine release. A) Prior to illumination with blue light, fluorescence signals were recorded for 5 seconds (only 100 ms is shown in the graph), followed by a blue light stimulation lasting for 10 ms (see the blue window over the graph). The reason for the prolonged rise is the closing-time of the shutter. Fluorescence signal from animals expressing both GEVI in BWMs and ChR2 in cholinergic neurons are shown in orange (+SEM), animals expressing just the GEVI are shown in red (+SEM). Signal decay time (Tau$_{off}$) was analyzed for Arch(D95N) in the presence of ChR2B) B) Quantification of the evoked ΔF/F [%] illustrated either as the peak maximum or the average of evoked fluorescence change within 10 ms illumination. N=7-8. FPS: ca. 190.

Arch(D95N) expressed in BWMs was also supplemented with the retinal-analog DMAR. As described before, DMAR showed a bright basal fluorescence signal, as compared to ATR, which could be observed even with low light intensities (25 mW/mm^2). However, to monitor voltage-dependent fluorescence changes high intensities (ca. 160 mW/ mm^2) are required. Changes in the fluorescence signal were monitored during spontaneous muscle activity. Electrical activities recorded from an exemplary animal expressing Arch(D95N) supplemented with DMAR are shown in figure 42 (see video no. XII). Here it was possible to monitor voltage fluctuations during spontaneous activity in three muscle cells in a representative animal; one dorsal muscle in the head and the opposed ventral muscle cell, as well as in the directly neighboring ventral muscle cell. The fluorescence changes in the opposite muscles occurred reciprocally, which is consistent with the movement strategy of *C. elegans*. Besides this, it can be seen that the de- and repolarization of the neighboring muscles occurred consecutively. The measured fluorescence rise in the signal during muscle depolarization is 6- 7% ΔF/F. This value is less than the mean of signal changes measured in pharynx (ca. 20% ΔF/F) for this sensor.

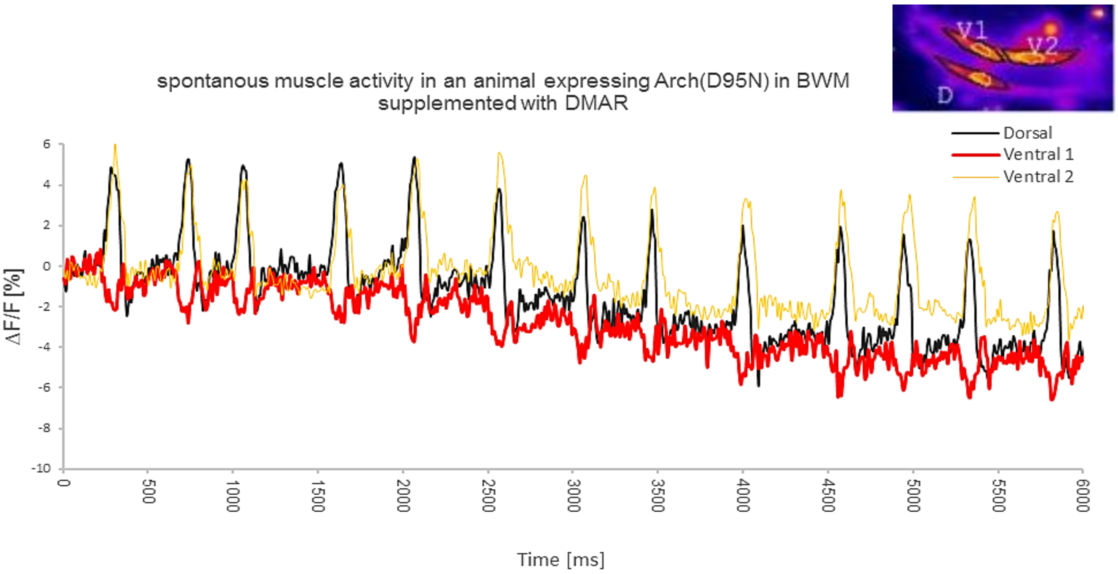

Fig. R-42: Monitoring action potentials during spontaneous muscle activity in BWMs with Arch(D95N) supplemented with DMAR. The contour of the three muscles (one dorsal(d) and two ventral(v) muscles) is marked in black in the miniature. Electrical events of the dorsal muscle are demonstrated in black and of the ventral muscles in red and orange. Recording speed: circa 106 fps, see video no. XI

The experimental procedure for calibration was performed for animals supplemented with DMAR as well. It was shown before that DMAR has two different absorption wavelengths, one at ca. 600 nm and at 450 nm. This property led to a further rise in the fluorescence signal for both groups during a blue light pulse. The difference graph demonstrates the pure voltage-sensitive signal, which shows ca. 10% changes in ΔF/F. The decay time of signal´s rise is 486.8 ± 18.76 [ms]. This is ca. 50 ms longer than the calculated decay time of Arch(D95N) supplemented with ATR.

Furthermore, it seems as if the additional light decelerates the repolarization massively or the absorbed blue light pulse is trapped by DMAR, since the return to the baseline level does not appear even 3 s after depolarization (see Fig. R-43).

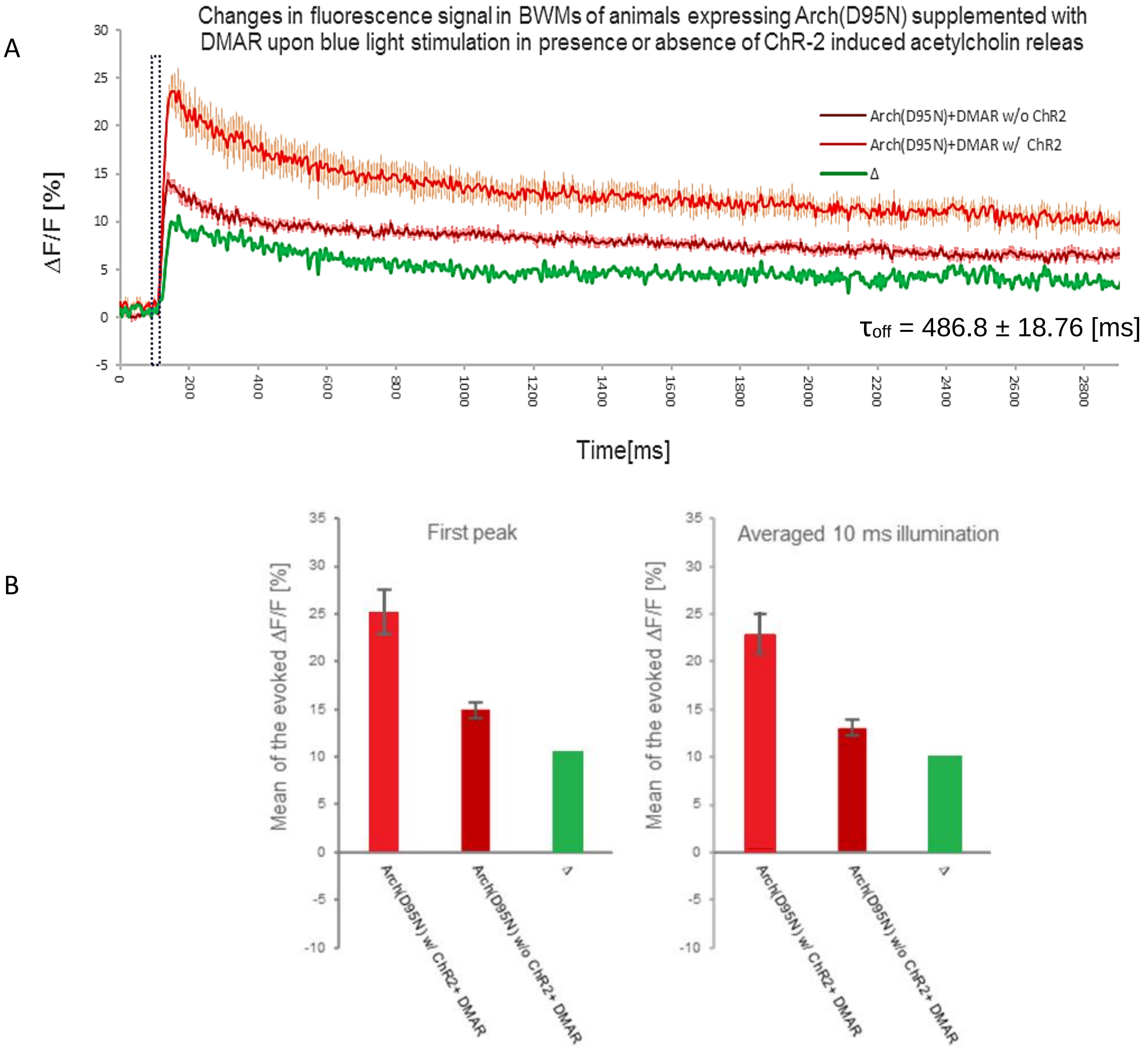

Fig. R-43: Changes in fluorescence signal of Arch(D95N) supplemented with DMAR in BWMs upon blue light stimulation in the presence or absence of Ch-R2 induced acetylcholine release. A) Prior to blue light stimulation, fluorescence signals were recorded for 5 seconds (only 3s are shown in the graph), followed by a blue light pulse lasting for 10 ms (indicated by the dashed blue box). The reason for the prolonged rise is the closing-time of the shutter and eventually the overexcitation of DMAR with a 470 nm light pulse. Fluorescence signal from animals expressing both GEVI in BWMs and ChR2 in cholinergic neurons are shown in red (+SEM), animals expressing just the GEVI are shown in dark red (+SEM). The animals with optically evoked acetylcholine release show ca. 10% stronger signal, which is shown as a difference graph in green marked as Δ. Signal decay time (Tau$_{\text{off}}$) was analyzed for the Δ-curve: 486.8 ± 18.76 [ms]. B) Quantification of the evoked ΔF/F [%] illustrated either as the peak maximum or the average of evoked fluorescence change within 10 ms illumination. N=7-8. Recordings were obtained at ca. 190 fps.

3.9.3: Arch(DETCDE)

The triple mutant variant of Arch(D95ET99CD106E) was explored for its potential of monitoring action potentials in BWMs. It was supplemented with both ATR and DMAR, whereas the concentration of ATR was 10x higher than DMAR, as described before for Arch(D95N), and as before, the gain value was set at 50 for measurements with the ATR-supplemented GEVI. In the first step, changes in the fluorescence signal were measured during spontaneous muscle activity. For calibration of the monitored signal with electrically measured signals during the current clamp, male animals expressing Arch(DETCDE) were crossed with hermaphrodites expressing ChR2 in cholinergic neurons, and both groups were compared during and following 10 ms blue light stimulation.

Fluorescence changes during spontaneous muscle activity of a representative animal supplemented with ATR are shown in figure 44 (see video no. XIII). The monitored signals exhibit changes of ca. 30% ΔF/F, detected from dorsal and ventral muscle arms. However, this reciprocal rise and drop in the signals lasted with a range of 2-6 seconds longer than expected, which might be a consequence of several overlapping depolarization events (see Fig. R-44).

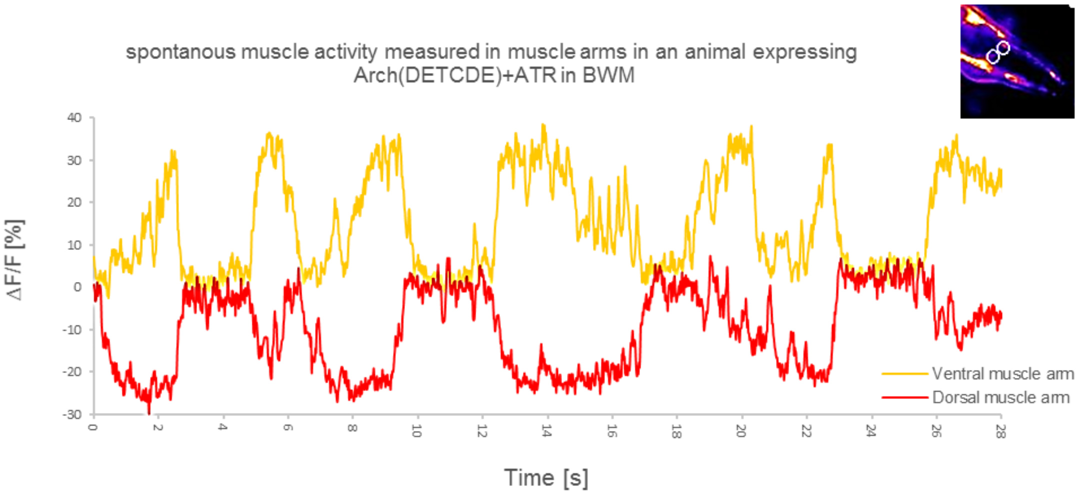

Fig. R-44: Monitoring action potentials during spontaneous muscle activity in dorsoventral muscle arms in the head of a representative animal with Arch(DETCDE) supplemented with ATR. Analyzed muscle arms are marked with a white circle. Data obtained from ventral and dorsal muscle arms are shown in orange and red, respectively. Recording speed: ca. 52 fps, see video no. XIII.

Like in animals expressing Arch(D95N), the experimental procedure for calibration was performed for animals expressing Arch(DETCDE) supplemented with ATR. A rise of ca. 25% in the fluorescence signal could be measured during the light-induced muscle depolarization of animals due to acetylcholine release in animals expressing both GEVI and ChR2. Blue light stimulation did not affect animals, lacking ChR2. The depolarization signal has reached its baseline again after ca. 200 ms (T_{off} = 194.16 ± 4.54 [ms]), which is almost 2.1-2.5 fold faster than the repolarization kinetics measured with Arch(D95N) either with ATR (~ 413 ms) or with DMAR (~ 484 ms) and indicates the faster kinetic of this sensor.

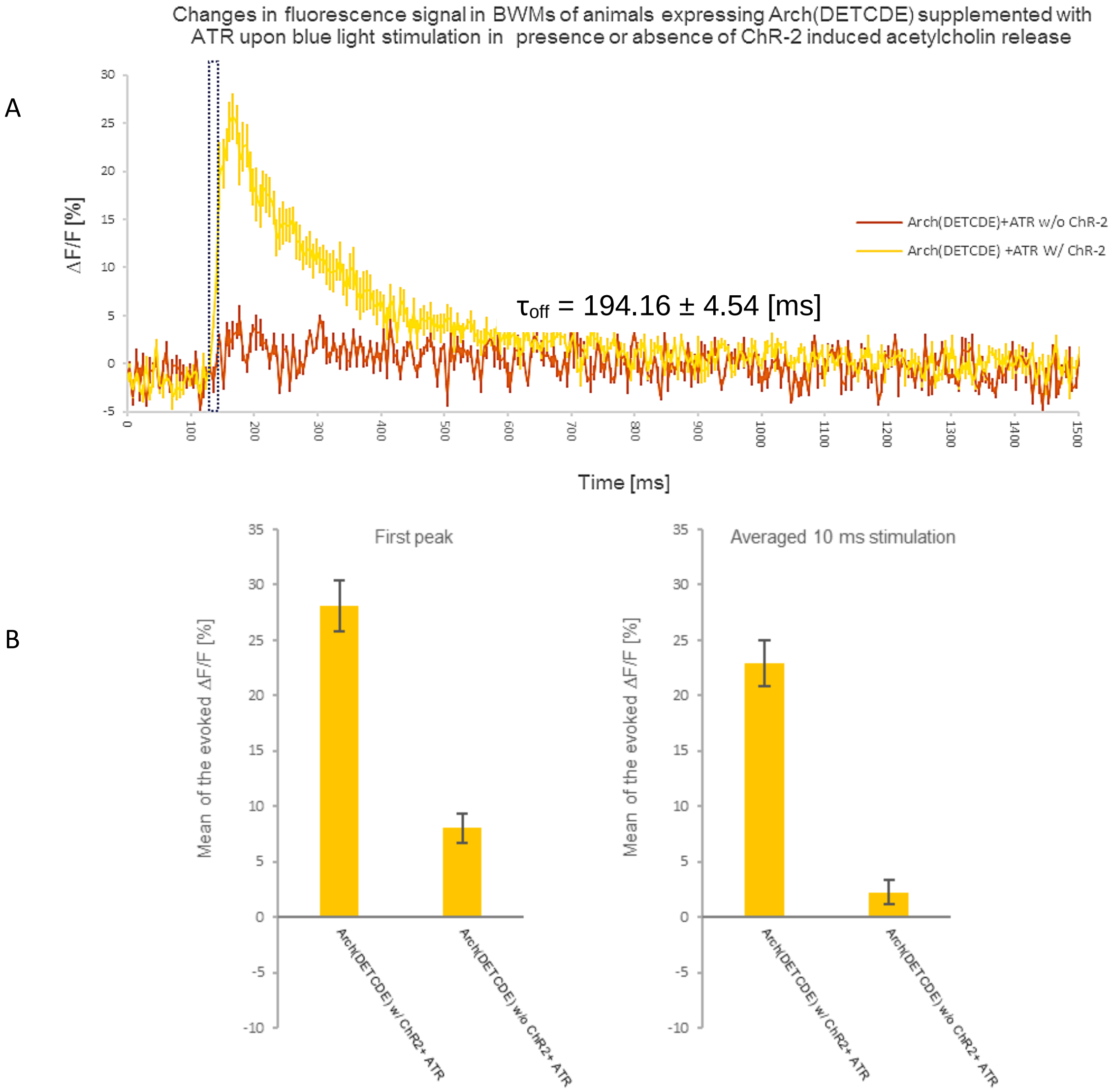

Fig. R-45: Changes in the fluorescence signal of Arch(DETCDE) supplemented with ATR in BWMs upon blue light stimulation in the presence or absence of ChR2 induced acetylcholine release. A) Prior to blue light stimulation, fluorescence signals were recorded for 5 seconds (only 1500 ms is shown in the graph), followed by a blue light stimulation lasting for 10 ms (see the blue window over the graph). Fluorescence signal from animals expressing both GEVI in BWMs and ChR2 in cholinergic neurons are shown in orange (+SEM), animals expressing just the GEVI are shown in dark red (+SEM). B) Quantification of the evoked ΔF/F [%] illustrated either as the peak maximum or the average of evoked fluorescence change within 10 ms illumination. N=7-8. FPS: ca. 190

Monitoring action potentials during spontaneous muscle activity of animals expressing Arch(DETCDE) was performed with DMAR as well. The changes in the fluorescence signal of an exemplary animal are demonstrated in figure 46 (see video IVX). Here, two neighbor dorsal muscles have been analyzed for their fluorescence signal changes during spontaneous muscle activity (The very bright spot is the anterior vulval muscle). As it is demonstrated in the graph, the rise in the fluorescence signal spreads from anterior to posterior. The rises in the signal last partly for more than a second, which may have occurred due to overlapping depolarization events since the recording speed was just ca. 52 fps.

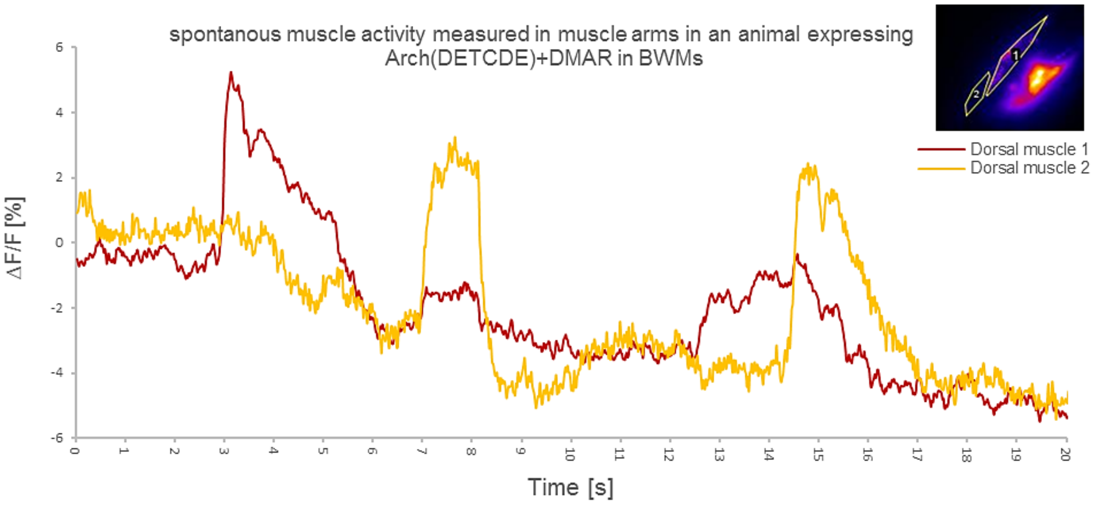

Fig. R-46: Monitoring action potentials during spontaneous muscle activity of an exemplary animal with Arch(DETCDE) supplemented with DMAR. Shown are two neighboring dorsal muscles situated directly opposite to vulva muscles (bright spot in the picture) supplemented with DMAR. Analyzed regions are marked in the picture with 1 (anterior) and 2 (posterior). See video IVX. Recording speed: ca. 52 fps

Calibration of signals measured with Arch(DETCDE) was also performed while this sensor was supplemented with DMAR. The results exhibit two new observations; on the one hand, blue light stimulation did not affect animals lacking ChR2, meaning the combination of this triple mutant+ DMAR may have changed the properties of either the sensor or the chromophore (e.g., absorption wavelength of the chromophore). On the other hand, animals expressing ChR2 show tonic fluorescence changes even before and after blue light stimulation, though in a small range of ca. 1%. This may be a hint that this sensor-chromophore combination is highly voltage-sensitive. The maximum rise of just ca. 3% in the fluorescence signal could be measured during the light-induced muscle depolarization of animals due to acetylcholine release in animals expressing both GEVI and ChR2 (Fig.47, A). It can be estimated that the rise in the signal has reached its baseline again after ca. 200 ms (the exact Tauoff value could not be calculated due to high fluctuations in the fluorescence signal), which is almost 2-fold faster than the repolarization kinetics measured with Arch(DETCDE) supplemented with ATR.

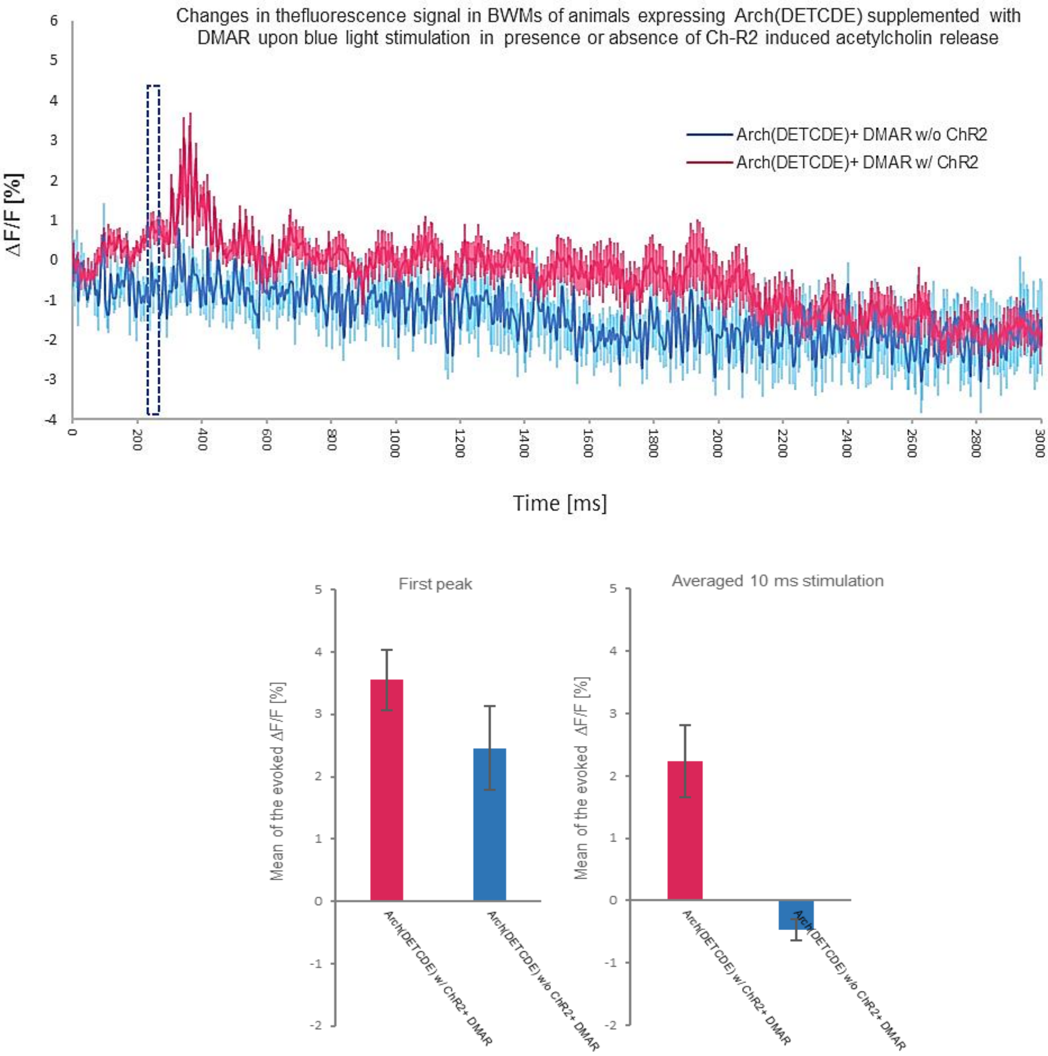

Fig. R-47: Changes in the fluorescence signal of Arch(DETCDE) supplemented with DMAR in BWMs upon blue light stimulation in the presence or absence of ChR2 induced acetylcholine release. A) Prior to blue light stimulation, fluorescence signals were recorded for 5 seconds (shown are only 200 ms) followed by a blue light stimulation lasting for 10 ms (see the blue window over the graph). Fluorescence signals from animals expressing both GEVI in BWMs and ChR2 in cholinergic neurons are shown in pink (+SEM) and in blue, animals lacking ChR2 and expressing just the GEVI are shown in red (+SEM). B) Quantification of the evoked ΔF/F [%] illustrated either as the peak maximum or the average of evoked fluorescence change within 10 ms illumination. N=7 for each group. The acquisition of the video was at ca.190 fps.

3.10: Electrophysiology in body wall muscles

Electrophysiology was performed during this project to compare the measured currents by electrical methods to those signals monitored with optical imaging. The main aim of this was to calibrate optically monitored voltage signals in body wall muscles. This aim was achieved via the current clamp, which is a method to measure the evoked action potentials. The APs were evoked by ChR2- induced depolarization and thus acetylcholine release from motor neurons resulting in body wall muscles' depolarization. The mean of such evoked APs (n=8) was ca. 29-30 mV (see figure R-42; this data was provided by Dr. Jana Liewald).

The induced depolarization of body wall muscles via ChR2 activation (with the same illumination protocol as in the current clamp measurements) in animals expressing Arch(D95N) in body wall muscles caused ca. 20% changes in ∆F/F (see figure R-35), if the animals were supplemented with ATR (n=8). This value was reduced to ca. 15% changes in ∆F/F in the case of DMAR (n=8, see Fig. R-37). The same experiment was also performed in animals expressing QuasAr-mOrange (eFRET-sensor) in BWMs. These animal (n= 13) show -10% changes in ∆F/F. The mean of the evoked ∆F/F in animals expressing Arch(DETCDE) was 28.06% when supplemented with ATR and 3.5% when supplemented with DMAR.

Based on these data optically monitored voltage signals can now be calibrated roughly, which are ca. 68% ∆F/F per 100mV for Arch(D95N)+ ATR; 51% ∆F/F per 100 mV for Arch(D95N)+ DMAR, 34% ∆F/F per 100 mV for QuasAr-mOrange, respectively. These analysis are consistent with already reported achieved values in other organisms (Hochbaum *et al.*, 2014). Voltage changes of the new introduced triple mutant Arch(DETCDE) corresponded 93.53% ∆F/F when supplemented with ATR and 11.6% ∆F/F while supplemented with DMAR.

This "indirect" way was used to calibrate the optically measured signals since a simultaneous optical and electrical measurement in body wall muscles was not possible. The main reason for this was the weak fluorescence signal in body wall muscles, especially in Arch(D95N) supplemented with ATR, which could not be analyzed on the microscope used for electrophysiology. The technical limitations in the electrophysiology setup were mainly the specific objective used, which has a high working distance and thus very low numerical aperture.

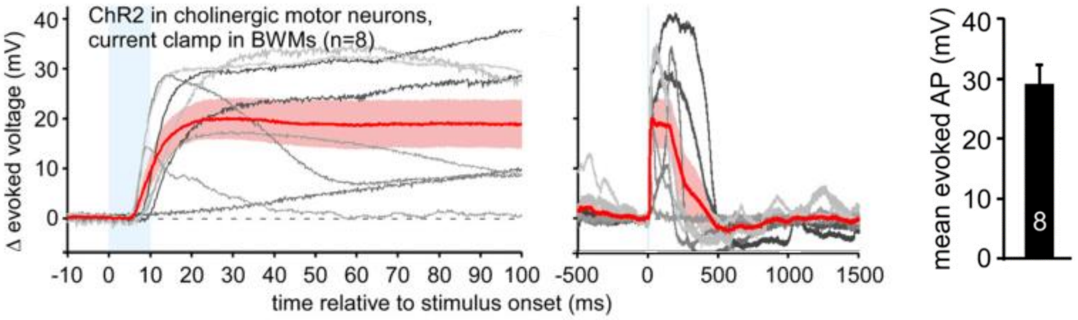

Fig. R-48: Electrical signals measured via current clamp in body wall muscles after ChR2 activation. Shown are optogenetically evoked APs in BWMs due to ChR2 activation with a blue light pulse (blue bar) for 10 ms during the current clamp in a short time scale on the left side and an extended time scale in the middle. Data from single animals are shown in gray, and the mean of the APs is shown as a red trace with SEM in red shadow. The mean of the APs from 8 animals with SEM is also demonstrated as a bar on the right side. The whole experiment and analysis were done by Dr. Liewald (Adopted from (Azimi Hashemi *et al.*, 2019)).

3.11: Electrophysiology in pharyngeal muscles

Due to the robust signal in the pharynx, such simultaneous measurements for precise calibration of MacQ-mCitrine could be performed by Dr. Christina Schüler via sharp electrode recording. The mean of the measured APs was ca. 95 mV (as reported already in literature; 80-115 mV (Davis *et al.*, 1999), (Steger *et al.*, 2005), (Franks *et al.*, 2002)) accompanied by ca. 20% changes in ΔF/F, as shown in figure R-49.

Interestingly there have been some differences between optically and electrically measured signals. Calculated τ_{on} and τ_{off} values indicate that the signal´s rise and drop last longer in optical signals than electrical signals (optical; electrical $\tau_{on:}$ ca. 30± 5 ms ; 7,5± 1 /$\tau_{off:}$ 39± 9 ms ; 5± 0,7 ms). This means that the optically monitored APs are ca. 4x slower in comparison to APs measured via electrophysiology. This analysis allows for the more precise calibration of optically measured MacQ-mCitrine signal, which is 19.5% ΔF/F per 100mV. Based on this analysis, it is possible to calibrate the Arch(D95N) signal in the pharynx, which is ca. 128% ΔF/F per 100 mV for Arch(D95N) supplemented with ATR and 24% ΔF/F per 100 mV equipped with DMAR. Comparing these values with those achieved from body wall muscles, it seems that Arch(D95N) is more sensitive by monitoring action potentials in pharynx than in body wall muscles (Azimi Hashemi *et al.*, 2019). QuasAr-mOrange demonstrates 10.5% ΔF/F per 100 mV. This value was ca. 34% ΔF/F per 100 mV for QuasAr-mOrange expressed in BWMs, which indicates that this sensor is more sensitive in body wall muscles than in the pharyngeal muscles. The signals from Arch(D95H) can be calibrated as well: ~72% ΔF/F per 100 mV, while supplemented with ATR and ~ -8% ΔF/F per 100 mV while supplemented with DMAR.

Simultaneous optical monitoring was not performed only during sharp electrode recording but also during EPGs. Optically measured EPGs coincided well to those electrically measured currents with this advantage that they can also deliver spatial information about de- and hyperpolarization of each pharyngeal section.

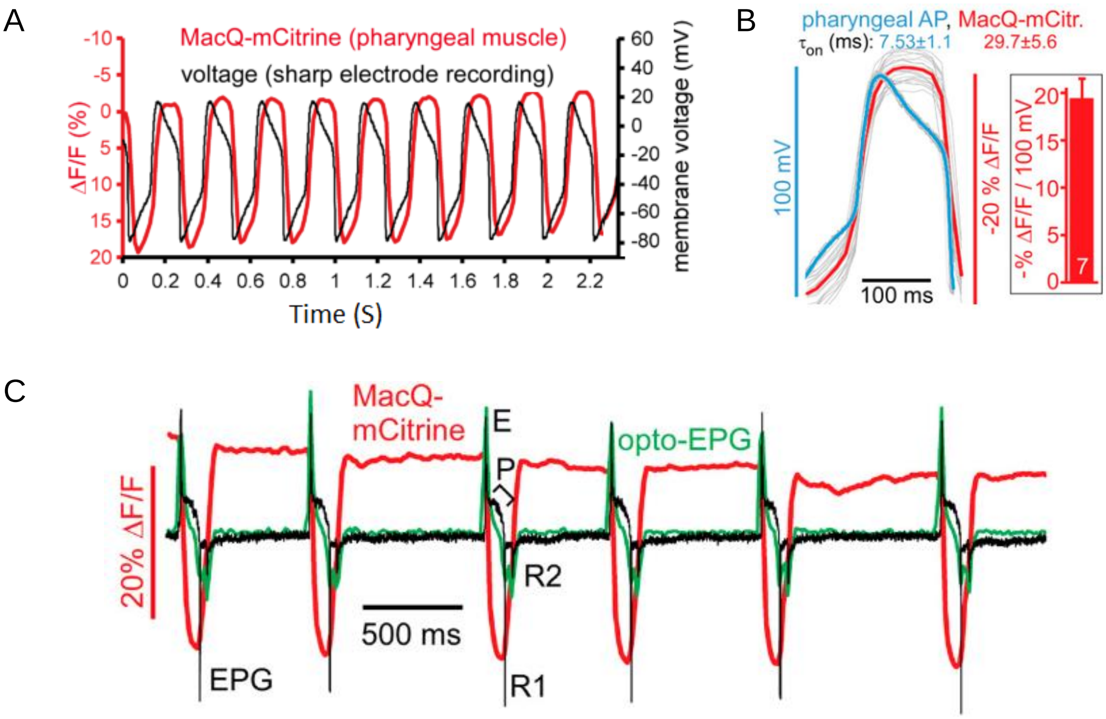

Fig. R-49: Electrophysiology in the pharyngeal muscle (terminal bulb; sharp electrode recordings) and EPGs, simultaneous and compared to optical AP measurements with MacQ-mCitrine. A) simultaneous optically (MacQ-mCitrine) and electrically measured APs from an exemplary animal. B) The mean of the APs measured via sharp electrode recording (in blue) or from optical monitoring (in red). The optically measured signals occur more slowly than those measured via sharp electrodes. C) Simultaneous monitoring of optically monitored APs (in red) and EPGs (in black) showing the E, P; R1 and R2 spikes, compared to the corresponding opto- EPG(green). The opto-EPG complies with the electrically measured EPG. Dr. Schüler performed all the experiments and the analysis (Adopted from (Azimi Hashemi *et al.*, 2019)).

4 Discussion

4.1: Conclusion

Changes in the membrane voltage act as a switch for the activity of excitable cells, thus monitoring the electrical events of the membrane is an important method to understand the mechanism of communication between the cells. In the framework of this project, it was possible to establish an *in vivo* voltage imaging method in the nematode *C. elegans* via the expression of different GEVIs in two tissues of this animal, namely pharyngeal and body wall muscles for the first time. This method can be used as a substitution for the very complicated experimental procedures in electrophysiology. Besides, it reports the electrical changes directly with a faster kinetic than the usually used indirect Ca^{+2} reporters. The established method introduced in this work uses lower light intensities (~180 mW/ mm^2) than reported before (8000 mW/ mm^2), which helps to maintain the physiological health of the animals during *in vivo* imaging.

Different GEVIs could be introduced and studied in detail. Two of them are the eFRET sensors QuasAr-mOrange and MacQ-mCitrine, which were able to deliver robust signals with the ability to monitor the electrical activity in pharyngeal and BWMs. Besides, Arch(D95N) was tested in both tissues for direct imaging of the rhodopsin fluorescence changes bearing either ATR or DMAR. Arch(D95N)+ATR in pharynx reveals a sensitivity of ~128% $\Delta F/F0$ per 100 mV, which is much stronger than the reported values before (Kralj *et al.*, 2012; Hochbaum *et al.*, 2014). All these three sensors expressed in pharyngeal muscles could monitor the deviations in the action potentials and thus the pharyngeal muscle depolarization in *egl-19* g.o.f mutants, caused by the mutation in the voltage-gated Ca^{2+}-channel. The rescue effect of the dihydropyridine Nema-A, a blocker of voltage-gated calcium channel, could be reported by all the sensors as well, though with different sensitivity.

The substitution of ATR with its analog DMAR in the sensors for direct imaging of rhodopsin shows a significant increase in the luminosity of the fluorescence signal, which may also evoke some new effects in the photocycle of some rhodopsins such as the briefly introduced sensor Arch(D95H), which has shown a decrease in its fluorescence upon light activation.

The application of sharp electrode measurements during simultaneous optical recording in the pharynx and current-clamp recording during optically induced depolarization in BWMs enabled the calibration of optical signals.

Moreover, the analysis of voltage dynamics across the whole pharynx provides the monitoring of compartmentalized de- and repolarization of anterior to posterior bulbs in the pharynx, which was described here as optical electropharyngeogram (Opto-EPG). All in all, this work provides new tools (see table D-1) for direct membrane voltage monitoring as a competitor to indirect Ca^{2+}-imaging and complementary an all-optical non-invasive substitution for complicated electrophysiology in the intact nematode *C. elegans*.

Table D-1: List of the stablished GEVIs for the usage in C. elegans pharyngeal and body wall muscles with their basal properties *=not calculated

GEVI	Targeted tissue	Sensitivity ΔF/F [%] per 100 mV	Excitation / emission [nm]	Tau_{on}, Tau_{off} [ms]
MacQ-mCitrine	Pharynx	-20	470/520	12.3/22.8
QuasAr-mOrange	Pharynx	-10.5	540/610	15.1/35.6
Arch(D95N)+ ATR	Pharynx	128	637/700	15.79/29.78
Arch(D95N)+DMAR	Pharynx	24	637/780	15.09/38.03
Arch(D95H)+ATR	Pharynx	71	637/740	*/*
Arch(D95H)+ATR	Pharynx	-8.9	637/780	*/*
QuasAr-mOrange	BWMs	-34	540/610	*/16.41
Arch(D95N)+ATR	BWMs	68	637/740	*/413.75
Arch(D95N)+DMAR	BWMs	51	637/780	*/486.8
Arch(DETCDE)+ATR	BWMs	93.5	637/740	*/194.16
Arch(DETCDE)+DMAR	BWMs	11.6	637/780	*/*

4.2: Expression of different GEVIs in *C. elegans*

During this project, different of GEVIs were reviewed for their feasibility of expression and localization in *C. elegans* body wall muscles, pharynx, or neurons. ASAP, Mac-derivatives, Butterfly, and different variants of Archaerhodopsin were surveyed.

In many cases, the expression level of the examined GEVI was low, meaning that either just a hardly detectable fluorescence signal of the protein of interest could be observed or the expression of the protein of interest was suppressed in advanced life stages, e.g., the expression of the sensor ASAP could be observed only until L3 to L4 stage. This observation was experienced by some other *C. elegans* labs (personal communication with Mei Zhen lab, Toronto).

In some other cases, it seemed that the expression of the sensor was toxic for the animal. For example, the effort failed to express the Arch(wt) or its mutated derivatives in PVD neurons. After the injection of the constructs for the specific expression in PVD neurons with a co-injection marker for expression in the pharynx, some transgenic animals could be generated that have shown only the expression of the marker, which was lost respectively in the next generation.

Besides the variety in the expression level of the protein, it could be observed that the transmission level for some of the sensors was not enough to cultivate enough number of transgenic animals for an experimental procedure. For example, the transmission rate of Arch(wt) in wild type animals was under 50%, which reduced in every coming generation. The line did not generate any transgenic animal after a while. The crossbreeding of wild type animals expressing Arch(wt) with *egl-19* mutants was successful after repeated trials. However, this line was not able to reproduce the protein after 3- 4 generations and was lost as well.

GEVIs with the most stable expression and high transmission level (up to 70% transgenic animals in the progeny), which have been used for the final experimental voltage imaging, have been introduced in detail in the last chapter. Pharynx and body wall muscles were the tissues, where successful expression of GEVIs could be achieved, and their electrical activity was monitored via rhodopsin-based voltage indicators.

The transmission rate of pharyngeal expression was similar for all the sensors (for both eFRET and direct-imaging tools). Over 85% of the animals have shown the expression of the desired GEVI in the progeny, and this remained stable for many generations.

At the very first glance and without performing any controlling assays like egg-laying or swimming assay, it seems that the expression of the GEVIs did not provoke deficiencies in the growth and development of the transgenic animals, and they behaved like the wild type. The only exception was observed by animals expressing Arch(wt) in the pharynx. They have grown very slowly. The transmission rate of the transgene was below 30% and was reduced gradually in every new generation so that the strain was lost after a while.

MacQ-mCitrine and QuasAr-mOrange were the two eFRET voltage indicators used in the pharynx. Both have shown to some extent aggregations their expression pattern, which did not affect their functionality. Arch(D95N) and Arch(D95H) could be expressed in pharyngeal muscle for rhodopsin direct-imaging and could be supplemented with both ATR and retinal analog DMAR. These mutant proteins did not incorporate retinal analog VI.

The expression of none of the GEVIs affected the functionality of the pharynx (e.g., feeding behavior or pumping rate) or BWMs (e.g., unexpected movement behavior) in wild type animals.

Crossing the wild type animals expressing GEVIs in the pharynx with *egl-19* mutants did not affect the expression level of the sensor in crossbred animals. However, since this mutation affects the muscles involved in egg-laying, especially in *egl-19(n2368),* the transmission rate was reduced in crossbred animals, and development was slowed down.

Nevertheless, there has been variability in the pharyngeal expression level of the GEVIs from animal to animal, since the injected extrachromosomal array was not integrated into the genomic DNA. The expression of the GEVIs was not homogenous throughout the pharynx, and it was stronger in the metacorpus and posterior bulb in comparison to the procorpus and the isthmus. This observation is promotor specific and is consistent with the described expression pattern of the *myo-2* promotor (Okkema *et al.*, 1993).

Alexander Hirschhäuser performed the integration of *pmyo3::QuasAr::mOrange in the* genomic DNA as a side-project of his master thesis. Amelie Bergs performed the integration procedure of the construct *pmyo3::Arch(D95N)::2xMyc-tag* into the genomic DNA. As described before, the expression of the GEVIs was stronger in the head and vulval muscles. The integration of the extrachromosomal arrays could not induce a homogenous expression of the GEVIs in all the muscles under the control of the *myo-3* promotor since this expression pattern is promotor specific and was consistent with the already described expression pattern of the *myo-3* gene (Fire and Waterston, 1989). However, the integration led to a notable reduction of mosaicism among the animals.

4.3: The basal fluorescence signal of the different GEVIs assessed in this thesis

Measuring the basal fluorescence of each GEVI was the first step to assess its qualification for voltage imaging. However, this quantification provides no information about the sensors´ voltage sensitivity, because it delivers information about the fluorescent signal during the resting potential of the animals.

In general, the fluorescence signal of eFRET sensors was notably higher than the sensors for rhodopsin direct- imaging. The signal in eFRET sensors originates from the fluorescence protein (either mCitrine or mOrange), which builds in FRET-pair with the rhodopsin (either QuasAr or Mac). This property makes the use of this sort of sensors more straightforward since low light intensities for excitation of the sensor are sufficient. However, eFRET sensors are not able to substitute the usage of direct-imaging tools, since direct-imaging tools are faster and can be better combined with other optogenetic tools due to their red-shifted spectrum. The observations with eFRET sensors during this project were performed with a common HBO-lamp, available in almost every microscopy laboratory. The intensity was set at 10-35 mW/ mm² for MacQ-mCitrine and QuasAr-mOrange, respectively.

QuasAr:mOrange expressed in pharynx showed 2.5- 4 folds stronger signal brightness and higher absolute gray value compared to MacQ-mCitrine. Although the absolute gray value for Arch(D95N) supplemented with DMAR is ca. 50% lower than that of MacQ-mCitrine, their signal luminosity defined as the signal contrast to the background, is in a similar range. The basal signal of ATR was very low and thus measuring it was affected by high background noise. Under the same condition used for eFRET, fluorescence signal could rarely be detected for Arch(D95N) supplemented with ATR. Higher absolute gray values comparable with Arch(D95N)+DMAR could be achieved by increasing the concentration of ATR from 0.1 - 1 mM and the adjustment of the gain value of the EMCCD camera from 1 to 50. As described before, the background noise was still so high, that signal/background contrast was half of the values for Arch(D95N)+DMAR.

Arch(D95H) has shown a strong signal to background contrast, which was ca. twofold higher than its competitor Arch(D95N) for both DMAR and ATR. This comparison counts for the absolute gray values, respectively. The measured absolute gray value of Arch(D95H) supplemented with DMAR was comparable with MacQ-mCitrine. Its signal brightness was even ca. twice as strong as that of MacQ-mCitrine (but still 50% less than that of QuasAr-mOrange).

The analyzed gray values and signal luminosity of Arch(wt) equipped with analog VI were in the same range as Arch(D95N) with DMAR. As described before, this protein/chromophore combination did not show any voltage sensitivity. However, analog VI can be used to visualize the expression of Archaerhodopsin wildtype in the absence of a reporter gene/ fluorescence tag.

The basal fluorescence signal of all the GEVIs expressed in body wall muscles has been in a lower range in comparison to the sensors expressed in the pharynx. E.g., even under the same recording conditions, the absolute gray value measured for QuasAr-mOrange in pharyngeal muscle was 10-fold higher than in BWMs. This observation may be due to the natural structure of the pharynx in comparison to the body wall muscles. Besides this, the expression level differed in both tissues. As in the pharynx, the absolute gray values and luminosity of the eFRET sensor QuasAr-mOrange were higher than those of the two Arch-variants tested for direct imaging, namely Arch(D95N) and Arch(DETCDE). The luminosity of both direct imaging tools in BWMs was in the same range. However, the gray values of Arch(D95N) supplemented with ATR were higher in comparison to Arch(D95N) with DMAR and Arch(DETCDE) with both ATR and DMAR.

In general, and independent of the target tissue, the eFRET sensors deliver a brighter and stronger basal signal in comparison to direct imaging tools. However, the weak signal of ATR could be boosted by its substitution with ATR-analog. Above this, the application of ATR-analogs increases the chance for the combination of direct-imaging tools with other optogenetic tools, since analogs can alter the properties of opsins.

4.4: Competence of the different GEVIs in monitoring electrical activity along the plasma membrane

GEVIs with the most stable expression and the strongest basal fluorescence signal were then tested for their ability and sensitivity for monitoring electrical activity.

It could be shown that the absolute fluorescence of a GEVI does not warrant its voltage sensitivity.

Considering the basal fluorescence signal in both eFRET sensors, namely QuasAr-mOrange or MacQ-mCitrine expressed in the pharynx, one would expect QuasAr-mOrange should also be the better GEVI because of its ca. 4x stronger basal fluorescence signal. However, MacQ-mCitrine has shown ca. 2.5 folds stronger sensitivity in monitoring the electrical activity of pharyngeal muscles (- 25% ∆F/F MacQ-mCitrine vs. -10% ∆F/F QuasAr-mOrange). Using the eFRET sensors, one can read out not only membrane voltage, but at the same time also pharyngeal activities such as timing and extent of contraction, and correlate this to AP onset and duration. Both sensors could monitor an alteration in the measured ∆F/F in *egl-19* mutants (up to 35- 50% reduction for *egl-19(n2368)* and 5% reduction for egl-*19(n582ad952)*). Furthermore, previously described prolonged pumping properties (ref) in *egl-19* mutants could be monitored with both eFRET-sensors as well.

The other imaging tools were the two non-pumping mutant variants of Arch, namely Arch(D95N) and Arch(D95H), for direct observation of fluorescence changes in rhodopsin during voltage changes. These have been supplemented with ATR and the retinal-analog DMAR. Although the basal fluorescence of these sensors was low and also exhibited a low SNR after supplementation with ATR, the mean of the fluorescence fluctuations (∆F/F [%]) was very high (~130% for Arch(D95N) and 70% for Arch(D95H)). Substitution of ATR with its analog DMAR improved the basal fluorescence and luminosity; however, the sensitivity for monitoring action potentials was not accordingly higher compared to ATR. The measured amplitude was ~23% ∆F/F, which is in a similar range to MacQ-mCitrine.

A new phenomenon was observed for Arch(D95H) with DMAR, namely the reduction of the fluorescence signal during pump events, which may be due to the alterations in the photocycle of the opsin in combination with DMAR. It was reported that Arch(D95H) is a mutant with optical bistability, which reaches its fluorescence state after illumination with blue light, and red light stimulates this fluorescence (Brinks *et al.*, 2016). Based on the experiences with the red-shifted activation spectrum of DMAR, Arch(D95H) was illuminated only with red light during the experiments and no blue light. This might be the reason for the observed reduction in the fluorescence signal during the action potential. It seems that the described blue light illumination (Brinks *et al.*, 2016) is inevitable to provoke the fluorescent state of Arch(D95H) and reaching the highest voltage sensitive stage of the photo cycle of this opsin. Besides this, it was reported before, that outward photocurrents of about 5 pA could be measured with this mutant. Although these currents are 200 times lower than the reported currents of Arch(wt), they might affect the strength of the voltage sensitivity of this sensor [114].

Arch(D95N) was also tested in *egl-19(n2368)* mutants. The obtained results match with the observations made using the eFRET sensors. 45-50% reduction in the signal amplitude (compared to wt) could be measured with Arch(D95N) supplemented with ATR or DMAR in *egl-19(n2368)*. This sensor was also able to monitor the alteration in pumping properties in *egl-19(n2368)* mutants.

Moreover, it could be shown that the application of Nemadipine- A (Nema-A), which is a blocker of the L-type voltage-gated calcium channel, could 'revert' the modified properties of the signals of pharyngeal action potentials caused by *egl-19* mutations. Especially the voltage-sensitive fluctuations in the fluorescence signals, which have been significantly lower (or have shown a tendency in the reduction of the signal) in *egl-19* mutants, could be restored to values in a similar range to non-treated wild type animals. There has been evidence that DMSO, which is the solvent of Nema-A, affects the electrical activity of the membrane. DMSO is broadly used in cell biology as a cryoprotectant or drug vehicle. It has been known that it induces cell fusion and cell differentiation (Yu and Quinn, 1998) and increases membrane permeability. Molecular dynamics (MD) simulations assume three modes of action of DMSO for this increased permeability: membrane loosening, pore formation, and bilayer collapse (de Ménorval *et al.*, 2012). Although the effects of DMSO on the membrane structure have been studied well, the mechanism by which DMSO invokes its effect on lipid membranes is still unknown. During the experimental procedure, the analyzed $\Delta F/F(\%)$ for DMSO-treated animals, was not in the same range for all the sensors. Although the expression of the GEVIs did not affect the functionality of the pharynx, however, their expression might have influenced the structure of the membrane in a manner that the described strategies of DMSO on enhancing the membrane permeability resulted in different $\Delta F/F$ values.

However, the effect of Nema-A in the reversion of the optical signals of pharyngeal action potentials back to a comparable level with non-treated wild type animals could be observed with all the studied sensors. It seems that both Nema-A and DMSO affect the voltage gated calcium channels, however the combination of both drug and vehicle abolishes the effects of pure DMSO.

Above this, eFRET sensors could monitor the rescue effect of Nema-A on pumping properties. After the Nema-A application, the prolonged pump duration of mutant animals was set back to a time scale measured for wild type animals. This observation is consistent with the already described rescue effect of Nema-A on pumping properties (Schüler *et al.*, 2015), emphasizing the ability of voltage indicators in monitoring electrical activities of the cell membrane in the pharynx.

4.5: Optical electropharyngeogram (Opto-EPG)

The pharynx is an organ consisting of differently acting anterior and posterior compartments. This compartmentation is a barrier in electrophysiology and makes sectional measurements very difficult. To analyze the development of voltage in different sections of pharynx “difference videos” were generated as described. Analysis of the fluorescence changes derived from the whole pharynx resembles an electrically measured EPG. The signals achieved from this so- called “optical EPG or opto-EPG” show typical excitatory and inhibitory spikes, which have been measured in electrophysiology. Above this it was also possible to analyze the electrical activity in an ensemble of electrically coupled cells in a spatiotemporal fashion along the longitudinal axis of pharynx. The analysis of the compartmentalized pharyngeal voltage made it possible to explore smaller subsections at the connection site of both compartments with noticeable electrical activity during anterior-posterior depolarization and repolarization. This observation can be evaluated in further projects using mutated animals with, e.g., malfunctions in gap-junctions or some specific cells.

4.6: Electrophysiology in pharyngeal and body wall muscles for calibration of optically measured voltage signals

Electrophysiological measurements have been performed to calibrate the optically monitored action potentials in the pharynx (by Dr. Schüler) and in body wall muscles (by Dr. Liewald).

Membrane voltage was recorded via sharp electrodes simultaneously to optical voltage imaging in a dissected pharynx expressing MacQ-mCitrine (Fig. R-49). The fluctuation in the pharyngeal signals could be calibrated precisely with this approach. This was ca. 20% $\Delta F/F$ per 100 mV in MacQ-mCitrine, corresponding ca. 10.5% $\Delta F/F$ per 100 mV for QuasAr-mOrange in pharyngeal muscles. The τ_{on} value, which represents the rising time of the signal, is for electrically measured signals in a dissected pharynx ca. 7.5 ms (Fig. R-49), and for an optically measured signal during *in-vivo* imaging ca. 12.5 ms (Fig. R-22, Panel F) in a similar range. However, the optically measured signal in a dissected animal is ca. 4x slower (Tau_{on}= 29.7 ms, see Fig. R-49) than the electrically measured voltage changes via sharp electrodes.

The calibration of signal fluctuations in body wall muscles was performed indirectly. This was achieved by the combination of blue light stimulation of an optical actuator, namely channelrhodopsin and red-shifted voltage imaging (QuasAr-mOrange at ca. 560nm and >700 nm for Arch(D95N)).

For this aim, evoked action potentials were recorded via the current clamp in animals expressing channelrhodopsin in cholinergic neurons. Channelrhodopsin stimulation induced the depolarization of cholinergic neurons and thus neurotransmitter release, which in turn led to the depolarization of muscle cells. Such evoked APs have been recorded with a mean of ca. 29 mV in current-clamp experiments. On the other hand, such evoked APs have shown up to 10% $\Delta F/F$ corresponding 34% $\Delta F/F$ per 100 mV.

The application of blue light for channelrhodopsin stimulation and orange-infrared voltage imaging is a new all-optical setup in electrophysiology, overcoming the complicated performance of electrophysiology in dissected animals. The all-optical method reveals a highlighted advantage in comparison to classical electrophysiology since it is performed in intact animals, which supports the endogenous physiological properties and prohibits any possible changes due to extracellular and pipette solution, which may affect the natural physiology in a dissected animal during the clamping procedure.

4.7: ATR-analogs

In an earlier project, several retinal-analogs have been introduced for the application in optogenetics, altering some opsin properties. In this project, two of those already described analogs are represented with a new feature, namely a bright fluorescence. Analog II (DMAR) reveals an infrared emission spectrum, which tuns this analog into an interesting choice for combining it with blue-shifted optogenetic tools. This characteristic helps to overcome the problem of overlapping spectra during the combination of different optogenetic tools. As described earlier, this analog shows a high luminosity and SNR in comparison to ATR, and it does not need high laser intensities or a sensitive camera to be observed. Interestingly the bright infrared fluorescence could be observed only in Archaerhodopsin mutated variants. It is possible to equip Arch(wt) or channelrhodopsin with DMAR while reserving their natural activity as a hyper- or depolarizer (with a red-shifted action spectrum); however, DMAR reveals no fluorescence in these proteins. This observation strengthens the hypothesis that in pump-dead variants of opsins, the energy, which initially is needed to activate the photocycle and thus the ion transfer, runs "in reverse" and becomes emitted (Fig. I-12, (Looger, 2012)).

Another introduced retinal-analog is analog VI. Interestingly, this analog can be incorporated only in wild type Archaerhodopsin. It was not possible to equip neither any of the studied Arch-mutants nor channelrhodopsin with analog VI. This chromophore is not able to activate the opsin during light illumination, meaning the cells expressing Arch(wt) or channelrhodopsin cannot be hyper- or depolarized after illumination if they are supplemented with analog VI. This might be due to the absence of two methyl-groups in its structure compared to the structure of the original ATR (see Fig. I-16). Nevertheless, it can be used as an expression marker in the absence of any other fluorescence reporter protein.

4.8: Analysis with the automated custom workflow

An R script was customized by Dr. W. Steuer Costa, enabling the automatic detection of the read-out signals in the form of minima to synchronize all the monitored voltage and pump signals. Although the detected minima have been verified through manual quality control, this script has eased the analysis tremendously and made it possible to synchronize and evaluate more than 1500 pump and voltage signals from hundreds of animals. Extracting the properties of the signals such as signal duration, τ-values, and pump-signal-delay facilitated the characterization of the sensors, which has given hints about the sensitivity and the potential of each of the studied sensors in monitoring electrical activity. The mathematical function, which mostly resembles the form of the optical signals is an exponential function that was used for fitting the monitored signals. Since the R script needs a clearly defined structure of an exponential function to analyze the τ-values of a signal, and not all the signals reveal the typical form of an exponential function, the numbers of the peaks and thus the animals, which were used for the final analysis of the τ-values were significantly reduced.

4.9: Outlook

The achieved results of this work, namely the establishment of GEVIs with robust signal and sensitivity in *C. elegans,* are the basis for further studies of neuronal circuits in this nematode as a simple model organism. In addition to the GEVIs generated in the framework of this doctoral thesis, it was possible to test also QuasAr and Archon as further tools for direct imaging in body wall muscles to supplement the imaging toolbox. The generation of this sensor and the experimental procedure were performed by Amelie Bergs. The monitored signals by these two sensors could be calibrated by the analysis of the optogenetically evoked de- or hyperpolarization of cholinergic motor neurons via the stimulation with either channelrhodopsin or ACR2. Upon ChR2 stimulation ∆F/F increase ca 22% for QuasAr and 13.3% for Archon. Hyperpolarization of cholinergic motor neurons led to a drop of ~14.6% ∆F/F. These correspond ca. 78% ∆F/F per 100 mV for QuasAr and 45% ∆F/F per 100 mV for Archon, which is consistent with already reported data (Piatkevich *et al.*, 2018), (Hochbaum *et al.*, 2014) (Fig. D-1).

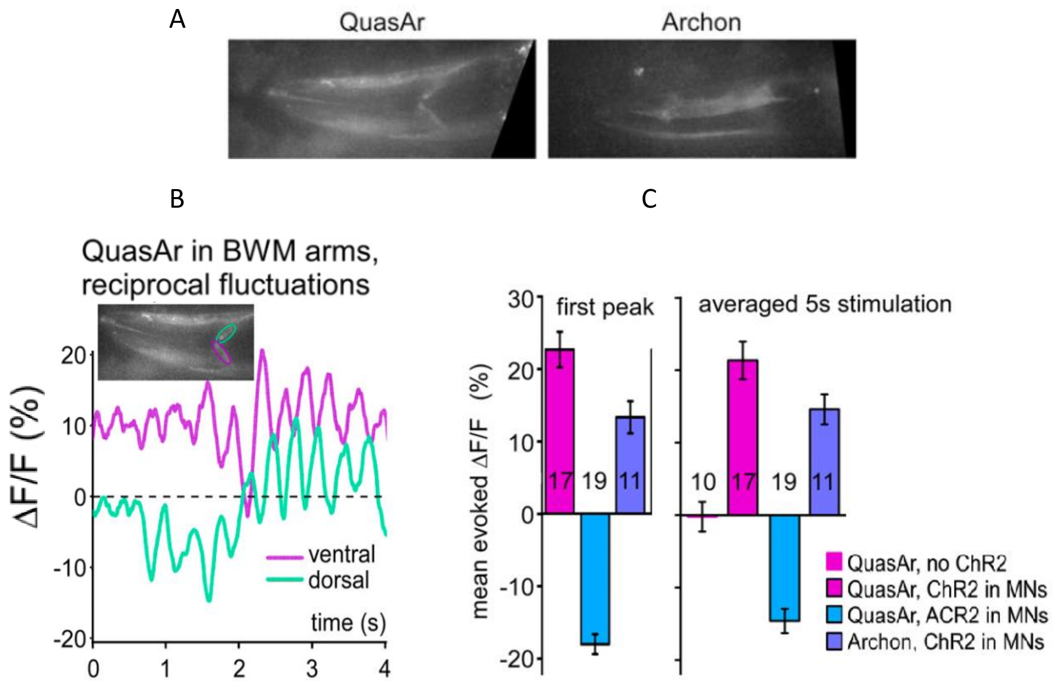

Fig. D-1: QuasAr and Archon as further voltage imaging tools in BWMs. A) Expression of QuasAr and Archon in BWMs. B) Reciprocal voltage changes in BWM arms of a representative animal expressing QuasAr. C) Mean of the evoked ∆F/F for the first peak and the averaged 5 ms blue light illumination (Experiments performed and analyzed by Amelie Bergs, modified from (Azimi Hashemi *et al.*, 2019)

The next aim after the establishment of GEVIs in muscles was to generate stable transgenic animals with GEVIs expressed in neurons. As already mentioned, there have been efforts during this project to express GEVIs in cholinergic and PVD neurons. However, the first neurons, whose electrical activity could be monitored via a GEVI (QuasAr) in the Gottschalk lab was the interneuron RIM (RIML and RIMR, see fig. D-2, left); the strain was generated and analyzed by Amelie Bergs). RIM shows slow changes in the fluorescence signal monitored by QuasAr, which is in line with Ca^{+2}-imaging from this interneuron. During voltage imaging in RIM, signals $< 1\%$ $\Delta F/F$ could be observed (fluctuations in black in figure D-1) that indicated phases of lacking strong activity. These fluctuations were interrupted by stronger signal fluctuations representing the de- and repolarization of RIM upon forward and reverse locomotion (Fig. D-1, green and pink shaded fluctuations).

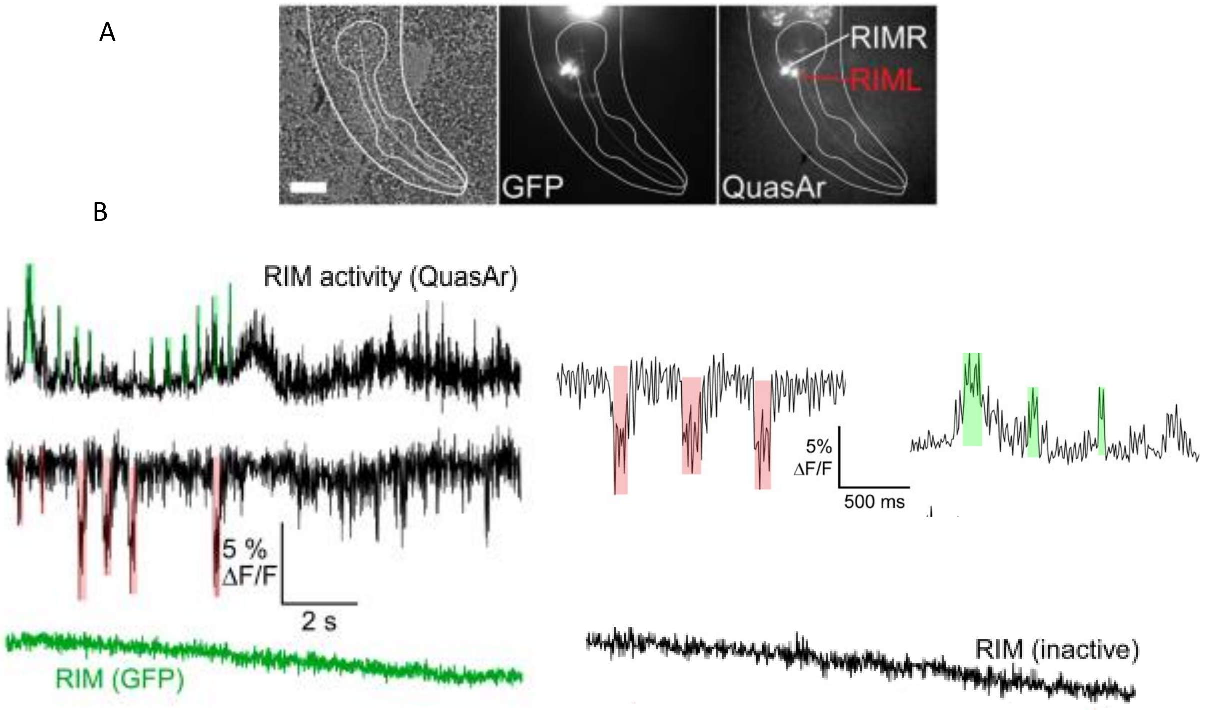

Fig. D-2: The expression of QuasAr in RIM and voltage monitoring in RIM via QuasAr. A) RIM is a set of interneurons located around the isthmus of the pharynx with cell bodies in the lateral ganglia of the head. RIM connects the muscles in the head via neuromuscular junctions to the nerve ring. The expression of QuasAr in RIM enabled voltage imaging in RIM. B) Fluctuations in the fluorescence signal during excitatory (green shaded) and inhibitory events (shaded rose).GFP-trace in green shown no fluctuations, but only photobleaching. Amelie Bergs did the experiments and the analysis (Modified from (Azimi Hashemi *et al.*, 2019)).

Additional to RIM, QuasAr was expressed in cholinergic motor neurons as well. It was possible to monitor rapid fluctuations in the fluorescence signal of ca. 4% ∆F/F in retrovesicular ganglion motor neurons. Cholinergic neurons are known to have graded potentials, whereas RIM has a bi-stable membrane potential (Piatkevich *et al.*, 2018). This difference in the activity pattern between these two group of neurons could be monitored with the rhodopsin-based voltage indicator, allowing the characterization of intrinsic neuronal and circuit activity (Azimi Hashemi *et al.*, 2019).

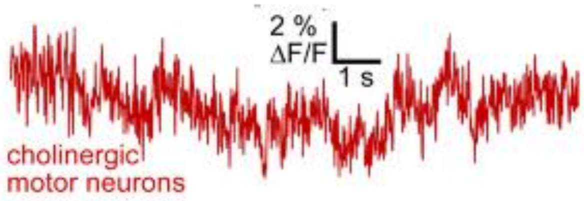

Fig. D-3: QuasAr fluorescence traces in cholinergic motorneurons. Rapid fluctuation up to ca. 4% ∆F/F could be monitored by QuasAr in cholinergic neurons. (Performance and analysis of the experiment: Amelie Bergs, (Azimi Hashemi *et al.*, 2019)).

One prominent advantage of the voltage indicators for direct imaging, namely their activation and emission spectrum in the infrared region of the light spectrum, enables the combination of these GEVIs with other optogenetic tools for up- or downstream activation or inhibition of the neuron of interest. This is, e.g., interesting for future studies about RIM or other mutants with defects in the neuromuscular junction, which are very small and difficult to be accessed for electrophysiology experiments by dissection. This combination of inhibitory- excitatory- imaging tools will enable all-optical electrophysiology in intact animals to explore neuronal circuits. The application of various ATR- analogs with red or blue-shifted activation- emission spectrum may further extend the versatility of this all-optical system.

5 References

Abdelfattah, A. S. *et al.* (2016) ‘A bright and fast red fluorescent protein voltage indicator that reports neuronal activity in organotypic brain slices’, *Journal of Neuroscience*. doi: 10.1523/JNEUROSCI.3484-15.2016.

Adam, Y. *et al.* (2019) ‘Voltage imaging and optogenetics reveal behaviour-dependent changes in hippocampal dynamics’, *Nature*. doi: 10.1038/s41586-019-1166-7.

Akemann, W. *et al.* (2010) ‘Imaging brain electric signals with genetically targeted voltage-sensitive fluorescent proteins’, *Nature Methods*. doi: 10.1038/nmeth.1479.

Akemann, W. *et al.* (2012) ‘Imaging neural circuit dynamics with a voltage-sensitive fluorescent protein’, *Journal of Neurophysiology*. doi: 10.1152/jn.00452.2012.

Akerboom, J. *et al.* (2012) ‘Optimization of a GCaMP calcium indicator for neural activity imaging’, *Journal of Neuroscience*. doi: 10.1523/JNEUROSCI.2601-12.2012.

Akerboom, J. *et al.* (2013) ‘Genetically encoded calcium indicators for multi-color neural activity imaging and combination with optogenetics’, *Frontiers in Molecular Neuroscience*. doi: 10.3389/fnmol.2013.00002.

Albeck, A. *et al.* (1989) ‘Factors affecting the absorption maxima of acidic forms of bacteriorhodopsin. A study with artificial pigments’, *Biophysical Journal*. doi: 10.1016/S0006-3495(89)82773-0.

Albertson, D. G. and Thomson, J. N. (1976) ‘The pharynx of Caenorhabditis elegans.’, *Philosophical transactions of the Royal Society of London. Series B, Biological sciences*. doi: 10.1098/rstb.1976.0085.

Alfonso, A. *et al.* (1993) ‘The Caenorhabditis elegans unc-17 gene: A putative vesicular acetylcholine transporter’, *Science*. doi: 10.1126/science.8342028.

All, A. H. *et al.* (2019) ‘Expanding the Toolbox of Upconversion Nanoparticles for In Vivo Optogenetics and Neuromodulation’, *Advanced Materials*, 1803474, p. 1803474. doi: 10.1002/adma.201803474.

Altun, Z. F. and Hall, D. H. (2009) *Worm Atlas*, *Wormatlas*. doi: 10.3908/wormatlas.1.14. Edited for the web by Laura A. Herndon. Last revision: April 30, 2012.

Altun, Z. F. and Hall, D. H. (2010) ‘Nervous system, neuronal support cells’, in *WormAtlas*. doi: 10.3908/wormatlas.1.19.

Ataka, K. and Pieribone, V. A. (2002) ‘A genetically targetable fluorescent probe of channel gating with rapid kinetics', *Biophysical Journal*. doi: 10.1016/S0006-3495(02)75415-5.

Avery, L. and Horvitzt, H. R. (1989) 'Pharyngeal pumping continues after laser killing of the pharyngeal nervous system of C. elegans', *Neuron*. doi: 10.1016/0896-6273(89)90206-7.

Avery, L. and Shtonda, B. B. (2003) 'Food transport in the C. elegans pharynx', *Journal of Experimental Biology*. doi: 10.1242/jeb.00433.

Azimi Hashemi, N. *et al.* (2019) ' Rhodopsin-based voltage imaging tools for use in muscles and neurons of Caenorhabditis elegans ', *Proceedings of the National Academy of Sciences*. doi: 10.1073/pnas.1902443116.

Azimihashemi, N. *et al.* (2014) 'Synthetic retinal analogues modify the spectral and kinetic characteristics of microbial rhodopsin optogenetic tools', *Nature Communications*. doi: 10.1038/ncomms6810.

Baker, B. J. *et al.* (2005) 'Imaging brain activity with voltage- and calcium-sensitive dyes', *Cellular and Molecular Neurobiology*. doi: 10.1007/s10571-005-3059-6.

Bamann, C. *et al.* (2008) 'Spectral Characteristics of the Photocycle of Channelrhodopsin-2 and Its Implication for Channel Function', *Journal of Molecular Biology*. doi: 10.1016/j.jmb.2007.10.072.

Bamann, C., Nagel, G. and Bamberg, E. (2010) 'Microbial rhodopsins in the spotlight', *Current Opinion in Neurobiology*. doi: 10.1016/j.conb.2010.07.003.

Bando, Y., Sakamoto, M., *et al.* (2019) 'Comparative Evaluation of Genetically Encoded Voltage Indicators', *Cell Reports*. doi: 10.1016/j.celrep.2018.12.088.

Bando, Y., Grimm, C., *et al.* (2019) 'Genetic voltage indicators'. BMC Biology, pp. 1–12.

Barnett, L. *et al.* (2012) 'A Fluorescent, Genetically-Encoded Voltage Probe Capable of Resolving Action Potentials', *PLoS ONE*. doi: 10.1371/journal.pone.0043454.

Beck, C., Zhang, D. and Gong, Y. (2019) 'Enhanced genetically encoded voltage indicators advance their applications in neuroscience', *Current Opinion in Biomedical Engineering*. doi: 10.1016/j.cobme.2019.10.010.

Bergs, A. *et al.* (2018) 'Rhodopsin optogenetic toolbox v2.0 for light-sensitive excitation and inhibition in Caenorhabditis elegans', *PLoS ONE*. doi: 10.1371/journal.pone.0191802.

Berndt, A. *et al.* (2009) 'Bi-stable neural state switches', *Nature Neuroscience*. doi: 10.1038/nn.2247.

Berndt, A. *et al.* (2014) ‘Structure-guided transformation of channelrhodopsin into a light-activated chloride channel’, *Science*. doi: 10.1126/science.1252367.

Boyden, E. S. *et al.* (2005) ‘Millisecond-timescale, genetically targeted optical control of neural activity’, *Nature Neuroscience*. doi: 10.1038/nn1525.

Boyden, E. S. (2011) ‘A history of optogenetics: The development of tools for controlling brain circuits with light’, *F1000 Biology Reports*. doi: 10.3410/B3-11.

Brinks, D. *et al.* (2016) ‘Painting with Rainbows: Patterning Light in Space, Time, and Wavelength for Multiphoton Optogenetic Sensing and Control’, *Accounts of Chemical Research*. doi: 10.1021/acs.accounts.6b00415.

Brown, J. *et al.* (2018) ‘Expanding the Optogenetics Toolkit by Topological Inversion of Rhodopsins’, *Cell*. doi: 10.1016/j.cell.2018.09.026.

Brown, L. S. (2004) ‘Fungal rhodopsins and opsin-related proteins: Eukaryotic homologues of bacteriorhodopsin with unknown functions’, *Photochemical and Photobiological Sciences*. doi: 10.1039/b315527g.

Carandini, M. *et al.* (2015) ‘Imaging the awake visual cortex with a genetically encoded voltage indicator’, *Journal of Neuroscience*. doi: 10.1523/JNEUROSCI.0594-14.2015.

Chanda, B. *et al.* (2005) ‘A hybrid approach to measuring electrical activity in genetically specified neurons’, *Nature Neuroscience*. doi: 10.1038/nn1558.

Chen, T. W. *et al.* (2013) ‘Ultrasensitive fluorescent proteins for imaging neuronal activity’, *Nature*. doi: 10.1038/nature12354.

Chien, M.-P. *et al.* (2017) ‘Two-photon photoactivated voltage imaging in tissue with an Archaerhodopsin-derived reporter’, *bioRxiv*. doi: 10.1101/211946.

Chow, B. Y. *et al.* (2010) ‘High-performance genetically targetable optical neural silencing by light-driven proton pumps’, *Nature*. doi: 10.1038/nature08652.

Clair, E. C. S. *et al.* (2012) ‘Conformational changes in the archaerhodopsin-3 proton pump: Detection of conserved strongly hydrogen bonded water networks’, *Journal of Biological Physics*. doi: 10.1007/s10867-011-9246-4.

Saint Clair, E. C. *et al.* (2012) ‘Near-IR resonance Raman spectroscopy of archaerhodopsin 3: Effects of transmembrane potential’, *Journal of Physical Chemistry B*. doi: 10.1021/jp309996a.

Cohen, L. B. and Lesher, S. (1986) ‘Optical monitoring of membrane potential: methods of multisite optical measurement.’, *Society of General Physiologists series*.

Cook, A., Franks, C. J. and Holden-Dye, L. (2006) ‘Electrophysiological recordings from the pharynx.’, *WormBook : the online review of C. elegans biology*.

Corsi, A. K. (2006) ‘A biochemist’s guide to C. elegans’, *Analytical biochemistry*. doi: 10.1016/j.bbi.2008.05.010.

Davis, M. W. *et al.* (1999) ‘A mutation in the C. elegans EXP-2 potassium channel that alters feeding behavior’, *Science*. doi: 10.1126/science.286.5449.2501.

Deisseroth, K. *et al.* (2006) ‘Next-Generation Optical Technologies for Illuminating Genetically Targeted Brain Circuits’, *Nature Methods*, 26(41), pp. 10380–10386. doi: 10.1523/JNEUROSCI.3863-06.2006.

Deisseroth, K. (2011) ‘Optogenetics’, *Commentary*, 8(1), pp. 26–29. doi: 10.1038/NMETH.F.324.

Deisseroth, K. (2015) ‘Optogenetics: 10 years of microbial opsins in neuroscience’, *Nature Neuroscience*. doi: 10.1038/nn.4091.

Dimitrov, D. *et al.* (2007) ‘Engineering and characterization of an enhanced fluorescent protein voltage sensor’, *PLoS ONE*. doi: 10.1371/journal.pone.0000440.

Donald L Riddle (1997) ‘C. elegans II. 2nd edition’, *Cold Spring Harbor Laboratory Press*.

Dugué, G. P., Akemann, W. and Knöpfel, T. (2012) ‘A comprehensive concept of optogenetics’, *Brain*, 196, pp. 1–28. doi: 10.1016/B978-0-444-59426-6.00001-X.

Enami, N. *et al.* (2006) ‘Crystal Structures of Archaerhodopsin-1 and -2: Common Structural Motif in Archaeal Light-driven Proton Pumps’, *Journal of Molecular Biology*. doi: 10.1016/j.jmb.2006.02.032.

Encell, L. P. (2012) ‘Development of a Dehalogenase-Based Protein Fusion Tag Capable of Rapid, Selective and Covalent Attachment to Customizable Ligands’, *Current Chemical Genomics*. doi: 10.2174/1875397301206010055.

Erbguth, K. *et al.* (2012) ‘Bimodal Activation of Different Neuron Classes with the Spectrally Red-Shifted Channelrhodopsin Chimera C1V1 in Caenorhabditis elegans’, *PLoS ONE*. doi: 10.1371/journal.pone.0046827.

Ernst, O. P. *et al.* (2014) ‘Microbial and animal rhodopsins: Structures, functions, and molecular mechanisms’, *Chemical Reviews*. doi: 10.1021/cr4003769.

Fire, A. and Waterston, R. H. (1989) ‘Proper expression of myosin genes in transgenic nematodes.’, *The EMBO Journal*. doi: 10.1002/j.1460-2075.1989.tb08506.x.

Flytzanis, N. C. *et al.* (2014) ‘Archaerhodopsin variants with enhanced voltage-sensitive fluorescence in mammalian and Caenorhabditis elegans neurons’, *Nature*

Communications. doi: 10.1038/ncomms5894.
Foster, K. W. *et al.* (1989) ‘Activation of Chlamydomonas Rhodopsin in Vivo Does Not Require Isomerization of Retinal’, *Biochemistry*. doi: 10.1021/bi00428a061.
Foster, K. W. *et al.* (2011) ‘Evidence from Chlamydomonas on the photoactivation of rhodopsins without isomerization of their chromophore’, *Chemistry and Biology*. doi: 10.1016/j.chembiol.2011.04.009.
Franks, C. J. *et al.* (2002) ‘Ionic basis of the resting membrane potential and action potential in the pharyngeal muscle of Caenorhabditis elegans’, *Journal of Neurophysiology*. doi: 10.1152/jn.00233.2001.
Franks, C. J. *et al.* (2006) ‘Anatomy, physiology and pharmacology of Caenorhabditis elegans pharynx: A model to define gene function in a simple neural system’, *Invertebrate Neuroscience*. doi: 10.1007/s10158-006-0023-1.
Ganapathy, S. *et al.* (2017) ‘Retinal-Based Proton Pumping in the Near Infrared’, *Journal of the American Chemical Society*. doi: 10.1021/jacs.6b11366.
Gao, S. and Zhen, M. (2011) ‘Action potentials drive body wall muscle contractions in Caenorhabditis elegans’, *Proceedings of the National Academy of Sciences of the United States of America*. doi: 10.1073/pnas.1012346108.
‘Genome sequence of the nematode C. elegans: A platform for investigating biology’ (1998) *Science*. doi: 10.1126/science.282.5396.2012.
Gong, Y. *et al.* (2014) ‘Imaging neural spiking in brain tissue using FRET-opsin protein voltage sensors’, *Nature Communications*. doi: 10.1038/ncomms4674.
Gong, Y. *et al.* (2015) ‘High-speed recording of neural spikes in awake mice and flies with a fluorescent voltage sensor’, *Science*. doi: 10.1126/science.aab0810.
Gong, Y., Li, J. Z. and Schnitzer, M. J. (2013) ‘Enhanced Archaerhodopsin Fluorescent Protein Voltage Indicators’, *PLoS ONE*. doi: 10.1371/journal.pone.0066959.
Govorunova, E. G. *et al.* (2015) ‘Natural light-gated anion channels: A family of microbial rhodopsins for advanced optogenetics’, *Science*. doi: 10.1126/science.aaa7484.
Grenier, V. *et al.* (2019) ‘Spying on Neuronal Membrane Potential with Genetically Targetable Voltage Indicators’, *Journal of the American Chemical Society*. doi: 10.1021/jacs.8b11997.
Grimm, J. B. *et al.* (2015) ‘A general method to improve fluorophores for live-cell and single-molecule microscopy’, *Nature Methods*. doi: 10.1038/nmeth.3256.

Grinvald, A. *et al.* (1982) 'Improved fluorescent probes for the measurement of rapid changes in membrane potential', *Biophysical Journal*. doi: 10.1016/S0006-3495(82)84520-7.

Grinvald, A. *et al.* (1988) 'Optical imaging of neuronal activity', *Physiological Reviews*. doi: 10.1152/physrev.1988.68.4.1285.

Grinvald, A. and Hildesheim, R. (2004) 'VSDI: A new era in functional imaging of cortical dynamics', *Nature Reviews Neuroscience*. doi: 10.1038/nrn1536.

Hashemi, N. A. *et al.* (2019) 'Rhodopsin-based voltage imaging tools for use in excitable cells of Caenorhabditis elegans', *bioRxiv*. doi: 10.1101/544429.

Hendricks, M. (2012) 'Compartmentalized calcium dynamics in a C. elegans interneuron encode head movement', *Nature*. doi: 10.1038/nature11081.

Hinner, M. J., Hübener, G. and Fromherz, P. (2006) 'Genetic targeting of individual cells with a voltage-sensitive dye through enzymatic activation of membrane binding', *ChemBioChem*. doi: 10.1002/cbic.200500395.

Hochbaum, D. R. *et al.* (2014) 'All-optical electrophysiology in mammalian neurons using engineered microbial rhodopsins', *Nature Methods*. doi: 10.1038/NMETH.3000.

Hontani, Y. *et al.* (2019) 'Photoreaction Dynamics of Red-Shifting Retinal Analogues Reconstituted in Proteorhodopsin', *Journal of Physical Chemistry B*. doi: 10.1021/acs.jpcb.9b01136.

Hoppmann, C. and Wang, L. (2019) 'Genetically encoding photoswitchable click amino acids for general optical control of conformation and function of proteins', in *Methods in Enzymology*. doi: 10.1016/bs.mie.2019.04.016.

Hou, J. H., Venkatachalam, V. and Cohen, A. E. (2014) 'Temporal dynamics of microbial rhodopsin fluorescence reports absolute membrane voltage', *Biophysical Journal*. doi: 10.1016/j.bpj.2013.11.4493.

Husson, S. J. *et al.* (2012) 'Microbial light-activatable proton pumps as neuronal inhibitors to functionally dissect neuronal networks in C. elegans', *PLoS ONE*. doi: 10.1371/journal.pone.0040937.

Ihara, K. *et al.* (1999) 'Evolution of the archaeal rhodopsins: Evolution rate changes by gene duplication and functional differentiation', *Journal of Molecular Biology*. doi: 10.1006/jmbi.1998.2286.

Jin, L. *et al.* (2012) 'Single Action Potentials and Subthreshold Electrical Events Imaged in Neurons with a Fluorescent Protein Voltage Probe', *Neuron*. doi: 10.1016/j.neuron.2012.06.040.

Kannan, M. *et al.* (2018) ‘Fast, in vivo voltage imaging using a red fluorescent indicator’, *Nature Methods*. doi: 10.1038/s41592-018-0188-7.

Kato, H. E. *et al.* (2012) ‘Crystal structure of the channelrhodopsin light-gated cation channel’, *Nature*. doi: 10.1038/nature10870.

Knöpfel, T. *et al.* (2010) ‘Toward the second generation of optogenetic tools’, in *Journal of Neuroscience*. doi: 10.1523/JNEUROSCI.4190-10.2010.

Knöpfel, T., Díez-García, J. and Akemann, W. (2006) ‘Optical probing of neuronal circuit dynamics: Genetically encoded versus classical fluorescent sensors’, *Trends in Neurosciences*. doi: 10.1016/j.tins.2006.01.004.

Kocabas, A. *et al.* (2012) ‘Controlling interneuron activity in Caenorhabditis elegans to evoke chemotactic behaviour’, *Nature*. doi: 10.1038/nature11431.

Kralj, J. M. *et al.* (2011) ‘Electrical spiking in Escherichia coli probed with a fluorescent voltage-indicating protein’, *Science*. doi: 10.1126/science.1204763.

Kralj, J. M. *et al.* (2012) ‘Optical recording of action potentials in mammalian neurons using a microbial rhodopsin’, *Nature Methods*. doi: 10.1038/nmeth.1782.

Kuhn, B., Fromherz, P. and Denk, W. (2004) ‘High sensitivity of Stark-shift voltage-sensing dyes by one- or two-photon excitation near the red spectral edge’, *Biophysical Journal*. doi: 10.1529/biophysj.104.040477.

Lam, A. J. *et al.* (2012) ‘Improving FRET dynamic range with bright green and red fluorescent proteins’, *Nature Methods*. doi: 10.1038/nmeth.2171.

Li, X. *et al.* (2005) ‘Fast noninvasive activation and inhibition of neural and network activity by vertebrate rhodopsin and green algae channelrhodopsin’, *Proceedings of the National Academy of Sciences of the United States of America*. doi: 10.1073/pnas.0509030102.

Liewald, J. F. *et al.* (2008) ‘Optogenetic analysis of synaptic function’, *Nature Methods*. doi: 10.1038/nmeth.1252.

Lin, J. Y. (2010) ‘A user’s guide to channelrhodopsin variants: Features, limitations and future developments’, *Experimental Physiology*. doi: 10.1113/expphysiol.2009.051961.

Lin, M. Z. and Schnitzer, M. J. (2016) ‘Genetically encoded indicators of neuronal activity’, *Nature Neuroscience*. doi: 10.1038/nn.4359.

Liu, P. *et al.* (2017) ‘Fluorogenic Targeting of Voltage-Sensitive Dyes to Neurons’, *Journal of the American Chemical Society*. doi: 10.1021/jacs.7b07047.

Looger, L. L. (2012) ‘Running in reverse: Rhodopsins sense voltage’, *Nature*

Methods. doi: 10.1038/nmeth.1817.

Looger, L. L. and Griesbeck, O. (2012) ‘Genetically encoded neural activity indicators’, *Current Opinion in Neurobiology*. doi: 10.1016/j.conb.2011.10.024.

Mackinnon, A. C. *et al.* (2002) ‘C. elegans PAT-4/ILK functions as an adaptor protein within integrin adhesion complexes’, *Current Biology*. doi: 10.1016/S0960-9822(02)00810-2.

Maclaurin, D. *et al.* (2013) ‘Mechanism of voltage-sensitive fluorescence in a microbial rhodopsin’, *Proceedings of the National Academy of Sciences of the United States of America*. doi: 10.1073/pnas.1215595110.

Madisen, L. *et al.* (2012) ‘A toolbox of Cre-dependent optogenetic transgenic mice for light-induced activation and silencing’, *Nature Neuroscience*. doi: 10.1038/nn.3078.

Manathunga, M., Yang, X. and Olivucci, M. (2018) ‘Electronic State Mixing Controls the Photoreactivity of a Rhodopsin with all- trans Chromophore Analogues’, *Journal of Physical Chemistry Letters*. doi: 10.1021/acs.jpclett.8b02550.

Mango, S. E. (2007) ‘The C. elegans pharynx: a model for organogenesis.’, *WormBook : the online review of C. elegans biology*.

Mattis, J. *et al.* (2012) ‘Principles for applying optogenetic tools derived from direct comparative analysis of microbial opsins’, *Online*, 2012(deceMbeR 2011). doi: 10.1038/NMeth.1808.

McIsaac, R. S. *et al.* (2014) ‘Directed evolution of a far-red fluorescent rhodopsin’, *Proceedings of the National Academy of Sciences of the United States of America*. doi: 10.1073/pnas.1413987111.

de Ménorval, M. A. *et al.* (2012) ‘Effects of dimethyl sulfoxide in cholesterol-containing lipid membranes: A comparative study of experiments in silico and with cells’, *PLoS ONE*. doi: 10.1371/journal.pone.0041733.

Method of the Year 2010 Optogenetics : controlling cell function with light (2011) *Methods*. doi: 10.1038/Nmeth.F.321.

Miesenböck, G., De Angelis, D. A. and Rothman, J. E. (1998) ‘Visualizing secretion and synaptic transmission with pH-sensitive green fluorescent proteins’, *Nature*. doi: 10.1038/28190.

Miyawaki, A. *et al.* (1997) ‘Fluorescent indicators for Ca2+ based on green fluorescent proteins and calmodulin’, *Nature*. doi: 10.1038/42264.

Mukohata, Y. *et al.* (1988) ‘An Australian halobacterium contains a novel proton pump retinal protein: Archaerhodopsin’, *Biochemical and Biophysical Research*

Communications. doi: 10.1016/S0006-291X(88)80509-6.

Müller, M. *et al.* (2011) ‘Projection structure of channelrhodopsin-2 at 6 Å resolution by electron crystallography’, *Journal of Molecular Biology*. doi: 10.1016/j.jmb.2011.09.049.

Mutoh, H. *et al.* (2009) ‘Spectrally-resolved response properties of the three most advanced FRET based fluorescent protein voltage probes’, *PLoS ONE*. doi: 10.1371/journal.pone.0004555.

Nagel, G. *et al.* (2003) ‘Channelrhodopsin-2, a directly light-gated cation-selective membrane channel’, *Proceedings of the National Academy of Sciences of the United States of America*. doi: 10.1073/pnas.1936192100.

Nagel, G. *et al.* (2005) ‘Channelrhodopsins: Directly light-gated cation channels’, in *Biochemical Society Transactions*. doi: 10.1042/BST0330863.

Nagel, Georg *et al.* (2005) ‘Light activation of Channelrhodopsin-2 in excitable cells of caenorhabditis elegans triggers rapid behavioral responses’, *Current Biology*. doi: 10.1016/j.cub.2005.11.032.

Ng, D. N. and Fromherz, P. (2011) ‘Genetic Targeting of a Voltage-Sensitive Dye by Enzymatic Activation of Phosphonooxymethyl-ammonium Derivative’, in *ACS Chemical Biology*. doi: 10.1021/cb100312d.

Nikolaev, D. M. *et al.* (2017) ‘A voltage-dependent fluorescent indicator for optogenetic applications, archaerhodopsin-3: Structure and optical properties from in silico modeling [version 3; referees: 3 approved]’, *F1000Research*. doi: 10.12688/f1000research.10541.3.

Oesterhelt, D. and Stoeckenius, W. (1971) ‘Rhodopsin-like protein from the purple membrane of Halobacterium halobium’, *Nature New Biology*. doi: 10.1038/newbio233149a0.

Okazaki, A. *et al.* (2014) ‘Optical silencing of C. elegans cells with light-driven proton pumps’, *Methods*. doi: 10.1016/j.ymeth.2014.02.030.

Okazaki, A., Sudo, Y. and Takagi, S. (2012) ‘Optical silencing of c. elegans cells with arch proton pump’, *PLoS ONE*. doi: 10.1371/journal.pone.0035370.

Okkema, P. G. *et al.* (1993) ‘Sequence requirements for myosin gene expression and regulation in Caenorhabditis elegans’, *Genetics*.

Okkema, P. G. and Fire, A. (1994) ‘The Caenorhabditis elegans NK-2 class homeoprotein CEH-22 is involved in combinatorial activation of gene expression in pharyngeal muscle’, *Development*.

Perron, A. *et al.* (2009) ‘Second and third generation voltage-sensitive fluorescent proteins for monitoring membrane potential’, *Frontiers in Molecular Neuroscience*. doi: 10.3389/neuro.02.005.2009.

Piao, H. H. *et al.* (2015) ‘Combinatorial mutagenesis of the voltage-sensing domain enables the optical resolution of action potentials firing at 60 Hz by a genetically encoded fluorescent sensor of membrane potential’, *Journal of Neuroscience*. doi: 10.1523/JNEUROSCI.3008-14.2015.

Piatkevich, K. D. *et al.* (2018) ‘A robotic multidimensional directed evolution approach applied to fluorescent voltage reporters article’, *Nature Chemical Biology*. doi: 10.1038/s41589-018-0004-9.

Pirri, J. K. and Alkema, M. J. (2012) ‘The neuroethology of C. elegans escape’, *Current Opinion in Neurobiology*. doi: 10.1016/j.conb.2011.12.007.

Platisa, J. *et al.* (2017) ‘Directed Evolution of Key Residues in Fluorescent Protein Inverses the Polarity of Voltage Sensitivity in the Genetically Encoded Indicator ArcLight’, *ACS Chemical Neuroscience*. doi: 10.1021/acschemneuro.6b00234.

Raymond, Y. N. L. *et al.* (1997) ‘Mutations in the α1 subunit of an L-type voltage-activated Ca2+ channel cause myotonia in Caenorhabditis elegans’, *EMBO Journal*. doi: 10.1093/emboj/16.20.6066.

Sakai, R. *et al.* (2001) ‘Design and characterization of a DNA-encoded, voltage-sensitive fluorescent protein’, *European Journal of Neuroscience*. doi: 10.1046/j.0953-816X.2001.01617.x.

Salzberg, B. M. *et al.* (1977) ‘Optical recording of neuronal activity in an invertebrate central nervous system: simultaneous monitoring of several neurons’, *Journal of Neurophysiology*. doi: 10.1152/jn.1977.40.6.1281.

Schüler, C. *et al.* (2015) ‘Arrhythmogenic effects of mutated L-Type Ca 2+ -channels on an optogenetically paced muscular pump in Caenorhabditis elegans’, *Scientific Reports*. doi: 10.1038/srep14427.

Schultheis, C. *et al.* (2011) ‘Optogenetic long-term manipulation of behavior and animal development’, *PLoS ONE*. doi: 10.1371/journal.pone.0018766.

Shen, Y. C. *et al.* (2018) ‘Red-Tuning of the Channelrhodopsin Spectrum Using Long Conjugated Retinal Analogues’, *Biochemistry*. doi: 10.1021/acs.biochem.8b00583.

Shtonda, B. and Avery, L. (2005) ‘CCA-1, EGL-19 and EXP-2 currents shape action potentials in the Caenorhabditis elegans pharynx’, *Journal of Experimental Biology*. doi: 10.1242/jeb.01615.

Siegel, M. S. and Isacoff, E. Y. (1997) ‘A genetically encoded optical probe of membrane voltage’, *Neuron*. doi: 10.1016/S0896-6273(00)80955-1.

Song, B. mi and Avery, L. (2012) ‘Serotonin activates overall feeding by activating two separate neural pathways in Caenorhabditis elegans’, *Journal of Neuroscience*. doi: 10.1523/JNEUROSCI.2064-11.2012.

Spudich, J. L., Sineshchekov, O. A. and Govorunova, E. G. (2014) ‘Mechanism divergence in microbial rhodopsins’, *Biochimica et Biophysica Acta - Bioenergetics*. doi: 10.1016/j.bbabio.2013.06.006.

St-Pierre, F. *et al.* (2014) ‘High-fidelity optical reporting of neuronal electrical activity with an ultrafast fluorescent voltage sensor’, *Nature Neuroscience*. doi: 10.1038/nn.3709.

Stauffer, W. R. *et al.* (2016) ‘Dopamine Neuron-Specific Optogenetic Stimulation in Rhesus Macaques’, *Cell*. doi: 10.1016/j.cell.2016.08.024.

Steger, K. A. *et al.* (2005) ‘The C. elegans T-type calcium channel CCA-1 boosts neuromuscular transmission’, *Journal of Experimental Biology*. doi: 10.1242/jeb.01616.

Stehfest, K. and Hegemann, P. (2010) ‘Evolution of the channelrhodopsin photocycle model’, *ChemPhysChem*. doi: 10.1002/cphc.200900980.

Storace, D. A. *et al.* (2015) ‘Monitoring brain activity with protein voltage and calcium sensors’, *Scientific Reports*. doi: 10.1038/srep10212.

Sulston, J. E. *et al.* (1983) ‘The embryonic cell lineage of the nematode Caenorhabditis elegans’, *Developmental Biology*. doi: 10.1016/0012-1606(83)90201-4.

Sundukova, M. *et al.* (2019) ‘A Chemogenetic Approach for the Optical Monitoring of Voltage in Neurons’, *Angewandte Chemie - International Edition*. doi: 10.1002/anie.201812967.

Takahashi, M. and Takagi, S. (2017) ‘Optical silencing of body wall muscles induces pumping inhibition in Caenorhabditis elegans’, *PLoS Genetics*. doi: 10.1371/journal.pgen.1007134.

Trojanowski, N. F. *et al.* (2014) ‘Neural and genetic degeneracy underlies Caenorhabditis elegans feeding behavior’, *Journal of Neurophysiology*. doi: 10.1152/jn.00150.2014.

Trojanowski, N. F., Raizen, D. M. and Fang-Yen, C. (2016) ‘Pharyngeal pumping in Caenorhabditis elegans depends on tonic and phasic signaling from the nervous system’, *Scientific Reports*. doi: 10.1038/srep22940.

Tsutsui, H. *et al.* (2008) ‘Improving membrane voltage measurements using FRET with new fluorescent proteins’, *Nature Methods*. doi: 10.1038/nmeth.1235.

Tsutsui, H. *et al.* (2013) ‘Improved detection of electrical activity with a voltage probe based on a voltage-sensing phosphatase’, *Journal of Physiology*. doi: 10.1113/jphysiol.2013.257048.

Uegaki, K., Sugiyama, Y. and Mukohata, Y. (1991) ‘Archaerhodopsin-2, from Halobacterium sp. aus-2 further reveals essential amino acid residues for light-driven proton pumps’, *Archives of Biochemistry and Biophysics*. doi: 10.1016/0003-9861(91)90014-A.

White, J. G. *et al.* (1983) ‘Factors that determine connectivity in the nervous system of Caenorhabditis elegans.’, *Cold Spring Harbor Symposia on Quantitative Biology*.

White, J. G. *et al.* (1986) ‘The Structure of the Nervous System of the Nematode Caenorhabditis elegans’, *Philosophical Transactions of the Royal Society B: Biological Sciences*. doi: 10.1098/rstb.1986.0056.

Wiegert, J. S. *et al.* (2017) ‘Silencing Neurons: Tools, Applications, and Experimental Constraints’, *Neuron*. doi: 10.1016/j.neuron.2017.06.050.

Wietek, J. *et al.* (2014) ‘Conversion of channelrhodopsin into a light-gated chloride channel’, *Science*. doi: 10.1126/science.1249375.

Williams, B. D. and Waterston, R. H. (1994) ‘Genes critical for muscle development and function in Caenorhabditis elegans identified through lethal mutations’, *Journal of Cell Biology*. doi: 10.1083/jcb.124.4.475.

Williams, P. D. E. *et al.* (2018) ‘Serotonin disinhibits a caenorhabditis elegans sensory neuron by suppressing Ca2+-dependent negative feedback’, *Journal of Neuroscience*. doi: 10.1523/JNEUROSCI.1908-17.2018.

Xu, Y. *et al.* (2018) ‘Hybrid Indicators for Fast and Sensitive Voltage Imaging’, *Angewandte Chemie - International Edition*. doi: 10.1002/anie.201712614.

Xu, Y., Zou, P. and Cohen, A. E. (2017) ‘Voltage imaging with genetically encoded indicators’, *Current Opinion in Chemical Biology*. Elsevier Ltd, 39, pp. 1–10. doi: 10.1016/j.cbpa.2017.04.005.

Yang, H. H. H. *et al.* (2016) ‘Subcellular Imaging of Voltage and Calcium Signals Reveals Neural Processing In Vivo’, *Cell*. doi: 10.1016/j.cell.2016.05.031.

Yu, Z. W. and Quinn, P. J. (1998) ‘The modulation of membrane structure and stability by dimethyl sulphoxide’, *Molecular Membrane Biology*. doi:

10.3109/09687689809027519.

Zemelman, B. V *et al.* (2003) ‘Photochemical gating of heterologous ion channels : Remote control over genetically designated’, *PNAS*, 100(3).

Zhang, F. *et al.* (no date) ‘Primer The Microbial Opsin Family of Optogenetic Tools’, *Cell*. doi: 10.1016/j.cell.2011.12.004.

Zou, P. *et al.* (2014) ‘Bright and fast multicoloured voltage reporters via electrochromic FRET’, *Nature Communications*. doi: 10.1038/ncomms5625.

III List of the figures and tables:

IV Data and figure contributions

All procedures described in this study were done by me, if not noted otherwise. These include the cloning of DNA-plasmids, the creation of transgenic *C. elegans* lines, microscopy performance and the recordings of voltage imaging, data analysis and the creation of figures.

The contribution of colleagues to create some of the transgenic lines are listed in tables M-10 and M-11.

The recording of voltage imaging in *egl-19(n2368)* animals with MacQ-mCitrine and QuasAr-mOrange was performed by Rebecca Scheiwe, however, completely analyzed by me.

Custom-written scripts for the software R script and Knime for the analysis of voltage imaging were designed and provided by Dr. W. Steuer Costa.

Electrophysiology experiments were performed and analyzed by Dr. Jana Liewald and Dr. Christina Schüler.

The contribution of colleagues in the figures presented in this work is as following:

Fig. M-11: Schematic presentation of the detection and definition of pharyngeal APs and contractions by KNIME. The image was designed by Prof. A. Gottschalk. Adopted from (Azimi Hashemi *et al.*, 2019).

Fig. R-48: Electrical signals measured via current clamp in body wall muscles after ChR2 activation. All the experiments and analyses were performed by Dr. J. Liewald. The image was designed by Prof. A. Gottschalk. Adopted from (Azimi Hashemi *et al.*, 2019)

Fig. R-49: Electrophysiology in the pharyngeal muscle (terminal bulb; sharp electrode recordings) and EPGs, simultaneous and compared to optical AP measurements with MacQ-mCitrine. All the experiments and the analysis were performed by Dr. C. Schüler. The image was designed by Prof. A. Gottschalk. Adopted from (Azimi Hashemi *et al.*, 2019).

Fig. D-1: QuasAr and Archon as further voltage imaging tools in BWMs.

Fig. D-2: The expression of QuasAr in RIM and voltage monitoring in RIM via QuasAr.

Fig. D-3: QuasAr fluorescence traces in cholinergic motor neurons.

All the experiments and analyses presented in figures D1-D3 were performed by A. Bergs. Images were designed by Prof. A. Gottschalk. Adopted from (Azimi Hashemi *et al.*, 2019)).

V Plasmid maps

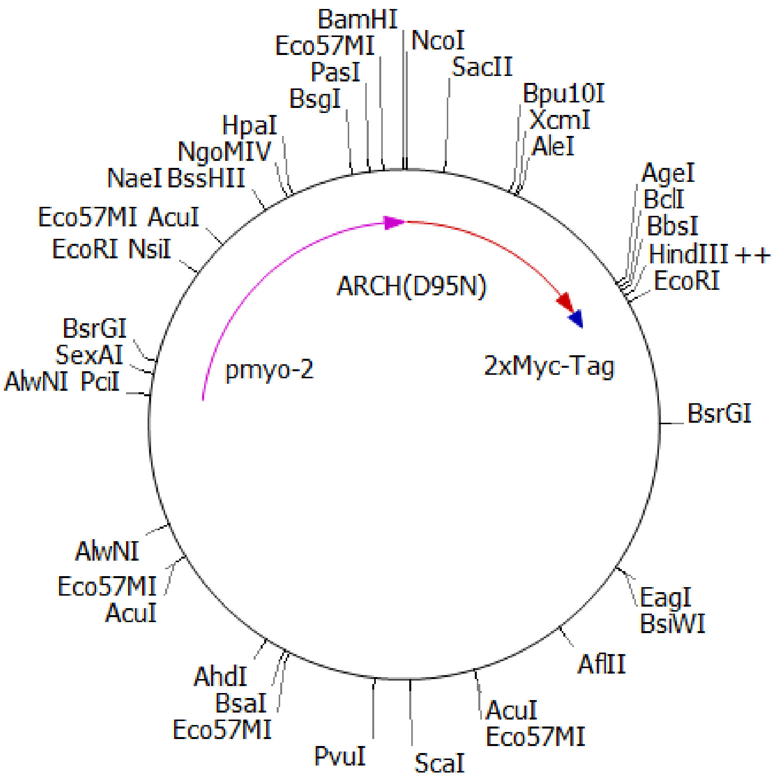

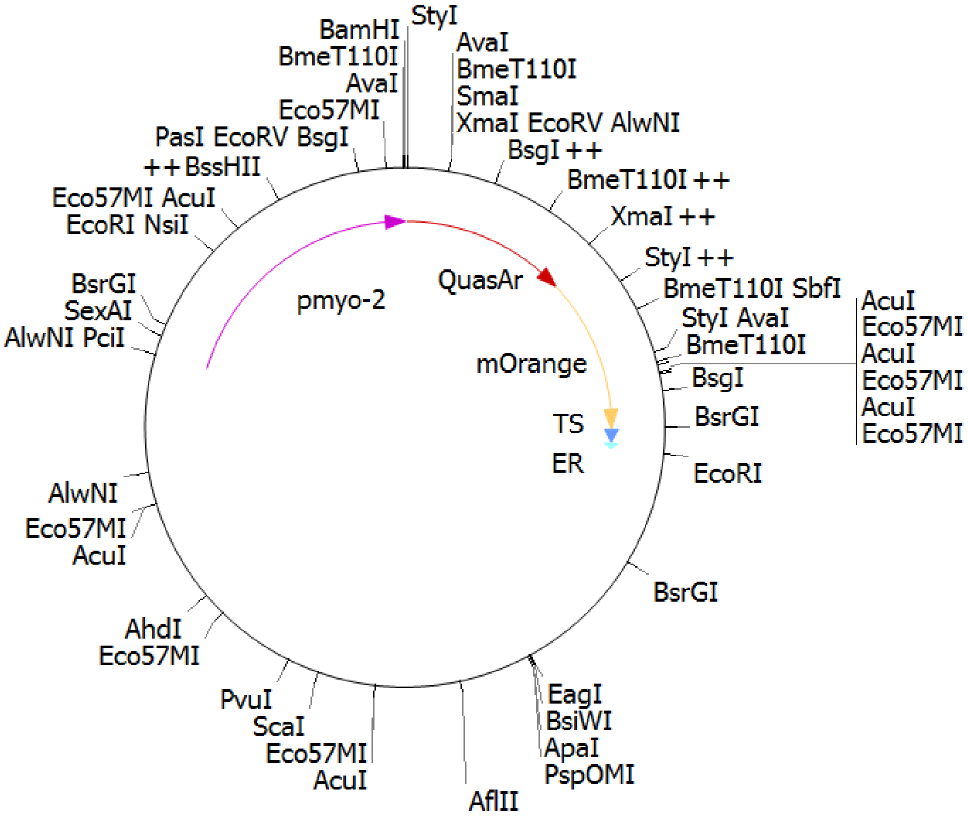

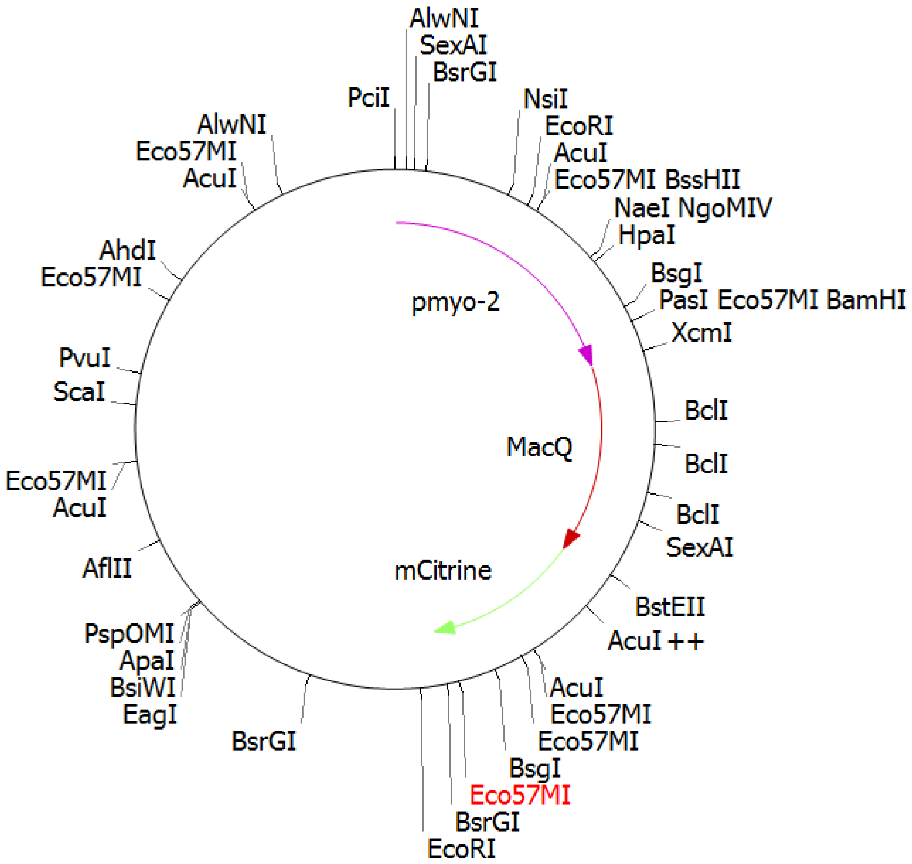
AlwNI
SexAI
BsrGI
PciI
NsiI
EcoRI
AcuI
Eco57MI BssHII
NaeI NgoMIV
HpaI
AlwNI
Eco57MI
AcuI
AhdI
Eco57MI
BsgI
PasI Eco57MI BamHI
XcmI
pmyo-2
PvuI
ScaI
BclI
BclI
MacQ
Eco57MI
AcuI
BclI
SexAI
AflII
mCitrine
BstEII
AcuI ++
PspOMI
ApaI
BsiWI
EagI
AcuI
Eco57MI
Eco57MI
BsrGI
BsgI
Eco57MI
BsrGI
EcoRI

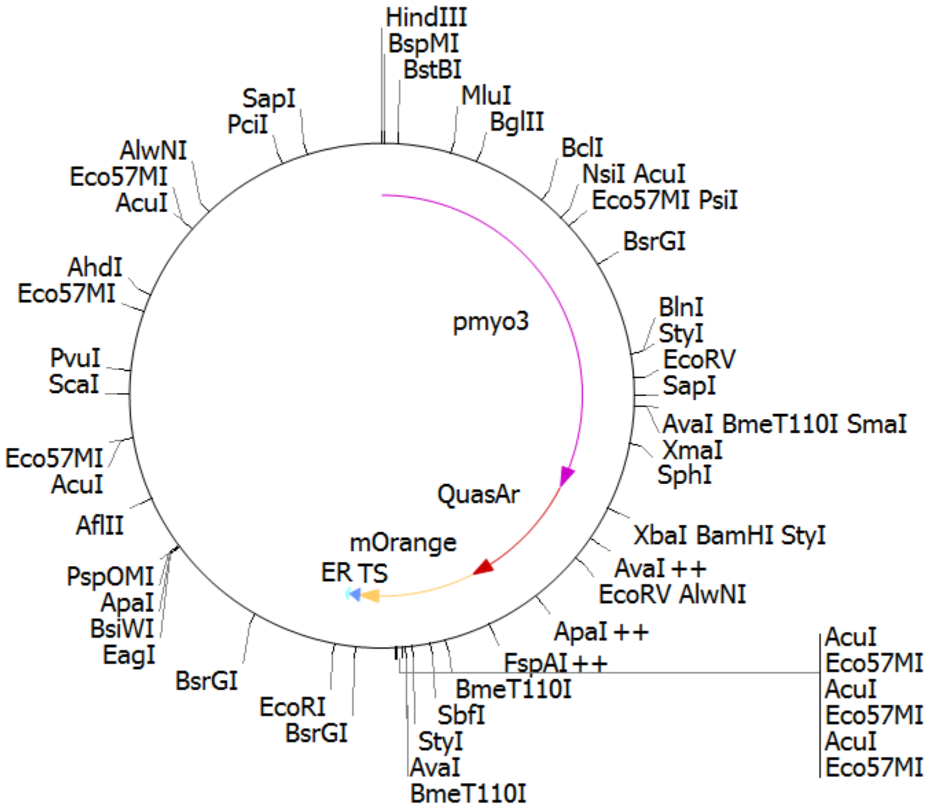
HindIII
BspMI
BstBI
MluI
BglII
SapI
PciI
AlwNI
Eco57MI
AcuI
BclI
NsiI AcuI
Eco57MI PsiI
BsrGI
AhdI
Eco57MI
pmyo3
BlnI
StyI
EcoRV
SapI
PvuI
ScaI
AvaI BmeT110I SmaI
XmaI
SphI
Eco57MI
AcuI
QuasAr
AflII
XbaI BamHI StyI
mOrange
AvaI ++
EcoRV AlwNI
ER TS
PspOMI
ApaI
BsiWI
EagI
ApaI ++
FspAI ++
AcuI
Eco57MI
AcuI
Eco57MI
AcuI
Eco57MI
BsrGI
EcoRI
BsrGI
BmeT110I
SbfI
StyI
AvaI
BmeT110I

VI Table of contents of CD-Rom

- PDF form of this thesis
- Video-records presented in this work:
    - I- MacQ-mCitrine w/o ATR
    - II- MacQ-mCitrine w/ ATR
    - III- QuasAr-mOrange
    - IV- Arch(D95N)+DMAR
    - V- Arch(D95N)+ATR
    - VI- Arch(D95H)+ATR
    - VII- Arch(D95H)+DMAR
    - IIX- “Difference video” of MacQ-mCitrine
    - IX- “Difference video” of Arch(D95N)
    - X- QuasAr-mOrange in BWMs
    - XI- Arch(D95N)+ATR in BWMs
    - XII- Arch(D95N)+DMAR in BWMs
    - XIII- Arch(DETCDE)+ATR in BWMs
    - XIV- Arch(DETCDE)+DMAR in BWMs